



Normandie Université

THÈSE

Pour obtenir le diplôme de doctorat

Spécialité : Énergetique

Préparé au sein du Laboratoire CORIA, UMR 6614 CNRS.

ÉTUDE NUMÉRIQUE DES INTERACTIONS ONDE DE CHOC/COUCHE LIMITE DANS LES TUYÈRES PROPULSIVES

présentée par

BOUBAKR ZEBIRI

**Thèse soutenue publiquement le 21 Sep 2020
devant le jury composé de**

Amer CHPOUN	Professeur, Université d'Evry-Val-d'Essone, France	Rapporteur
Paola CINNELLA	Professeure, Arts et Métiers-ParisTech, France	Rapporteur
Niklas ANDERSSON	Professeur, Chalmers University of Technology, Suède	Examinateur
Marie-Claude DRUGUET	Chargée de Recherches, CNRS, IUSTI UMR 7343, Aix-Marseille, France	Examinatrice
Pascale DOMINGO	Directrice de Recherches, CNRS, CORIA UMR 6614, France	Examinatrice
Olivier THOMINE	Ingénieur-Docteur, CEA Saclay, France	Examinateur
Mostafa S. SHADLOO	Maître de conférences, INSA de Rouen, France	Examinateur
Abdellah HADJADJ	Professeur, INSA de Rouen, France	Dir. de thèse

■ **Thèse dirigée par** Abdellah HADJADJ, CORIA UMR – 6614, CNRS, France.



Normandie Université

DISSERTATION

Submitted in the partial fulfillment for the award of Doctor of Philosophy

Specialized in : **Energetic**

From CORIA, UMR 6614 CNRS.

NUMERICAL STUDY OF SHOCK WAVE/BOUNDARY LAYER INTERACTIONS IN PROPULSIVE NOZZLES

by

BOUBAKR ZEBIRI

**Thesis defended publicly on the 21st Sep, 2020
in front of the jury comprising of:**

Amer CHPOUN	Professor, University of Evry-Val-d'Essone, France	Reviewer
Paola CINNELLA	Professor, Arts et Métiers-ParisTech, France	Reviewer
Niklas ANDERSSON	Professor, Chalmers University of Technology, Sweden	Examiner
Marie-Claude DRUGUET	Researcher, CNRS, IUSTI UMR 7343, Aix-Marseille, France	Examiner
Pascale DOMINGO	Research Director, CNRS, CORIA UMR 6614, France	Examiner
Olivier THOMINE	Engineer-Doctor, CEA Saclay, France	Examiner
Mostafa S. SHADLOO	Assistant professor, INSA Rouen, France	Examiner
Abdellah HADJADJ	Professor, INSA Rouen, France	Supervisor

■ Under the supervision of Abdellah HADJADJ, CORIA UMR – 6614, France.

Abstract

The need for a better understanding of the driving mechanism for the observed low-frequency unsteadiness in an over-expanded nozzle flows was discussed. The unsteady character of the shock wave/boundary layer remains an important practical challenge for the nozzle flow problems. Additionally, for a given incoming turbulent boundary layer, this kind of flow usually exhibits higher low-frequency shock motions which are less coupled from the timescales of the incoming turbulence. This may be good from an experimenter's point of view, because of the difficulties in measuring higher frequencies, but it is more challenging from a computational point of view due to the need to obtain long time series to resolve low-frequency movements. In excellent agreement with the experimental findings, a very-long LES simulation run was carried out to demonstrate the existence of energetic broadband low-frequency motions near the separation point. Particular efforts were done in order to avoid any upstream low-frequency forcing, and it was explicitly demonstrated that the observed low-frequency shock oscillations were not connected with the inflow turbulence generation, ruling out the possibility of a numerical artefact. Different methods of spectral analysis and dynamic mode decomposition have been used to show that the timescales involved in such a mechanism are about two orders of magnitude larger than the time scales involved in the turbulence of the boundary layer, which is consistent with the observed low-frequency motions. Furthermore, those timescales were shown to be strongly modulated by the amount of reversed flow inside the separation bubble. This scenario can, in principle, explain both the low-frequency unsteadiness and its broadband nature.

Keywords:

Nozzle flows, Wall modeling, Supersonic Turbulent Boundary Layer, Large-Eddy Simulation, Low-frequency shock Oscillations, Separation bubble, Planar nozzle, Supersonic conical diffuser, Shock unsteadiness, Side-loads, Spectra analysis, Dynamic mode decomposition.

Résumé

La nécessité d'une meilleure compréhension du mécanisme d'entraînement pour l'instabilité à basse fréquence observée dans un écoulement dans une tuyère sur-détendue a été discutée. Le caractère instable de l'onde de choc/couche limite reste un défi pratique important pour les problèmes des écoulements dans les tuyères. De plus, pour une couche limite turbulente incidente donnée, ce type d'écoulement présente généralement des mouvements de choc à basse fréquence plus élevés qui sont moins couplés aux échelles de temps de la turbulence en amont. Cela peut être bon du point de vue d'un expérimentateur, en raison de difficultés à mesurer des fréquences plus élevées, mais c'est plus difficile d'un point de vue calcul numérique en raison de la nécessité d'obtenir des séries temporelles plus longues pour résoudre les mouvements à basse fréquence. En excellent accord avec les résultats expérimentaux, une série de calcul LES de très longue durée a été réalisée, il a été clairement démontré l'existence de mouvements énergétiques à basse fréquence et à large bande près du point de séparation. Des efforts particuliers ont été faits pour éviter tout forçage à basse fréquence en amont, et il a été explicitement démontré que les oscillations de choc à basse fréquence observées n'étaient pas liées à la génération de turbulence d'entrée, excluant la possibilité d'un artefact numérique. Différentes méthodes d'analyse spectrales, et en décomposition en mode dynamique ont été utilisées pour montrer que les échelles de temps impliquées dans un tel mécanisme sont environ deux ordres de grandeur plus grandes que les échelles de temps impliquées dans la turbulence de la couche limite, ce qui est cohérent avec les mouvements de basse fréquence observés. En outre, ces échelles de temps se sont avérées être fortement modulées par la quantité de flux inversé à l'intérieur de la bulle de séparation. Ce scénario peut, en principe, expliquer à la fois l'instabilité des basses fréquences et sa nature à large bande.

Mots clés:

Écoulements dans les tuyères, Modèle de parois, Couche limite turbulente supersonique, Large-Eddy Simulation, Oscillations de chocs à basse fréquence, Bulle de séparation, Tuyère planaire, Diffuseur conique supersonique, Instabilité du choc, Charges latérales, Analyse spectrale, Décomposition en mode dynamique.

Acknowledgements

First and foremost, I would like to express my gratitude towards my esteemed supervisor Prof. Abdellah HADJADJ for providing me the opportunity to work on this deeply interesting topic of nozzle flow separation. His sense of direction and guidance kept me motivated throughout the course of my research work. He helped me learn the basic and advanced concepts related to nozzle flows. I would also like to massively thank him for his pushing support providing a good sense of direction to my research work. I am also grateful to the reviewers of my thesis namely, Prof. Amer CHPOUN and Prof. Paola Cinnella, and also the jury members Mme. Pascale DOMINGO, Prof. Niklas ANDERSSON, Mme. Marie-Claude DRUGET, Dr. Olivier THOMINE and Dr. Mostafa SAFDARI-SHADLOU for investing their valuable time in evaluating this manuscript.

I would like to acknowledge the access to HPC resources provided by the regional computing center of Normandy CRIANN (1998022). The funding resources provided by the Algerian Government is deeply appreciated.

Furthermore, I would also like to extend my thanks to Dr. Mostafa SAFDARI-SHADLOU and the former PhD/postdocs of our group i.e. Dr. Arthur PIQUET, Dr. Vineet SONI for their precious support and fruitful discussions. Dr. PIQUET helped me a lot to familiarize the structure of our solver which definitely sped-up the progress of the work, so thanks a lot for always being there to help. I am thankful to my lab buddies Nassim, Sushank, Margio with whom I started this journey of PhD. And, also Ms. Fatemeh and Mr. Celep who joined us later on.

Finally, I could not thank enough to my lovely parents; Nezzar, and Souad DAOUI, my wife; Fatima, my brothers and my sisters for bearing with me through the highs and lows of this journey. They are an endless source of motivation, encouragement, and support. They endured me throughout my life and also during this journey being my backbone, and made the things worthwhile.

Contents

Abstract	i
Symbols	vii
List of Publications	xii
1 Introduction	1
1.1 Main types of propulsive nozzles	1
1.2 Nozzle flow	2
1.3 Nozzle flow unsteadiness	9
1.3.1 Shock wave/boundary layer interaction (SWBLI)	9
1.3.2 Post-shock region unsteadiness	16
1.3.3 Recirculation bubble and lip vortex	18
1.4 Planar <i>vs.</i> axisymmetric nozzle flow	21
1.5 Scope of the present work	24
1.6 Outline of the dissertation	25
2 Governing equations and numerical methods	27
2.1 Governing equations	28
2.1.1 Subgrid-scale model	31
2.1.2 Generalized curvilinear coordinates	32
2.2 Numerical method	33
2.2.1 Spatial scheme	33
2.2.2 Temporal scheme	37
2.3 Code validation	38
2.3.1 Vortex advection	39
2.3.2 Compressible flow over a circular cylinder	42
2.3.3 Poiseuille flow	42
2.3.4 Turbulent channel flow at $Re_\tau = 220$	45
2.4 Test case description	49

3	Wall modeling for LES of supersonic boundary layer with separation	51
3.1	Introduction	52
3.2	Governing equations and numerical methodology	54
3.2.1	Wall modeling	55
3.3	DNS of a turbulent boundary layer under APG/FPG.	57
3.4	Model validation	60
3.4.1	A priori test	60
3.4.2	A posteriori test	61
3.5	Boundary-layer separation in a supersonic planar nozzle	65
3.6	Varying the nozzle pressure ratio	67
3.6.1	Time-averaged and instantaneous flow-field	68
3.6.2	Spectra analyses	70
3.7	Concluding remarks	73
4	Shock-Induced Flow Separation in an Overexpanded Supersonic Planar Nozzle	75
5	Low-frequency phenomena in supersonic planar nozzle	87
5.1	Introduction	88
5.1.1	Computational strategy and domain	90
5.2	Results and discussion	91
5.2.1	Validation	92
5.2.2	The inlet influence	93
5.2.3	Wall pressure fluctuations	94
5.2.4	Low-Frequency Oscillations (LFO)	101
5.2.5	Shock motion	105
5.3	Concluding remarks	106
6	Dynamic mode decomposition analysis of shock-wave unsteadiness in conical supersonic nozzles	109
7	Wall temperature effects on shock wave/turbulent boundary layer interactions	125
7.1	Introduction	126
7.1.1	Computational strategy and computational domain	127
7.2	The Influence of heating/cooling the walls	128
7.2.1	Mean flow parameters	128
7.2.2	Low-frequency oscillations	132
7.3	Concluding remarks	135

8	Conclusions and perspectives	137
A	DNS of a turbulent boundary layer with zero-pressure gradient (ZPG)	143
B	Multi-resolution Dynamic Mode Decomposition.	145
	List of Figures	147
	List of Tables	154
	Bibliography	155

Symbols

c	speed of sound
C_f	friction coefficient
C_p	heat capacity at constant pressure
C_v	heat capacity at constant volume
e_i	internal energy
e	total energy
f	additionnal force
F	thrust or side loads
Fo	Fourier number
H	enthalpy
H_t	nozzle throat height
k	turbulent kinetic energy
K	kinetic energy
L_x, L_y, L_z	streamwise, wall-normal and spanwise domain lengths
L_d	nozzle divergent length
M	Mach number
m	mass
N	Number of grid points
Pr	Prandlt number
p	static pressure
Re	Reynolds number
r	heat capacity ratio
R	gas constant
S	entropy
\mathbf{S}	strain rate tensor
St	Strouhal number
t	time
T	temperature
\mathbf{T}	deviatoric stress tensor

u, v, w	velocity compnents
U, V, W	contravariant velocity compnents
x, y, z	Cartesian coordinates
ξ, η, ζ	curvilinear coordinates

Greeks

δ	boundary-layer thickness
δ_1, δ^*	displacement thickness
δ_{ij}	Kronecker symbol
ϵ	turbulent dissipation
ε	nozzle area ratio
γ	heat capacity ratio
κ	wave number
λ	thermal conductivity
μ	dynamic viscosity
μ''	second viscosity
μ_b	bulk viscosity
ν	kinematic viscosity
ρ	density
σ	stress tensor
τ	shear stress tensor
θ	momentum thickness

Subscripts

i, j, k	Einstein notation, 1: stream-wise, 2: wall-normal and 3: span-wise direction
∞	freestream flow variable
0	total/stagnation variable
t	throat based variable
w	wall variable
τ	friction variable
rms	root mean square

Superscripts

$+$	wall-units normalized variable
-----	--------------------------------

Operators

$\vec{\varphi}$ or $\{\varphi\}_i$	vector notation
------------------------------------	-----------------

φ or $\{\varphi\}_{ij}$	tensor notation
$\langle \varphi \rangle$	time averaging quantity
$\bar{\varphi}$	filtered/spatial averaging quantity
$\tilde{\varphi}$	Favre averaging quantity
$\hat{\varphi}$	Fourier transform quantity

Abbreviations

APG	Adverse Pressure Gradient
BL	Boundary Layer
DNS	Direct Numerical Simulations
FPG	Favorable Pressure Gradient
LES	Large-Eddy Simulations
NPR	Nozzle Pressure Ratio, NPR(= (chamber pressure/ ambient pressure)
RANS	Reynolds Averaged Navier Stocks
RMS	Root-Mean-Square
SRA	Strong-Reynolds Analogy
SW	Shock Wave
TBLE	Thin-Boundary Layer Equations
WCNS	Weighted Compact Nonlinear Scheme
WENO	Weighted-Essentially Non-Oscillatory
ZPG	Zero-Pressure Gradient
LFO	Low Frequency Oscillations
SWBLI	Shock Wave/Boundary Layer Interaction
WM	Wall Modeled
DMD	Dynamic Mode Decomposition
SGS	Sub-Grid Scale

List of Publications

Peer-reviewed journals:

1. **Zebiri B.**, Piquet A. & Hadjadj A. (2020), Shock-Induced Flow Separation in an Overexpanded Supersonic Planar Nozzle, *AIAA Journal*, **58:5**, 2122-2131.
2. Piquet A., **Zebiri B.**, Hadjadj A. & Shadloo M. S. (2019), A parallel high-order compressible flows solver with domain decomposition method in the generalized curvilinear coordinates system, *International Journal of Numerical Methods for Heat and Fluid Flow*, **30:1**, 2-38.
3. **Zebiri B.**, Piquet A. & Hadjadj A. (2020), Analysis of shock-wave unsteadiness in conical supersonic nozzles, submitted to *Aerospace Science and Technology*. (accepted)
4. **Zebiri B.**, Piquet A. & Hadjadj A. (2020), On the use of a two-layer model for large-eddy simulation of supersonic boundary layer with separation, submitted to *International Journal of Heat and Fluid Flow*. (under review)
5. **Zebiri B.** & Hadjadj A. (2020), Low frequency phenomena in supersonic planar nozzle, to be submitted to *Physics of Fluids*. (under preparation)

International conference:

1. **Zebiri B.**, Piquet A. & Hadjadj A. (2019), Numerical study of side loads generation in over-expanded conical nozzles, *8th European Conference For Aeronautics And Aerospace Sciences (EUCASS 8)*, Jul 2019, Madrid, Spain.
2. **Zebiri B.**, Piquet A. & Hadjadj A. (2019), Shock-induced flow separation in an over-expanded supersonic planar nozzle, *32nd International Symposium on Shock Waves (ISSW32)*, Jul 2019, Singapore, Singapore.
3. **Zebiri B.**, Piquet A. & Hadjadj A. (2018), Large-eddy simulations of an over-expanded planar nozzle, *4th International Conference on Energy, Materials and Applied Energetics (ICEMAEP'2018)*, Apr 2018, Constantine, Algeria.

Awards:

1. **Student Competition: Best Paper Award** attributed by the International Shock Wave Institute (ISWI) during the *32nd International Symposium on Shock Waves (ISSW32), Jul 2019, Singapore, Singapore.*

Résumé

1 Contenu de la thèse

La nécessité d'une meilleure compréhension du mécanisme d'entraînement, des instabilités à basse fréquence observées dans un écoulement dans une tuyère sur détendue, a été établie. Il a été démontré que cela a alimenté la recherche dans ce domaine pendant plusieurs décennies. Le caractère instable des interactions Onde de choc/couche limite reste un défi pratique important pour les problèmes des écoulements dans les tuyères. En fait, ce type d'écoulement présente généralement des mouvements de choc à très basse fréquence qui sont plus difficiles à étudier d'un point de vue calcul numérique, en raison de la nécessité d'obtenir des séries temporelles plus longues à résoudre. Le travail suivant vise à mettre en évidence ce problème, en utilisant des simulations à grande échelle (LES) comme outil principal pour générer les données. Les données sont ensuite analysées dans le but d'éclaircir quelques rares questions fondamentales concernant les impacts de divers paramètres physiques sur ces phénomènes. En particulier, nous visons de :

- Valider l'approche du modèle de paroi utilisée à travers des études de sensibilité et des comparaisons avec l'expérimental. Cela permettra d'étudier les phénomènes de basse fréquence à travers de longs signaux LES.
- Étudier les implications de différents paramètres physiques en amont et en aval tels que le rapport de pression de la tuyère, la température des parois et les variations des conditions aval sur les oscillations de choc à basse fréquence.
- Étudier les phénomènes de basse fréquence en utilisant à la fois l'analyse spectrale et la décomposition en mode dynamique.

2 Aperçu de la thèse

Un aperçu complet de la littérature révèle que de nombreuses questions importantes concernant la séparation des écoulements dans les tuyères ainsi que les phénomènes accompagnés, sont encore ouvertes. Par conséquent, le courant aborde certains d'entre eux. Cette thèse est organisée comme suit :

Chapitre 2 : présente les équations gouvernantes en utilisant à la fois des formes cartésiennes et curvilinéaires en mettant l'accent sur les équations de Navier – Stokes compressibles 3D filtrées. Les stratégies numériques utilisées sont décrites après.

Chapitre 3 : Dans ce chapitre, la méthodologie du modèle de paroi est présentée, en particulier la manière dont le modèle est implémenté dans le code LES. Ensuite, l'évaluation de ses performances à travers un ensemble d'exemples comprenant des simulations d'une plaque plane, avec et sans gradient de pression, et

une comparaison avec une DNS précédente. Le modèle est ensuite testé sur un long WM-LES sur un écoulement dans une tuyère supersonique pour démontrer sa capacité à reproduire avec précision la séparation de la couche limite, ainsi que le mouvement de choc à basse fréquence. Les principaux résultats sont soumis à International Journal of Heat and Fluid Flow.

Chapitre 4 : Le problème de la séparation d'un écoulement, induits par le choc dans une tuyère plane supersonique sur détendue, est étudié numériquement, dans ce chapitre, au moyen d'une très longue simulation tridimensionnelle à grands échelle avec paroi modélisée (WM-LES). L'objectif est d'identifier l'origine des oscillations de choc basse fréquence ainsi que la génération de charges latérales associée dans les tuyères planes. Les résultats des calculs sont comparés aux données expérimentales pour validation. Un scénario des oscillations de choc à basse fréquence, confirmant les conclusions d'études antérieures, est décrit dans ce chapitre. Les résultats sont publiés dans AIAA Journal.

Chapitre 5 : Dans la continuité, l'étude se concentre sur différents mécanismes conduisant aux oscillations de choc à basse fréquence (LFO) dans une tuyère plane. Ainsi, nous nous concentrons principalement sur l'effet de la bulle de recirculation, sa taille et sa localisation dans la génération du LFO. Une attention particulière est portée à l'étude du choc et de ses oscillations. Enfin, une formule est faite empiriquement afin de prédire le ton principal. Les résultats sont en considération pour la publication dans Physique des fluides.

Chapitre 6 : Dans le présent chapitre, nous utilisons à la fois la WM-LES et la WR-LES pour simuler l'écoulement dans une tuyère conique sur détendue. L'objectif est d'étudier en détail les différents phénomènes d'écoulement complexes tels que la couche limite turbulente, le choc interne et la couche de mélange séparée, dans le but de fournir une compréhension perspicace des phénomènes de basse fréquence, se produisant au sein d'une tuyère conique. L'analyse de décomposition en mode dynamique (DMD) est utilisée pour mieux comprendre le comportement de ces phénomènes. Les résultats sont publiés dans Aerospace science and technology.

Chapitre 7 : Ce chapitre présente les effets de la température de la paroi sur un écoulement dans une tuyère. L'accent est mis sur les changements dans la structure du choc et le rôle de ces changements dans le contrôle de son mouvement. Les résultats ne sont pas encore publiés.

Chapitre 8 : Un résumé des travaux de recherche entrepris ainsi que les remarques finales sont donnés dans le dernier chapitre. Cela ouvre également de multiples possibilités pour différentes œuvres en perspective.

3 Conclusions et perspectives

Cette thèse est consacrée à l’analyse de l’interaction onde de choc/couche limite (SWBLI) dans les tuyères sur-détendue. Le phénomène SWBLI est généralement associé à une instabilité de choc à basse fréquence qui entraîne la génération ou l’amplification des charges dynamiques agissant sur la paroi de la tuyère. Ces charges, appelées charges latérales, sont préjudiciables à l’intégrité de la structure mécanique de la tuyère et peuvent provoquer de graves dommages. Cette étude vise à clarifier la physique des écoulements complexes liée à SWBLI dans les tuyères supersoniques, en utilisant une technique de simulation numérique haute-fidélité, capable de reproduire les aspects instationnaires de l’écoulement turbulent, la structure tridimensionnelle de l’interaction ainsi que les oscillations de choc, dans les gammes d’énergie basse fréquence, avec des excursions à grande échelle. Le manuscrit commence par une section d’introduction qui résume les aspects physiques les plus pertinents de la séparation de des écoulements dans les tuyères, avant de présenter les différents scénarios de phénomènes d’oscillations de choc basse fréquence dans SWBLI. L’influence des perturbations aval / amont qui interviennent lors de la SWBLI est également soulignée, en plus des différentes instabilités post-choc, se produisant principalement dans les bulles de recirculation et dans la couche de mélange en aval de la zone d’interaction. La comparaison entre les écoulements de tuyères planaires et axisymétriques est fournie en mettant l’accent sur l’aspect symétrie / non-symétrie de la séparation.

En termes de simulations numériques, un effort particulier est fait pour évaluer l’outil numérique utilisé dans le cadre de la présente étude. Ce code, appelé CHOC-WAVES (Compressible High-Order Code using Weno Adaptive Stencils), résout les équations de Navier-Stokes compressibles en trois dimensions avec la méthode de décomposition de domaine dans le système de coordonnées curvilignes généralisées (pour les géométries complexes). Le code est validé par un ensemble de test, y compris (mais sans s’y limiter) la couche limite supersonique, l’écoulement du canal compressible, l’écoulement autour d’un cylindre, les jets et la couche de mélange. Dans le cadre de l’étude LES, un modèle de paroi, basé sur des équations de couches limite minces (TLBLE), est utilisé pour rendre compte des effets proches de la paroi, permettant de gagner un temps CPU significatif et de réaliser de très longues intégrations. Une présentation complète de ce modèle est fournie, ainsi qu’une qualification des paramètres du modèle par des tests a priori et a posteriori. On constate qu’en plus de sa relative simplicité de mise en œuvre dans un code LES existant, le modèle de paroi LES est capable d’économiser un temps de calcul considérable, tout en fournissant des résultats assez satisfaisants en termes de vitesse d’écoulement moyenne et de turbulence. En examinant à la fois les tuyères supersoniques plane et conique, les résultats du LES ont permis de tirer les principales conclusions :

3.1 Oscillations de choc dans les tuyères planes

- L'objectif initial était de vérifier s'il existe ou non une instabilité de basculement du jet entre les parois de la tuyère supérieure et inférieure dans la plage du rapport de pression de tuyère sélectionné (NPR de 1,7). Si ce phénomène se produisait, il aurait une basse fréquence très caractéristique. Pour cela, des simulations très longues ont été réalisées sur un temps d'intégration 18 fois plus long que Piquet (2017), Olson & Lele (2011) et Papamoschou & Johnson (2006). Le temps d'intégration était suffisamment long pour capturer plusieurs excursions de choc, offrant ainsi une meilleure convergence des statistiques. À la connaissance de l'auteur, il s'agit de la durée d'intégration la plus longue jamais atteinte à ce jour dans des écoulements de tuyères séparées. Au cours de cette longue simulation, le jet s'est avéré stable, collant d'un côté de la paroi de la tuyère, sans basculer de l'autre côté pendant toute la simulation.

- Diverses configurations d'écoulement avec différents modèles de chocs sont ensuite étudiées. Toutes les simulations ont clairement établi le comportement de symétrie/asymétrie du jet ainsi que l'oscillation de choc à basse fréquence (LFO) trouvée dans les expériences. L'activité LFO est considérée comme la plus importante au voisinage du pied de choc réfléchi et caractérisée par un spectre couvrant plus de trois décennies de fréquences.

- Il a été établi que le pic, correspondant aux mouvements à basse fréquence dans le spectre pondéré, se situe trois ordres de grandeur en dessous du pic associé à la turbulence de la couche limite amont. Cela confirme que la couche limite amont n'est pas responsable de la génération du LFO.

De plus, une étude paramétrique a été réalisée dans le but de mettre en évidence l'effet du rapport de pression de la tuyère sur les oscillations de choc à basse fréquence. À la lumière de cette étude, il a été constaté que :

- Les mouvements à basse fréquence sont liés aux contractions et dilatations successives de la bulle de séparation. Plus la bulle est large, plus la durée des oscillations est grande. - De plus, l'écoulement de retour s'avère fortement corrélé aux mouvements de choc à basse fréquence, confirmant les conclusions précédentes des écoulements avec un λ choc plus important. - Pour le mouvement du choc, une différence dans le comportement de l'ensemble de la structure du choc est notée. Il a été constaté que le Mach stem se déplace en réponse à un pur forçage à basse fréquence. Cependant, le mouvement du pied du choc est affecté à la fois par les perturbations basse fréquence et certaines perturbations haute fréquence provenant des régions entièrement turbulentes, y compris la couche limite et de mélange. - Une analyse attentive du champ d'écoulement instantané a indiqué que le Mach stem se déplace à une vitesse presque constante lors de ses mouvements de va-et-vient, confirmant les observations antérieures de Gonzalez Dolling (1993).

- Plus de détails sont également fournis concernant le mouvement de choc. Par

exemple, dans son mouvement de va-et-vient, le choc progresse de manière discontinue avec une pause (pauses), jusqu'à ce qu'il atteigne sa position maximale. Le nombre de ruptures effectuées dans un sens (amont) est supérieur à celui réalisé dans l'autre sens (aval). Ainsi, pendant un temps donné (t_1), le choc peut parcourir une plus grande distance en aval du fait de moins de ruptures. Sachant que le choc a une vitesse constante dans les deux sens, cela fait apparaître la vitesse moyenne du choc en aval supérieure à celle en amont. - Enfin, une relation empirique est proposée pour modéliser la tonalité acoustique principale. En ce qui concerne les effets de la température des parois sur les oscillations de choc à basse fréquence, il a été constaté que : - Le refroidissement de paroi conduit à une réduction considérable des échelles de longueur d'interaction, affectant ainsi la taille de la bulle de séparation, alors que l'inverse vaut pour le transfert de chaleur avec chauffage de paroi. - En termes de structure de choc, on remarque que le refroidissement de la paroi transforme en fait le choc lambda du cas adiabatique en un choc lambda quasi symétrique, avec un Mach stem plus large. Cela crée un équilibre entre l'écoulement rentrant par le bas et le haut de la tuyère. Le choc est donc plus stable et fait des oscillations plus courtes. Par conséquent, de basses fréquences oscillations de faible énergie sont présentes dans les spectres de la paroi refroidie.

3.2 Oscillations de choc dans les tuyères coniques (axisymétriques)

Une comparaison entre un écoulement dans une tuyère conique et le même écoulement dans une tuyère plane équivalent montre que : - Alors que les deux configurations partagent certaines caractéristiques d'écoulement communes, telles que des structures turbulentes à grande échelle et des modèles d'ondes de choc, elles présentent des contrastes sur la symétrie de l'écoulement et la dynamique des chocs. - L'amplitude de l'emplacement de séparation est moins importante dans le cas cylindrique en raison du gradient de pression accru, en amont du col, du fait de la section réduite par rapport au cas plan. - L'analyse fréquentielle de l'écoulement révèle l'existence de phénomènes à basse fréquence résultant de l'oscillation du système de choc. L'analyse DMD met en évidence l'existence de deux modes distinctifs ; i) le mode non hélicoïdal (flopping) qui est principalement un mode de basses fréquences, clairement visible dans le spectre des forces axiales. ii) le mode hélicoïdal qui est un mode basé sur les hautes fréquences, apparaissant principalement dans les spectres des charges latérales. - Sur la base de l'analyse actuelle, une classification des différents modes est proposée, basée sur le nombre de Strouhal :

- $St \in]..., 0.017]$: Le mode dans cet intervalle est flopping, qui est à l'origine de l'amplification des forces axiales par le mouvement oscillatoire du système

de choc.

- $St \in]0.017, 0.10]$: Le mode dans cette plage se révèle être hélicoïdal, ce qui représente des structures tourbillonnaires de différentes tailles qui deviennent plus fines lorsque la fréquence augmente. Ces structures apparaissent très proches de la paroi de la tuyère en aval de la zone de choc, conduisant à considérer ces modes comme les principaux responsables de l'amplification des charges latérales.
- $St \in [0.10, 0.40]$: Ce mode est causé par les structures tourbillonnaires à haute énergie, en raison des activités de la couche de mélange. Ce mode est moins impliqué dans le spectre des charges latérales.

1

Introduction

The objective of this chapter is to present the state-of-the-art related to supersonic over-expanded nozzle flows. Through which, the different flow aspects are presented. Particular interest is focused on the study of shock wave/turbulent boundary layer interaction (SWBLI) and different physical mechanisms that induce/influence the low-frequency shock oscillations.

1.1 Main types of propulsive nozzles

Before approaching the different operating modes of a nozzle and in particular the phenomenon of separation in an over-expanded regime, it is important to recall the characteristics of conventional nozzles. Indeed, the separation is dependent on the geometry of the divergent. Two main nozzle-geometry families can be distinguished (Mouronval (2004) (see figure 1.1):

1. The conical nozzles which were very widely used in the design of the first rocket engines due to their simplicity and ease of construction. Generally, these nozzles have angles of divergence between 15 and 25 degrees. They are currently still used to equip very small engines (used, for example, to control the altitude of satellites).
2. The curved nozzles, which form the second family of conventional nozzles, offering serious advantages over the previous ones in terms of size and performance although, like the previous, they perform optimally only at a given altitude.

Furthermore, this latter nozzle family can itself be divided into sub-families. So, we distinguish:

- (a) The truncated ideal nozzles (called TIC, Truncated Ideal Contoured).

An ideal nozzle, if not truncated, would produce a uniform flow profile at the nozzle exit. The last part of their outline presents only a slight inclination, which gives them a large length. However, the slight slope at the exit only makes a negligible contribution to the thrust. Consequently, truncating these nozzles facilitates their use for rocket engines, without significant loss in performance due to the non-uniformity of the outlet flow. Using this approach, [Ahlberg et al. \(1961\)](#) proposed an optimization method which results in a contour presenting a maximum performance for a given section ratio. The nozzles of the Russian RD-0120 and European Viking engines are of this type.

- (b) The optimized thrust nozzles (called TOC, Thrust-Optimized Contoured).

[Rao \(1958\)](#) proposed a method for optimizing the performance of a nozzle for a given length. The typical length of a Rao's nozzle is 75 to 85% of the length of a 15-degree conical nozzle with the same section ratio.

- (c) The parabolic optimized nozzles (known as TOP, Thrust-Optimized Parabolic).

It has also been shown by [Rao \(1960\)](#) that the profile of the nozzle obtained by this method could be approached by a parabola, without significant loss of performance. This approach is frequently used for the design of modern rocket engine nozzles such as the American SSME or European Vulcan engine.

Other non-conventional nozzles can exist such as annular aerospike nozzles and TICTOP nozzles. The latter represents a new concept that combines two types of nozzles; TIC and TOP [Frey et al. \(2017\)](#).

1.2 Nozzle flow

After the brief description of the different characteristics of conventional nozzles. One would recall some of the different aspects of a nozzle flow.

In fact, when starting a rocket engine on the ground, the chamber pressure is not high enough for the flow to be supersonic in the entire nozzle: the flow is recompressed through a shock wave so to adapt to the external pressure. This recompression is accompanied with a boundary layer separation and a loss of symmetry of which generates lateral forces. This phenomenon, already observed on several real engines, can have serious consequences linked to its random nature. Thus, these forces can cause deformations of the nozzle and movements relative to its attachment system. The constraints generated by these efforts, unsteady in module and direction, are likely to be amplified by dynamic effects. They, therefore, constitute a constraining factor in the design of the structure of

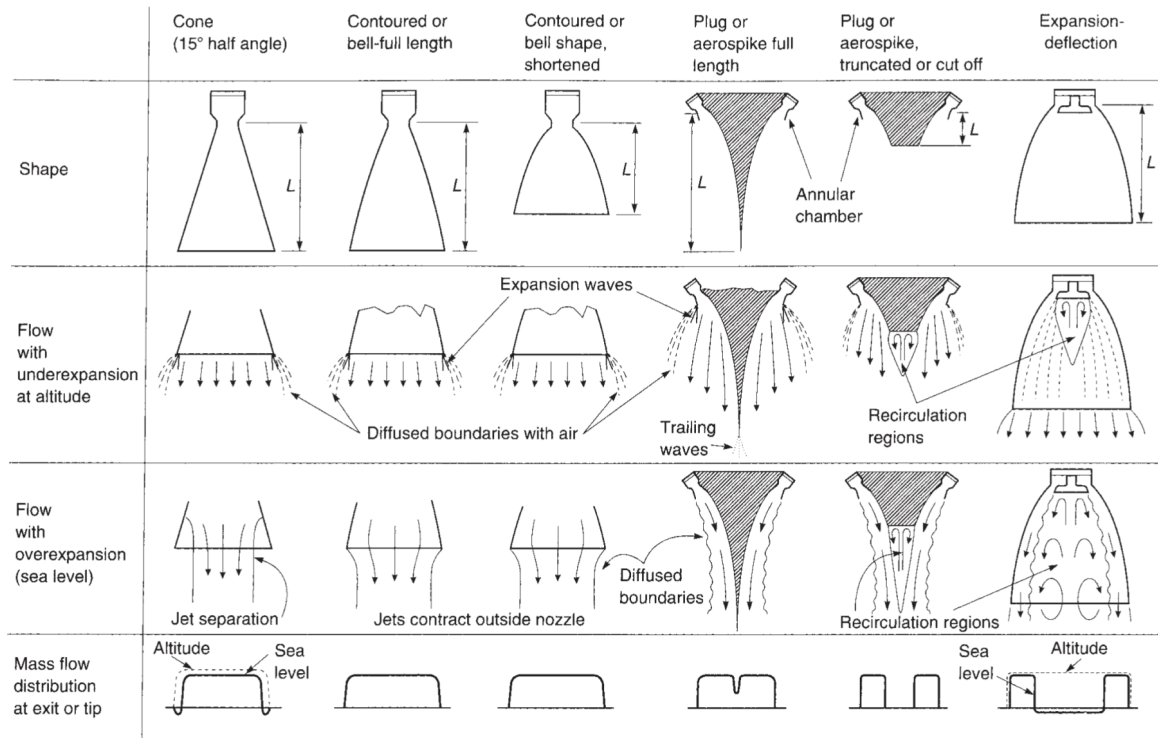


Figure 1.1: Simplified diagrams of different generic nozzle configurations and their flow effects from Sutton & Biblarz (2016)

the nozzle since they require having thicker nozzle walls, therefore heavier or shorter and consequently entail a reduction in the payload transported. When the nozzle is primed (amorced), the flow regime depends only on the ratio between the ambient pressure p_a and the total pressure at the inlet. In practice, for these operating modes, a distinction is made between non-separated flows and separated flows. When the flow in the divergent remains attached to the wall, the wall pressure profile is not influenced by the external ambient pressure but mainly depends on the chamber pressure, p_c , and the geometry of the nozzle used. This type of flow occurs when the engine is operating at/or beyond the altitude for which it has been adapted. In terms of pressure ratio, this corresponds to $p_a/p_e = 1$ the nozzle is said to be adapted to ambient or external pressure, or it corresponds to $p_a/p_e < 1$ then the nozzle is said to be under-expanded nozzle. If the downstream pressure continues to increase and exceeds a certain threshold, the nozzle will be in a regime of high over-expansion ($p_a/p_e \gg 1$), see figure 1.2.

There comes a time when the boundary layer can no longer counter the adverse pressure gradient which has become too important and separates. It should be emphasized at this point that the prediction of this pressure threshold is an important issue for engine manufacturers since they often wish to avoid or control separation. Several types of shock structure can be observed in the jet. When the evolution of the nozzle profile is smooth (case of the TIC type rocket engine nozzles), the separated shock is reflected

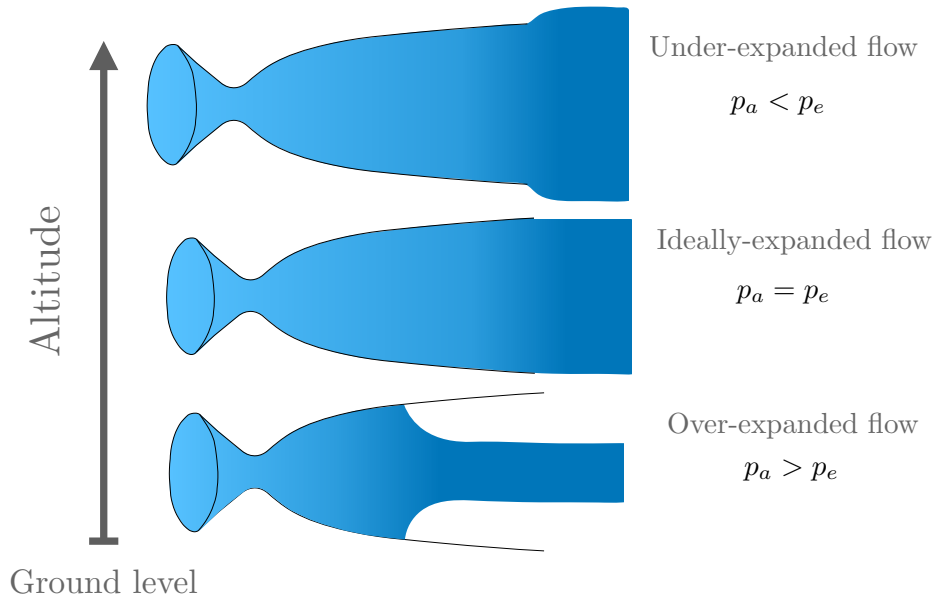


Figure 1.2: Nozzle flow regime during flight.

on the axis of symmetry. Two types of reflection can then occur, (see figure 1.3): the first is so-called "regular" where the incident shock (IS) is reflected directly on the axis of symmetry forming a reflected oblique shock (IR) (observed only in the planar nozzles); the other, known as "singular" or "Mach", in which the incident shock (IS) is reflected by forming a normal shock called the Mach disc (see figures 1.4). From the triple point (TP), where the incident shock, the reflected shock and the Mach disc meet, emanates a slip line (SL) (see figure 1.4). This isobar discontinuity separates the subsonic pocket, downstream of the strong shock, from the supersonic region located downstream of the reflected shock (IR).

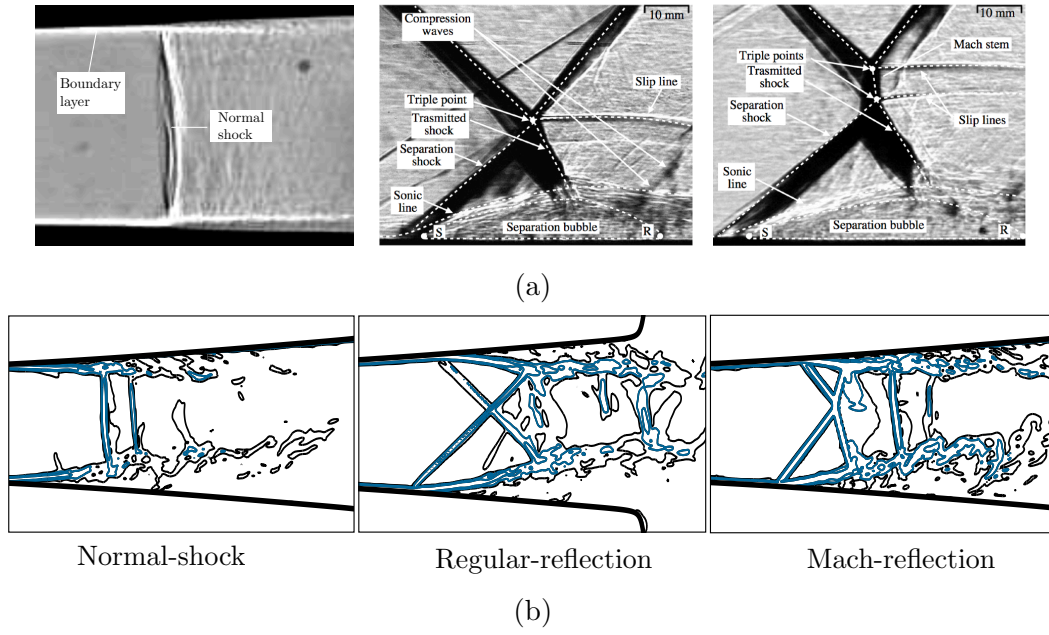


Figure 1.3: (a) Different shock reflections found in a nozzle flow from left to right: normal shock [Papamoschou & Johnson \(2006\)](#), regular-reflection (RR) and Mach-reflection (MR) [Grossman & Bruce \(2018\)](#), (b) A schematic showing different shock reflections found in nozzle flows.

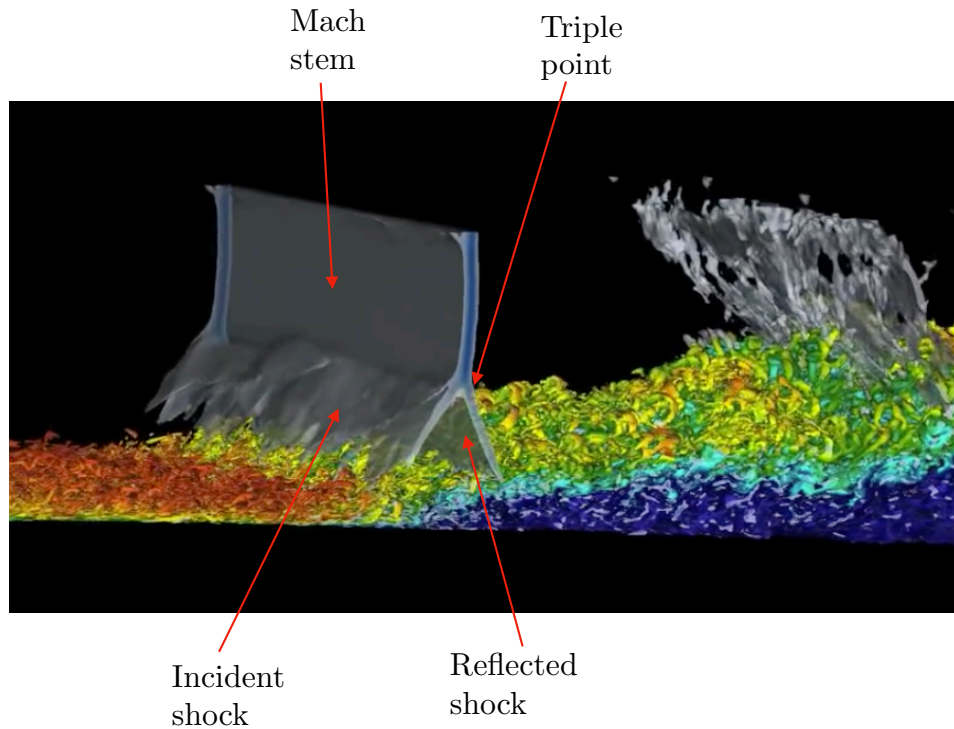


Figure 1.4: Isovolume of $|\nabla u|$ showing the topology of a λ -shock [Olson & Lele \(2011\)](#).

It is noted that getting one of these reflections strongly depends on the pressure ratio and the contour of the nozzle. Moreover, the transition phenomenon between these reflections can involve a hysteresis effect. When the evolution of the nozzle profile is

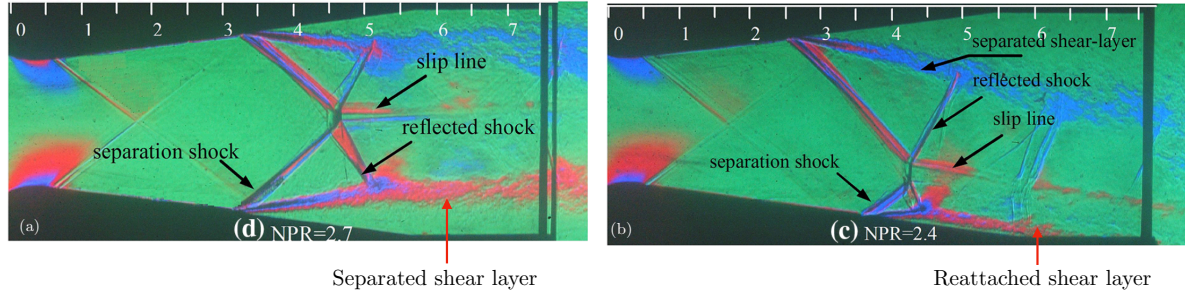


Figure 1.5: Color schlieren images of the exhaust flow from Verma & Manisankar (2014) showing flow topology with (left) Free Shock Separation (FSS) and (right) Restricted Shock Separation (RSS).

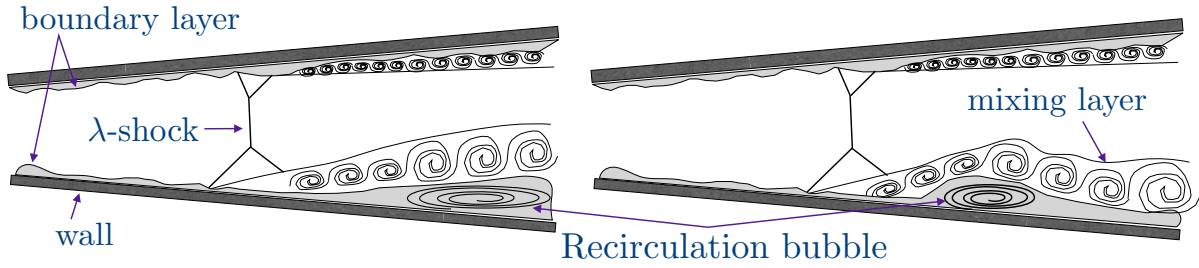


Figure 1.6: A schematic representation of (left) Free Shock Separation (FSS) and (right) Restricted Shock Separation (RSS).

strongly optimized in thrust (TOC and TOP), an internal focusing shock (IS) is formed. This shock is due to the change in curvature of the wall at the level of the throat. The interference of this internal shock with the separation shock (I) can lead to a complex shock structure known as "a hat". This structure would be the result of the interference between the separation shock and the inverse Mach reflection of the internal shock on the axis of symmetry. Finally, concerning the separation itself, two configurations, observed experimentally then confirmed numerically, are represented in both figures 1.5 and 1.6. Most often, the separation encountered is a Free Shock Separation type (FSS) in which the jet separates from the nozzle wall before its outlet lip and is ejected freely therefrom. However, for certain types of nozzles, the second type of separation, called Restricted Shock Separation (RSS), may be encountered. The latter is characterized by a rapid reattachment of the separated boundary layer as shown in figure 1.6. The evolution of the wall pressure p_w can be considered as partly governed by the physics of the shock wave/boundary layer interactions (SWBLI) in supersonic flow. The first deviation of the wall pressure from its evolution in a vacuum is called the incipient separation pressure. It is denoted p_i . The wall pressure then increases rapidly until a plateau pressure p_p , generally lower than the ambient pressure p_a .

It appears that the FSS involves two very distinct mechanisms. The first is associated

with the separation of the jet from the wall and governed by the pressure jump p_i/p_p while the second is linked to the ambient flow sucked into the recirculation zone and controls the evolution of the p_p/p_a ratio. In the 1970s, a second type of separation was observed by [Nave & Coffey \(1973\)](#) during tests on models of the J-2S engine supplied with cold gases. The existence of this new type of separation, known as "restricted" (RSS) due to the small extent of the recirculation zone, was confirmed in 1994 by the numerical simulations of [Chen et al. \(1994\)](#). Subsequently, it was encountered on other models on a reduced scale but also on real engines, although originally the scientists thought that this configuration only took place for models on a reduced scale operating in cold gases. In fact, this configuration is mainly influenced by the profile of the nozzle and not by its size. For this flow regime, occurring only at certain pressure ratios, the flow quickly separates and then reattaches on the wall of the nozzle. The evolution of the wall pressure downstream of the separation is irregular, with wall pressure exceeding sometimes the ambient pressure. This phenomenon is attributed to the reattachment of the separated flow. Indeed, this induces compression and expansion waves in the supersonic jet.

The transition from free separation to restricted separation occurs at a well-defined pressure ratio p_c/p_a . The FSS \rightarrow RSS transition is accompanied by a sudden downstream movement of the separation point. When the pressure increases further, the recirculation bubble moves downstream and the point of reattachment finally reaches the outlet of the nozzle. The recirculation zone then opens to the ambient. This is accompanied by an increase in pressure in the recirculation zone. As a result, the separation point is pushed upstream. Thus, the recirculation zone can be closed, resulting in a new pressure drop and a downstream movement of the separation location. A cyclic movement, connected to the opening and closing of the recirculation zone, is then observed [Pilinski \(2002\)](#). This RSS \rightarrow FSS transition is known in the literature as the "end effect". The same phenomena can be observed during the engine shutdown phase. [Frey & Hagemann \(2000\)](#) proposed an explanation for the restricted detachment from experimental observations and numerical simulations. According to their results, the hat shock structure described before would be the key element of the FSS \rightarrow RSS transition. They conclude that this transition can only occur in the nozzles presenting an internal shock. The existence of a hysteresis phenomenon concerning the shift between the two configurations was firstly demonstrated by [Sellam et al. \(2014\)](#).

Shock-induced boundary-layer separation in transonic and supersonic flows are of great importance in many practical applications, such as rocket propulsion systems, transonic airfoils, refrigeration ejectors, etc. These unsteady phenomena are associated with undesirable effects such as shock oscillations, wall-pressure fluctuations, boundary-layer separation and vortex shedding, which are the major causes of vibration, noise and side-

load generations. A comprehensive review of this topic can be found in [Hadjadj & Onofri \(2009\)](#). Flow separation in supersonic nozzles has been the subject of several experimental and numerical investigations, with the aim to understand the different shock patterns occurring in overexpanded nozzle regime [Papamoschou & Johnson \(2006\)](#), [Xiao et al. \(2007\)](#), [Hunter \(2004\)](#), [Bourgoing & Reijasse \(2005\)](#), [Johnson & Papamoschou \(2010\)](#), [Olson & Lele \(2011\)](#), [Verma et al. \(2018\)](#), [Dussauge et al. \(2006\)](#), [Dupont et al. \(2005\)](#), [Shimshi et al. \(2015\)](#), [Chaudhuri & Hadjadj \(2016\)](#). According to these studies, three typical flow separation configurations can be identified: i) incipient boundary-layer separation with normal shock (observed only in planar nozzles), ii) symmetric boundary-layer separation with two-symmetric λ -shocks and iii) asymmetric boundary-layer separation with two-asymmetric λ -shocks. As for the separation location, it was found to be sensitive to the flow disturbances, that may originate from the roughness of the wall [Shimshi et al. \(2015\)](#) or from the improper initialization of the flow [Chaudhuri & Hadjadj \(2016\)](#). To address the problem of nozzle flow separation, [Papamoschou & Johnson \(2006\)](#) investigated a planar nozzle experimentally with a flexible geometry and different nozzle pressure ratios ($\text{NPR} \in [1.269 - 2.4]$). They found that the flow could be asymmetric without flipping during the test run, but the jet flow could change direction from one nozzle side to another during a restart of a run. According to their study, the shock selects its orientation at the nozzle starting and retains it throughout the run. Additionally, RANS simulations were performed by [Xiao et al. \(2007\)](#), in which they roughly confirmed the experimental findings of [Papamoschou & Johnson \(2006\)](#). For a fixed nozzle area ratio and over a wide range of NPR (1.269 - 2.4), they found that the flow can be asymmetric for NPR (1.5 - 2.4), which is consistent with the experiments of [Papamoschou & Johnson \(2006\)](#). [Xiao et al. \(2007\)](#) demonstrated that the asymmetric behavior of the flow separation could be forced on either the top or the bottom wall by means of perturbations placed near one of the nozzle walls. They also found that the separated-flow region is largely enhanced within the core of the nozzle flow, which exhibits a higher level of unsteadiness. Detailed investigations of flow separations were made by [Hunter \(2004\)](#), who studied experimentally and numerically an overexpanded planar nozzle and found that the flow is mainly dominated by the shock-boundary layer interaction dynamics. He proposed a scenario in which the separation could be a natural response of the flow in its tendency to reach a thermodynamically stable state. Based on his study, the author suggested to classify the separation into two categories according to the NPR; i) a non-stationary three-dimensional separation with a partial re-attachment and ii) a stationary two-dimensional separation with an abrupt transition existing between the two. The origin of the flow asymmetry was also investigated experimentally by [Verma & Manisankar \(2014\)](#) using three different Mach 2 planar nozzles with a fixed area ratio and

different divergent-wall angles. In their study, the authors found that the boundary-layer transition is one of the main reasons for the flow asymmetry. They also showed that the transition from free-shock separation (FSS) to restricted-shock separation (RSS) could initiate the flow asymmetry, but later the transition from (RSS) to (FSS) seems to make the flow symmetric again. Similarly, the presence of (RSS), was pointed out by [Fournier et al. \(2018\)](#) as one of the causes of the asymmetry in nozzle flows. Another origin of asymmetry, reported by [Verma & Manisankar \(2014\)](#), was the proximity of the separated shear layer to the nozzle wall.

1.3 Nozzle flow unsteadiness

1.3.1 Shock wave/boundary layer interaction (SWBLI)

Due to their ubiquity in high speed applications and their impact on flight performance and component safety, shock wave/boundary layer interactions phenomenon, represented in figure 1.7, have been studied for about 70 years. The story begins with [Ferri \(1940\)](#) in 1939 who made the first observations of this phenomenon during a test of an air profile in a high-speed wind tunnel. These observations were the beginning of decade of research in this area. Shortly after, the importance of the phenomenon was underlined by several studies, specifying that the nature of these interactions depends critically on the state of the incoming boundary layer. Among these studies, we cite the work of [Fage & Sargent \(1947\)](#), [Ackeret et al. \(1947\)](#) and [Liepmann \(1946\)](#). Unfortunately, little information was collected during these tests which lacked precision. As these experiments were, generally, made for a transonic regime and in the presence of a downstream pressure gradient, it was too difficult to investigate the properties systematically. To overcome this problem, late 1940 and early 1950 experienced a series of experiments made for a true supersonic boundary layer. These works were done on basic geometries such as: flat plates with steps and axisymmetric bodies. These works provided very useful data on the effects of Mach number, Reynolds number and reinforced previous observations of the importance of the state of the boundary layer. Much of the work up to 1955 has been summarized by [Holder et al. \(1954\)](#). This period was marked by the famous work of [Chapman et al. \(1958\)](#) in which they were able to show several very important new knowledge on laminar, transitional and turbulent interactions. Their results gave birth to the concept of free interaction. They subsequently showed that pressure distributions through separation for different model configurations and at different Reynolds numbers could be collapsed when the pressure and distance axes were scaled appropriately in terms of the skin-friction coefficient. Their technique worked very well for both laminar and turbulent

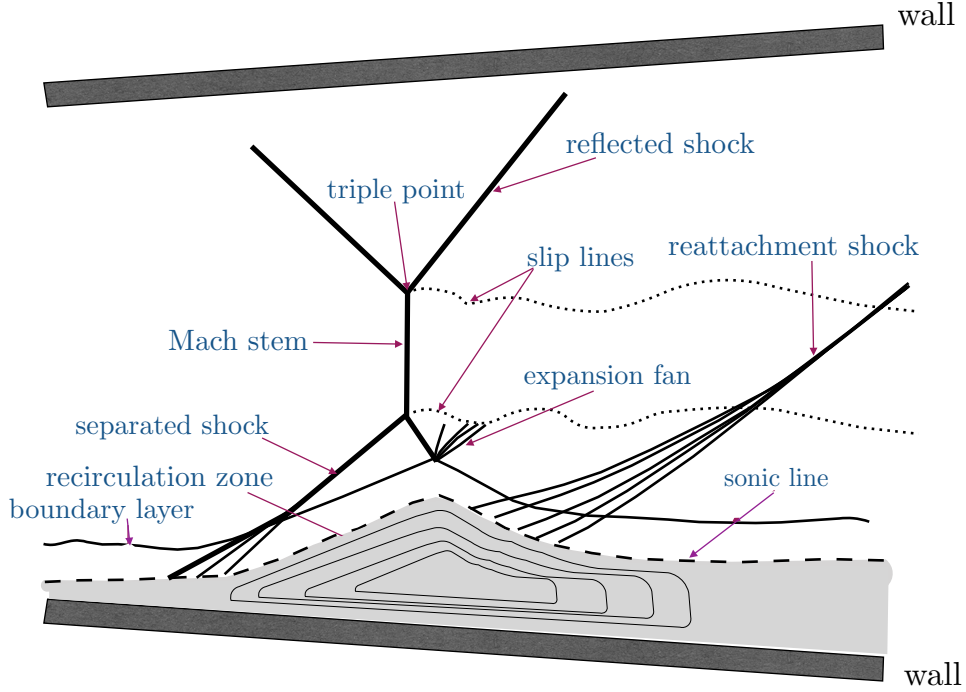


Figure 1.7: Schematic representation of the SWBLI.

flows, suggesting that the same physical processes occurred in both.

In their quest to support the experimental work, the researchers embarked on numerical simulations. The aim of these attempts was above all to try to understand the deep details of this phenomenon as well as the desire to control the conditions of the experiment, whether they are initial or limit conditions. These attempts were affected by the strict standards of [Aeschliman & Oberkampff \(1998\)](#), of which they specify that each experiment had to be designed from the beginning in order to be validated by a simulation afterwards and that each isolated attempt to validate an experimental work that had not been designed for this purpose is unacceptable. Given their very strict criteria, at the beginning of the 90s, only 105 experiments specifically fulfilled these conditions, among them 5 experiments in hypersonic regime.

Given this very limited number of accepted experiments, these two researchers called for carrying out numerous experiments verifying the criteria in order to cover the serious shortage in the following themes: 1) interactions involving real gas effects, 2) turbulence data and unsteady phenomena 3) more complex types of building block experiments and 4) emphasis on three-dimensional rather than two-dimensional interactions. Regarding the unsteadiness which is perhaps the most significant breakthroughs in understanding the phenomenology and the physics of SWBLI. The SWBLI has been the area of numerous studies to understand the genesis of the prominent low-frequency component inherent in SWBLI. Recently, brilliant works proposed several physical mechanisms to shed more

Low-frequency shock oscillations sources	
Upstream conditions	Downstream conditions
<ul style="list-style-type: none"> - Coherent structures of the incoming TBL Andreopoulos & Muck (1987). - Passage of turbulence fluctuations through the interaction Erengil & Dolling (1993). - Thickening and thinning of the upstream BL Ünal mis & Dolling (1994) - Upstream velocity fluctuations Beresh et al. (2002). - The existence of very long coherent structures Ganapathisubramani et al. (2007). 	<ul style="list-style-type: none"> - The breathing of the separation bubble Piponniau et al. (2009). - The eddies in the separated region Dussauge & Piponniau (2008). - The acoustic resonance Zaman et al. (2002). - pressure imbalance between the pressure level downstream the shock and the ambient Martelli et al. (2019). - The acoustic disturbance resulting from the interaction of the coherent structures Pirozzoli & Grasso (2006).

Table 1.1: A summary of the most pertinent sources of the LFO found in the literature.

light on the unsteady aspect of these phenomena. However, it is still a challenging task to just distinguish the causation from the correlation. These efforts may be broadly classified into two categories: The first category points out the upstream influence of the incoming turbulent boundary layer while the second underscores the downstream influence via the interaction between the separated boundary layer, the recirculation region, and the shock system. Few hypotheses can be found for the first category. For example, [Andreopoulos & Muck \(1987\)](#) try to point out the coherent structures of the incoming turbulent boundary layer as the main reason. They found that the frequency of the shock motion scales on the bursting frequency of the incoming boundary layer. It appears that there exists a strong correlation between the eddies of the incoming turbulent boundary layer and the shock displacements. More ideas about the relationship between the shock-foot and the incoming turbulent boundary layer can be found in the literature. [Erengil & Dolling \(1993\)](#) for example, have presented the small-scale motions of the shock as a response to the passage of turbulence fluctuations through the interaction. While, [Hunt & Nixon \(1991\)](#), [Wu & Miles \(2000\)](#) looked to the so-called hairpin structures as a strong influencer that can significantly impact the shock motion. However, the hairpin structures have a frequency higher than the low frequency of the shock motion and cannot yet be directly related. For compression-corner flow, [Ünal mis & Dolling \(1994\)](#) argued that the shock position oscillations could be driven by a low-frequency thickening and thinning of the upstream boundary layer or by the upstream velocity fluctuations as found by [Beresh et al. \(2002\)](#). These authors found significant correlations between upstream velocity fluctuations and the shock motions at a frequency of 4-10 kHz which is one order of magnitude lower than the characteristic frequency of the large-scale structure

of the incoming turbulent boundary layer that they studied. It is worth mentioning that, the frequency level, found by Beresh et al. (2002), is still far enough from the one found in the recent studies of Dupont et al. (2005) which can reach 0.4 kHz. The effect of a laminar boundary layer on the shock motion was investigated by Fournier et al. (2015). They found that the boundary layer separates, then undergoes transition towards turbulence, with a large-timescale periodic shedding of vortical structures. This low-frequency vortical shedding was interpreted as the reason, at least partly, of the oscillatory shock motion. Ganapathisubramani et al. (2007) reported the existence of very long coherent structures of fifty boundary-layer thicknesses long. They were able to find a correlation between the low-frequency response of the separation point and these large-scale structures of the incoming turbulent boundary layer. Furthermore, the structures are found to scale with \bar{u}_1/λ where \bar{u}_1 is the incoming freestream velocity and λ is the size of the structure. This scale was confirmed when compared with the work of Dupont et al. (2005).

More models can be found in the second category. They may differ in the mechanism in which the low-frequency phenomena occur but they are all produced by the downstream conditions. Piponniau et al. (2009) propose a model in which they explained the breathing of the separation bubble and the low-frequency shock motion in terms of fluid entrainment in the mixing layer, whereby the fluid from the separation bubble is continuously entrained in the mixing layer, shed downstream, and must be replenished at a time scale corresponding to the low-frequency shock oscillations. In another study, Fournier et al. (2018) pointed out that the flow unsteadiness is a result of the mass imbalance between the reversed flow at the reattachment point and the scavenged flow from the separation point. This imbalance is, thus, responsible for the breathing motion of the separation bubble. Dussauge & Piponniau (2008) considered the eddies in the separated region as the main excitation source of the Low Frequency Oscillations (LFO). Pirozzoli & Grasso (2006) proposed that the LFO may be produced by acoustic disturbance resulting from the interaction of the coherent structures, shed by the mixing layer next to the separation point, and the incident shock. Zaman et al. (2002) investigated experimentally and theoretically the shock-wave oscillation in transonic diffusers. They concluded that the mechanism creating those low-frequency oscillations is stimulated by an acoustic resonance, where the low-frequency mode corresponds to the case when the one-quarter wavelength is fitted within the approximate distance from the foot of the shock to the nozzle exit. The same conclusions were made by Johnson & Papamoschou (2010) when investigating, experimentally, the flow in a supersonic planar nozzle.

Simulations have also explored the phenomenology as well as the underlying mechanisms. Rizzetta et al. (2001) found similar LFO to the frequency of the incoming BL

in terms of magnitude. A first detailed study of the LFO was presented by the DNS of [Pirozzoli & Grasso \(2006\)](#). In which, they proposed an acoustics-based resonance mechanism in which waves are generated by the interaction of the incident shock with coherent structures. They also developed a simplified model based on similarities to cavity flows and jet screech. Further elaborating on the dynamics are proposed by [Prièbe & Martin \(2012\)](#), they confirm the breathing of the bubble and further show that shock motion is more correlated to the downstream flow features. [Agostini et al. \(2012\)](#) connected the shock motion to the kinematics of the vortical structures and the foot of the separation shock. [Touber & Sandham \(2009\)](#) perturbed the mean flow obtained from LES with white noise to reproduce the dynamics in the context of a global mode to explain the broadband nature of the low-frequency phenomena. [Olson & Lele \(2011\)](#) investigated numerically the same nozzle as [Papamoschou & Johnson \(2006\)](#) and confirmed the previous findings. [Martelli et al. \(2019\)](#) found, for the same nozzle, that the self-sustained oscillation is driven by a pressure imbalance between the pressure level downstream the shock and the ambient.

Moreover, the validity of many of the previous mechanisms was evaluated by [Morgan et al. \(2013\)](#) through extensive LES database, but still no evident mechanism is found. However, the second class becomes more evident since it has been demonstrated to exist even in the absence of white noises in the boundary layer, as found by [Touber \(2010\)](#).

Additionally, stability analysis was applied to SWBLI in order to understand the origin of low frequency shock unsteadiness. [Robinet \(2007\)](#) used BiGlobal linear-stability analysis to find a 3D global instability leading to self-sustained LFO when exceeding a critical angle. [Touber \(2010\)](#) also found an unstable 2D global mode with growth time scale like the observed one in low frequency bubble breathing. Always by using BiGlobal linear-stability analyses, [Pirozzoli & Grasso \(2006\)](#) identified several weakly damped oscillatory modes resembling bubble breathing.

As [Touber \(2010\)](#) explained that the impact of the upstream turbulent events on the shock motion is evident, since the shock will be inevitably displaced when impacted by an upstream-eddy. However, such high-frequency dynamics is far to be thought to be related to the low-frequency shock motion. Furthermore, the previous idea could be considered in one case if we consider the shock to be a low-pass filter. The latter filters the fluctuations in the incoming boundary layer up to a given cut-off frequency, which would lead to the observed low-frequency unsteadiness as suggested by [Dussauge & Piponnier \(2008\)](#).

Indeed, to be compatible with the shock-motion timescales, those events must be at least at an order of ten-boundary-layer-thicknesses long. For example, [Ganapathisubramani et al. \(2007\)](#) have reported coherent superstructures of about fifty boundary-thicknesses long. They reported also a significant low-frequency shock oscillations at

about $\bar{u}_1/(115\delta_0)$, where δ_0 is the upstream 99% boundary-layer thickness. Using the above superstructure-scaling argument, different kinds of flow with SWBLI; compression corner and shock-reflection experimental studies (Dolling 2001, Dussauge & Piponniau 2008, Dupont et al. 2005, Piponniau et al. 2009) are found to be consistent with the previous scaling, making the upstream superstructures argument questionable unless the shock is truly playing a low-pass filter role.

However, it is worth reminding the very important remarks made by Toubert (2010). First, it must have a deep look at the way in which these correlations are made. For example, if we consider that the shock motions are detected first, then correlated to an earlier event in the incoming boundary layer, traveling at a constant-local mean velocity. In that case, the downstream events are likely excluded to be behind the low-frequency motion. Second, involving arbitrary threshold values would directly influence the level of correlations seen which is the case of Ganapathisubramani et al. (2007) who defines the separation front every spanwise zones with a velocity less than 187 m s^{-1} , due to the difficulty in finding the zero-velocity contour line from the PIV and the impossibility of using a criterion based on the zero skin-friction contour. The previous assumptions led them to report the correlation of the shock motion to the presence of both low- and high-speed regions. The previous findings were impossible to be verified experimentally, but thanks to the DNS of Wu & Martin (2008) one can verify finally that the low-momentum structures are less likely to affect the shock motion. To demonstrate the effect of using arbitrary threshold values, Wu & Martin (2008) used the same criterion as Ganapathisubramani et al. (2007). As a result, more important correlation between the shock motion and the low-momentum structures is clearly noticed.

The three-dimensionality nature of the shock is of capital importance, nevertheless it is often not documented and few are the studies considering this aspect. Mainly, the fewer studies considering the way in which the shock moves are done on compression-ramps trying to answer one question; does the shock oscillate as a block or does it wrinkle in the spanwise direction? One of the existing answers can be found with Wu & Miles (2000) and Edwards et al. (2008). All of them reported the existence of evident spanwise-shock displacement due to the passage of turbulent structures.

After presenting the possible upstream correlation, in what follows we will present the most relevant results concerning the possible correlation between the downstream conditions and the low frequency movement of the shock. Starting with the vortical structures emerging from the shear layer which are considered by Dussauge & Piponniau (2008) as a source of excitation. Pirozzoli & Grasso (2006) take the same way as Dussauge et al. (2006) and they went further by proposing a mechanism in which the vortical structures generate low frequency motion. According to them, when the large coherent structures

interact with the incident shock, an acoustic disturbance is produced and propagates upstream in the subsonic layer, inducing low-frequency oscillatory motion of the shock. The large-scale low-frequency unsteadiness would then be sustained by an acoustic resonance mechanism. The proposed model missed a small detail concerning the possible decoupling between the acoustic field and the turbulence. The previous decoupling was proven by [Borodai & Moser \(2001\)](#), thus the effect of the acoustic field on the turbulence could be neglected. Always with the mixing layer as a source of low frequencies [Piponniau et al. \(2009\)](#) proposed a model based on the mass-entrainment timescale in which the main parameter controlling the low-frequency shock motions is the spreading rate of the compressible mixing layer. The model is thus associated with the separation bubble and the developing mixing layer. The authors denied any influence of the geometry of the flow on the low-frequency motions. On the other hand, they related them to the presence of a separated region downstream of the shock in the presence of a separation-bubble sufficiently large. Moreover, the authors find that the characteristic frequency of the shock motions are affected by the shock intensity and not directly related to any time scale from the upstream boundary layer. Yet more alternative approaches have been suggested in the literature. One particularly interesting approach is based on Dallmann's conjecture [Dallmann \(1988\)](#), which states that multiple recirculation zones occur inside the primary bubble which finally leads to a global structural flow change with "multiple structurally unstable saddle-to-saddle connections", before unsteady vortex shedding occurs. That is why [Boin & Robinet \(2004\)](#) believe that this extends to supersonic flows and SWBLI and that it could explain the first stage of the establishment of the unsteady low frequency. Finally, as [Touber \(2010\)](#) mentioned in his thesis we admit that *"despite the numerous studies cited above, there remain uncertainties regarding possible external sources of unsteadiness"*.

Nerveless one must be cautious, either in his simulations or his experiments, about the use of the different technics used. For instance, the Taylor's hypothesis used on the existence of the observed superstructures, as well as the turbulence-generation technique which often introduces characteristic frequencies that could be of the same order of magnitude as the observed low-frequency oscillations. Further attention must be payed when using periodic boundary conditions, usually used with unsufficient spanwise extent which may results in low-frequency "span-wise tornadoes", as found by [Dussauge & Piponniau \(2008\)](#). These span-wise tornadoes may strength the SWBLI interaction by reducing the effective cross section as reported by [Garnier \(2009\)](#) when simulating a wind tunnel. Another problem that may be faced, when studying low-frequency shock motion, is the integration time, which is usually too short to cover low-frequency oscillation, making the interpretation of the correlation functions subject to caution.

1.3.2 Post-shock region unsteadiness

Whether in the case of free or restricted separation, a recirculation bubble appears in the divergent of the nozzle for a wide range of NPRs. The interface between this bubble and the supersonic jet is characterized by a shear layer which results from the speed difference between these two zones. This layer can be assimilated to a plane mixing layer and is the seat of Kelvin-Helmholtz (KH) instabilities.

1.3.2.1 Development of Kelvin-Helmholtz instability

Flow instabilities may be broadly divided into two categories, convective and global. Convective flow instabilities involve disturbances that undergo spatial growth as they are convected away from their inception point. The resulting coherent structures are responsible for the transport of mass, momentum and energy, and the radiation of acoustic waves. In such cases, all regions of the flow eventually return to their equilibrium state, once the disturbance has passed. In parallel or weakly non-parallel frameworks, the dynamics of such flows are underpinned by local, convectively unstable, downstream-traveling modes, such as the Kelvin-Helmholtz (KH) mode [Martini et al. \(2019\)](#).

This kind of instability is characterized by a dynamic of convective movement resulting when two fluids move at different speeds. These structures, shown in figure 1.8, are of major interest because of their influence on many flow properties, such as mixing, acoustics, heat transfer, etc. For the flows with free sheared layers, the main instability, from which originate large-scale organized structures, is the Kelvin-Helmholtz instability. This instability is caused by the destabilizing effect of the shear when it becomes preponderant under the stabilizing effect of the stratification. This leads to an undulation of the interface, creating concave and convex parts which lead to the amplification of the undulation. Finally, the difference in the velocity of the two fluids causes a spiral rolling up.

The KH mechanism has long been invoked to describe coherent structures in both transitional and turbulent planar shear layers and jets. Various studies carried out were able to highlight the two-dimensional character of these structures. It exists two types of vortices in this kind of flow: two-dimensional cylindrical vortices aligned perpendicularly to the direction of the flow: the so-called primary vortices. 2) the longitudinal counter-rotating vortices superimposed on the main vortices which connect them together: so-called secondary vortices.

Strictly speaking, the mechanism itself is not defined outside of the context of parallel/quasi-parallel laminar shear layers, where, in the spatial stability theory, KH is an unstable modal solution with an associated spatial growth rate. For jets, the solution is typi-

cally a convective instability. Under spreading of the flow, an initially growing wave (at a fixed frequency) will eventually become neutral and decay [Crighton & Gaster \(1976\)](#). For the axisymmetric azimuthal wavenumber, $m = 0$, the resulting wavepacket has a nearly constant phase speed as shown by [Schmidt et al. \(2018\)](#). According to the parallel theory, the mode is unstable at low frequencies but with a growth rate that goes to zero faster than the frequency. In more recent global stability [Nichols & Lele \(2011\)](#) and resolvent analyses [Lesshafft et al. \(2019\)](#) found that the optimal resolvent response is related to the KH mechanism from $St \in [0.3, 1]$, possessing similar characteristics described above through quasi-parallel analysis. In free-shear flows, the downstream-travelling mode is frequently a KH instability, whereas the nature of the upstream-travelling mode may vary depending on the flow considered. [Powell \(1953\)](#) proposed that acoustic waves are responsible for the feedback that underpins tonal behaviour observed in underexpanded supersonic jets which screech, a concept later used to explain the tonal dynamics of impinging jets and cavity flows. In these flows, upstream disturbances are spatially amplified up to some downstream point at which they undergo an interaction (with a solid surface where impinging jets and cavities are concerned, with shock cells in the case of screeching jets) that causes them to be scattered into, among other things, upstream-travelling sound waves, which are then reflected in the nozzle plane. When the phases of the upstream- and downstream-travelling waves are matched at the boundaries, and the reflection conditions are such that positive gain is possible, one has resonance, as well as global instability.

1.3.2.2 Vortex pairings

The development of turbulent structures in a mixing layer was studied by [Ho & Huang \(1982\)](#). The authors conducted an analysis of the response of a free planar mixing layer to a forcing frequency on either side of the separating plate. They observe that the response frequency, f_r , at which the vortices form in the sheared layer, is not necessarily that of the forcing frequency f_f . Indeed, the authors found that when the forcing frequency, f_f , is close to the most likely natural frequency (without forcing), f_m , the response frequency, f_r , is identical to the frequency forcing. On the other hand, if the forcing frequency becomes less than a threshold value, the response frequency switches discontinuously to a higher frequency. The study shows that the forcing frequency influences the position and the number of structures of the mixture layer which merge by modifying the growth rate of the thickness of local vorticity and the associated characteristic frequencies. In their study, the authors distinguish four ranges of response frequencies according to the forcing frequency. The transition between each of the ranges, depending on the forcing is done discontinuously.

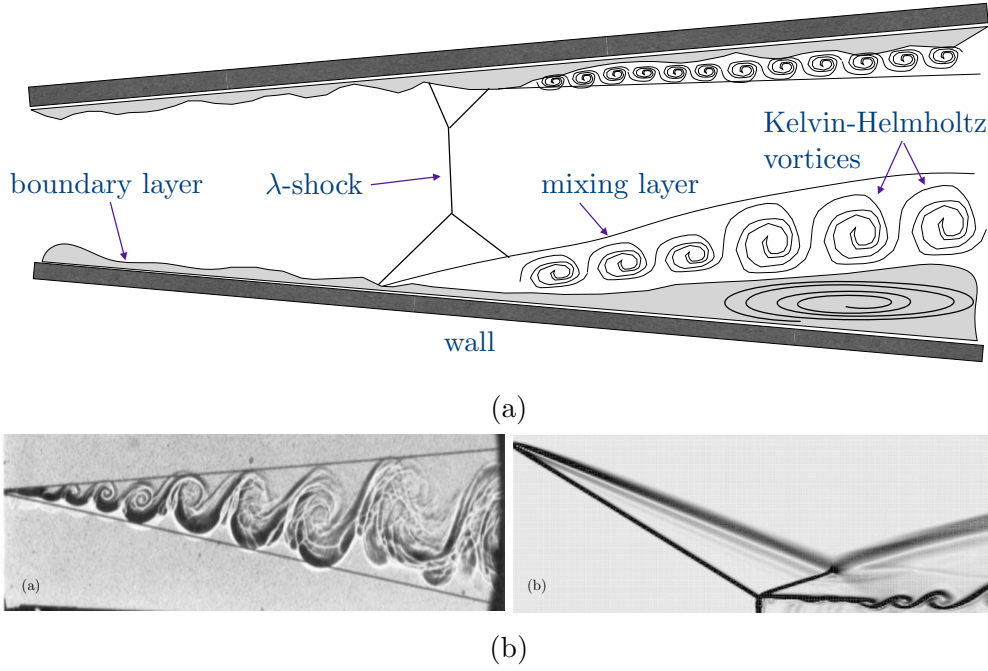


Figure 1.8: (a) Schematic of Kelvin-Helmholtz vortices originating from a separated mixing layer in a planar nozzle. (b) Different topologies of the Kelvin-Helmholtz instabilities; (a) a shadowgraph visualization of Kelvin-Helmholtz vortices originating from a subsonic plane mixing layer [Brown & Roshko \(1974\)](#), (b) Kelvin-Helmholtz vortices emanating from the triple point [Hadjadj et al. \(2004\)](#).

1.3.3 Recirculation bubble and lip vortex

It is well known that the existence of an adverse pressure gradient, in an over-expanded nozzle, leads to the separation of the boundary layer and to the formation of a recirculation zone. When this happens, a sheared layer is formed as a result of the interaction between the recirculation bubble and the detached supersonic jet. The current situation provokes a recirculating current which ensures the mass supply by the fluid return at the nozzle exit lip. This recirculating current leads, also, to the formation of a lip vortex having its own dynamic and fed by the return current.

1.3.3.1 Recirculation bubbles

The various studies, carried out so far, have highlighted the cycle of expansion and contraction of the recirculation bubble, shown in figure 1.9. This cycle is attributed to a phenomenon of "breathing" which results from an imbalance between the rate of entrainment of the fluid by the shear layer and the backflow. Interestingly, this breathing is characterized by a very low frequency as reported by [Piponnier et al. \(2009\)](#). The characteristic frequency of this phenomenon is representative of the convection of turbulent structures of large scales. Indeed, the study [Kiya & Sasaki \(1983\)](#) highlighted an

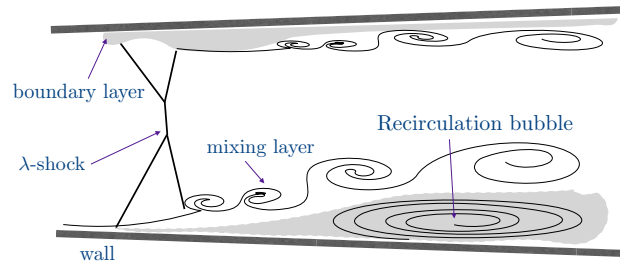


Figure 1.9: Schematic representation showing a recirculation zone in a planar nozzle.

increase in the size of the bubble due to an accumulation of the angular momentum in the recirculation zone. When it reaches a critical size, part of the energy is released in the form of vortex bundles, thereby reducing the volume of recirculation. In order to prevent the formation of the recirculating flow, [Boccaletto \(2011\)](#) presents a process for controlling the separation, called Boccajet. Thus, a small annular aerospike type nozzle is installed at the level of the diverging outlet lip. This nozzle generates a supersonic jet which prevents outside flow from entering the divergent. This maintains a low-pressure level in the divergent and prevents the delamination of the boundary layer.

1.3.3.2 Lip vortex

As mentioned at the beginning of this section, the three-dimensional structures of the flow show that the return current forms a recirculating ring at the level of the nozzle exit lip (see figure 5.8). This ring, which has a significant influence on the recirculating flow rate, is strongly conditioned by the geometry of the outlet lip. Indeed, this dynamic structure directly influences the recirculation zone and can, therefore, be the cause of a change in the position of the separation line. [Pilinski \(2002\)](#) has carried out a numerical study on three different lip geometries to study the influence of lip thickness on recirculation. In the case of an infinitely thick lip (wall), the author notes the appearance of a moderate depression associated with a small vortex. Similarly, in the case of a lip having a thickness equal to $0.1 R_e$, with R_e the exit radius of the divergent, the author notes that the size of the vortex and the associated depression are equivalent to those observed in the case of the lip of infinite thickness. This configuration presents a small difference. Indeed, a small swirl takes place on the lip edge. On the other hand, in the case of a lip of almost zero thickness, the author notes the appearance of a much greater depression due to the presence of a vortex of a significantly larger size. Thus, the air sucked undergoes two successive very close expansion, and the fact that the thickness of the wall is almost zero prevents the flow from gradually modifying its trajectory. This results in a greater angle of velocity relative to the leading edge of the divergent, favoring the development of a larger lip vortex.

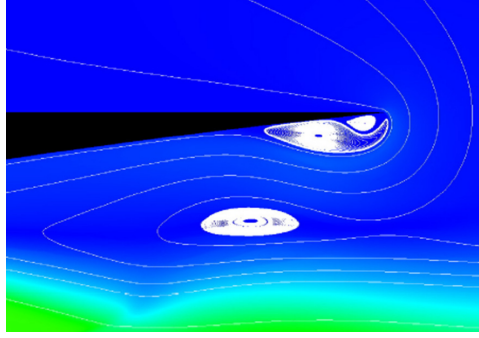


Figure 1.10: Trapped vortex at the nozzle lip, see [Hadjadj et al. \(2015\)](#).

1.3.3.3 Flapping movement of the jet

Among the unsteady phenomena occurring within the mixing layer, the low-frequency flappy movement of the jet (FJ). This phenomenon refers to the intermittent-radial two-dimensional flip-flop motion of the mixing layer, with respect to the major plane of symmetry of the nozzle (see figure 1.11). It has many practical application, for instance it is found in various control devices to disturb the shear layer or to enhance heat transfer, not only for single-phase flows but also for multi-phase flows. As a result, there have been numerous investigations of these flows following the pioneering work of [Viets \(1975\)](#). The latter presented in his study, an experimental nozzle characterized by a significant instability of the main jet at the outlet. This instability arises from the fact that a jet confined by walls sufficiently close is unstable and may possibly oscillate between the two walls. In addition, a small pressure fluctuation at the exit of the nozzle can lead the jet to change its side. This highly fluctuating nature of the jet at the exit results from a process of feedback of the fluid in the chamber which causes the deflection of the jet on one side then on the other of the nozzle. [Platzer et al. \(1978\)](#) compared the entrainment rates of an FJ with a non-flapping jet (NFJ) and found that the FJ is superior over the NFJ in entrainment of the ambient fluid. [Morris et al. \(1992\)](#) reported data describing the motion of air and particles in a FJ flow. More detailed experimental results were provided by [Raman & Rice \(1994\)](#), who investigated not only the characteristics of the flow outside the nozzle, but also the mechanism of the nozzle extended from [Viets \(1975\)](#) and its geometric configuration. However, these previous investigations have only provided limited measurements of the turbulent mixing characteristics of FJ flows. The frequencies of such phenomena has been reported in the literature for instance [Mi et al. \(2001\)](#) reported that the phenomon could be observed at a Strouhl number of the order of $6.7 \cdot 10^{-4}$, which is nearly one order of magnitude below the one found in [Viets \(1975\)](#) ($St = 5.0 \cdot 10^{-4}$). In a preliminary investigation using a single hot-wire probe and a phase averaging scheme, [Mi et al. \(2001\)](#) concluded that the nozzle produces a jet with a “flag-like” flapping motion and that this easily detectable large-scale oscillation decays rapidly

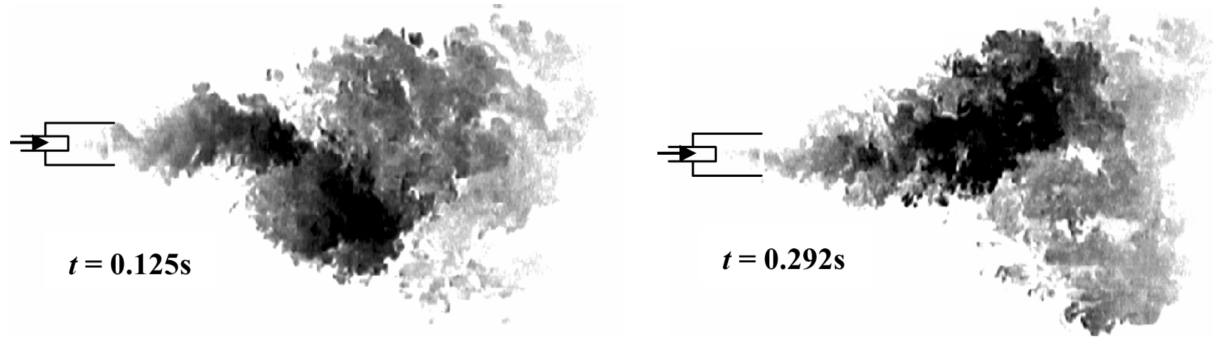


Figure 1.11: A sequence of images of an external flapping jet at $St = 7.0 \cdot 10^{-4}$ obtained by laser induced fluorescence, see [Mi et al. \(2001\)](#).

so that it could not be captured in the far field.

1.4 Planar vs. axisymmetric nozzle flow

Having described the different characteristics of a flow in a propulsive nozzle as well as the most important types of instabilities that can be encountered in such flow, it is worth remembering that all the phenomenology described before can be observed in all kinds of nozzles whether curved, conical or planar. However, since the majority of the present work deals with these instabilities in planar nozzles, as well as a conical nozzle, it is very important to clarify; first, the peculiarity of these phenomena observed in planar nozzles compared to the so-called realistic-geometry nozzles, secondly, the phenomena observed exclusively in this type of nozzle.

1. The asymmetry of the jet

Starting with the asymmetry of the jet, it turns out that the asymmetry of the jet is less present in the axisymmetric nozzles while it is very present in the planar ones for very precise NPR intervals reported in the literature, such as [Hunter \(2004\)](#) who found the jet to be axisymmetric for NPR interval ranging from 1.4 to 2.4, or [Verma & Manisankar \(2014\)](#) who reported the asymmetry of the jet for NPR interval ranging from 1.5 to 2.9. As for the direction of the asymmetry, it turns out to be random and only the initial conditions can influence it, as reported by [Papamoschou et al. \(2009\)](#). The natural change (*i.e.* without excitation) of the asymmetry direction, during the same run, is a phenomenon already seen in the curved nozzles, but it is very rarely seen in the planar nozzles. But apart from [Verma & Manisankar \(2014\)](#), no one has ever seen it. In the end, it is a phenomenon that happens at a very low frequency, consequently it is very hard to be reproduced by computation for reasons of the computation costs. In the literature, researchers report that this phenomenon never occurs in the same run. However, the direction of the jet can

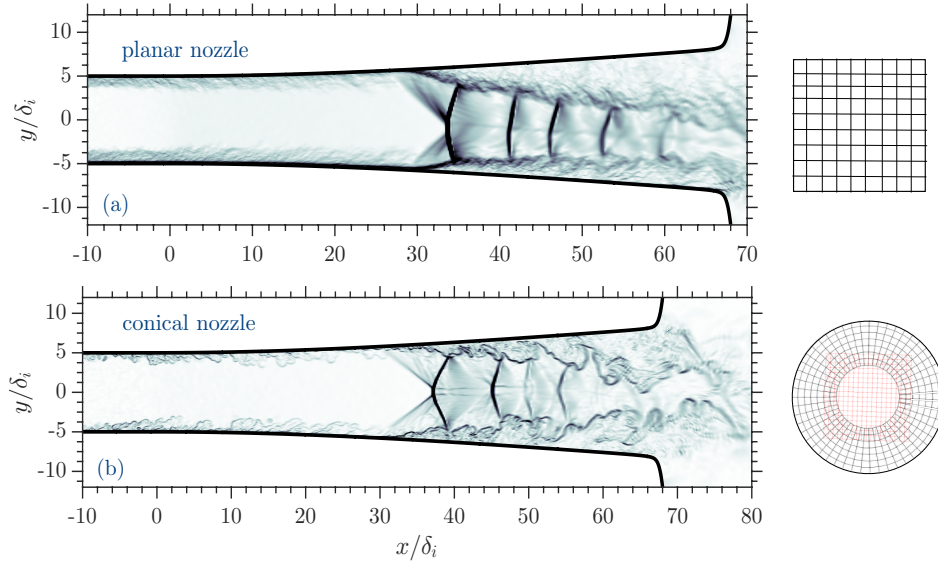


Figure 1.12: z-averaged numerical “Schlieren” imaging contour $\nabla|\rho|$; (a) planar nozzle, (b) conical nozzle for identical flow conditions, from Piquet (2017).

switch from one side to the other for different runs Johnson & Papamoschou (2010). In addition, it has been reported that the thermal or the dynamic forcing of the jet can push the jet to change its direction Xiao et al. (2007). Many people have tried to understand or formulate this asymmetry, such as Telega et al. (2019) who tried to parametrize the shock waves topology finding that the normalized height of the top and bottom λ -feet remain the same in both asymmetric and symmetric cases. The authors have confirmed their observations through both experimental and CFD results. Sun et al. (2020) developed a theoretical model for the asymmetry of the shock train in supersonic flows base on the properties of the fluid entrainment in the mixing layer and momentum conservation. Flow deflection angles downstream of different SBLI regions were successfully deduced from this model. Finally, it is important to remember that in the case of a conical nozzle undergoing the same conditions (*i.e.* initial, limits and geometrical) as a planar nozzle, the jet turns out to be symmetrical as reported by Piquet (2017) (see figure 1.12). A possible explanation for this is as follows: we can say that having two separation zones (in the upper wall and the lower wall) not communicating in the planar case and the presence of the periodic conditions for the spanwise direction, reinforces the asymmetry comparing to the conical case where there is one zone consequently the flow establishes a certain thermodynamic equilibrium each time to keep the symmetry of the jet.

2. The shock movement:

The shock movements are more important in the planar case. These movements

are observed by several authors [Hunter \(2004\)](#), [Verma & Manisankar \(2014\)](#), [Papamoschou et al. \(2009\)](#), [Martelli et al. \(2019\)](#), [Zaman et al. \(2002\)](#), [Bogar et al. \(1983\)](#). They are less important in the axisymmetric cases such that for the same conditions (*i.e.* initials, limits and geometrical), wider shock oscillations are observed in the planar case than the other cases [Piquet \(2017\)](#). The mechanism generating these oscillations is always ambiguous. Indeed, they depend on several parameters or physical phenomena as it was already shown at the beginning of this introduction. In the planar case, the shock movements strongly depend on the recirculation bubbles, on the flow conditions either downstream or upstream, as well as some acoustic phenomena. More details on this subject will be given later in this work. The amplitude of the shock oscillations depends on the NPR, the geometry of the nozzle and the configuration of the jet (*i.e.* symmetrical or asymmetrical). Generally, the more asymmetrical is the jet, the greater is the distance swept by the shock. Finally, it should be remembered that these movements have a very important influence on the streamwise forces but they participate in a moderate way in the side loads. This is mainly due to the fact that the amplitude of these oscillations is greater in the streamwise direction than the other directions.

3. Recirculation bubbles:

Recirculation bubbles are found in all separated-nozzle flows regardless of their types. Nevertheless, their influence is more remarkable in the planar nozzles. Generally, we found two bubbles in a separated planar-nozzle flow. The first is usually very wide and opened while the second is small and closed. The two bubbles do not communicate with each other. The largest of this bubble is often open to the ambient. This difference in size is caused by the famous λ -asymmetric shock. It has been shown that the activities of these bubbles, in particular, the largest one generates low frequencies. To understand the mechanism through which these bubbles generate low frequencies, several scenarios have been proposed such as that of [Piponnier et al. \(2009\)](#) in which they found that the bubble breathing mechanism which results in the emptying of the recirculation region is responsible for the low-frequencies. The mass of air in the bubble is progressively entrained by the vortex structures of the mixing layer. This mass training continues until the volume of dead air is greatly reduced. The bubble then sucks in a new mass of air downstream to reform the detached bulb. The time of a drain-fill cycle constitutes the period of oscillation of the bulb. For NPRs where the jet is symmetrical, the two bubbles are almost identical. This situation is more stable and consequently fewer oscillations are observed.

4. Lip vortices:

A major difference between this phenomenon observed in a planar nozzle and that observed in an other type of nozzle is its shape. Obviously, the lip vortex has a toroidal shape in all types of nozzles [Georges-Picot \(2014\)](#) (see figure 1.13, apart from the planar nozzle where it appears as a longitudinal cylinder at the exit of the planar nozzle. In addition, it turns out that the height of the lips of the nozzle plays an important role in the formation of this type of instability.

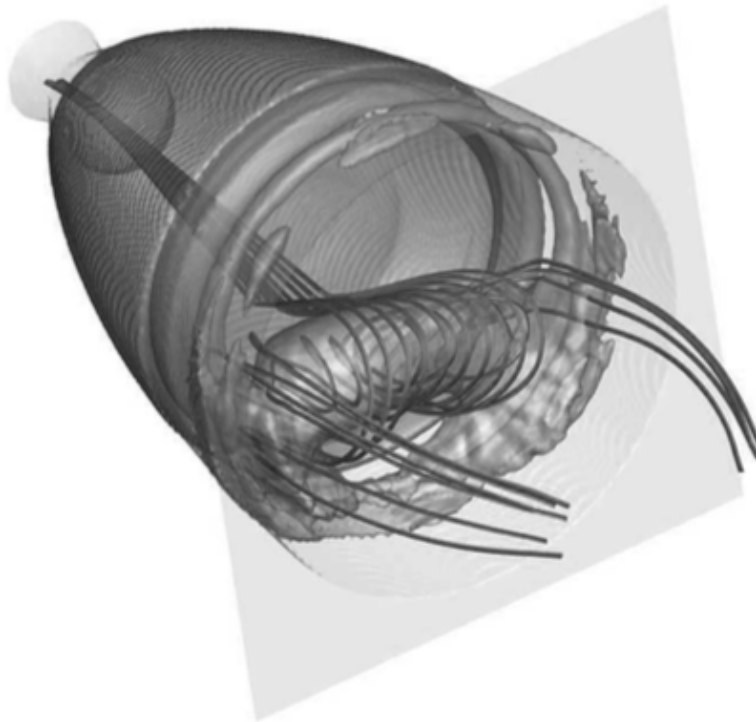


Figure 1.13: Iso-volume of pressure showing the toroidal shape of the lip vortices from [Georges-Picot \(2014\)](#).

1.5 Scope of the present work

Based on the above discussion of the existing literature, the need for a better understanding of the driving mechanism, for the observed low-frequency unsteadiness in an over-expanded nozzle flows, was established. This was shown to have been driving research in this area for several decades. The unsteady character of SWBLI remains an important practical challenge for the nozzle flow problems. In fact, this kind of flow usually exhibits very low-frequency shock motions which are more challenging to study from a computational point of view, due to the need to obtain longer time series to be

resolved.

The following work intends to highlight this problem, using large-eddy simulations as the primary tool to generate the data. The data are then analyzed with the intention of shedding light on some scarce fundamental questions, concerning the impacts of various physical parameters on the phenomena. In particular, we aim to:

1. Validate the wall model approach used through sensitivity studies and comparisons with experiment. This will allow to investigate the low-frequency phenomena through long LES runs.
2. Investigate the implications of different upstream and downstream physical parameters such as the nozzle pressure ratio, the wall-temperature and the downstream conditions variations on the low-frequency shock oscillations.
3. Study the low frequency phenomena using both spectral analysis and dynamic mode decomposition.

1.6 Outline of the dissertation

As mentioned earlier, a comprehensive overview of the literature reveals that many important questions regarding the separation of the nozzle flow as well as the accompanied phenomena are still open. Therefore, the present work addresses some of them. This thesis is organized as follows:

Chapter 2: introduces the governing equations using both Cartesian and curvilinear forms with an emphasis on the filtered 3D compressible Navier–Stokes equations. The numerical strategies used are described afterword.

Chapter 3: In this chapter, the wall-model methodology is presented, in particular the way in which the model is implemented in the LES code. Then, the assessment of its performance through a set of examples including simulations of a flat plate, with and without pressure gradient, and the comparison with a previous DNS results. The model is afterwards tested through long Wall Modeled (WM)-LES on supersonic nozzle flow to demonstrate its ability to accurately reproduce the separation of the boundary layer, as well as the shock movement at low frequency. The main results are submitted to: *International Journal of Heat and Fluid Flow*.

Chapter 4: The problem of shock-induced flow separation in an overexpanded

supersonic planar nozzle is investigated numerically, by means of a very long three-dimensional wall-modeled large-eddy simulations. The objective is to identify the origin of the low-frequency shock oscillations and of the associated side-loads in planar nozzles. The computational results are compared with the experimental data for validation. A scenario of the driving low-frequency shock oscillations, confirming conclusions from earlier studies, is described in this chapter. The results are published in: *AIAA Journal* (Zebiri et al. 2020).

Chapter 5: The study focuses on different mechanisms leading to the low-frequency shock oscillations (LFO) in a planar nozzle. Thus, we mainly focus on the effect of the recirculation bubble, its size and its location on the generation of LFO. A particular attention is made to study the shock and its back and forth oscillations. Finally, a formula is made empirically in order to predict the main tone. The results are under consideration for publication in: *Physics of fluids*.

Chapter 6: In this sixth chapter, we use both wall-resolved-LES and wall-modeled-LES to simulate the flow in an over-expanded conical nozzle. The objective is to study in details the different complex flow phenomena such as the turbulent boundary layer, the internal shock and the separated mixing layer, for the purpose of providing an insightful understanding of the low-frequency phenomena, occurring in a conical nozzle. Dynamic mode decomposition (DMD) analysis is used to better understand the behavior of these phenomena. The results are published in: *Aerospace science and technology*.

Chapter 7: This chapter presents the effects of wall temperature in nozzle flows. The focus is on the changes in shock structure and the role of these change in controlling its movement. The results are not yet published.

Chapter 8: The summary of the research work undertaken along with the concluding remarks are given in the last chapter. This also opens multiple possibilities for different perspective works.

2

Governing equations and numerical methods

Highlights

- Three dimensional filtered Navier-Stokes equations are presented in a conservative form in both Cartesian and generalized curvilinear coordinates.
- The convective fluxes are discretized using a sixth-order central scheme for smoothed solutions, and a sixth-order Weighted-Essentially-Non-Oscillatory (WENO) for shocked regions.
- Time advancement is achieved through a fourth-order Runge-Kutta (RK4) time stepping.
- The robustness of the overall numerical scheme is assessed through a series of numerical test problems that include vortex advection, 2D supersonic flow over a cylinder, Poiseuille flow and a 3D turbulent channel flow.

Introduction

This chapter presents the governing equations in both Cartesian and generalized curvilinear forms along with the numerical methods used to perform the simulations. Meanwhile, some code validation cases are presented and a brief description of the test case is given at the end of this chapter.

2.1 Governing equations

The Large Eddy Simulation (LES) approaches are based on the idea of a distinction of scale. The main idea is to completely solve the most energetic turbulence structures on a large scale and to model only the effect of the smaller unresolved scales, in order to reduce, as much as possible, the number of degrees of freedom of the continuous system and to stay as truthful as possible to the continuous system. In the end, all of this is done in order to reduce the cost of computation associated with the resolution. In reality, the operation goes through several stages. First, we must define the computation grid. Afterward, we choose, supposedly, the greatest distance existing between two successive points in the grid, *i.e.* Δx . This distance corresponds to the cutting off the highest wavenumber k defined as follows: $k = \pi/\Delta x$, in a Fourier space. Finally, using this low-pass Nyquist filter, all eddies smaller than $2\Delta x$ will be systematically modeled and will not be computed. The present filter is applied to the three-dimensional compressible Navier-Stokes equations (the conservation of mass, momentum and energy) initially defined, in Cartesian coordinate $x_i = (x, y, z)$, as follows:

$$\frac{\partial \rho}{\partial t} + \frac{\partial \rho u_j}{\partial x_j} = 0, \quad (\text{Continuity})$$

$$\frac{\partial \rho u_i}{\partial t} + \frac{\partial \rho u_i u_j}{\partial x_j} = -\frac{\partial p}{\partial x_i} + \frac{\partial \tau_{ij}}{\partial x_j}, \quad (\text{Momentum})$$

$$\frac{\partial \rho e}{\partial t} + \frac{\partial (\rho e + p) u_j}{\partial x_j} = \frac{\partial \tau_{ij} u_i}{\partial x_j} - \frac{\partial \dot{q}_j}{\partial x_j}, \quad (\text{Energy})$$

where ρ is the density, u_i the velocity components, p the pressure, T the temperature, e the total energy, τ_{ij} the viscous stress tensor and \dot{q}_i the heat diffusion flux.

The perfect gas state is considered with

$$p = \rho r T, \quad (2.1)$$

The total energy is expressed as:

$$e = e_i + K = C_v T + \frac{1}{2}(u_i u_i), \quad (2.2)$$

the shear stress tensor:

$$\tau_{ij} = 2\mu S_{ij} + \mu'' \delta_{ij} \frac{\partial u_k}{\partial x_k}, \quad (2.3)$$

$$S_{ij} = \frac{1}{2} \left(\frac{\partial u_i}{\partial x_j} + \frac{\partial u_j}{\partial x_i} \right), \quad (2.4)$$

and the heat diffusion flux:

$$\dot{q}_j = -\lambda \frac{\partial T}{\partial x_j}. \quad (2.5)$$

The viscous stress tensor is composed of a viscous part and a dilatation part, where S_{ij} denotes the strain rate tensor and μ'' the second viscosity. On the assumption of a Newtonian fluid, the second viscosity can be expressed by the relation of Stokes (2.6) where μ_b denotes the bulk viscosity:

$$\mu_b = \mu'' + \frac{2}{3}\mu. \quad (2.6)$$

The dynamic viscosity follows the Sutherland law:

$$\mu(T) = \mu_{ref} \frac{T^{2/3}}{S + T}, \quad \text{with } S = 110.4K, \quad (2.7)$$

where the constant μ_{ref} depends on the fluid parameters.

The Prandtl number Pr is taken equal to 0.72, the heat capacity ratio $\gamma = 1.4$, the viscosity constant $\mu_{ref} = 1.456 \times 10^{-6} [kg \, m^{-1} s^{-1}]$, the bulk viscosity $\mu_b = 0 [kg \, m^{-1} s^{-1}]$ and the specific gas constant $r = 287 [m^2 K^{-1} s^{-2}]$.

The error associated with the modeling of the unresolved scales is called the projection error. In this kind of calculation, the projection error is often associated with two other errors: the description error and the discretization resolution error. The origin of the first is the approximation of the partial derivatives of the continuous problem by their discrete counterparts. While the second is associated with the contribution of missing scales via the non-linear terms.

Therefore, the best LES approach possible is where the description error cancels the discretization error. This is generally attempted using one of the two different families of approaches: either we introduce a forcing term (the sub-grid scale model) in the equations to cancel the resolution error, or we design the numerical schemes in such a way that the discretization error cancels the resolution error.

In some how the LES problem is often treated as an application of a low-pass convolution filter to Navier-Stokes equations. The properties of such a filter are first described in the following, then applied to the compressible Navier - Stokes equations. A spatial-scale filtering is introduced using the convolution product:

$$\bar{\vec{\varphi}} = \int_D G(\vec{x} - \vec{z}; \bar{\Delta}) \vec{\varphi}(\vec{z}) d^3\vec{z}, \quad (2.8)$$

where $\vec{\varphi}$ is any vector field, G the convolution filter kernel and $\bar{\Delta}$ the characteristic cutoff length scale. The convolution filter kernel can be any filter function but is often assimilated to a top-hat function. Typically, the filter function is an infinitely differentiable function of bounded support in a bounded domain and normalized to ensure the conservation of constants such that:

$$\int_D G(\vec{x} - \vec{z}; \bar{\Delta}) d^3\vec{z} = 1, \quad (2.9)$$

It should be recalled that the grid filter, designated by the overline notation, must be distinguished from the test filter, which corresponds to an explicit filtering operation, performed on the resolved field in order to compute the subgrid-scale model terms.

The spatial-scale filter (2.8) is applied to the Navier-Stokes equations, where $\tilde{\varphi} = \bar{\rho}\varphi/\bar{\varphi}$ is the Favre-averaging, $\varphi'' = \varphi - \tilde{\varphi}$ the Favre-fluctuation and $\varphi' = \varphi - \bar{\varphi}$ the Reynolds-fluctuation:

$$\frac{\partial \bar{\rho}}{\partial t} + \frac{\partial \bar{\rho} \tilde{u}_j}{\partial x_j} = 0, \quad (\text{Continuity})$$

$$\frac{\partial \bar{\rho} \tilde{u}_i}{\partial t} + \frac{\partial \bar{\rho} \tilde{u}_i \tilde{u}_j}{\partial x_j} = -\frac{\partial \bar{p}}{\partial x_i} + \frac{\partial \bar{\tau}_{ij}}{\partial x_j} - \frac{\partial \overline{\rho u_i'' u_j''}}{\partial x_j}, \quad (\text{Momentum})$$

$$\frac{\partial \bar{\rho} \tilde{e}}{\partial t} + \frac{\partial (\bar{\rho} \tilde{e} + \bar{p}) \tilde{u}_j}{\partial x_j} = \frac{\partial \bar{\tau}_{ij} \tilde{u}_i}{\partial x_j} - \bar{q}_j - \frac{\partial \overline{\rho e'' u_j''}}{\partial x_j} - \frac{\partial \overline{p' u_j'}}{\partial x_j} - \frac{\partial \overline{\tau'_{ij} u_i'}}{\partial x_j}, \quad (\text{Energy})$$

$$\bar{q}_j = -\bar{\lambda} \frac{\partial \bar{T}}{\partial x_j} - \lambda' \frac{\partial \overline{T'}}{\partial x_j}. \quad (2.10)$$

The subgrid viscous term $\bar{\tau}_{ij}$ can also be split into a filtered part and a fluctuation part. The subgrid-scale stress tensor $\tau_t = \overline{\rho u_i'' u_j''}$ and the subgrid-scale Reynolds heat flux $\lambda' \frac{\partial T'}{\partial x_j}$ which comes from the filtered equations, are known as the SubGrid-Scale terms (or SGS). Some of the SGS terms are negligible compared to others. For instance, the subgrid-scale pressure terms and viscous terms are known to be relatively small compared to the other terms.

The most common approach is to model those terms by an eddy viscosity approach

such as:

$$\tau_t = 2\mu_t \overline{S_{ij}} + \mu_t'' \delta_{ij} \frac{\partial \overline{u_k}}{\partial x_k}, \quad (2.11)$$

$$\lambda' \frac{\partial \overline{T'}}{\partial x_j} = \lambda_t \frac{\partial \overline{T}}{\partial x_j} = \frac{\mu_t C_p}{P_{rt}} \frac{\partial \overline{T}}{\partial x_j}. \quad (2.12)$$

2.1.1 Subgrid-scale model

The resolution of the full set of filtered equations cannot be achieved unless the subgrid-scale terms are modeled and related to the computed variables. Among the multiple models to compute the subgrid-scale viscosity existing in literature, the WALE model, presented in this section, has been selected to be used in this work thanks to its ability to simulate wall-bounded flow. The WALE model [Nicoud & Ducros \(1999\)](#) is based on the square of the velocity gradient tensor, its spatial operator consists of mixing both the local strain and the rotation rates. Thus all the turbulence structures relevant for the kinetic energy dissipation are detected by the model. The model does not use any constant adjustment or damping function since the eddy-viscosity goes naturally to zero in the vicinity of a wall. In the case of pure shear, the model produces zero eddy viscosity. Moreover, it is invariant to any coordinate translation or rotation and only local information are needed so that it is well-suited for LES in complex geometries [Nicoud & Ducros \(1999\)](#).

The WALE model has been developed to handle wall-bounded flow and transitional problem. The form of the eddy viscosity term can be expressed as follows:

$$\mu_t = \rho (C_m \Delta)^2 \frac{(S_{ij}^d S_{ij}^d)^{3/2}}{(S_{ij} S_{ij})^{5/2} + (S_{ij}^d S_{ij}^d)^{3/2}}, \quad (2.13)$$

$$S_{ij}^d = \frac{1}{2} \left(\left(\frac{\partial u_i}{\partial x_j} \right)^2 + \left(\frac{\partial u_j}{\partial x_i} \right)^2 \right) - \frac{1}{3} \delta_{ij} \left(\frac{\partial u_k}{\partial x_k} \right)^2, \quad (2.14)$$

where $C_m = \sqrt{10.6} C_s$ is a model constant, proportional to the LES Smagorinsky's constant C_s defined by $C_s = \frac{1}{\pi} \left(\frac{3C_K}{2} \right)^{-5/4}$ and S_{ij}^d an operator based on the traceless symmetric part of the square of the velocity gradient. In a shear layer, the term $S_{ij}^d S_{ij}^d$ tends to zero near the wall to conserve the property of wall-bounded flow. The WALE model has the advantage of reproducing the asymptotic scaling in $O(y^3)$ of the eddy viscosity near the wall.

2.1.2 Generalized curvilinear coordinates

In order to succeed in simulations with fairly complex geometries, it is necessary to deploy the necessary tools which justifies the choice of the WALE model. However, that is not enough because the Cartesian coordinates have trouble marrying complex and arbitrary forms. This is why the present code used in this study is written in generalized curvilinear coordinates. The generalized curvilinear coordinates are obtained through the transformations from computational space to physical space. In general, the transformation from physical space to computational space is not known a priori and the physical mesh is directly described by the x , y and z space coordinates. It is common, then, to use the inverse of the metrics, which represent the transformation from physical to computational space, by numerically deriving the physical mesh coordinates (ξ , η and ζ) through a finite difference scheme. More details can be found in [Piquet \(2017\)](#). To get the LES in the transformed system, chain rule expansions are used:

$$\left(\frac{\partial}{\partial x} \quad \frac{\partial}{\partial y} \quad \frac{\partial}{\partial z} \right)^T = \mathbf{J} \left(\frac{\partial}{\partial \xi} \quad \frac{\partial}{\partial \eta} \quad \frac{\partial}{\partial \zeta} \right)^T. \quad (2.15)$$

where $\mathbf{J} = \partial(\xi, \eta, \zeta) / \partial(x, y, z)$ is the Jacobian matrix of the transformation. The equations are then written in the conservative form as follows:

$$\begin{aligned} \frac{\partial \bar{\rho}}{\partial t} + \frac{\partial \bar{\rho} \tilde{U}_j}{\partial \xi^j} &= 0 & (\text{Continuity}) \\ J \frac{\partial \bar{\rho} \tilde{u}_i}{\partial t} + \frac{\partial \bar{\rho} \tilde{u}_i \tilde{U}_j}{\partial \xi^j} &= - \frac{\partial \overline{J \xi_i^j p}}{\partial \xi^j} + \frac{\partial \overline{J \xi_j^k \tau_{ij}}}{\partial \xi^k} - \frac{\partial \overline{J \xi_j^k \tau'_{ij}}}{\partial \xi^k} & (\text{Momentum}) \\ J \frac{\partial \bar{\rho} \tilde{e}}{\partial t} + \frac{\partial (\bar{\rho} \tilde{e} + \bar{p}) \tilde{U}_j}{\partial \xi^j} &= \frac{\partial \overline{J \xi_i^k \tau_{ij} \tilde{u}_j}}{\partial \xi^k} - \frac{\partial \overline{J \xi_j^k \dot{q}_j}}{\partial \xi^k} - \frac{\partial \overline{J \xi_i^k \tau'_{ij} \tilde{u}_j}}{\partial \xi^k} & (\text{Energy}) \\ \tau_{ij} &= \mu(\bar{T}) \left[\left(\xi_i^l \frac{\partial \tilde{u}_j}{\partial \xi^l} + \xi_j^l \frac{\partial \tilde{u}_i}{\partial \xi^l} \right) - \frac{2}{3} \delta_{ij} \xi_m^l \frac{\partial \tilde{U}_m}{\partial \xi^l} \right] & (2.17) \end{aligned}$$

$$\bar{q}_j = -\lambda(\bar{T}) \xi_j^l \frac{\partial \bar{T}}{\partial \xi^l}, \quad (2.18)$$

where $\xi_i = (\xi, \eta, \zeta)$ for consistency and $U = J \xi_j u_j$ is called the contravariant velocity which can be considered as the projection of the velocity components on the computational space. The subgrid shear-stress tensor, $\overline{\tau'_{ij}}$, and the subgrid heat-diffusion flux, \bar{q}_j , are modeled according to the eddy-viscosity hypothesis [Lilly \(1992\)](#).

2.2 Numerical method

The code used for this study is based on an existing *in-house* solver developed at the CO-RIA laboratory in Rouen (Hadjadj & Kudryavtsev 2005, Chaudhuri, Hadjadj, Chinnayya & Palerm 2011). The code, called ChocWaves (Compressible High-Order Code using Weno AdaptatiVE Stencils), is a Cartesian explicit Navier–Stokes solver with WENO / Central scheme for space discretization and compact RK3 for time integration. It uses the Immersed Boundary Method (IBM) (Chaudhuri, Hadjadj & Chinnayya (2011), Piquet et al. (2016)) to simulate compressible turbulent flows over complex geometries (Chaudhuri et al. (2012), Chaudhuri & Hadjadj (2016), Hadjadj (2012), Shadloo & Hadjadj (2017)).

The version of the code used for this work was developed by Piquet (2017). It is a curvilinear explicit finite-difference Navier–Stokes solver with WCNS / Central / Hybrid scheme for space discretization and RK4 for time integration. The solver uses the HDF5 library for IO and the MPI library for parallelization. Its scalability been tested on more than 20k CPUs and shows a very good performance even for a large number of nodes (see Piquet (2017)).

2.2.1 Spatial scheme

In supersonic flows, the use of sufficiently robust numerical schemes in regions of strong gradients or close to a discontinuity (such as a shock wave) as well as in regions of turbulence, is essential. The WENO (Weighted Essentially Non-Oscillatory) schemes are based on the numerical flux construction, at a high order, from a convex linear combination reconstructed on a weighting of lower-order polynomials (stencils). The weighting of the stencils aims to maximize the accuracy of the diagram in the so-called smooth regions (without gradients), while canceling the effect of the adaptive stencil near the discontinuity.

Nevertheless, since the present solver is written in the general curvilinear coordinates, it is worth remembering that the spatial scheme may deal with issues of freestream preservation and metric cancelation. These errors arising from the finite-difference discretization of the terms in strong-conservative form can lead to unphysical behavior of the flow and numerical instability.

The WENO (Weighted Essentially NonOscillatory) scheme applies a weighted averaging procedure directly to the flux. It is then impossible both to evaluate the discretization scheme used on the metrics and to force the freestream preservation. Thus, the WENO scheme can only be used in the non-conservative form of the Euler equations which do not impose global conservation on the set of equations. Deng & Zhang (2000) devel-

oped a fifth-order Weighted Compact Nonlinear scheme (WCNS) where the conservative variables are interpolated using a weighted averaging procedure similar to the WENO scheme. In this formulation, the freestream condition can be imposed because the metrics are evaluated by the same numerical finite-difference scheme used in the WCNS. [Nonomura et al. \(2010\)](#) compared WENO and WNCs schemes on curvilinear grid and proved that the WCNS imposes the freestream preservation. [Nonomura & Fujii \(2013\)](#) developed a compact form of the WCNS scheme to reduce the stencil and found a new technique for freestream preservation of the WENO scheme ([Nonomura et al. 2015](#)).

2.2.1.1 Convective terms

Different methodologies are used to discretize the convective terms, whether by a local conservative central difference scheme, by a WCNS scheme or by a hybrid scheme.

Conservative central difference scheme

Following the work of [Pirozzoli \(2010\)](#), the standard central difference formulas can be applied to the convective term by using a split form which improves the stability and the energy preservation properties. The convective term is discretized by a conservative finite-difference scheme:

$$\frac{\partial \varphi}{\partial \xi} = F_{i+1/2} - F_{i-1/2}, \quad (2.19)$$

where $F_{i+1/2}$ is the numerical flux.

The 6th-order form of the central finite-difference scheme is used to match the WCNS's order (5th-order). The numerical flux is computed using a generalized curvilinear Euler equation by the following (for the x -component):

$$F_{i+1/2} = 2 \sum_{l=1}^6 a_l \sum_{m=0}^{l-1} (f, g, h)_{j-m,l}, \quad (2.20)$$

$$(f, g, h)_{j,l} = \frac{1}{8} (f_j + f_{j+l})(g_j + g_{j+l})(h_j + h_{j+l}), \quad (2.21)$$

where $a_1 = 3/4$, $a_2 = a_3 = -3/20$, $a_4 = a_5 = a_6 = 1/60$ and (f, g, h) represents variables used in the curvilinear Euler equation $((f, g, h) = (\rho, \vec{u}, \vec{U}))$.

WCNS scheme

Following the work of both [Deng & Zhang \(2000\)](#) and [Nonomura et al. \(2010\)](#), the 5th-order WCNS is used to discretize the generalized curvilinear coordinates of the Euler's

equations as follows:

$$J \frac{\partial \vec{Q}}{\partial t} + \sum_{j=1}^3 \frac{\partial \vec{E}_j}{\partial \xi^j} = 0, \quad (2.22)$$

where \vec{Q} is the conservative vector $\vec{Q} = (\rho, \rho u, \rho v, \rho w, \rho e)^t$ and \vec{E}_j is convective terms $\vec{E}_j = (\rho U_j, \rho u U_j + J \xi_x^j p, \rho v U_j + J \xi_y^j p, \rho w U_j + J \xi_z^j p, (\rho e + p) U_j)^t$.

The spatial derivative $\partial E / \partial \xi^j$ can be evaluated by a sixth-order midpoint to computational-node difference scheme,

$$\frac{\partial E}{\partial \xi} = \frac{75}{64} (E_{i+1/2}^{\text{WCNS}} - E_{i-1/2}^{\text{WCNS}}) - \frac{25}{384} (E_{i+3/2}^{\text{WCNS}} - E_{i-3/2}^{\text{WCNS}}) + \frac{3}{640} (E_{i+5/2}^{\text{WCNS}} - E_{i-5/2}^{\text{WCNS}}), \quad (2.23)$$

where $E_{i+1/2}^{\text{WCNS}}$ is the WCNS numerical flux calculated at a midpoint.

The WCNS weighted averaging procedure is applied to the characteristic variables W_i , to find the left and right interpolated fluxes, $Q_{i+1/2}^{\text{WCNS},L}$ and $Q_{i+1/2}^{\text{WCNS},R}$, respectively. The transformation from conservative to primitive variables is detailed in the following equations:

$$J \frac{\partial Q}{\partial t} + A_j \frac{\partial Q}{\partial \xi^j} = 0, \quad (2.24)$$

$$A_j = \frac{\partial E_j}{\partial Q} = R \Lambda L, \quad (2.25)$$

where A is the flux Jacobian, L the left eigenvector, R the right eigenvector and Λ the diagonal matrix with the eigenvalues of A . By definition, $L = R^{-1}$. The transformation from conservative to characteristic is defined by the following equation:

$$W_{i,m} = L_{i^*,m} Q_i, \quad (2.26)$$

where i^* denotes the Roe's averaging procedure (Roe 1981) at the i th grid point bounded by $(i, i+1)$ and m the m th characteristic variable.

Finally, the left and the right conservative variables can be reconstructed from characteristic variables by:

$$Q_{i+1/2}^{\text{WCNS},L} = \sum_m W_{i+1/2,m}^{\text{WCNS},L} R_{i^*,m}. \quad (2.27)$$

The WCNS numerical flux $E_{i+1/2}^{\text{WCNS}}$ from equation 2.23 can be reconstructed by the Roe's flux difference splitting Roe (1981):

$$E_{i+1/2}^{\text{WCNS}} = \frac{1}{2} \left(E_\star(Q_{i+1/2}^{\text{WCNS},L}) + E_\star(Q_{i+1/2}^{\text{WCNS},R}) - R_{i^*} \Lambda_{i^*} L_{i^*} (Q_{i+1/2}^{\text{WCNS},R} - Q_{i+1/2}^{\text{WCNS},L}) \right), \quad (2.28)$$

where i^* denotes the Roe's averaging procedure at the i th grid point bounded by (L, R) .

The left and right fluxes $E(Q_{i+1/2}^{\text{WCNS}, L/R})$ are computed using the interpolated metrics from the following sixth-order Lagrange interpolation scheme:

$$(J\xi_x)_{i+1/2}^{\text{WCNS}} = \frac{75}{128} ((J\xi_x)_i + (J\xi_x)_{i+1}) - \frac{25}{256} ((J\xi_x)_{i-1} + (J\xi_x)_{i+2}) + \frac{3}{256} ((J\xi_x)_{i-2} + (J\xi_x)_{i+3}). \quad (2.29)$$

In order to preserve the freestream, the metrics are discretized by the same computational-node to midpoint interpolation scheme (Eq. 2.23) and the same midpoint interpolation scheme (Eq. 2.29).

Hybrid scheme

A hybrid scheme developed by Piquet (2017) is used to deal with the strong dissipation of the WCNS / WENO scheme when capturing the shock. The hybrid scheme acts as a switch between the WCNS scheme and the centered difference scheme. Thus, the numerical dissipation of the WCNS scheme can be confined in the shocked regions and the centered difference can be applied in the free shock region to ensure accuracy and stability. The hybrid scheme is defined by:

$$\frac{\partial \varphi}{\partial x}^{\text{Hybrid}} = (1 - \Theta) \frac{\partial \varphi}{\partial x}^{\text{Centered}} + \Theta \frac{\partial \varphi}{\partial x}^{\text{WCNS}}. \quad (2.30)$$

However, the presence of a high gradient of pressure, velocity or temperature, in the shock regions, can affect the stability of the centered scheme. For that reason, Ducros et al. (1999) shock sensor θ is used, in the present code, as a switch Θ equal to 0 or 1 where θ_0 is the limiter value:

$$\theta = \frac{(\vec{\nabla} \cdot \vec{u})^2}{(\vec{\nabla} \cdot \vec{u})^2 + (\vec{\nabla} \times \vec{u})^2 + \varepsilon}, \quad (2.31)$$

where $\varepsilon = 10^{-30}$ is a positive real number chosen to prevent numerical divergence.

$$\begin{cases} \Theta = 1, & \text{if } \theta > \theta_0 \\ 0, & \text{otherwise} \end{cases} \quad (2.32)$$

2.2.1.2 Viscous terms

The viscous terms in the curvilinear Navier-Stokes have been discretized by a 4th-order central scheme. To improve the stability of the code, each derivative is separated into two derivatives by a Laplacian operator. As an example, the first viscous term written

with a Laplacian operator, from equation 2.3, gives:

$$\frac{\partial(\mu_{\xi_x} J_{\xi_x})}{\partial \xi} \frac{\partial u}{\partial \xi} = \frac{\partial(\mu_{\xi_x} J_{\xi_x})}{\partial \xi} \frac{\partial u}{\partial \xi} + \mu_{\xi_x} J_{\xi_x} \frac{\partial^2 u}{\partial \xi^2}. \quad (2.33)$$

Equations 2.34 and 2.35 show the 4th-order central scheme for the first derivative and the second derivatives, respectively.

$$\frac{\partial \varphi}{\partial \xi} = \frac{-\varphi_{i+2} + 8(\varphi_{i+1} - \varphi_{i-1}) + \varphi_{i-2}}{12}, \quad (2.34)$$

$$\frac{\partial^2 \varphi}{\partial \xi^2} = \frac{-(\varphi_{i+2} + \varphi_{i-2}) + 16(\varphi_{i+1} + \varphi_{i-1}) - 10\varphi_i}{12}. \quad (2.35)$$

Because of the high number of viscous terms to be computed, a special care has been taken with the viscous subroutine in term of optimization. The averaged consumption of this routine is around 40% per iteration.

2.2.2 Temporal scheme

The temporal integration schemes implemented in the present solver are mainly explicit algorithms of Runge-Kutta type. These diagrams act in concordance with the restriction on the time increment which must be sufficiently small, taking into account the unsteady nature of the flows studied. For the present study, the governing equations are advanced in time by an explicit 4th-order Runge-Kutta (RK4) method, used by many for its broad stability properties. The scheme uses four sub-integrations and two temporary arrays. A low-storage method has been developed by Williamson (1980) to remove one temporary array. The RK4 is described as follows, where Δt is the time step:

$$\frac{\partial F(t, \vec{x})}{\partial t} = Q(t, \vec{x}), \quad (2.36)$$

$$\begin{aligned}
&\bullet F^{n+1/4} = F^n + \frac{\Delta t}{6} Q(F^n) \\
&\quad F_1^* = F^n + \frac{\Delta t}{2} Q(F^n) \\
&\bullet F^{n+2/4} = F^{n+1/4} + \frac{\Delta t}{3} Q(F_1^*) \\
&\quad F_2^* = F^n + \frac{\Delta t}{2} Q(F_1^*) \\
&\bullet F^{n+3/4} = F^{n+2/4} + \frac{\Delta t}{3} Q(F_2^*) \\
&\quad F_3^* = F^n + \Delta t Q(F_2^*) \\
&\bullet F^{n+1} = F^{n+3/4} + \frac{\Delta t}{6} Q(F_3^*)
\end{aligned} \tag{2.37}$$

The drawback of time-explicit schemes comes from the constraint applied on the time step for stability purpose [Cinnella & Cedric \(2015\)](#). To avoid the divergence of the temporal scheme, two parameters have been used to compute the time step Δt . From the von Neumann analysis, one can find the Courant-Friedrichs-Lewy condition on the convection terms and the Fourier condition on the viscous terms.

For the 3D curvilinear equations, the minimal physical time step Δt is computed by:

$$C_{\Delta t} = \frac{1}{J} \left(\sum_i |u\xi_i| + \sum_i |v\eta_i| + \sum_i |w\zeta_i| + c \sum_{i=1}^3 \left(\sum_{j=1}^3 |\xi_i^j| \right) + \frac{1}{\gamma_{\text{Fo}} J} \left(\frac{\mu}{Pr} + \frac{\mu_t}{Pr_t} \right) \left(\sum_{i=1}^3 |\xi_i^2| \right) \right), \tag{2.38}$$

$$\Delta t = \min \left(\frac{\text{CFL}}{C_{\Delta t}} \right), \tag{2.39}$$

where CFL is a parameter of stability depending on the numerical schemes used and Fo the critical Fourier number.

2.3 Code validation

In this section, four different test cases will be presented as the basis for the code validation, together with analytical and numerical/experimental results from earlier studies. The main objective is to gain sufficient confidence with the numerical approach and to justify the choices of grid methodology, to be used in the final nozzle flow simulations.

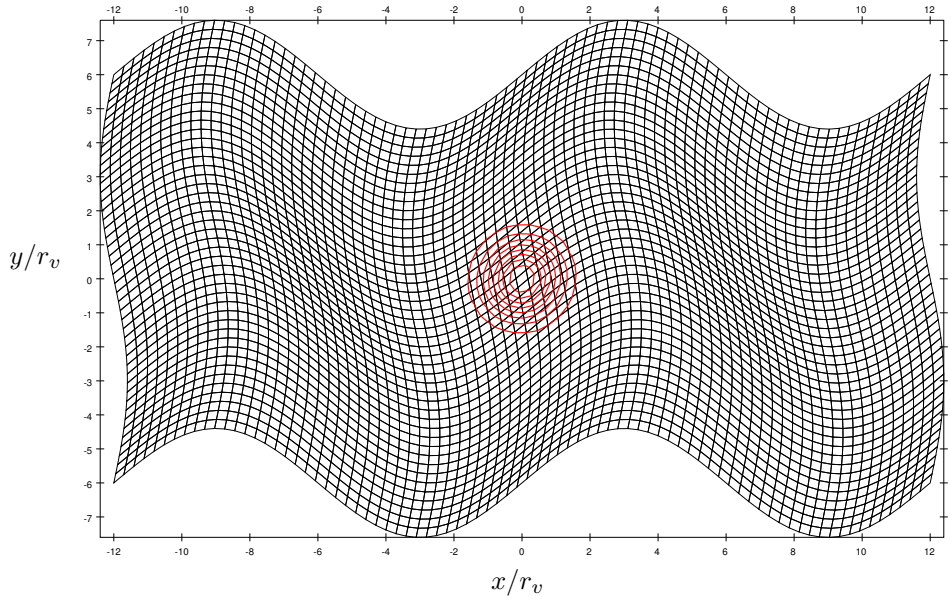


Figure 2.1: Grid of the vortex test case

2.3.1 Vortex advection

The first test case consists in the advection of a circular, homentropic, zero circulation vortex. This test is widely used in literature (Visbal & Gaitonde 2002, Kawai & Lele 2008). A curvilinear grid has been generated through the analytical function from Kawai & Lele (2008) (figure 2.1).

The vortex is initialized using the same parameters as Pirozzoli (2011). The number of grid points is set to $N_\xi = 81$ and $N_\eta = 45$. Periodic boundary conditions are applied at the left and the right sides. The vortex and the free-stream Mach numbers are set to $M_v = 0.5$ and $M_\infty = 0.5$, respectively. This is equivalent to a strongly compressible vortex.

The simulations are run for fifteen flow through time. Figure 2.2 shows a comparison between different orders of accuracy of the centered scheme presented in sec 2.2.1. The numerical solutions for the 2th- and the 4th-order centered schemes exhibit an oscillatory behavior while 6th- and 8th-order centered schemes highlight better results.

Hybrid scheme has also been applied to this test case. Since the hybrid sensor was unable to activate the WENO scheme due to the smooth solution, the result was comparable to the centered solution. This lead to conclude that the implementation of the Euler equations in the code is properly done as observed by the accurate results from high-order schemes. For the next simulations, the 6th-order centered scheme is used to discretize the convective terms, unless otherwise specified.

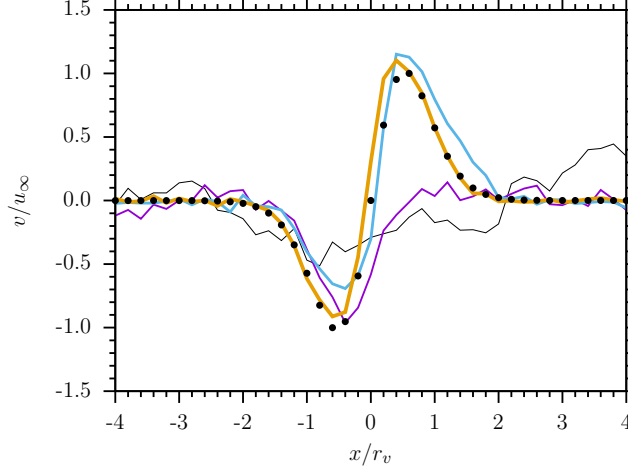


Figure 2.2: Comparison of centered schemes with different order of accuracy; —: 2th order, —: 4th order, —: 6th order, —: 8th order, ·: Exact solution.

2.3.1.1 Cylindrical grid

The implementation of the curvilinear terms, to be used within the present code, ought to be validated. A simple test case which efficiently tests this is the advection of a zero circulation homentropic vortex. At the center, the skewness angle of the cells becomes critical and boundary conditions are difficult to apply. Periodicity along the circumference is not possible and thus, the zero-gradient boundary condition is applied along the circumference. Periodicity is used in the θ -direction. The grid (figure 2.3) has been generated using:

$$x(\xi, \eta) = R \frac{\xi}{N_\xi} \cos(2\pi \frac{\eta}{N_\eta}), \quad (2.40)$$

$$y(\xi, \eta) = R \frac{\xi}{N_\xi} \sin(2\pi \frac{\eta}{N_\eta}), \quad (2.41)$$

where R is the radius of the external BC.

The flow is initialized with the same parameters as the first test. The vortex is advected from left to right passing through the center of the mesh (figure 2.4).

The pressure field distribution at different time step is shown in figure 2.3, where the normalized time is giving by $t^* = t u_\infty / r_v$ with r_v and u_∞ are the cylinder radius and the free stream velocity respectively. The x-axis is shifted for the sake of comparison, where $x' = x - t u_\infty + 0.6$. The final solution shows good accuracy compared to the initial flow field. The singularity at the axis in finite-differences solver does not lead to a spurious solution of the flow as it would do in finite-volumes code due to the infinite flux at the axis. Nonetheless, the singularity can cause spurious oscillations due to the small volume at the center.

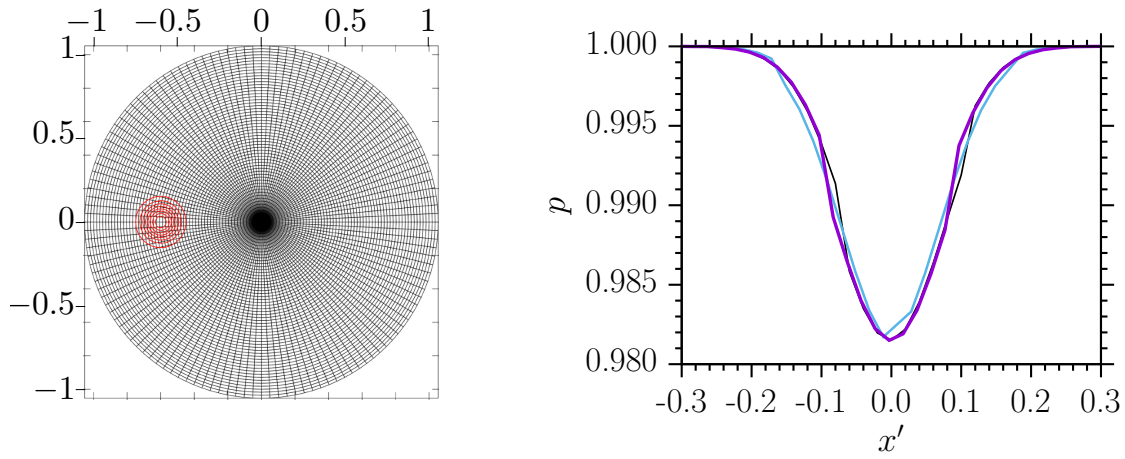


Figure 2.3: Grid of the cylindrical vortex test case (*left*) and shifted pressure distribution at different time step (*right*); —: $t^* = 0$, —: $t^* = 5.9$, —: $t^* = 11.8$.

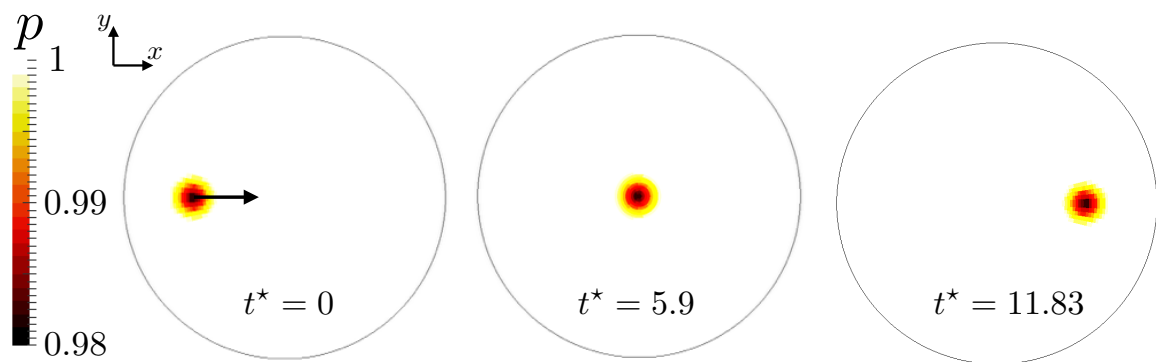


Figure 2.4: Pressure field contour at different time step.

2.3.2 Compressible flow over a circular cylinder

The description of this test case can be found in [Burbeau & Sagaut \(2002\)](#). A circular cylinder of radius R is placed in a viscous compressible flow at Mach 2 and a Reynolds number of $Re = 100$. A detached curved shock is formed ahead of this cylinder, while a viscous wake is established downstream. This test case can validate the implementation of the 2D viscous terms in generalized curvilinear coordinates. Burbeau *et al.* [Burbeau & Sagaut \(2002\)](#) used a bidimensional unstructured meshes with high-order discontinuous Galerkin method. The curvilinear grid (figure 2.5) used for this simulation has been generated by:

$$x(\xi, \eta) = \left(R + (R_a - R) \left(1 + \tanh(r_v(\xi/N_\xi - 1))/\tanh(r_v) \right) \right) \cos(2\pi \frac{\eta}{N_\eta}), \quad (2.42)$$

$$y(\xi, \eta) = \left(R + (R_a - R) \left(1 + \tanh(r_v(\xi/N_\xi - 1))/\tanh(r_v) \right) \right) \sin(2\pi \frac{\eta}{N_\eta}), \quad (2.43)$$

where $R_a = 25R$ is the external radius and $r_v = 3.0$ the stretching parameter.

A stretching function has been used along r -direction to account for the viscous effect along the cylinder wall. The number of grid points is set to $N_\xi = 128$ and $N_\eta = 256$, giving 32,768 cells. The boundary layer is correctly resolved in our case compared to the unstructured mesh of Burbeau ($N = 7,478$). The WCNS scheme is used to account for the presence of shock waves. Adiabatic no-slip condition is applied along the external cylinder.

The obtained results are quite comparable to [Burbeau & Sagaut \(2002\)](#). The bow shock is well captured and gives the same angle of deflection. The solution of [Burbeau & Sagaut \(2002\)](#) was made to show the robustness of their Galerkin methods applied to unstructured meshes. Figure 2.6 shows a steady-state solution which is highlighted by the Mach number contours. Compared to the Burbeau's solution, the current one is less noisy. Both the boundary layer and the shock wave are well captured.

2.3.3 Poiseuille flow

Originally, Poiseuille flow describes a laminar flow of a viscous liquid in a cylindrical pipe, it has been widely investigated ([Don et al. 2018](#), [Schlichting & Gersten 2003](#)). In this test case, the Poiseuille flow from [Schlichting & Gersten \(2003\)](#) is used as a test case for further validation. The analytical solution is used as a reference solution. The fully developed laminar boundary layer solution is obtained for the case of steady flow in a channel with two parallel plates where the pressure gradient ($\frac{dp}{dx}$) is set to:

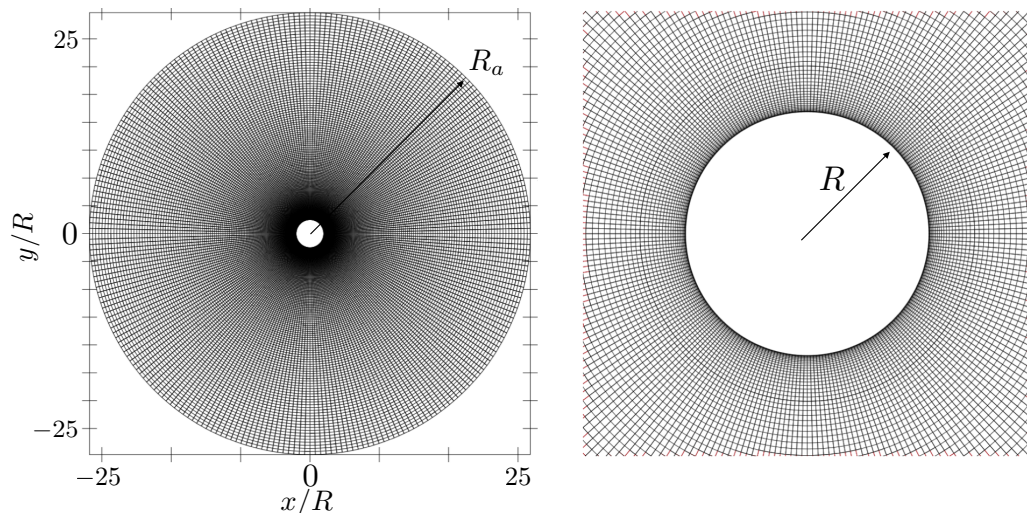
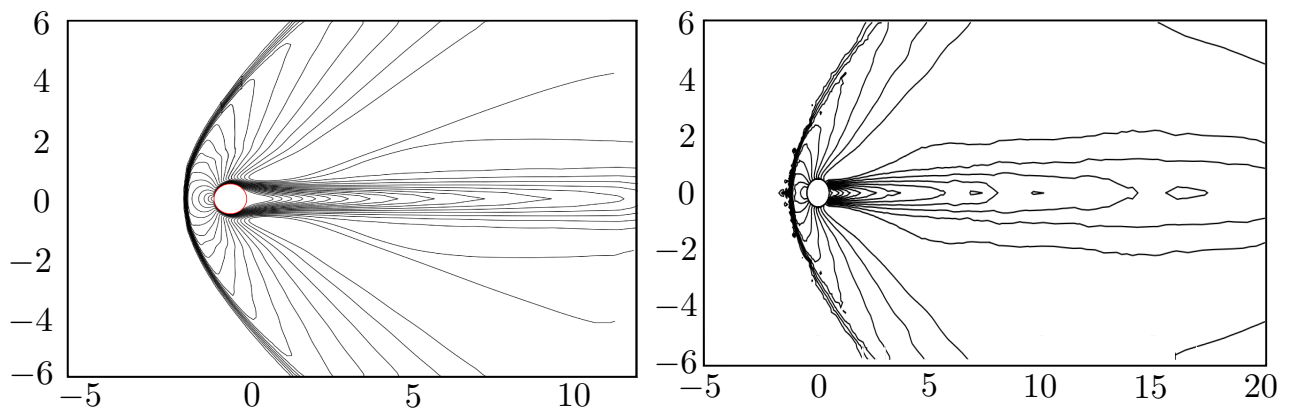


Figure 2.5: Grid of the compressible flow over a circular cylinder test case

Figure 2.6: Mach number contours; *Left*: current simulation, *Right*: [Burbeau & Sagaut \(2002\)](#)

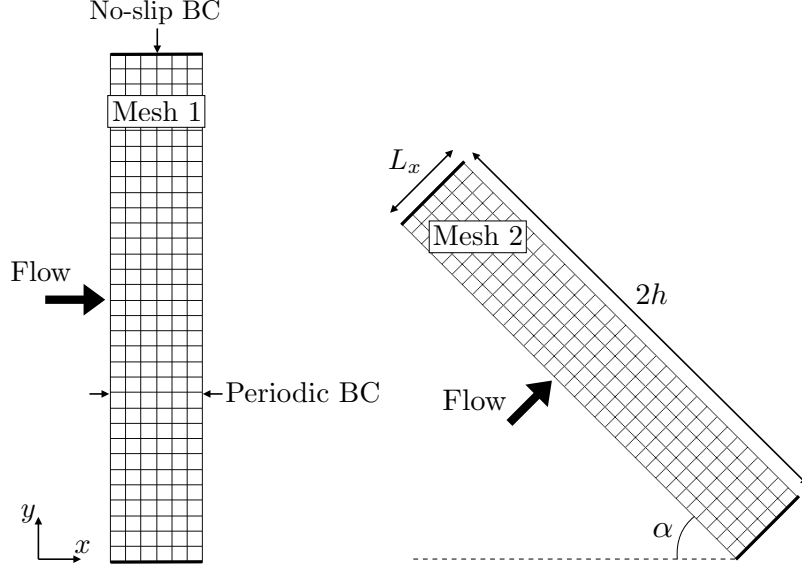


Figure 2.7: Grid representation for Mesh 1 (*left*) and Mesh 2 (*right*) showing every 4th grid-line

$$\frac{dp}{dx} = \mu \frac{d^2 u}{dy^2}. \quad (2.44)$$

In this simulation, the pressure gradient is imposed by an external force, $F = dp/dx$. Using the boundary condition, $u = 0$, one can find the following velocity profile:

$$u(y) = -\frac{1}{2\mu} \frac{dp}{dx} (h^2 - y^2) = -\frac{F}{2\mu} (h^2 - y^2), \quad (2.45)$$

where $L_y = 2h$ is the height of the channel.

Both velocity and temperature profiles are summarized as follows:

$$u(y) = u_m \left(1 - \frac{y^2}{h^2} \right), \quad (2.46)$$

$$T(y) = T_w + (T_m - T_w) \left(1 - \frac{y^4}{h^4} \right), \quad (2.47)$$

where $u_m = -\frac{F h^2}{2\mu}$ and $T_m = T_w + \frac{\mu u_m^2}{3\lambda}$ are the velocity and the temperature at the centre of the channel, respectively.

In order to activate the curvilinear terms of the code, two meshes are computed (figure 2.7). Mesh 1 is computed in the Cartesian coordinates and mesh 2 is inclined by an angle α following Eqs. 2.48 and 2.49. The number of grid points is set to $N_\xi = 20$ and $N_\eta = 128$. The streamwise dimension is not important in this test case since the solution

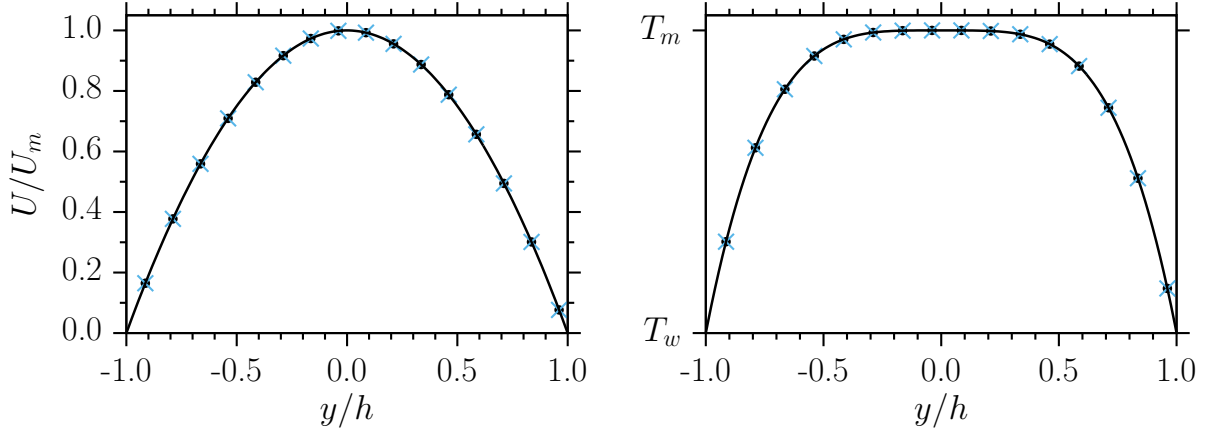


Figure 2.8: Streamwise velocity (*left*) and temperature (*right*) profiles; —: Poiseuille analytical solution, •: Mesh 1, ×: Mesh 2.

is fully developed (one dimensional). Periodic boundary condition and isothermal no-slip condition are applied in the streamwise and spanwise directions, respectively.

$$x(\xi, \eta) = \cos(\alpha)(\xi/N_\xi L_x - \eta/N_\eta 2h), \quad (2.48)$$

$$y(\xi, \eta) = \sin(\alpha)(\xi/N_\xi L_x + \eta/N_\eta 2h). \quad (2.49)$$

The flow is initialized with a uniform flow field at a velocity u_m and a temperature T_w . The results from figure 2.8 are showing and excellent agreement is obtained between the current simulation and the analytical solution in terms of velocity and temperature.

2.3.4 Turbulent channel flow at $Re_\tau = 220$

For further validation and verification of the code, a turbulent channel flow at a friction Reynolds number of 220 is performed by means of direct numerical simulation considering isothermal walls. This problem is one of the classical test case of turbulent flow due to the simplicity of the geometry and the boundary conditions. Turbulent statistics can be explored to study near-wall turbulence behavior, such as first- ($\phi' = \phi - \langle \phi \rangle$) or second-order turbulent statistics ($\langle \phi'_i \phi'_j \rangle$).

2.3.4.1 Test case description

As in Foyi et al. (2004), the flow is periodic in both x - (streamwise) and z - (spanwise) directions. Figure 2.9 shows the actual configuration and table 2.1 summarizes the grid and the geometry parameters.

This simulation uses a centred 6th-order scheme for convective terms and the 4th-order scheme for the viscous terms. The grid is regularly spaced in the x - and z -direction and

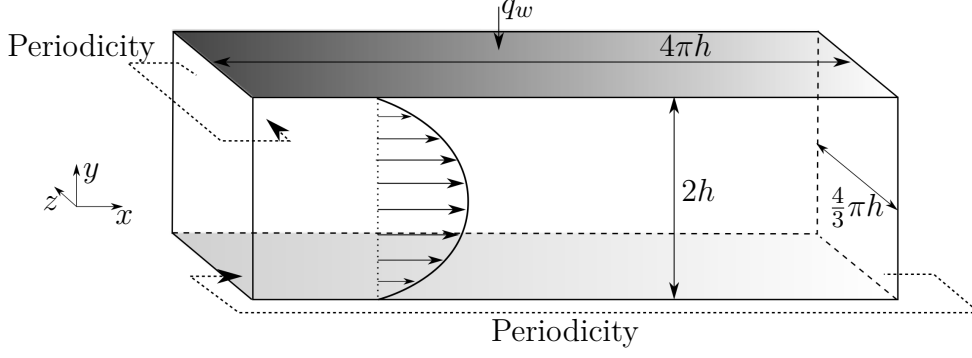


Figure 2.9: Configuration of the channel flow

L_x	L_y	L_z	N_x	N_y	N_z	h (mm)
$4\pi h$	$2h$	$4/3\pi h$	192	150	128	6.85

Table 2.1: Channel flow domain

the wall-normal direction grid is stretched in order to capture the viscous sublayer. A grid sensitivity study has been conducted by [Foyi et al. \(2004\)](#), resulting in the parameters shown in table 2.1. Flow properties are summarized in table 2.2.

The fully developed boundary layer is supersonic and the Mach number is set to 1.5. The initial averaged velocity field follows a fully developed profile extracted from [Foyi et al. \(2004\)](#). The Klein method has been used to initiate the turbulent fluctuations. The Reynolds number, the friction Reynolds number, the bulk velocity and averaged parameters are calculated as: $Re = \frac{\rho u_b h}{\mu}$, $Re_\tau = \frac{\rho_w u_\tau h}{\mu_w}$, $u_b = \frac{1}{\rho_m h} \int_0^h \rho u dy$ and $\rho_m = \frac{1}{h} \int_0^h \rho dy$ respectively.

Since the flow is periodic in the streamwise direction, the pressure drops because of the wall friction. To account for the pressure drop, additional terms in the momentum and energy equations are used as in ([Foyi et al. 2004](#), [Taieb 2010](#)). These terms are applied to counteract the friction forces acting along the wall. Eq 2.50 shows the formulation of this term added to the **Momentum** and **Energy** equations.

$$f_x = \frac{\left(\overline{\langle \sigma_{12} \rangle} \Big|_{y=0} - \overline{\langle \sigma_{12} \rangle} \Big|_{y=2h} \right)}{2h \rho_m} = \frac{\langle \tau_w \rangle}{h \rho_m}. \quad (2.50)$$

Re	Re_τ	u_τ (m/s)	M	u_b (m/s)	T_w (K)
3000	220	35	1.5	680	500

Table 2.2: Channel flow properties

2.3.4.2 Statistical results

All the statistics have been averaged over approximately 150 non-dimensional time unit, $t^* = t u_b / L_x$. Several probes are located along the spanwise direction to collect data for scatter plots. Figure 2.10 provides a comparison of the averaged-streamwise velocity profile compared to the DNS of Foysi et al. (2004). Overall, the results are in good agreement. Figure 2.11 is a similar comparison for temperature, pressure and density to the DNS of Foysi et al. (2004). The three parameters are in a perfect good agreement with the previous DNS.

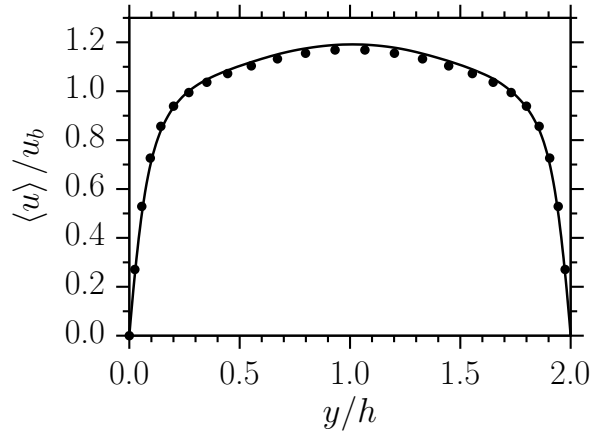


Figure 2.10: Averaged velocity profile along the wall-normal direction; \bullet : Foysi et al. (2004).

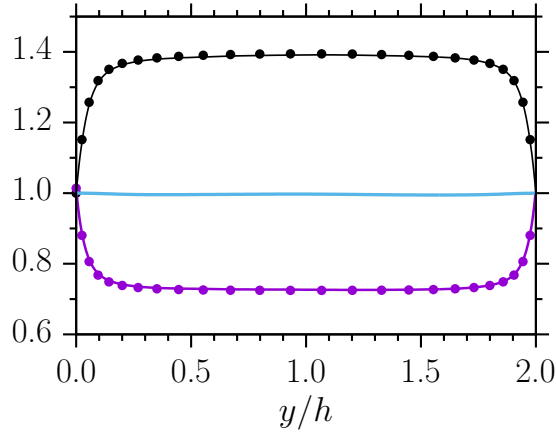


Figure 2.11: Averaged temperature (—), pressure (—) and density (—) profile along the wall-normal direction; \bullet : Foysi et al. (2004).

The law of the wall, represented in figure 2.12 with normalized velocity based on van-Driest formulation (Eq. 2.52), denotes a satisfactory agreement between the present results and the DNS of Foysi et al. (2004). The wall-unit normalization is based on local-wall quantities. The wall-unit length y^+ is given by:

$$y^+ = \frac{\rho_w u_\tau y}{\mu_w}, \quad (2.51)$$

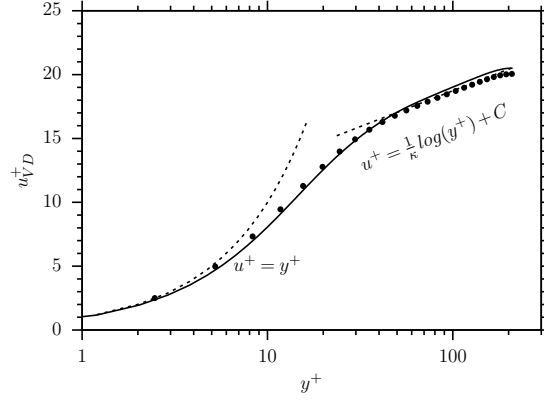


Figure 2.12: Van Driest velocity profile along the wall-normal direction; the dashed line: viscous sublayer and logarithmic law, • Foysi et al. (2004). Here, κ and C are the Von Karman and log-law constants, respectively.

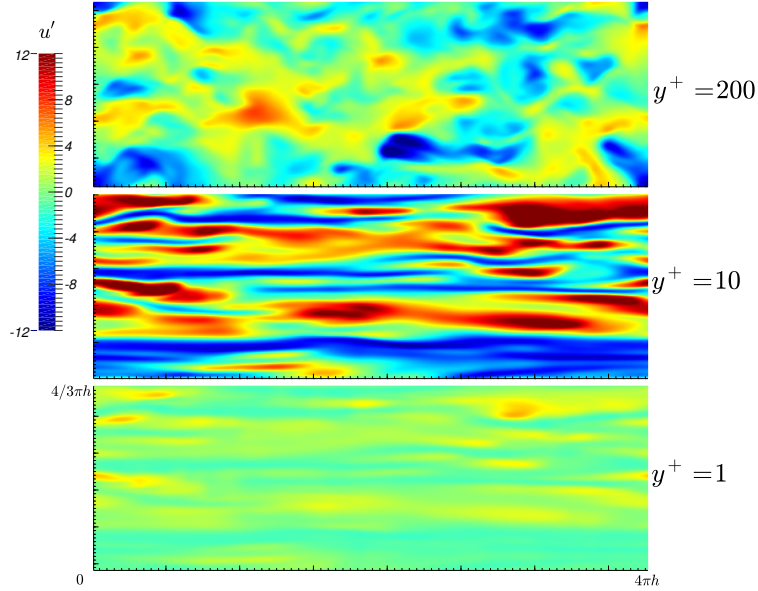


Figure 2.13: Instantaneous contours of the fluctuating streamwise velocity in x - z plane at $t^* \approx 150$ for different y^+

where $u_\tau = \sqrt{\tau_w/\rho_w}$ is the friction velocity.

$$u_{VD}^+ = \int_0^{u^+} \left(\frac{\rho}{\rho_w} \right) du^+ \quad (2.52)$$

2.3.4.3 Turbulence structure

Figure 2.13 shows the fluctuating velocity field at different position in the wall-normal direction. Those streaks, predicted by Coleman et al. (1995), can be seen in the buffer layer of the boundary layer, where the viscous sublayer is connected to the log-law layer.

At $y^+ \sim 10$, the velocity fluctuations are maximum (figure 2.14) and the streaks are clearly visible. Vortices are convected by the flow, creating the streak motions. The

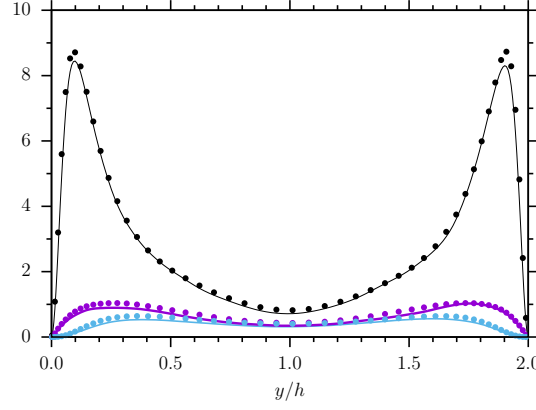


Figure 2.14: Reynolds stress tensor along y-direction along the wall-normal direction; —: $\langle \rho \rangle \widetilde{u''u''}/\tau_w$, —: $\langle \rho \rangle \widetilde{v''v''}/\tau_w$, —: $\langle \rho \rangle \widetilde{w''w''}/\tau_w$, •: Foysi et al. (2004).

red values of figure 2.13 represent the ‘ejection’ process and the blue ones, the ‘sweep’ process. In the viscous sublayer ($y^+ < 5$), molecular diffusion is dominant compared to the convection ($Re < 1$) and thus, the flow is dominated by the viscosity, creating hence a vorticity component in the velocity flowfield. In the streamwise direction, the flow is separated into two regions: a low-speed region where $\partial u'/\partial y > 0$ and a high-speed region where $\partial u'/\partial y < 0$. The ‘streaks’ can be seen as a rolling motion where particles are ejected from the viscous sublayer to the outer layers in the low speed region and are swept from the outer layer to the high-speed region.

The Reynolds stress along the wall-normal direction is plotted in figure 2.14. The results show a good agreement of our DNS with the data of Foysi et al. (2004), which gives confidence on our newly developed code.

2.4 Test case description

The flow considered in this work corresponds to the experiment performed by Papamoschou & Johnson (2006). It consists in two flexible plates forming the upper and lower walls of a planar nozzle. A diagram for their experimental schematic is shown in figure 2.15. The configuration of this experiment is well described in both Olson & Lele (2011) and Piquet (2017). The experiments of Papamoschou & Johnson (2006) quantified integral quantities, such as shock location, mean pressure profiles and mean velocity profiles. Spectra of the fluctuating pressure were calculated near the walls and in the separated shear layer. It reveals a large asymmetry in the two-dimensional shock structure as well as in the region of separation downstream of the nozzle. Large scale unsteadiness of the shock wave was also present. They found that the instability of the shock wave position and the subsequent separated shear layer destabilized the exhaust jet exterior to the nozzle and led to enhanced mixing. The calculation attempts to maintain the same

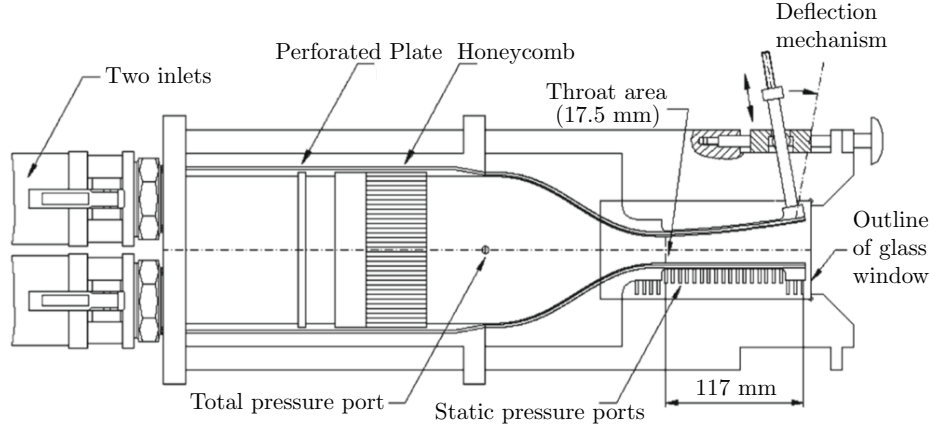


Figure 2.15: Schematic of the Experimental setup.

H_t (mm)	L_d (mm)	NPR	ε
17.8	117	[1.45 : 1.9]	[1.4 : 1.7]

Table 2.3: The geometrical parameters of Papamoschou *et al.* 's planar nozzle.

geometric and physical characteristics of the experiment, such as the ratio of the nozzle throat height to boundary layer thickness (δ/H_t), but exceeds the observed experimental ratio by a factor of 2. While the experimental value of (δ/H_t) is approximately 1/20, the present work value is about 1/10, even so, the large-scale features of the flow, such as shock location and separation point are minimally affected by the modeled boundary layer as shown by [Olson & Lele \(2011\)](#) and [Piquet \(2017\)](#). The nozzle throat-height based Reynolds number is of $Re = 9.10^4$.

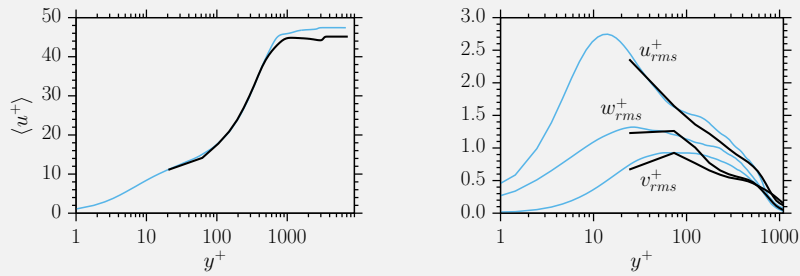
As for the problem setup, for all the cases treated in this work, the mesh is structured and the incoming flow is generated using a synthetic turbulent boundary-layer inlet based on the method of [Xie & Castro \(2008\)](#). To ensure a fully developed boundary layer at the nozzle throat, the computational inlet is shifted upstream using a buffer zone. The flow in the spanwise direction is assumed to be homogeneous with periodic boundary conditions. The outlet boundary conditions are treated as non-reflective using the NSCBC method from [Poinsot & Lelef \(1992\)](#) in conjunction with an external buffer zone with a stretched grid to further damp the reflected waves. Unless otherwise stated, both upper and lower walls are considered as adiabatic with no-slip boundary conditions.

Wall modeling for LES of supersonic boundary layer with separation

International Journal of Heat and Fluid Flow (under review).

Highlights

- A wall-model based on simplified Thin-Boundary-Layer Equations (TBLE) for large-eddy simulations is designed and applied to non-equilibrium turbulent flows with boundary-layer separation.
- *A-priori* as well as *a-posteriori* tests are performed on a supersonic boundary layer over a flat plate with and without pressure gradient.
- The prediction capability of the wall model, concerning the mean velocities and Reynolds stresses, is satisfactory, even on relatively coarse LES grids.
- Applied to supersonic nozzle flow with boundary layer separation, the model correctly reproduces the general flow trends. Particularly interesting when varying the nozzle-pressure ratio, the boundary layer separation exhibits different flow patterns varying from symmetric to asymmetric flow configurations, confirming earlier experimental findings.



(a) Normalized velocities, (b) Normalized velocities RMS along the wall-normal direction in the presence of an adverse pressure gradient; —: WM-LES, —: DNS.

Abstract

The two-layer modeling approach has been identified as a promising wall modeling strategy for large-eddy simulation (LES) in the past ten years. This paper concerns the use of a wall model based on Thin boundary Layer Equations (TBLE) for high speed flows. The model, used in this study, is a combination of the models from Kawai & Larsson (2013) and from Duprat et al. (2011). It is destined for non-equilibrium flows and is able to simulate high-Reynolds number boundary layer subjected to pressure gradient. The modeling methodology is efficiently implemented into a compressible LES solver and validated against Direct Numerical Simulations (DNS) of a spatially evolving compressible boundary layer subjected to pressure gradient. The results show a good agreement with the DNS. The velocity fluctuations are found to match the DNS profiles even with an adverse pressure gradient, especially in the outer layer. The application of the wall model to more complex flows, such as the flow separation in an over-expanded planar nozzle, brings clear evidence of the existence of broadband and energetically-significant low frequency oscillations (LFO) in the vicinity of the separation shock.

3.1 Introduction

Full numerical solutions of turbulent boundary layers (BL), at high-Reynolds number, is prohibitive due to the excessive cost of computations, even with the current computation power. To overcome this problem, large-eddy simulation (LES) can be used to reduce the computational resources. For wall-bounded flows, very refined grids are needed close to the wall and the resources are strongly dependent on the Reynolds number, Re . As a result, at very high Re , the cost of the wall-resolved LES becomes prohibitive as explained Schumann (1975). Consequently, it is common to use a near-wall modelling in order to decrease the grid point near the wall and thus the time step too. Various wall-modeling approaches have been proposed in the literature (Spalding 1961, Schumann 1975, Grötzbach 1987, Cabot & Moin 2000, Piomelli & Balaras 2002). The objective is to accurately predict the skin friction and the heat flux at the wall. These approaches can generally be classified into two categories Kawai & Larsson (2013): (i) modeling the wall shear stress, (ii) switching to a Reynolds-averaged Navier-Stokes (RANS) description in the inner layer which include hybrid LES/RANS and detached eddy simulation (DES). A third category for wall modeling, based on the so-called P-function, can be found in the literature. The main concept of this approach is to relate the total flux of momentum to the total flux of heat (Irrenfried & Steiner 2017, Steiner & Irrenfried 2019). It concerns mainly RANS-type simulations and it has been well established for describing

the logarithmic temperature profile inside the inertial sub-range.

The wall-modeling approach proposed in this study is suitable for non-equilibrium turbulent boundary layer. It is based on the first approach in which the LES resolves only the outer layer, giving the instantaneous velocity field. The thin boundary layer equations (TBLE), that include the convection and pressure-gradient terms, are, then, solved providing the instantaneous-modeled wall shear stress.

The effects of pressure gradient on the wall stress models have been studied by [Manhart et al. \(2008\)](#). Despite the fact that their model was adapted for streamwise pressure gradient, they neglected the Reynolds stresses effects, which limits the range of validity of the model to the viscous sublayer, *i.e.* $y^+ < 5$. Later on, [Duprat et al. \(2011\)](#) have extended the work of [Manhart et al. \(2008\)](#) by including the inertial layer, *i.e.* $y < 0.1 \delta$. They proposed an analytical formulation of the streamwise velocity taking into account both streamwise pressure gradient and Reynolds stresses effects of the buffer layer. Their model was validated using a periodic channel flow and a periodic arrangement of hills subjected to both favorable and adverse pressure gradients. Good results are obtained for the first-order statistics even when the first near-wall point was located in the logarithmic region. Also, flow separation phenomenon was reproduced even on coarse grid. However, the module was formulated for incompressible flows.

For compressible flows several models are proposed. For instance, [Wang & Moin \(2002\)](#) have proposed a similar method where they added the energy equation to the model in order to compute the temperature profile for compressible flow. In [Kawai & Larsson \(2012, 2013\)](#) models, two equations (TBLE) are solved neglecting both pressure gradient and convective terms, thus assuming that the boundary layer, below the exchanging height of the wall model, is in an equilibrium state. It is believed that the lack of these terms in the TBLE does not imply that the pressure gradients cannot be captured by the coupled Wall-Modeled LES (WM-LES).

The present wall-model is designed to be able to reproduce phenomena that occur in non-equilibrium flows such as supersonic nozzle flows, In particular, the separation of the boundary layer as well as the low-frequency phenomena resulting from the movement of the shock system. Taking advantage of the efficiency of the [Kawai & Larsson \(2013\)](#) model, we introduced the pressure-gradient term following [Duprat et al. \(2011\)](#) model. The wall model is being included, in an in-house curvilinear solver called ChocWaves-C (Compressible High-Order Code using Weno AdaptatiVE Stencils written in Curvilinear coordinates) [Piquet et al. \(2019\)](#), [Sharma et al. \(2019\)](#).

In this study, we present the working methodology, in particular the way in which the model is composed. We start with the qualification of different parameters for equation 3.9 through multiple simulations of a flat plate by comparing with previous DNS.

Afterward, a very long WM-LES of a supersonic nozzle-flow is performed to demonstrate that the wall modeling is able to capture the unsteadiness of the shock wave motion, while requiring far fewer grid points. The present work is organized as follows. The next section introduces the governing equations followed by a complete description of the wall-modeling methodology. Then, a sequence of DNS tests are presented, followed by the validation of the wall model with discussion. The examination of the wall model through nozzle flows is introduced afterwards. Finally, a summarizing conclusion ends the present study.

3.2 Governing equations and numerical methodology

Three-dimensional Navier-Stokes equations are solved using filtered compressible equations given by:

$$\frac{\partial \mathcal{Q}}{\partial t} + \sum_{i=1}^3 \frac{\partial \phi_i}{\partial x_i} + \sum_{i=1}^3 \frac{\partial q_i}{\partial x_i} = 0 \quad (3.1)$$

with $\mathcal{Q} = \{\bar{\rho} \bar{\rho} \tilde{u}_i \bar{\rho} \tilde{E}\}^t$, ($i = 1, 2, 3$), is the vector of the filtered-conservative variables and $\phi_i = \{\bar{\rho} \tilde{u}_i (\bar{\rho} \tilde{u}_i \tilde{u}_j + \bar{p}) (\bar{\rho} \tilde{E} \tilde{u}_i + \tilde{u}_j \bar{p})\}^t$, $q_i = \{0 (-\check{\sigma}_{ij} + \tau_{ij}) (-\check{u}_i \sigma_{ij} + \check{q}_j + \tilde{u}_i \tau_{ij} + \mathcal{Q}_j)\}^t$ are the advective and viscous fluxes in the j^{th} coordinate direction, respectively.

$\bar{\rho}$, \tilde{u}_i , \bar{p} and \tilde{T} are the filtered density, velocity, pressure and temperature, respectively. The ‘breve’-symbol ($\check{\cdot}$) indicates that the quantity is based on primitive filtered variables. Thus, \check{E} refers to the resolved total energy. The resolved viscous stress tensor, $\check{\sigma}_{ij}$, and the heat flux, \check{q}_j are defined as $\check{\sigma}_{ij} = 2\mu(\tilde{T})(\tilde{S}_{ij} - \partial_k \tilde{u}_k \delta_{ij}/3)$, and $\check{q}_j = -\lambda(\tilde{T}) \partial_j \tilde{T}$ respectively, with $\mu(\tilde{T})$ and $\lambda(\tilde{T})$ are the viscosity and the thermal conductivity corresponding to the filtered temperature \tilde{T} and $\tilde{S}_{ij} = (\partial_j \tilde{u}_i + \partial_i \tilde{u}_j)/2$. The low-pass filter procedure generates several unclosed terms; most of these are neglected, except for the sub-grid heat flux \mathcal{Q}_j and the sub-grid stress τ_{ij} which are modeled according to the eddy-viscosity hypothesis as:

$$\mathcal{Q}_j = -k_{sgs} \partial_j \tilde{T}, \quad (3.2)$$

$$\tau_{ij} = -\mu_{sgs} (\partial_j \tilde{u}_i + \partial_i \tilde{u}_j - \frac{2}{3} \partial_k \tilde{u}_k \delta_{ij}) + \frac{2}{3} k_{sgs} \delta_{ij}, \quad (3.3)$$

$$\mu_{sgs} = C_d \Delta^2 \bar{\rho} |\check{S}|, \quad k_{sgs} = C_I \Delta^2 \bar{\rho} |\check{S}|^2, \quad \kappa_{sgs} = c_p \mu_{sgs} / Pr_{sgs} \quad (3.4)$$

where c_p is the heat capacity at constant pressure and k_{sgs} the subgrid-scale kinetic

energy. The modeling parameters C_d , C_I , and Pr_{sgs} are determined through the dynamic procedure of Lilly (1992), Moin et al. (1991) and Germano et al. (1991) with filtering and averaging in the homogeneous (periodic) z -direction. Δ is the filter-width associated with the wavelength of the smallest scale retained by the filtering operation.

3.2.1 Wall modeling

The averaged Navier–Stokes equations are used to develop the wall-model. By following the proposition of Piomelli & Balaras (2002) in which the filtered velocity is equivalent to the averaged velocity close to the wall, the system of TBLE is given by:

$$\partial_t \tilde{u}_i + \partial_j (\tilde{u}_i \tilde{u}_j) = -\frac{1}{\bar{\rho}} \partial_i \bar{p} + \partial_j [(\nu + \nu_t) \partial_j \tilde{u}_i], \quad (3.5)$$

$$\partial_t \tilde{E} + \partial_j \tilde{E} \tilde{u}_j = -\frac{\tilde{u}_j}{\bar{\rho}} \partial_j \bar{p} + \partial_j [(\nu + \nu_t) \tilde{u}_j \partial_j \tilde{u}_j + C_p \left(\frac{\nu}{Pr} + \frac{\nu_t}{Pr_t} \right) \partial_j \tilde{T}], \quad (3.6)$$

where \tilde{u}_i , $\bar{\rho}$ and \bar{p} are the filtered parameters, ν_t the turbulent viscosity, Pr is the Prandtl number and Pr_t the turbulent Prandtl number.

Wang *et al.* Wang & Moin (2002) neglected the advection terms in the vicinity of the wall and they showed that the pressure gradient term is very important for non-equilibrium flow and that its inclusion improves the model predictions. Duprat et al. (2011) proposed to reduce the TBLE to the terms of the right-hand side. Under these assumptions, the simplified velocity streamwise momentum can be computed as follows:

$$\partial_y(\tilde{u}) = \frac{\partial_x(\bar{p})y + \tau_w}{(\mu + \mu_t)}, \quad (3.7)$$

where the wall-shear stress τ_w and the turbulent viscosity μ_t are the unknown variables of the equation. Similarly, the temperature can be computed from the adiabatic boundary conditions, using:

$$\partial_y(\tilde{T}) = \frac{(\mu + \mu_t) \tilde{u} \partial_y(\tilde{u}) + \partial_x(\bar{p})y \tilde{u}}{c_p \left(\frac{\mu}{Pr} + \frac{\mu_t}{Pr_t} \right)}. \quad (3.8)$$

The system of equations needs at least one predicted variable to be closed. The turbulent viscosity defined by Nituch et al. (1978) and Balaras et al. (1996) is given by:

$$\mu_t = \mu \kappa y^* [\alpha + y^* (1 - \alpha)^{3/2}]^\beta \left(1 - \exp \left(\frac{-y^*}{(1 + A \alpha^3)} \right) \right)^2. \quad (3.9)$$

where $\alpha = u_\tau^2 / u_{\tau,p}^2$ is a non-dimensional parameter that quantifies the preponderant effect between the shear stress and the streamwise pressure gradient, κ is the Von Karman constant, A and β are two constants determined through *a priori* tests and y^* is the

non-dimensional length, given by Eq. 3.11.

In order to scale the boundary layer subjected to the pressure gradient, Manhart et al. (2008) introduced new non-dimensional variables, taking into account the wall shear stress and the streamwise pressure gradient so that the velocity u^\star and the length scale y^\star are defined as follow:

$$u^\star = \frac{\bar{u}}{u_{\tau,p}}, \quad (3.10)$$

$$y^\star = \frac{\bar{\rho} y u_{\tau,p}}{\bar{\nu}}, \quad (3.11)$$

where $u_{\tau,p} = \sqrt{u_\tau^2 + u_p^2}$ is the combined velocity with $u_\tau = \sqrt{\tau_w/\bar{\rho}}$ the friction velocity and $u_p = \left| \bar{\mu}/\bar{\rho}^2 \partial \bar{p}/\partial x \right|^{1/3}$ the pressure gradient based velocity as proposed by Simpson (1983).

Near the wall, the TBLE model is solved using a fine mesh in the region below a certain height $y = y_{wm}$, while the LES approach is applied above this height on a regular grid. Thus, y_{wm} is defined as the exchanging height between the two models. An “input-output” process starts in which the information extracted from the LES becomes the upper boundary condition for the TBLE model. This latter is then resolved numerically, using its own grid of length y_{wm} , to compute the wall-shear stress and the heat flux; that are injected back into the LES.

The model allows the use of a coarser grid where the first near-wall point has to lie in the inertial layer, *i.e.* $y < 0.1\delta$. Duprat et al. (2011) showed that their model was accurate until roughly 100 wall units. Furthermore, they estimated that the best results are found when the first near-wall cell lies in the buffer layer, *i.e.* $y_1^+ < 40$. Kawai & Larsson (2013) proposed a similar location for the first grid point, *i.e.* $y_1^+ > 50$.

Due to the poor near-wall resolution in the LES mesh, errors coming from the accuracy of the numerical method and subgrid modeling are expected to be large in the first grid point of the LES. In order to deal with this problem, Kawai & Larsson (2013) proposed to increase the length y_{wm} , *i.e.* $y_{wm} \neq y_1$, while respecting the validity range of the turbulent viscosity model where the wall-model top boundary needs to lie in the inertial layer, *i.e.* $y_{wm} < 0.1\delta$.

A schematic representation of the TBLE near the wall using the off-set method of Kawai & Larsson (2013) is shown in figure 3.2, with $y_{wm}/y_1 = 3$. In the following, the model will be validated through *a priori* and *a posteriori* comparisons with direct numerical simulations of the evolving boundary layer subjected to a favorable/adverse pressure gradient (*FPG/APG*).

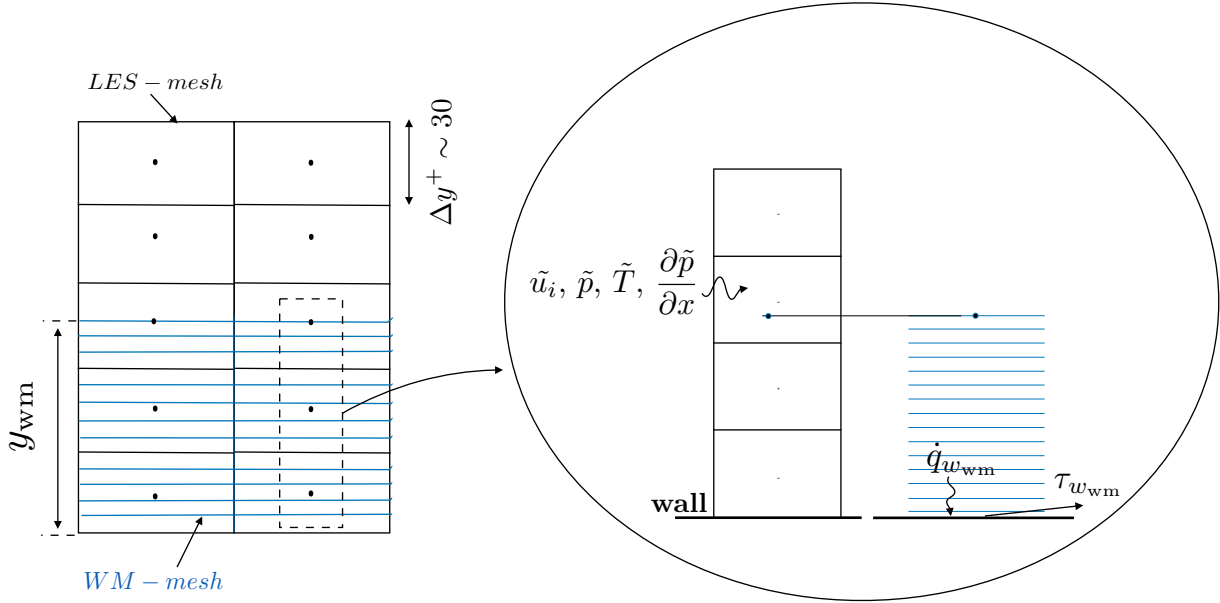


Figure 3.2: Schematic representation of the TBLE and the WM-LES mesh.

3.3 DNS of a turbulent boundary layer under APG/FPG.

A DNS of spatially-evolving supersonic boundary layer over an adiabatic flat plate at $M_\infty = 2.25$ is performed with zero pressure gradient using ChocWaves (see appendix A). The computational domain varies from $x_{in} = 4''$, corresponding to $Re_x = 2.54 \times 10^6$, to $x_{out} = 9''$. The normal direction extends up to $0.5''$ and the grid is stretched in this direction with a minimum spacing near the wall of $\Delta y_{min}^+ \sim 1$. The spanwise length of the domain is $0.175''$ and the total number of points used is $N_x \times N_y \times N_z = 3584 \times 128 \times 256$. This mesh resembles closely to the one used in the DNS of Pirozzoli et al. (2004). The freestream-flow conditions are set to a static temperature of $169K$ and a momentum-thickness Reynolds number past the transition equals to $Re_\theta = 4260$ ($Re_x = 4.5 \times 10^6$). The pressure is kept constant along the wall-normal direction. At the inlet, both temperature and velocity profiles are prescribed according to the procedure given in White's book White & Corfield (2006). The perturbation model is similar to the one implemented by Guarini et al. (2000) and follows the specification of Pirozzoli et al. (2004). The region of perturbation extends from $x = 4.5''$ to $x = 5''$. The random numbers are created by a normal/gaussian distribution using the Mersenne Twister random number generator with a cycle of $2^n - 1$ ($n=199937$) to avoid repetitive signal patterns.

The statistics have been averaged in space and time over 10 characteristic time $t^* = U_\infty t / \delta_i$. Results are shown in appendix A. Then, a DNS of a turbulent boundary layer under APG/FPG is performed using results from A. The simulation uses the same parameters as A. The domain has been extended in the streamwise direction to

allow the separation/reattachment phenomena to occur within the length of the domain. The wall-normal length has been increased to $L_y = 1''$ to avoid reflection of the separation shock on the boundary layer. The spanwise length is kept constant through which a periodic boundary condition is imposed. Due to difficulties in predicting the response of the pressure gradient to the imposed force, a first attempt to simulate the flow was made using boundary layer informations from the previous DNS simulation (see appendix. A). The amplitude of the adverse/favorable pressure gradient has been designed using the Clauser's parameter β from previous simulation of separated flow found in the literature as following:

$$\beta = \frac{\delta^*}{\tau_w} \frac{d\bar{p}}{dx}, \quad (3.12)$$

where δ^* is the displacement thickness, τ_w the wall-shear stress and $\frac{d\bar{p}}{dx}$ the streamwise pressure gradient.

As shown in figure 3.3-top, this attempt led to a strong separation of the boundary layer, with a very large recirculating bubble and a strong separation shock upstream of the separation accentuating the separation phenomenon. More over, an instability of the separation line was evidenced. This instability has been observed, in which the separation line was constantly sliding upstream and reaching the transition zone. Despite the fact that this simulation led to an interesting flow field, the reduction of the pressure gradient, applied on the boundary layer in this simulation, has been decided because of the instability observed. Figure 3.3-bottom shows that boundary layer handles, this time, a moderate pressure gradient. Moreover, a weak oblique shock can be observed but it does not lead to an unstable flow as in the first test.

For the current DNS, the pressure gradient is enforced by an additional force. This additional force allows a better and more precise control of both the pressure gradient location and its amplitude, than the wall-normal velocity BC *i.e.* $\frac{dp}{dy} = 0$. An additional term is added both to the streamwise momentum and to the total energy equations, *i.e.* $\rho f \propto \frac{dp}{dx}$.

The pressure gradient is set as a constant F_{pg} in the favorable and adverse zone. To connect the three regions with zero, adverse and favorable pressure gradients, a smoothing function has been used. Before the outlet, the pressure gradient is decreased to a zero pressure gradient to avoid over-constraint boundary condition.

Figure 3.4 shows the Van Driest velocity for several x-positions ($x/\delta_{in} = 170, 250$ and 330) corresponding to different values of the pressure gradient parameter $\Delta p^+ = \nu/(\rho u_\tau^3) dp/dx$, *i.e.* $\Delta p^+ = 0, 0.0075$ and -0.0025 , respectively. One can observe that the self similar solution of the velocity profile, for both the adverse and favorable pressure

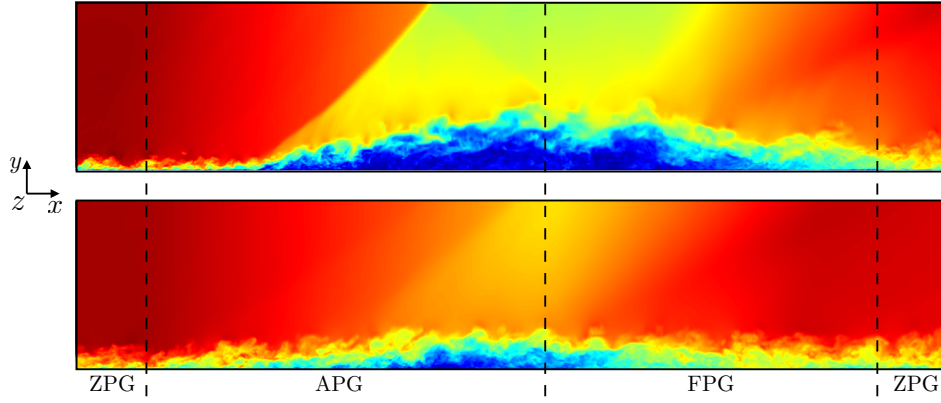


Figure 3.3: Color maps of Mach-number flow field in the $x-y$ plane (*top*) strong pressure gradient, (*bottom*) moderate pressure gradient. Red color being the highest positive value and dark-blue color the lowest value.

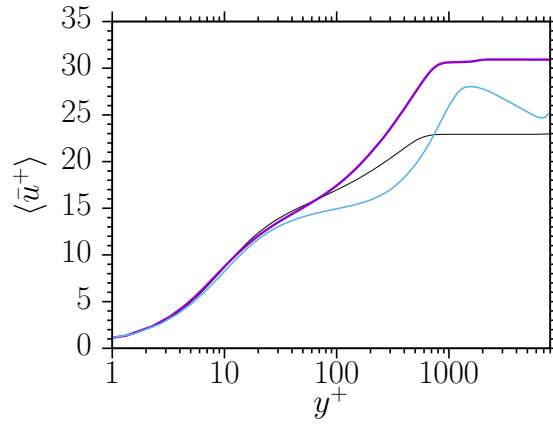


Figure 3.4: Van Driest velocity along the wall-normal direction; —: zero-pressure gradient $\Delta p^+ = 0$, —: adverse pressure gradient $\Delta p^+ = 0.0075$, —: favorable pressure gradient $\Delta p^+ = -0.0025$

gradients, is changing along the boundary layer. For both APG and FPG cases, the classical log-law, *i.e.* $\kappa \sim 0.41$ and $C^+ \sim 5.0$ Örlü et al. (2010), does not apply anymore. For the adverse pressure gradient region, one could fit the log-law with different coefficients as proposed by Nagano et al. (1993), Nagib & Chauhan (2008) and Lee & Sung (2009). One could also confirm that the log-law zone is reduced compared to the zero-gradient region, *i.e.* $y_{\text{log-law,APG}}^+ = [30 : 90]$ and that it extends to the half-power law region from $y^+ \sim 100$. For the favorable pressure gradient region, a log-law can also be fitted in a region slightly shifted compared to the zero-pressure gradient region, *i.e.* $y_{\text{log-law,FPG}}^+ = [60 : 200]$.

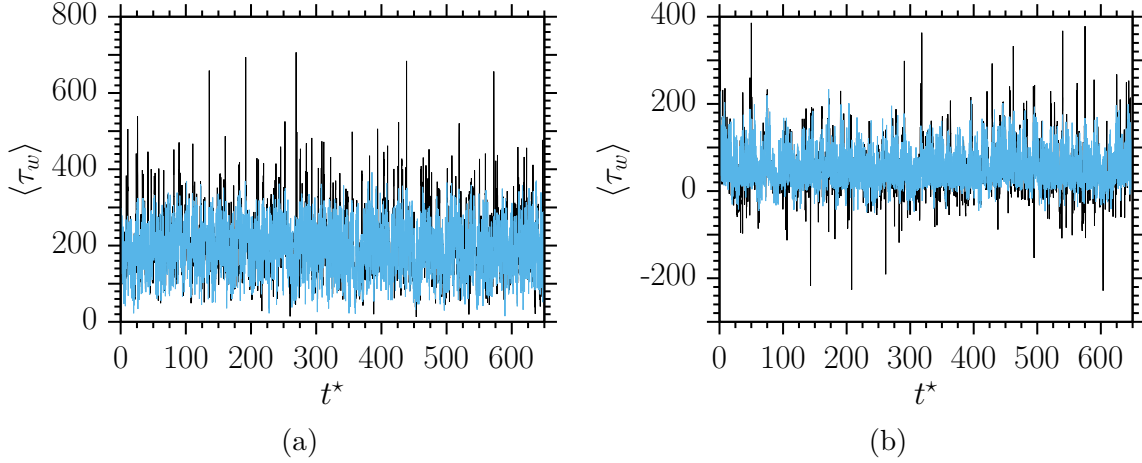


Figure 3.5: Wall-shear stress over time with zero-pressure gradient(a) and adverse pressure gradient (b); —: Wall-resolved data, —: Reconstructed data using the STBLE model.

3.4 Model validation

3.4.1 A priori test

The model is first validated by *a priori* tests using the DNS data. A and β coefficients from equation 3.9 have to be determined through these *a priori* tests. The DNS data along the wall-normal direction at two x -locations (ZPG and APG) are used as inputs to feed the TBLE ODEs. The wall-shear stress and the wall temperature computed by the wall model are then compared to the resolved wall-shear stress and the resolved wall temperature. The streamwise pressure gradient, $\partial p / \partial x$, computed by the LES and injected into the TBLE, has been averaged in z -direction to avoid spurious fluctuations of the wall-modeled solution due to the turbulence of the pressure field. The pressure gradient, injected into equations 3.7 and 3.8, is computed by:

$$\frac{\partial \bar{p}}{\partial x} = \frac{1}{L_z} \frac{\partial}{\partial x} \int_0^{L_z} \bar{p} \, dz. \quad (3.13)$$

Figure 3.5 shows a wall-shear stress comparison over time for zero- and adverse-pressure gradient. For these tests, the length in wall-units y_{wm}^+ is set to 25, or equivalently $\Delta y_{\text{wm}}^+ = 50$ for both zero and adverse pressure gradient regions. This means that the dimensional length y_{wm} is changed accordingly to the wall-shear stress to keep the wall unit length constant.

The coefficient A and β have been setup in order to reduce the L1-error on the wall-shear stress defined as $\text{L1-error} = \langle (\tau_{\text{wwm}} - \tau_w) / \tau_w \rangle$. The best choice for β is found to be $\beta = 0.4$ which is lower than the previously chosen value of $\beta = 0.78$ from Duprat et al. (2011) but closer to the value used by Nituch et al. (1978) of 0.5. The damping coefficient A is fixed at 18. The values proposed in the literature are similar for the

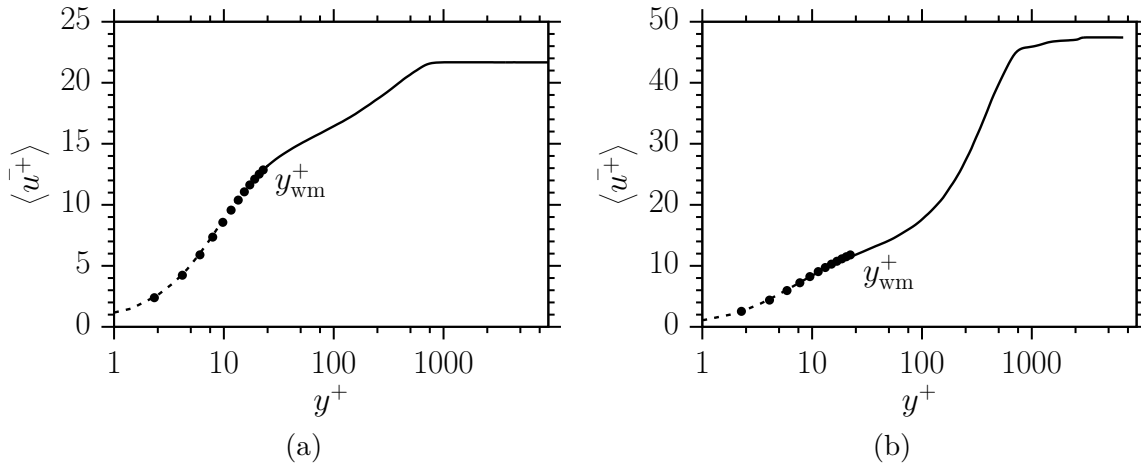


Figure 3.6: Van Driest velocity along the wall-normal direction with zero-pressure gradient (a) and adverse pressure gradient (b); —: Wall-resolved data (---: Subtracted data), •: Reconstructed data using the STBLE model showing every 4th-grid line.

Pressure gradient	y_{wm}	N_{wm}	L1-error
Zero	25	50	1%
Adverse	15	50	−2.5%

Table 3.1: Results of the *a priori* test using the DNS results.

equilibrium flow, *i.e.* $\alpha = 1$. The damping function from equation 3.9 is expressed by $(1 - \exp(-y^*/(1 + A\alpha^3)))$. Without pressure gradient, Wang & Moin (2002) and Cabot & Moin (2000) used $(1 - \exp(-y^*/19))$ and $(1 - \exp(-y^*/17))$, respectively. Which is almost the same as the value $(1 - \exp(-y^*/19))$ computed in the *a priori* test. For non-equilibrium flow, Duprat et al. (2011) found a similar value of $(1 - \exp(-y^*/18))$.

The Van Driest velocity is presented in figure 3.6. The averaged profile computed by the wall-modeled simulation is similar to the DNS data profile, especially for the zero-pressure gradient case. In the APG region, the law of the wall is slightly over-predicted at y_{wm} by less than 1%. Table 3.1 shows the L1-error of the wall-shear stress prediction. The L1-error gives good results for both regions therefore it has been used to determine the unknown coefficients of the wall-model. The under-prediction of the wall-shear stress RMS can be seen on figure 3.5, especially on the large fluctuation of the wall-shear stress where the model cannot handle the spurious fluctuations of the inner layer turbulence.

3.4.2 A posteriori test

WM-LES is performed using a boundary layer configuration similar to the previous DNS. The grid resolution and accuracy of the wall-model in (LES) have been discussed by Kawai & Larsson (2012). They suggested that the inner layer of the boundary layer in free-stream flow, *i.e.* $y/\delta < 0.1$, can be modeled by a universal law. They assumed that

	L_x/δ_{in}	L_y/δ_{in}	L_z/δ_{in}	N_x	N_y	N_z	Δx^+	Δy_1^+	Δz^+	Re_θ
WM-LES	80	13	2.5	768	64	64	67	45	45	4260
Kawai & Larsson (2013)	15	15	3	-	-	-	613	154	368	50×10^3

Table 3.2: Grid requirements for the WM-LES

the first near-wall grid point must be located in the log-layer, *i.e.* $y_1^+ > 40 - 50$. Using the off-set method explained above, the first point where the wall-model takes as input the instantaneous solutions from the LES should be at least $y_{wm}^+ > 50$. In this WM-LES, the momentum thickness Reynolds number is lower than the simulation of Kawai and Larsson, *i.e.* $Re_\theta \sim 4.3 \times 10^3$. Using the same grid resolution will end up with an under-resolved boundary layer due to the reduced size of the boundary layer. The first grid point in wall-unit, Δy_1^+ , is set to 45. For the streamwise and spanwise direction, the grid spacing is $\Delta x^+ = 67$ and $\Delta z^+ = 45$. The grid requirements are summarized in table 3.2. The WM-LES uses the WALE sub-grid scale model.

The inlet boundary layer is then generated by the same synthetic turbulence inflow boundary condition as that used in DNS. The inlet profiles are extracted from the DNS in the fully-turbulent zone ($x/\delta_{in} = 200$). The streamwise length L_x is similar to the previous DNS. The first part of the streamwise length is used as a buffer for the synthetic inflow boundary condition. The figures are taken at a specific x where the flow is fully turbulent, away from the synthetic inlet.

As for the DNS, the WM-LES uses an additional force to impose the pressure gradient along the streamwise direction. The x -direction is normalized by the incoming turbulent boundary layer thickness δ_{in} which is different from section 3.3 where the incoming boundary layer is laminar. The statistics are averaged over 200 non-dimensional time units. The wall-model is implemented using the following algorithm:

Algorithm 1 WM-LES

- 1: **procedure** AT EACH ITERATION
 - 2: LES calculation
 - 3: The LES solutions at a specific y_{wm} is injected in the top TBLE BC
 - 4: The TBLE is solved to compute $\tau_{w_{wm}}$ and $\dot{q}_{w_{wm}}$
 - 5: $\tau_{w_{wm}}$ and $\dot{q}_{w_{wm}}$ are injected back to LES through an additional force at y_1 .
-

Duprat et al. (2011) used an additional viscosity term to impose the wall-shear stress at the wall. This corrective parameter assimilated to a viscosity is computed using the wall-shear stress computed by the LES and the wall-shear stress predicted by the wall-modeled simulation. This method is suitable for finite volume code but can lead to spurious results with finite difference code. Other methods exist in the literature to impose a wall-shear stress (BC). The method implemented in this study is an additional force

integrated along the wall-normal direction following equation 3.14 (Piquet 2017). This force is added to the x -momentum equation with an additional energy source computed by the wall-modeled heat diffusion term ($\dot{q}_{w\text{wm}}$). The wall boundary condition uses the regular no-slip condition with a fixed temperature computed by the wall-modeled heat diffusion term.

$$F_x = \frac{\tau_{w\text{wm}} - \tau_{w\text{LES}}}{y_1}. \quad (3.14)$$

Figure 3.7 shows the normalized velocity profiles where the solution of the inner layer is plotted using the previous DNS. It shows (a) the zero-pressure gradient solutions taken at a similar Re_θ and (b) the adverse pressure gradient profiles taken at a similar Δp^+ . The velocity has not been normalized by the Van Driest formulation, as it should be the case in compressible flow, due to integration term along the wall-normal direction which misses the information of the inner layer in the WM-LES. The grid resolution can be seen in the plot at $y_1^+ = 22$ and $y_2^+ = 68$. These two first-points are slightly underestimated due to the unavoidable numerical and sub-grid modeling errors emanating from the wall-modeled simulation. For the ZPG, the outer layer is in good agreement with the DNS. For the APG, the first part of the outer layer is well captured, while the normalized velocity is underestimated outside of the boundary layer (the friction velocity u_τ is over-predicted in the APG zone). This behavior is due to the fact that we are comparing the profile at a similar Δp^+ and not at a comparable Re_θ .

Figure 3.8 shows the velocities RMS along the wall-normal direction for both ZPG and APG. The region in the range $100 < y^+ < 500$ is under predicted in all directions with a maximum difference of 6%. This behavior can be explained by the fact that we are cutting the most energetic part of the fluctuations, *i.e.* $y^+ < 50$. The upper layer is then unresolved due to the lack of energy from the buffer layer that has been removed by the grid near the wall. In the APG region, the wall-modeled boundary layer is underestimated near the wall, especially for the wall-normal and spanwise velocities. Despite that, the wall-model implemented from Kawai & Larsson (2013) and from Duprat et al. (2011) shows reasonably good agreement with the previous resolved DNS. The velocity fluctuations match the DNS profiles even with an adverse pressure gradient, especially in the outer layer.

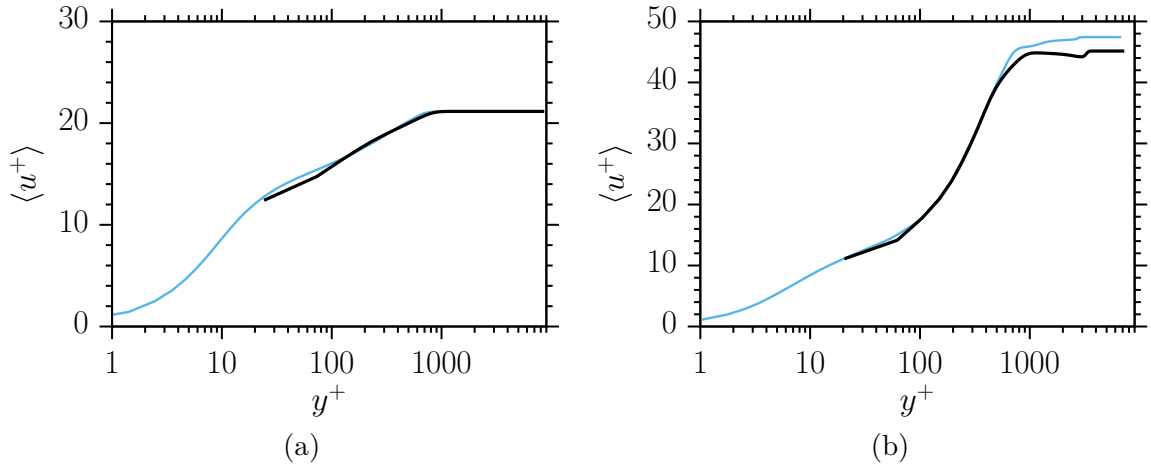


Figure 3.7: Normalized velocity along the wall-normal direction, zero-pressure gradient (a) and adverse pressure gradient (b); —: WM-LES, —: DNS.

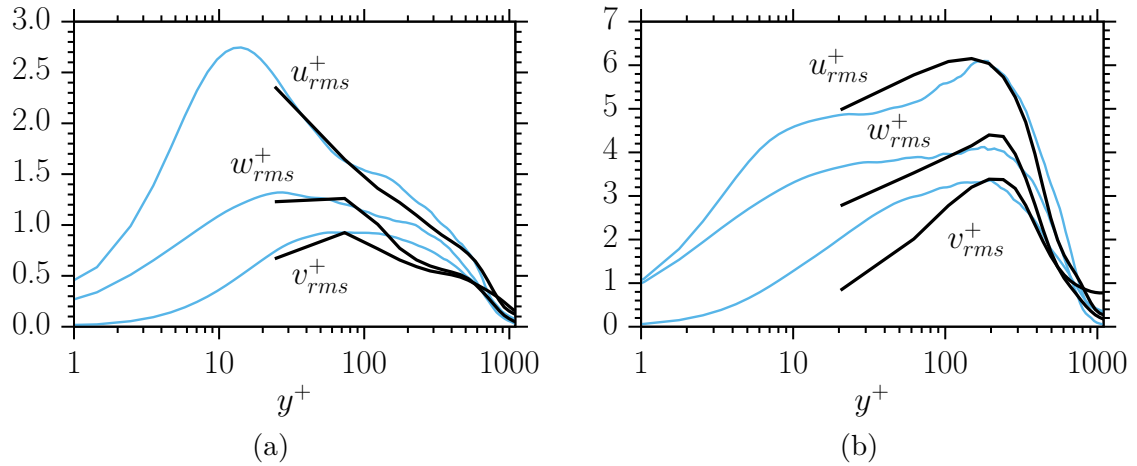


Figure 3.8: Normalized velocities RMS along the wall-normal direction, zero-pressure gradient (a) and adverse pressure gradient (b); —: WM-LES, —: DNS.

3.5 Boundary-layer separation in a supersonic planar nozzle

We further investigate the ability of the wall model to reproduce the low-frequency shock oscillations that are ubiquitous in most shock/boundary layer interaction problems. These phenomena involve different time and length scales and require a long-time integration encompassing a large number of low-frequency cycles, which cannot be easily achieved by a wall-resolved LES approach. The considered test case is a transonic planar nozzle investigated experimentally by [Johnson & Papamoschou \(2010\)](#) and computed numerically by [Olson & Lele \(2011\)](#) and [Zebiri et al. \(2020\)](#). The nozzle has a weak diverging-part angle of almost 4° (see figure [3.9](#)) and is open to the atmosphere. For comparison purposes, both wall-resolved (WR-) and wall-modeled WM-LES are performed. The first objective is to assess the ability of the present WM-LES in reproducing some mean quantities such as pressure and velocity for which existing numerical and experimental data can be used for comparison. Table [3.3](#) summarizes the grid parameters used in both WR- and WM-LES compared to the resolutions used by [Olson & Lele \(2011\)](#) in their WR-LES. Compared to the WR-LES, the total number of grid points of the present wall modeled LES is lower almost 5 times. An overall grid coarsening is applied in all directions, keeping a minimum resolution near the wall as required by the WR-LES specifications given by [Kawai & Larsson \(2012\)](#). As for the resolution of the wall-model, a one-dimensional overlapped Cartesian grid with a constant mesh spacing is setup orthogonally to the nozzle wall with a cell-Reynolds number equals to unity. The computed test case corresponds to an over-expanded nozzle operating at a Nozzle-Pressure Ratio (NPR) of 1.7 (NPR being the ratio of the chamber p_0 to the ambient p_a pressure). Due to the relatively intense pressure gradient imposed between the inlet and the outlet of the domain, the boundary layer inside the nozzle detaches from the wall, creating thereby a strong interaction between the incident oblique shock and the boundary layer. This separation occurs in an asymmetric manner forming two Lambda-shock structures with different sizes acting on both upper- and lower-nozzle walls (see figure [3.10](#)). Both simulations using WR- and WM-LES simulations reached a full convergence of the main statistical quantities of interest, with the latter being 40 times faster than the WR-LES counterpart. The obtained results are compared with the available LES and experimental data in terms of mean-pressure distribution and velocity profiles.

Figure [3.11-a](#) shows a comparison of the wall model pressure distribution at the center of the nozzle with wall-resolved one. The averaged shock location is well predicted by the wall-model. The expansion pressure at the throat is slightly lower in the wall-modeled case, due to a stronger pressure gradient in the buffer section in the wall model. Globally,

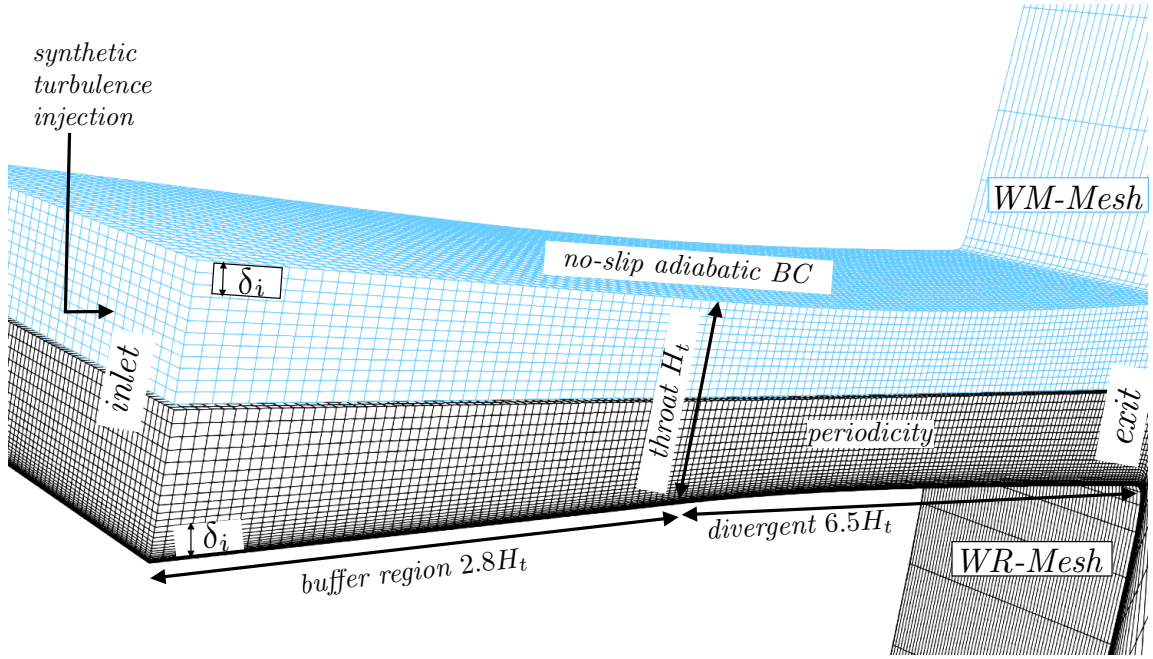


Figure 3.9: Grid representation of both WR nozzle (in black) and WM nozzle (in cyan) test-cases showing every 10^{th} grid-line. The nozzle throat is located at $x = 0$.

		N_ξ	N_η	N_ζ	L_z/H_t	L_b/H_t	Δx_i^+	Δy_i^+	Δz_i^+	Nb cells
Olson <i>et al.</i>	(B)	768	256	256	2	3	30	[1 : 23]	20	50.3 M
WR-LES		896	256	320	2	2.8	30	[1 : 29]	20	73.4 M
WM-LES		672	128	160	2	2.8	60	45	40	13.7 M

Table 3.3: Grid parameters for the WR/WM-LES of the planar nozzle flow.

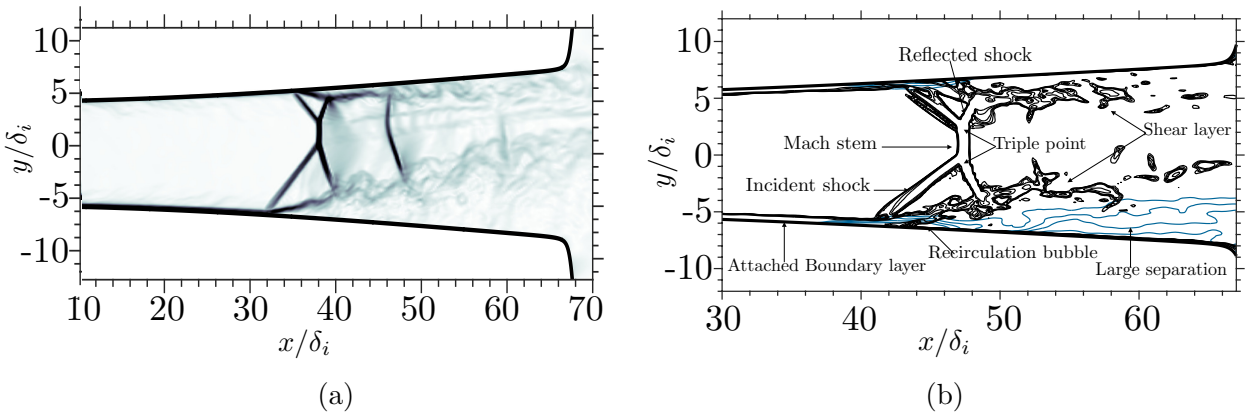


Figure 3.10: (a) Instantaneous z-averaged numerical “Schlieren” imaging contour $|\nabla\rho|$ in the $x - y$ plane for $npr=1.7$, (b) Schematic representation of the density-gradient field showing different phenomena occurring inside the nozzle.

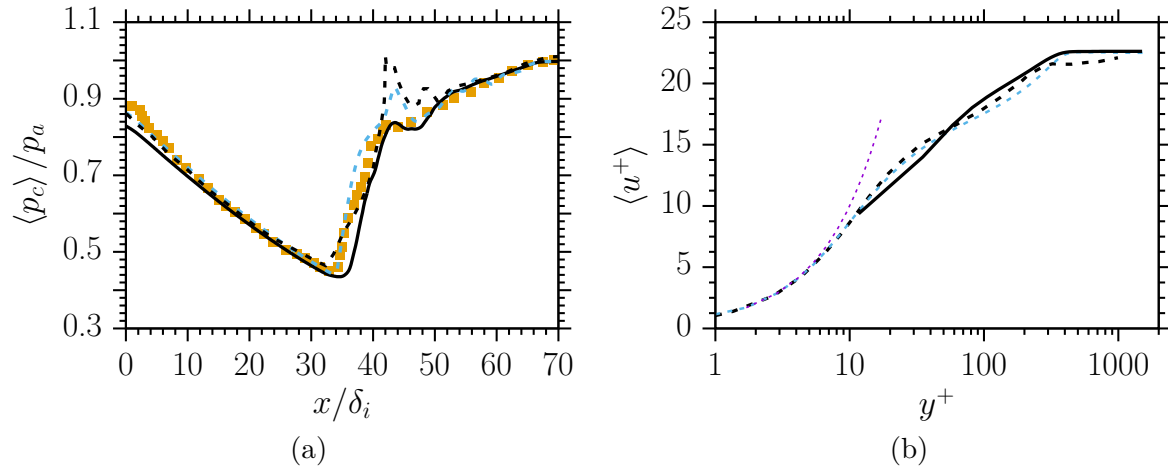


Figure 3.11: (a) Pressure distribution at the center of the nozzle; - : WR-LES, - : WR-LES from Olson & Lele (2011), - : WM-LES and ■ : Experimental results from Johnson & Papamoschou (2010). (b) Van Driest velocity along the wall-normal direction at $x/\delta_i = -10$; -- : WR-LES, --- : $u^+ = y^+$ - : WM-LES, -- : WR-LES from Olson & Lele (2011).

the pressure distribution is in an acceptable agreement with the experimental data as well as with the wall-resolved simulations. Figure 3.11-b shows the normalized streamwise velocity along the wall-normal direction at $x/\delta_i = -10$. The first near-wall cells are located at $y^+ \sim 20$, *i.e.* $\Delta y^+ \sim 40$. The results are in good agreement with the previous wall-resolved of Olson & Lele (2011), especially in the outer part of the boundary layer and in the log-law region. An overall good agreement is observed between the modeled and the resolved simulations.

Velocity-defect profiles, at the upper wall, for different nozzle locations ($x/\delta_i = -10$, $x/\delta_i = -5$, $x/\delta_i = 0$ and $x/\delta_i = 5$) normalized by U_τ are shown in figure 3.12-a. The present results for both the WR-LES and WM-LES display excellent collapse to a single curve. In figure 3.12-b, the mean velocity slope diagnostic function for the log-law Ξ , is shown. One can see that the plateau region, where the data can be approximated to $u^+ = \frac{1}{\kappa} \ln(y^+) + B$, is very tiny which means that the previous expression is not an exact description for this region, as we do not have a clear plateau in Ξ .

3.6 Varying the nozzle pressure ratio

More tests are performed to inspect the attitude of the model towards the low-frequency phenomena. Thus, in this Section, we shed light on the flow physics for a fixed area ratio and over a range of nozzle pressure ratio. The computations were carried out using three different Nozzle Pressure Ratios (NPR); 1.4, 1.7 and 2.5

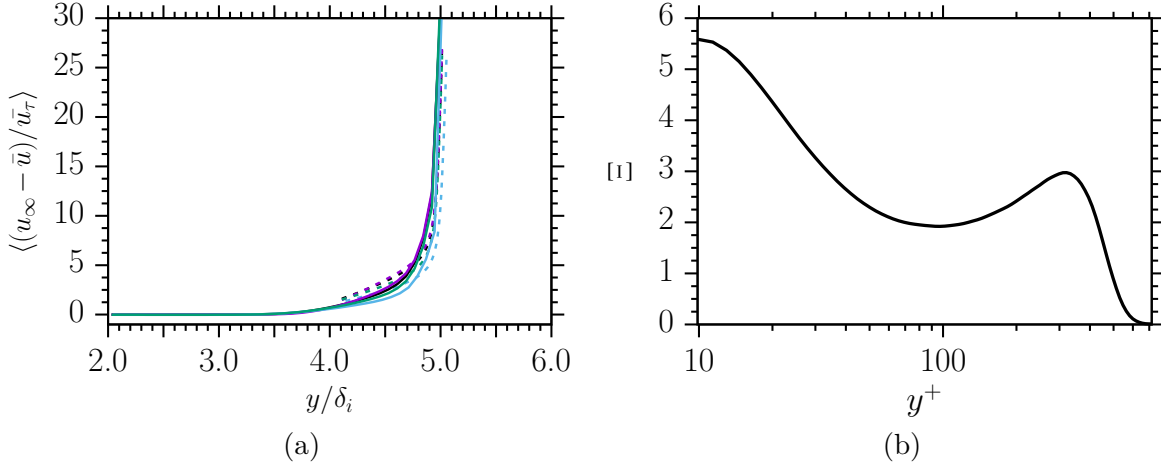


Figure 3.12: (a) Mean velocity-defect normalized by the friction velocity along the wall-normal direction at —: $x/\delta_i = -10$;—: $x/\delta_i = -5$, —: $x/\delta_i = 0$ and —: $x/\delta_i = 5$ with dash line representing WR-LES and solid line representing WM-LES. (b) WR-LES Log-law diagnostic function $\Xi = y^+ du^+ / dy^+$ at $x/\delta_i = 0$.

3.6.1 Time-averaged and instantaneous flow-field

Figures 3.13-(a, c, e) show the numerical Schlieren of the instantaneous pressure flow-field for the three cases, when the classical shock pattern expected in divergent nozzles is a lambda shock-wave structure. This pattern consists of an incident shock (IS), a reflected shock (RS) and a short Mach stem (MS). In this configuration, the separation of the boundary layer, due to the high adverse pressure gradient, creates an separation shock impinging the Mach stem at the triple point (TP). The reflected shock realigns the incident flow in the original direction. The Mach stem, which is a stronger shock, reduces substantially the flow velocity behind it to a subsonic state. Figures 3.13-(b, d, f) show the mean density distribution contours, they show also the mean size of the recirculation bubbles. The enlargement of this region is indicated by the red-colored region. For NPR=1.4, the two regions of recirculation are not equivalent in size which confirms that the flow in this case is asymmetric. For NPR=1.7, one of the two circulation regions has large size while the other is very small, this is due to the reattachment of the jet at the upper wall. For NPR=2.5, the two zone are equivalent. Furthermore, the numerical simulation reveals the existence of small recirculation bubbles trapped between the wall and the separated mixing layer (see figures 3.13-(b, d, f)). These small recirculation bubbles are believed to play an important role in the amplification of the flow oscillations and to involve a strong global unsteadiness with very large amplitude fluctuations.

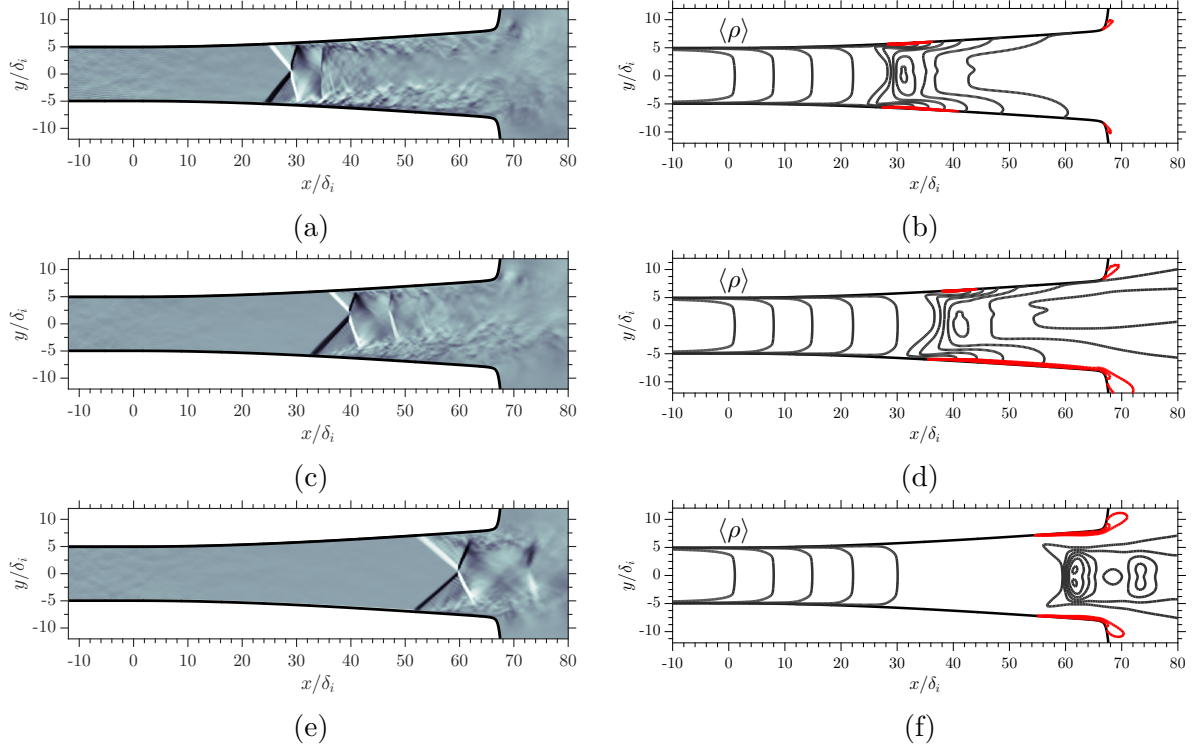


Figure 3.13: Numerical Schlieren pictures and mean density flows contours for: (a) and (b) NPR=1.4, (c) and (d) NPR=1.7, (e) and (f) NPR=2.5. Red lines represent the trapped recirculation bubbles

Figure 3.14-a shows the streamwise mean pressure along the lower wall, the pressure is normalized by the inlet pressure. For the three NPRs the pressure profile have the classical shape that consists of an expansion, a shock jump and a recovery. Downstream of the shock the pressure recovery is done in a smooth way for NPRs 1.4 and 1.7, but for NPR=2.5, it is more immediate compared to the latters. The raison for the immediate recovery in the last case is the nearness of the shock to the exit, and the smooth recovery for the NPR =1.4 and NPR=1.7 is due to the under-expansion observed downstream the shock.

Figure 3.14-b shows the profile of pressure fluctuations RMS normalized by the inlet pressure. One can notice that all the graphs consist of 3 zones. First, an initial zone with very weak RMS value associated with the attached boundary layer, this zone extends from the throat to the separation position. In this region, the intensities of the wall pressure fluctuations for the three simulations are found to steadily increase with Re_τ , at least in the Reynolds number range accessible to simulations as shown in figure 3.14-c. A curve fit of the WM-LES data gives: $(P_{RMS}/\tau_w)^2 = 131.7 \log(Re_\tau) - 427.72$. Then a sharp peak with very intense pressure fluctuations which are in consistence with the shock motion. Finally, a last part that extends all-over the separation zone, the pressure

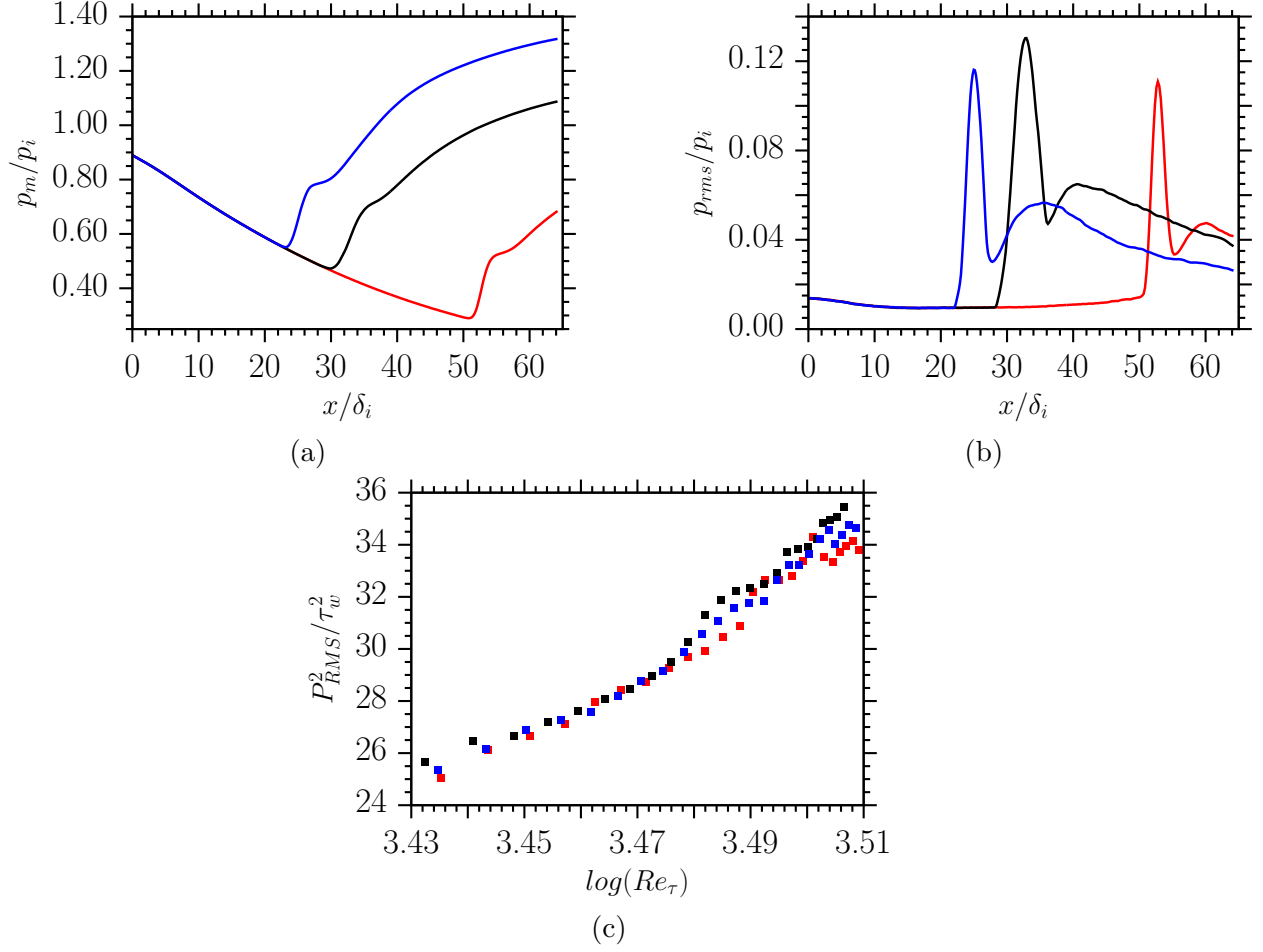


Figure 3.14: (a) Pressure distribution at the lower wall , (b) P_{rms} distribution at the lower wall and (c) Root-mean-square level of wall pressure fluctuations normalized by the wall shear stress (τ_w), with p_i is the inlet static pressure, (—) NPR=1.4, (—) NPR=1.7, (—) NPR=2.5.

fluctuations in this part are small but larger than the attached boundary layer. It can be noticed that the width of the peaks differs from an NPR to another because of the difference in the distance traveled by the shock in its motion, one can notice also that the value of the high peak is the same in both NPRs 1.4 and 2.5 but it is bigger for NPR=1.7 which indicates that more shock activities can be found in this NPR.

3.6.2 Spectra analyses

The unsteady character of the shock motion is further illustrated by the analysis of the pressure fluctuations. Figure 3.15 shows the normalized pre-multiplied spectra of the pressure fluctuations at the lower wall, defined as $St\mathcal{F}(p'/p_{rms})^* = St\mathcal{F}(p'/p_{rms})/\int_{St} St\mathcal{F}(p'/p_{rms})dSt$, as a function of the Strouhal number St and the streamwise coordinates. The spectral map is characterized by three different zones; the first one extends from $x/\delta_i = 0$ to $x/\delta_i = 40$, is a typical feature of turbulent boundary

layer; the second zone is associated with the dynamics of the shock system, is identified by means of a substantial energy at low frequency with a peak at $St = 0.003$ defined as the main tone. The mechanism of low-frequency unsteadiness in over-expanded nozzle flow has been observed by Zaman *et al.* Zaman *et al.* (2002) in their experiments of the transonic diffuser. They show that the resonant tones happen; when the length between the separation and the shock is similar to a quarter wavelength at the speed of sound; for small opening angle; for transonic jet Mach number and for smooth nozzle walls (roughness). Zaman *et al.* proposed the following correlation to compute the resonant tone $f_r = (c_0^2 - u_c^2)/4c_0L_{s,e}$. The last zone is the signature of the turbulent activities in the after-separation zone. Figure 3.16 shows the pre-multiplied spectra (PSD) of the pressure fluctuations at the lower wall in four different location (throat, nozzle exit, mean separation position and the separation zone) as a function of the Strouhal number and the stream-wise coordinates. Figures 3.16-a,-b show similar spectra for NPRs 1.4 and 1.7 for the both positions *i.e.* the throat and the exit. However, a small difference is observed in the case of NPR=2.5 probably due to the proximity of the shock from the exit. Figures 3.16-c and 3.16-d show pre-multiplied spectra of normalized fluctuating forces in both x and y directions. The figures show a large range of frequency including very low frequencies that go down to $St = 10^{-4}$.

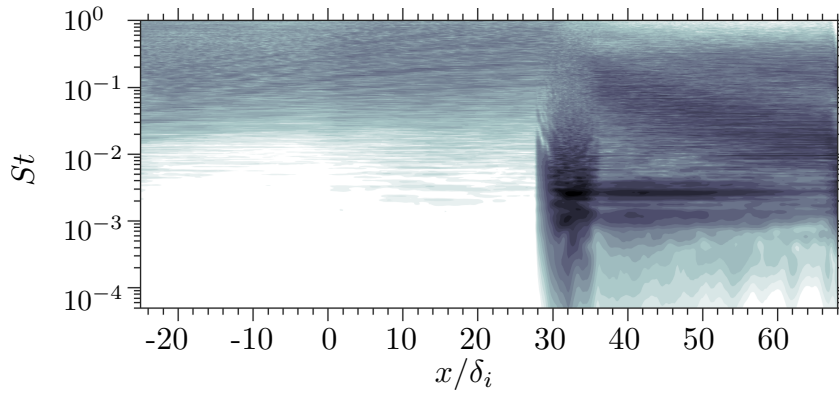


Figure 3.15: Normalized pre-multiplied spectra of wall-pressure fluctuations distribution along the streamwise direction for $NPR = 1.7$.

The results exhibit the development of low-frequency shock motion and significant

NPR	\bar{x}_s/δ_i	Main tone St	
		Measured	theoretical
1.4	24.34	$1.90 \cdot 10^{-3}$	$2.40 \cdot 10^{-3}$
1.7	31.90	$2.60 \cdot 10^{-3}$	$2.60 \cdot 10^{-3}$
2.5	51.53	$6.50 \cdot 10^{-3}$	$6.30 \cdot 10^{-3}$

Table 3.4: Main tone comparison

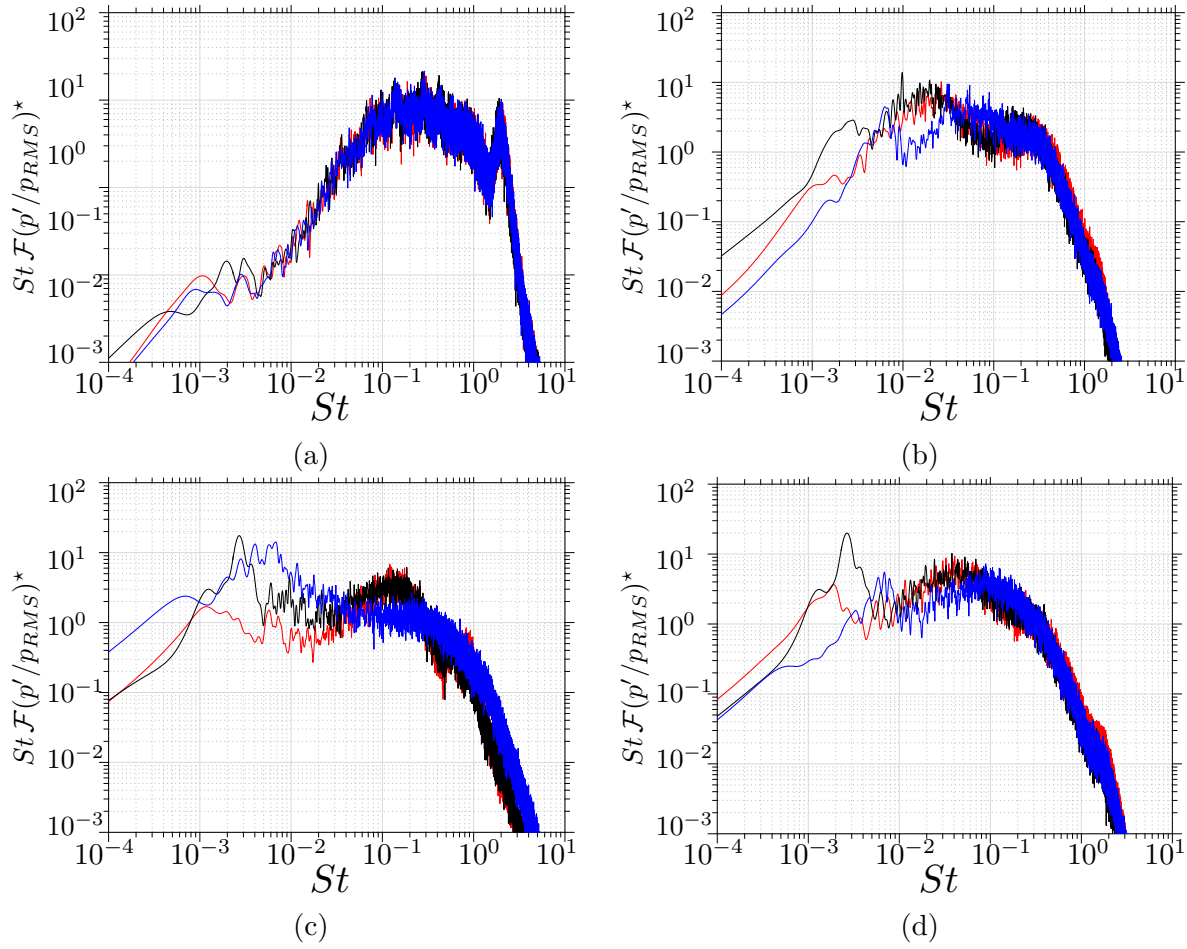


Figure 3.16: Normalized pre-multiplied spectra of the pressure fluctuations at the lower wall at: (a) throat, (b) nozzle exit, (c) mean separation position, (d) the separation zone, for different NPRs with (—) NPR=1.4, (—) NPR=1.7, (—) NPR=2.5.

side-loads due to the evolving asymmetry. Consistent with the previous findings, no jet flipping movement was observed even for very long runs. The mechanisms for the unsteady shock motion is due to a transonic resonant tone between the shock location and the exit as predicted by Zaman et al. (2002). In fact, for $NPR = 1.7$, the resonant tone is captured in the separation region at $St \sim 0.003$ which is in quite good agreement with the findings of Zaman. The rest of the results are shown in table 3.4. The subsonic flow downstream of the separation is trapped between the mixing layer and the wall, which produces small unsteady eddies oscillating at $St = 0.01$ (recirculation bubbles). This phenomenon is strongly impacting the lateral forces (side-loads). The mixing layer developing from the separation is observed $St = 0.1$. The two-dimensional Kelvin-Helmholtz rollup vortices impact the exit conditions, modifying thereby the effective exit area and the position of the separation shock.

3.7 Concluding remarks

This study concerns the use of a two-layer model approach in the context of large-eddy simulations of supersonic turbulent boundary layer subjected to both moderate and strong pressure gradients. The latter induces flow separation and shock oscillations. The current wall-modeling approach is based on the Thin-Boundary Layer Equations model proposed by Kawai & Larsson (2013) in which a pressure correction term is added following Duprat et al. (2011) model. *A-priori* as well as *a-posteriori* tests were first performed on a flat plate supersonic boundary layer before addressing the complex problem of flow separation in nozzles. The prediction capability of the developed model is shown to provide a quite satisfactory results, in terms of mean-flow velocity and turbulent Reynolds stresses. The main advantage of using such a model is its relative simplicity of implementation in an existing LES code and more importantly its capability of saving a considerable amount of computational time compared to the wall-resolved LES counterpart. This point is essential when dealing with very low-frequency phenomena that are often encountered in shock/boundary layer interaction problems. In this study, we addressed the problem of supersonic boundary layer separation in a planar nozzle, with focus on the dynamics of the separation shock and the associated low-frequency oscillations. It is shown that when varying the nozzle-pressure ratio, by imposing different pressure gradients, the separation exhibits different flow patterns with symmetric to asymmetric flow separations at different pressure-fluctuations picks and shock-excursion extents. In particular, the results showed that the shock wave is enhanced when the pressure is changed and that the different flow scenarios are likely to occur depending on the extent of the recirculation

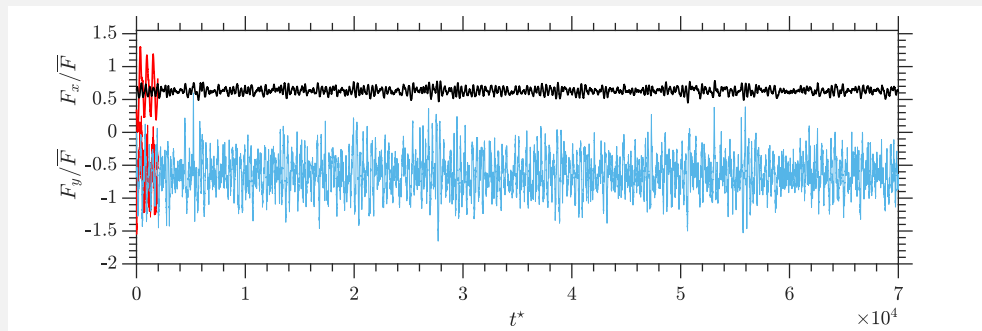
bubble and its response to the outer flow perturbations. On the basis of the present investigation, we intend to extend the study to include the effects of the far-field external pressure oscillations and their influence on the separation location inside the nozzle. These computations require the acquisitions of very long time series of data that could be tediously achieved without the use of such a wall-modeling approach.

Shock-Induced Flow Separation in an Overexpanded Supersonic Planar Nozzle

AIAA journal, Volume 58, Number 5, May 2020

Highlights

- Low-frequency shock oscillations are correctly captured using the wall-modeled LES approach with less grid points compared to the wall-resolved LES counterpart.
- A very long time integration is achieved (basically 18 times the one used in [Piquet \(2017\)](#), [Olson & Lele \(2011\)](#) and in [Johnson & Papamoschou \(2010\)](#)) allowing to resolve several cycles of shock excursions, with a better statistics convergence.
- The simulations bring clear evidence of the existence of broadband and energetically significant LFO, essentially in the vicinity of the separation shock.



Instantaneous wall-pressure forces integrated along the upper and the lower walls, data have been filtered with a cutoff Strouhal number of 0.2; —: streamwise forces, —: side loads. —WR-LES from [Piquet \(2017\)](#).



Shock-Induced Flow Separation in an Overexpanded Supersonic Planar Nozzle

B. Zebiri,* A. Piquet,[†] and A. Hadjadj[‡]
University of Rouen, 76000 Rouen, France

and

S. B. Verma[§]

*Council of Scientific and Industrial Research–National Aerospace Laboratories,
 Bangalore 560 017, India*

<https://doi.org/10.2514/1.J058705>

Shock-induced flow separation in an overexpanded supersonic planar nozzle is investigated numerically by means of three-dimensional wall-modeled large-eddy simulations (LES). The objective of this study is to identify the origin of the low-frequency shock oscillations (LFO) and the associated side-loads generation in planar nozzles. The computational results are compared with the experimental data for validation. The promise of the near-wall LES modeling approach, adopted in this study, is supported by its satisfactory performance in correctly predicting the shock-induced flow separation and offering a major advantage of being 30–40 times faster than the wall-resolved LES counterpart, allowing thereby the capture of very-low-frequency shock oscillations with much better statistics convergence. The simulations bring clear evidence of the existence of broadband and energetically significant LFO in the vicinity of the separated shock, whose forward and backward movements are mainly driven by changes in the downstream flow conditions. The complex interactions between the backflow, the separation bubbles, and the large-scale turbulent structures developing in the shear-layer region strongly influence the shock unsteadiness, which in turn drives the LFO. A scenario of the LFO, confirming conclusions from earlier studies, is described in this work.

Nomenclature

A	=	nozzle effective area
c	=	speed of sound
E	=	total energy
F	=	force
H_t	=	nozzle-throat height
L	=	characteristic length
M	=	Mach number
p	=	static pressure
Q_j	=	subgrid heat flux
\dot{q}_j	=	heat-diffusion flux
$R_{\alpha\alpha}$	=	two-point correlation function
St	=	Strouhal number
T	=	temperature
t	=	time
u_i	=	velocity components
x, y, z	=	Cartesian coordinates
δ	=	boundary-layer thickness
δ_{ij}	=	Kronecker symbol
λ	=	thermal conductivity
μ	=	dynamic viscosity
ν	=	kinematic viscosity
ξ, η, ζ	=	generalized curvilinear coordinates

ρ	=	density
σ_{ij}	=	viscous-stress tensor
τ_{ij}	=	subgrid shear-stress tensor

Subscripts

a	=	ambient conditions
e	=	exit-nozzle variable
i	=	inlet-nozzle variable
r	=	resonant tone period
rms	=	root mean square
s	=	separation-point variable
sgs	=	subgrid scale
th	=	throat-based variable
w	=	wall variable
τ	=	friction variable
0	=	total/stagnation variable
∞	=	freestream condition

Superscripts

+	=	wall-units variable
'	=	fluctuating quantity
★	=	normalized quantity

I. Introduction

SHOCK-INDUCED boundary-layer separation in transonic and supersonic flows is of great importance in many practical applications, such as rocket propulsion systems, transonic airfoils, and refrigeration ejectors. These unsteady phenomena are associated with undesirable effects such as shock oscillations, wall-pressure fluctuations, boundary-layer separation, and vortex shedding, which are major causes of vibration, noise, and side-loads generation. Comprehensive reviews of the topic can be found in [1].

Flow separation in supersonic planar nozzles has been the subject of several experimental and numerical investigations, with the aim to understand the different shock patterns occurring in the overexpanded nozzle regime [2–13]. According to these studies, three typical flow separation configurations can be identified: 1) incipient boundary-layer separation with normal shock, 2) symmetric boundary-layer

Received 5 June 2019; revision received 3 December 2019; accepted for publication 10 December 2019; published online 13 February 2020. Copyright © 2019 by the American Institute of Aeronautics and Astronautics, Inc. All rights reserved. All requests for copying and permission to reprint should be submitted to CCC at www.copyright.com; employ the eISSN 1533-385X to initiate your request. See also AIAA Rights and Permissions www.aiaa.org/randp.

*Ph.D. Student, National Institute of Applied Sciences, Centre National de la Recherche Scientifique, Unité Mixte de Recherche 6614, Avenue de l'Université; also CORIA INSA de Rouen; boubakr.zebiri@insa-rouen.fr.

[†]Research Engineer, CORIA INSA de Rouen; arthur.piquet@intradef.gouv.fr.

[‡]Professor, National Institute of Applied Sciences, Centre National de la Recherche Scientifique, Unité Mixte de Recherche 6614, Avenue de l'Université; also CORIA INSA de Rouen; abdellah.hadjadj@insa-rouen.fr.

[§]Deputy Head, Experimental Aerodynamics Division, and Group Head, Flow Structure Management and Aircraft and Spacecraft Aerodynamics; sbverma@nal.res.in. Associate Fellow AIAA.

separation with two-symmetric λ shocks, and 3) asymmetric boundary-layer separation with two-asymmetric λ shocks (see Fig. 1). As for the separation location, it was found to be sensitive to the flow disturbances, which may originate from the roughness of the wall [12] or from the improper initialization or startup of the flow [13]. To address the problem of nozzle flow separation, Papamoschou and Johnson [2] investigated a planar nozzle experimentally with a flexible geometry and different nozzle pressure ratios (NPR). They found that the flow could be asymmetric without flipping during the test run, but the jet flow could change the direction from one nozzle side to another during a restart of a run. According to their study, the shock selects its orientation at the nozzle startup and retains it throughout the run. Additionally, Reynolds-averaged Navier–Stokes (RANS) simulations were performed by Xiao et al. [3], in which they roughly confirmed the experimental findings of [2]. For a fixed nozzle area ratio and over a wide range of NPR (1.269–2.4), they found that the flow can be asymmetric for NPR 1.5–2.4, which is consistent with the experiments of [2]. Xiao et al. [3] demonstrated that the asymmetric behavior of the flow separation could be forced on either the top or the bottom wall by means of perturbations placed near one of the nozzle walls. They also found that the separated-flow region is largely enhanced within the core of the nozzle flow, which exhibits a higher level of unsteadiness. Detailed investigations of flow separations were made by Hunter [4], who studied experimentally and numerically an overexpanded planar nozzle and found that the flow is mainly dominated by the shock–boundary-layer interaction dynamics. He proposed a scenario in which the separation could be a natural response of the flow in its tendency to reach a thermodynamically stable state. Based on his study, the author suggested to classify the separation into two categories according to the NPR: 1) a nonstationary three-dimensional separation with a partial re-attachment and 2) a stationary two-dimensional separation with an abrupt transition existing between the two. The origin of the flow asymmetry was also investigated experimentally by Verma and Manisankar [5] using three different Mach 2 planar nozzles with a fixed area ratio and different divergent-wall angles. In their study, the authors found that the boundary-layer transition is one of the main reasons for the flow asymmetry. They also showed that the transition from free-shock separation (FSS) to restricted-shock separation (RSS) could initiate the flow asymmetry, but later the transition from RSS to FSS seems to make the flow symmetric again. Another origin of asymmetry, reported by [5], was the proximity of the separated shear layer to the nozzle wall.

In terms of unsteadiness, the separated flow often induces shock oscillations, associated with low-frequency motions. Two main origins of low-frequency shock oscillation (LFO) mechanisms can be broadly reported: The first concerns the upstream influence of the incoming turbulent boundary layer [14], whereas the second one (which is the most consensual today) supports the idea of the influence of the downstream conditions via the interaction between the separated boundary layer, the recirculation bubble, and the shock–train system [6–11,15,16]. Obviously, The ultimate question is the following: According to which physical mechanisms can these

low-frequency phenomena occur? Many scenarios are proposed in the literature. For instance, Zaman et al. [15], in their theoretical and experimental studies of transonic diffusers, concluded that the mechanism creating LFO is stimulated by acoustic resonance, where the low-frequency mode corresponds to the case when the one-quarter wavelength is fitted within the approximate distance from the foot of the shock to the nozzle exit. The same conclusions were made by Johnson and Papamoschou [7] when investigating experimentally the flow in a supersonic planar nozzle. Olson and Lele [8] investigated numerically the same nozzle and confirmed the previous findings. An interesting study of the effects of forced downstream conditions in a diffuser was conducted by Bruce and Babinsky [17]. The authors have found that the normal shock undergoes a coherent and reproducible periodic motion with regard to the sinusoidal variations of the downstream pressure. They also proposed a model for the trajectory of the shock that can be easily calculated by integrating the already predictable shock velocity. Thus, they define the shock movement as a mechanism by which the shock system can adapt itself to satisfy the NPR change. As a result, the frequency of the disturbance has no effect on the shock velocity. The effect of geometry was also studied through a nonviscous one-dimensional model. The authors were able to define a critical frequency, beyond which the amplitude of the shock is largely dependent on the angle of the divergent. Recently, Martelli et al. [18] found, for the same nozzle as [7,8], that the self-sustained shock oscillations are mainly driven by a pressure imbalance between the pressure level downstream of the shock and the ambient flow. Based on the above discussion, it is clear that the flow separation in supersonic planar nozzles with unsteady flow conditions is still an active research topic where much effort is still needed to better understand the physical mechanism of the LFO. Intending to shed more light on this complex fluid problem, large-eddy simulations (LES), solving three-dimensional compressible Navier–Stokes equations with wall modeling approach, are used to study the flow separation in an overexpanded planar nozzle. The present paper is organized as follows. The next section introduces the governing equations followed by a complete description of both wall-modeling methodology and numerical methods. Then, the simulation setup is presented, followed by the results and discussion. Finally, conclusions are drawn at the end of the paper.

II. Governing Equations, Turbulence Modeling, and Numerics

The filtered compressible Navier–Stokes equations are written as

$$\partial_t \bar{\rho} + \partial_j (\bar{\rho} \tilde{u}_j) = 0 \quad (1)$$

$$\partial_t (\bar{\rho} \tilde{u}_i) + \partial_j (\bar{\rho} \tilde{u}_i \tilde{u}_j) + \partial_i \bar{p} = \partial_j \tilde{\sigma}_{ij} - \partial_j \tau_{ij} \quad (2)$$

$$\partial_t (\bar{\rho} \tilde{E}) + \partial_j (\bar{\rho} \tilde{E} \tilde{u}_j) + \partial_i (\tilde{u}_i \bar{p}) = \partial_j (\tilde{u}_i \tilde{\sigma}_{ij}) - \partial_j \tilde{q}_j - \partial_j (\tilde{u}_i \tau_{ij}) - \partial_j \mathcal{Q}_j \quad (3)$$

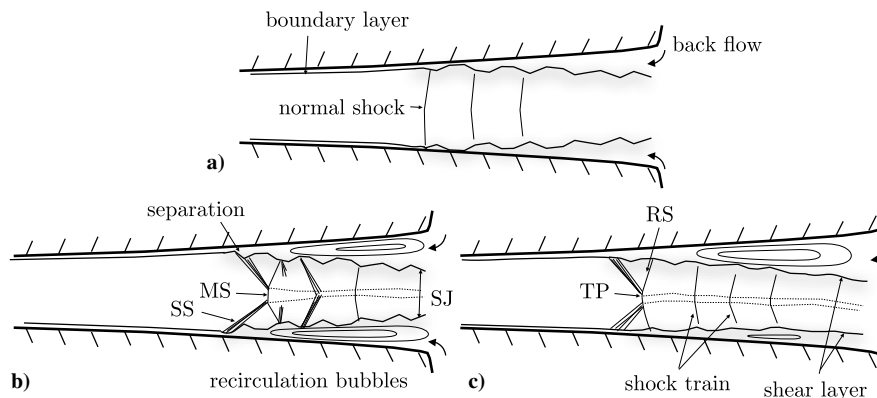


Fig. 1 Schematic representation of the typical flow regimes in a planar nozzle. MS: Mach stem; SS: separated shock; RS: reflected shock; TP: triple point; SJ: supersonic jet.

where $\bar{\rho}$, \tilde{u}_i , \bar{p} , and \tilde{T} are the filtered density, velocity, pressure, and temperature, respectively. Unlike the “bar” (Reynolds) and the “tilde” (Favre) filters, the “breve” symbol does not denote a filter operation but indicates that the quantity is based on primitive filtered variables. Thus, \tilde{E} refers to the resolved total energy, which is not equal to the filtered total energy. The resolved viscous stress tensor $\tilde{\sigma}_{ij}$ and the heat flux \tilde{q}_j are defined as $\tilde{\sigma}_{ij} = 2\mu(\tilde{T})(\tilde{S}_{ij} - \partial_k \tilde{u}_k \delta_{ij}/3)$ and $\tilde{q}_j = -\lambda(\tilde{T})\partial_j \tilde{T}$, respectively, where $\mu(\tilde{T})$ and $\lambda(\tilde{T})$ are the viscosity and the thermal conductivity corresponding to the filtered temperature \tilde{T} and $\tilde{S}_{ij} = (\partial_j \tilde{u}_i + \partial_i \tilde{u}_j)/2$. The low-pass filtering procedure generates several unclosed terms; most of these are neglected, except for the subgrid heat flux Q_j and the subgrid stress τ_{ij} , which are modeled according to the eddy-viscosity hypothesis as

$$Q_j = -k_{sgs}\partial_j \tilde{T} \quad (4)$$

$$\tau_{ij} = -\mu_{sgs}\left(\partial_j \tilde{u}_i + \partial_i \tilde{u}_j - \frac{2}{3}\partial_k \tilde{u}_k \delta_{ij}\right) + \frac{2}{3}k_{sgs}\delta_{ij} \quad (5)$$

$$\mu_{sgs} = C_d \Delta^2 \bar{\rho} |\tilde{S}|, \quad k_{sgs} = C_l \Delta^2 \bar{\rho} |\tilde{S}|^2, \quad \kappa_{sgs} = c_p \mu_{sgs} / Pr_{sgs} \quad (6)$$

where c_p is the heat capacity at constant pressure and k_{sgs} is the subgrid-scale kinetic energy. The modeling parameters C_d , C_l , and Pr_{sgs} are determined through the dynamic procedure of Lilly [19], Moin et al. [20], and Germano et al. [21] with filtering and averaging in the homogeneous (periodic) z direction. Δ is the filter width associated with the wavelength of the smallest scale retained by the filtering operation.

A. Near-Wall Turbulence Modeling

The near-wall turbulence modeling is required in order to reduce the computational cost of fully resolving all turbulent scales in the boundary layer. Various strategies have been reported in the literature for the past decades, and many of those are case sensitive. The wall-modeling approach, adopted in this study, consists of using a regular LES grid near the wall combined with a wall model, to mimic the dynamical effects of the turbulent eddies in the near-wall layer. In this study, a thin-boundary-layer equations (TBLE) approach is adopted as in Kawai and Larsson [22]. The TBLE model of Kawai and Larsson [22] includes neither the pressure gradient nor the convective terms. This assumes that the boundary layer, below the exchange height of the wall model (y_{wm}), is in equilibrium and by assuming that the pressure gradient from the LES domain is propagating onto the wall model through its top boundary condition. For the present study, a moderate pressure gradient is considered along the diverging section of the nozzle flow. Additionally, we have included a new formulation of the viscosity eddy, following the work of Duprat et al. [23], to partially account for the pressure gradient using a set of nondimensional variables derived from the work of Manhart et al. [24].

The final formulation of the TBLE model used in this study is as follows:

$$\partial_t(\bar{\rho}\tilde{u}_i) + \partial_j(\bar{\rho}\tilde{u}_i\tilde{u}_j) = -\partial_x \bar{p} + \partial_y[(\mu + \mu_t)\partial_y \tilde{u}_i] \quad (7)$$

$$\begin{aligned} & \partial_t(\bar{\rho}\tilde{E}) + \partial_x(\bar{\rho}\tilde{E}\tilde{u}) \\ & = -\tilde{u}_j\partial_x \bar{p} + \partial_y\left[(\mu + \mu_t)\tilde{u}_j\partial_y \tilde{u}_j + c_p\left(\frac{\mu}{Pr} + \frac{\mu_t}{Pr_t}\right)\partial_y \tilde{T}\right] \end{aligned} \quad (8)$$

where μ_t , Pr , and Pr_t are the eddy viscosity, the Prandtl number, and the turbulent Prandtl number, respectively. Following the work of Duprat et al. [23], the TBLE are reduced to the terms of the right-hand side. Under these assumptions, the simplified velocity streamwise momentum can be computed as follows:

$$\partial_y(\tilde{u}) = \frac{\partial_x(\bar{p})y + \tau_{w_{wm}}}{(\mu + \mu_t)} \quad (9)$$

where the wall-modeled shear stress $\tau_{w_{wm}}$ and the turbulent viscosity μ_t are the unknown variables of the equation. Similarly, for adiabatic boundary conditions, the temperature can be computed using

$$\partial_y(\tilde{T}) = \frac{(\mu + \mu_t)\tilde{u}\partial_y(\tilde{u}) + \partial_x(\bar{p})y\tilde{u}}{c_p((\mu/Pr) + (\mu_t/Pr_t))} \quad (10)$$

The pressure gradient effect on the eddy viscosity is modeled by a nondimensional parameter $\alpha = u_\tau^2/u_{\tau,p}^2$, which quantifies the balance between the shear stress and the streamwise pressure gradient. The turbulent viscosity is defined by

$$\mu_t = \mu\kappa y^*[\alpha + y^*(1 - \alpha)^{3/2}\gamma\left(1 - \exp\left(\frac{-y^*}{(1 + A\alpha^3)}\right)\right)]^2 \quad (11)$$

where κ is the von Kármán constant, y^* is the nondimensional length, and A and γ are the wall-model constants.

Dimensionless variables have been introduced to scale the boundary layer subjected to the pressure gradient, taking into account the wall-shear stress and the streamwise pressure gradient. The nondimensional velocity u^* and the length scale y^* are defined as $u^* = \tilde{u}/u_{\tau,p}$ and $y^* = yu_{\tau,p}/\bar{\nu}$, where $u_{\tau,p} = \sqrt{u_\tau^2 + u_p^2}$ is the combined velocity with $u_\tau = \sqrt{\tau_{w_{wm}}/\bar{\rho}}$ the friction velocity, and $u_p = |\bar{\mu}/\bar{\rho}^2\partial_x(\bar{p})|^{1/3}$ the pressure-gradient-based velocity.

The wall model is characterized by an “input-output” exchange process, where the information extracted from the LES becomes the upper boundary condition for the TBLE model. The latter is then resolved numerically using the local one-dimensional grid of height y_{wm} , to compute the wall-shear stress $\tau_{w_{wm}} = (\mu\partial_y \tilde{u})_{y=0}$ and the heat flux $\dot{q}_{w_{wm}} = -(\lambda\partial_y \tilde{T})_{y=0}$, which are injected back into the LES. Figure 2 shows a representation of the wall model methodology near the wall using the off-set method proposed by Kawai and Larsson [22].

The wall model has been implemented and assessed through a Direct Numerical Simulation (DNS) of a spatially evolving compressible boundary layer subjected to a pressure gradient. A comparison of the existing DNS of Pirozzoli et al. [25] has been first done to generate a developing boundary layer. The Reynolds number is taken as $Re_x = 2.54 \times 10^6$, and the same perturbation model between $x = 4.5''$ to $x = 5''$ is used as [25]. The inlet flow is set at Mach 2.25 and a static temperature of 169.44 K. The domain has been extended in the streamwise direction to have enough space to capture the separation/reattachment phenomena of the TBL. Then, the numerical data have been used to perform a DNS of a turbulent boundary layer under both adverse and favorable pressure gradients. Finally, the DNS of the nonequilibrium boundary layer was used to validate the correct implementation of the model through both a priori and a posteriori tests. The wall-model constants $A = 17.2$ and $\gamma = 0.78$ were determined through a priori tests (more details can be found in [26]).

B. Numerical Flow Solver

Numerical simulations are carried out using an in-house-validated compressible code. The convective terms are discretized using a

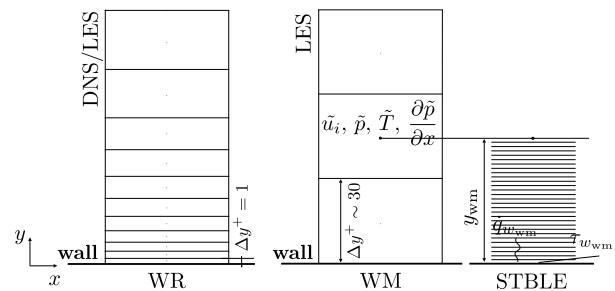


Fig. 2 Schematic representation of the wall-resolved and wall-modeled LES approaches.

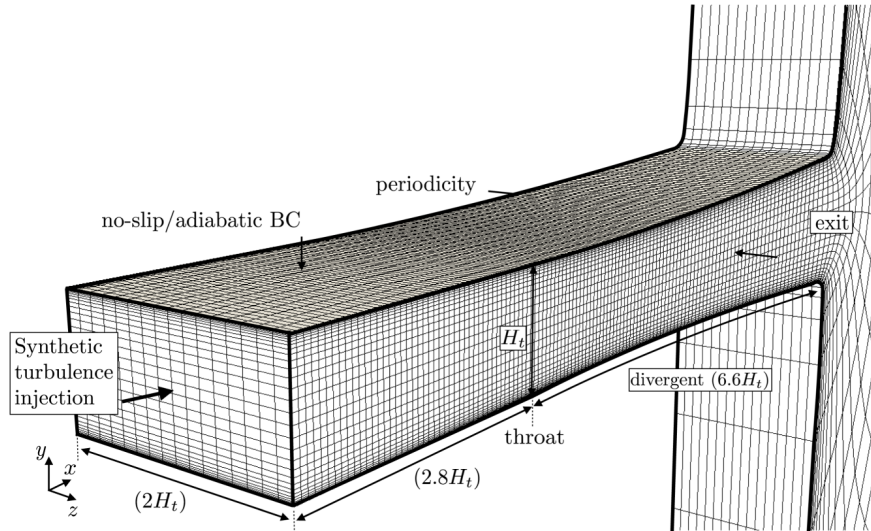


Fig. 3 Grid representation of the wall-resolved nozzle test case showing every 10th grid line. The grid stretching function is defined as $f_{\text{str},y} = \tanh(r_{v,y}(2\eta/N_y - 1)) / \tanh r_{v,y}$, where N_y is the number of point and η is the generalized curvilinear coordinate in wall-normal direction with $r_{v,y} = 2.3$. For the WM-LES, the grid is regularly spaced following $f_{\text{str},y} = (2\eta/N_y - 1)$. The nozzle throat is located at $x = 0$.

sixth-order weighted compact nonlinear scheme (WCNS) developed by Deng and Zhang [27] in generalized curvilinear coordinates, whereas the viscous terms are discretized using a fourth-order central scheme with a split form of the Laplacian tensor for stability reason. The time is advanced using a fourth-order Runge–Kutta (RK4) scheme. The Courant–Friedrichs–Lewy (CFL) stability limit is near unity for all calculations. The solver is explicit and fully parallelized using MPI libraries.

III. Problem Setup

The test case considered in this study is the planar nozzle used in Olson and Lele [8], which is based on the experiments of Johnson and Papamoschou [7]. In the present simulations, the mesh is structured (see Fig. 3) and the incoming flow is generated using a synthetic turbulent boundary-layer inlet based on the method of Xie and Castro [28]. Similarly to [8], the converging part of the nozzle is not simulated here in order to reduce the computational cost of the overall simulations. To ensure a fully developed boundary layer at the nozzle throat, the computational inlet is shifted upstream using a buffer zone of length $L_b = 2.8H_t$, where H_t is the throat height. The flow in the spanwise direction is assumed to be homogeneous with periodic boundary conditions ($L_z = 2H_t$). The outlet boundary conditions are treated as nonreflective using the NSCBC method [29] in conjunction with an external buffer zone with a stretched grid to further damp the reflected waves.

Both upper and lower walls are considered as adiabatic with no-slip boundary conditions applied on the wall model. An NPR of 1.7 is considered, which corresponds to the experiments of Johnson and Papamoschou [7], with stronger shock amplitude and an asymmetric separation behavior. Olson and Lele [8] performed their LES for the same NPR and captured the same asymmetric separation behavior. The flow properties at the inlet (mainly the boundary-layer thickness (δ_i) and the freestream velocity ($u_{i,\infty}$)) are used as scaling parameters for $t^* = tu_{i,\infty}/\delta_i$ and $St_\delta = f\delta_i/u_{i,\infty}$. Although the current study is based on the use of a wall-modeled (WM-LES) approach, we have performed calculations using a wall-resolved (WR-LES) approach over a shorter period of time to ensure that the WM-LES restores the main trends of shock–boundary-layer interaction. Table 1 summarizes the grid resolutions used in both WR- and WM-LES compared with the one used by Olson and Lele [8].

IV. Results and Discussion

Mean flow quantities are collected from time averaging of the instantaneous three-dimensional fields that are extracted from a long-time series of the WM-LES data covering almost 70,000 characteristic time scales (t^*). This represents one of the longest time scale ever reached in separated nozzle flow simulations so far. Part of the WR-LES data is not shown here for concision. Figure 4 highlights an instantaneous picture of the complex three-dimensional nozzle flow-field showing the shock-wave–boundary-layer interaction pattern, with an asymmetric λ -shock structure. The whole shock pattern consists of an incident shock (IS), a reflected shock (RS), and a Mach stem (MS). In this configuration, the boundary-layer separation due to the high adverse pressure gradient creates an incident shock impinging the Mach stem at the triple-point TP. The reflected shock realigns the incident flow to the original direction. The Mach stem, which is a stronger shock, reduces the flow velocity substantially behind it to a subsonic state. The sonic line that bounds the shear layer and the recirculation zone can be seen as a virtual wall that defines the effective geometry of the nozzle. Because the effective nozzle geometry is shorter and has a lower expansion ratio, the resulting area reduction acts as an additional confinement effect of the flow, which compresses the flow and produces multiple shocks organized in a shock-train structure that is typically present in planar nozzles or transonic ducts.

A. Mean Profiles

The WR/WM LES pressure distribution at the wall is presented in Fig. 5a. The result agrees well with both experimental and previous LES results. The concordance between the data shows that the wall-modeled simulation is able to correctly reproduce the pressure gradient effect on the boundary layer. One can also notice a small difference in the separated region, where the experimental data and the WR computation show a smoother pressure jump compared with the wall-modeled simulation. This behavior is due to the strong compression waves in the wall-modeled simulation applying in the interaction zone upstream of the separation point.

Table 1 Grid parameters at the inlet of the nozzle

	Δx_i^+	Δy_i^+	Δz_i^+	Number of cells
Olson and Lele [8]	30	[1:23]	20	50.3M
WR-LES	30	[1:29]	20	73.4M
WM-LES	60	45	40	13.7M

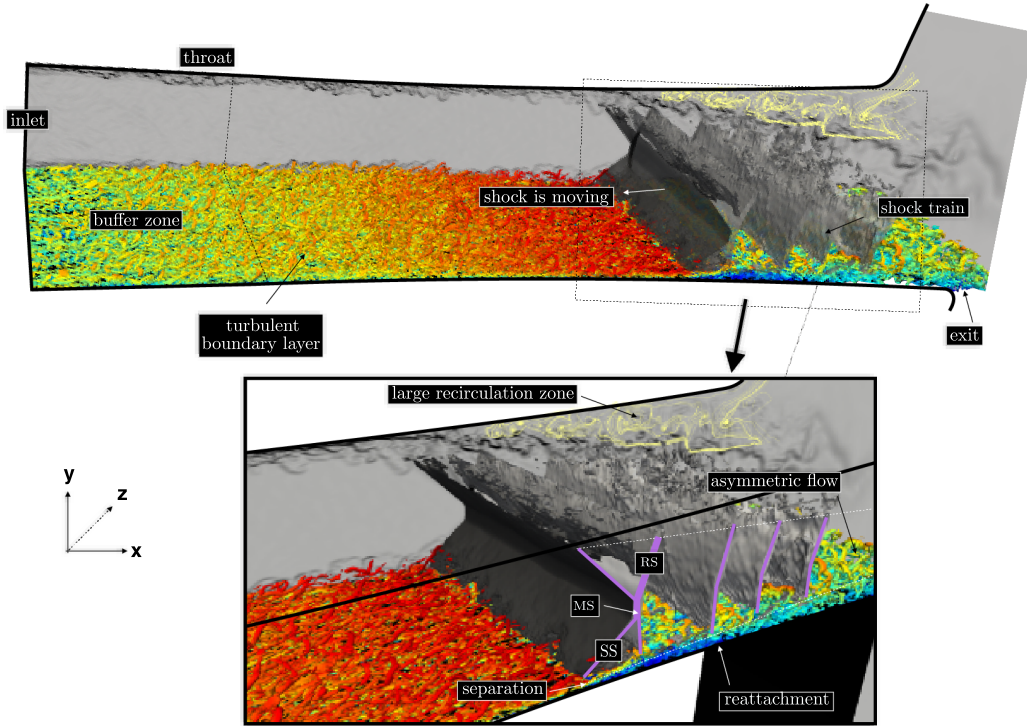


Fig. 4 Instantaneous three-dimensional nozzle flowfield showing isocontours of Q -criterion colored by the velocity field (blue: slow; red: fast). Grayscale surface represents schlieren imaging background in the x - y plane, whereas grayscale volume is the isovolume of the velocity gradient $\nabla\|u\|$. The image is taken when the separated shock was moving upstream toward the throat. See Fig. 1 for other notations.

The coarse grid of the wall-modeled case reduces the length of the interaction and increases the strength of the compression waves, resulting in a slightly stronger separated shock. Figure 5b shows a comparison of the normalized pressure gradient using the Clauser's parameter $\beta = \delta^* \partial_x(\bar{p})/\tau_w$, where $\delta^* = \delta/\delta_i$ is the normalized boundary-layer thickness. Upstream of the nozzle throat, the experimental data do not perfectly coincide with the simulations due to the difference in the converging part of the nozzle geometry. Note that the effect of the pressure gradient is accurately reproduced by the simulations, except in a region near the throat, where a small difference is noticeable.

B. Shock Motion and Spectral Analysis

To study the shock dynamics, one can track the separation position on both sides of the wall. The separation is found based on the location where the near-wall velocity becomes negative. Then, the noisy data are smoothed using a moving-average filter. The separation location is found to exhibit an oscillating behavior in a low-frequency range. Broadband and energetically significant LFO in the vicinity of the separated shock were also observed. The magnitude of the observed oscillations is close to the value found in [7], which is $8\delta_i$. The flow separation at this particular NPR exhibits an asymmetric character with a jet flow being stuck on one side of the

nozzle without flipping, as reported in the experiments of Johnson and Papamoschou [7].

The mechanism of low-frequency unsteadiness in overexpanded nozzle flow has been described by Zaman et al. [15] in their experiments of transonic diffuser. They showed that the resonant tones occur when the length between the separation and the shock is similar to a quarter wavelength at the speed of sound (c). This is true for small opening angles, transonic jet-Mach number and smooth-nozzle walls. Zaman et al. [15] proposed the following correlation to compute the resonant tone, $f_r = (c^2 - u_e^2)/4cL_{s,e}$, where $L_{s,e}$ is the length between the averaged separation location and the exit of the nozzle, c the speed of sound within the separated boundary layer, and u_e the velocity at the exit.

Zaman's correlation provides a closer value to the resonant tone in comparison with the present WM-LES (i.e., $St_\delta \sim 0.003$). In the present case, the jet Mach number M_j is equal to 0.76 and the maximum half-angle of the nozzle is about 4° , which fits the transonic tone requirements. Similarly, Olson and Lele [8] concluded that the unsteady mechanism was due to a transonic resonant tone between the shock location and the nozzle exit. They found a two-way coupling between the shock and the shear layer combined with a time lag leading to the unsteady LFO.

Figure 6a highlights the correlation between the effective exit area A_e and the velocity separation shock. It shows a time lag of

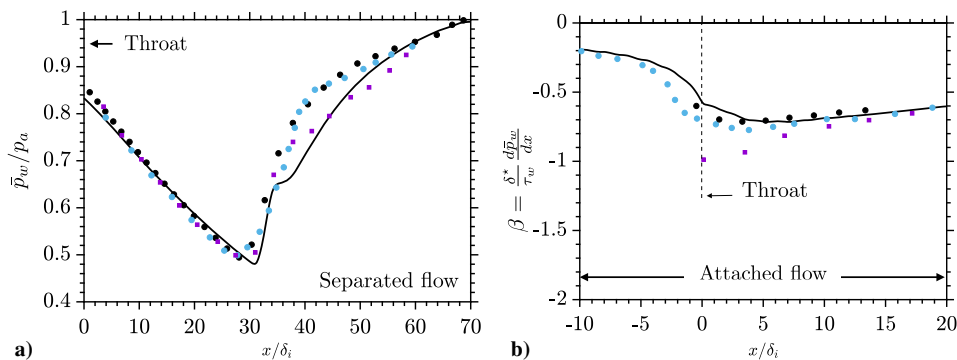


Fig. 5 a) Normalized mean wall-pressure distribution. b) Clauser's parameter along the longitudinal direction. —: WM-LES; •: WR-LES from [26]; •: WR-LES from [8]; ■: experimental results from [7].

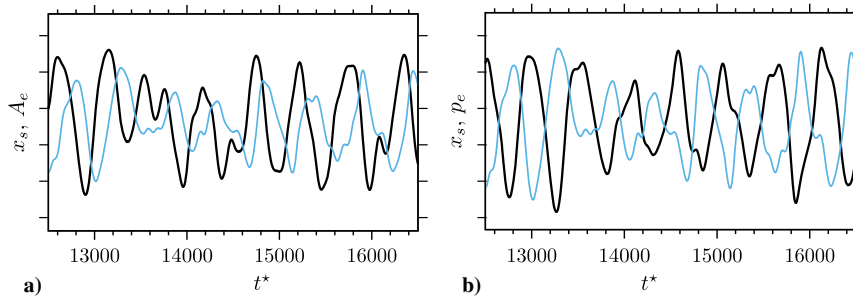


Fig. 6 a) Time delay between the effective exit area A_e (—) and the separation location x_s (—). b) Time delay between the exit pressure p_e (—) and the separation location x_s (—).

approximately one-quarter wavelength, confirming the prediction of Olson and Lele [8] with respect to the resonant tone. Similarly, Fig. 6b shows the anticorrelation between the exit pressure p_e and the separation location x_s . When the shock is located at its downstream position, the pressure is minimal because of the increased effective area. Conversely, when the shock is at its upstream position, the pressure is maximum considering the small effective area, which confirms the findings of Martelli et al. [18]. A small delay of $\Delta t^* \sim 40$ can be observed between the shock location and the exit pressure due to the acoustic waves that propagate upstream to the shock. In the present LES, the observed lag time between the shock-position signal and the effective-area signal was about one-quarter wavelength (i.e., $\Delta t^* \sim 150$), confirming the resonance phenomenon observed by Zaman et al. [15]. This difference is not due to the time needed for the pressure waves from the confined exit area to propagate upstream of the shock (i.e., $\Delta t^* \sim 40$), as addressed by Olson and Lele [8], but to the constant change of the effective area downstream of the shock.

The complex dynamics of the streamwise back and forth shock movement shown in Fig. 7 are summarized hereby, confirming previous scenarios of the following [8,18]:

1) The separated shock moves downstream with a maximum shock speed $u_{s,max}$. Because of the highly effective pressure at the nozzle exit resulting from the change of the effective geometry of the nozzle, the flow is then sucked up by the atmospheric pressure $p_e > p_a$. The relative speed of the incident shock is reduced because of the suction effects. At the end of this step, the incident shock vanishes to a series of compression waves that transform the λ -shock pattern into one normal shock.

2) At one-quarter wavelength, the exit pressure is lower than the ambient pressure, creating a slight backflow from the exit. This reversal flow starts to increase the deflection angle of the mixing layer and changes the effective geometry of the nozzle. The effective area starts to decrease with one-quarter delay compared with the position of the shock. Because of inertia (flow resistance), the shock is still moving toward the exit, whereas the backflow intensifies. At this stage, the flow is mildly symmetric and a backflow occurs on both sides of the nozzle.

3) When the shock is standing at its maximum position, the exit pressure is weak and the backflow from the ambient pressure increases. The mixing layer reattaches one of the nozzle walls (either upper or lower depending on the initial condition). The effective area is decreased compared with (2) and the flow is thermodynamically unbalanced, forcing thereby the shock position to adapt to the new state.

4) The shock moves upstream with a minimum shock speed $u_{s,min}$. The mixing layer is fully attached to the lower wall, and the large recirculation bubbles emerge along the upper wall. The backflow acts only on the upper wall, which is opened to the atmosphere. The effective geometry of the nozzle downstream of the shock behaves as a convergent nozzle, where the subsonic flow accelerates to a supersonic stream and forms a series of shocks known as “shock train.”

5) After five quarters of wavelength, the shock is still moving upstream but the exit pressure becomes higher than the atmospheric one. As for the one quarter wavelength time step, the effective cross-sectional area of the nozzle starts to increase, which unbalanced the total pressure at the exit.

6) The shock is now at its most upstream location within the cycle. The suction effect from the ambient pressure forces the mixing

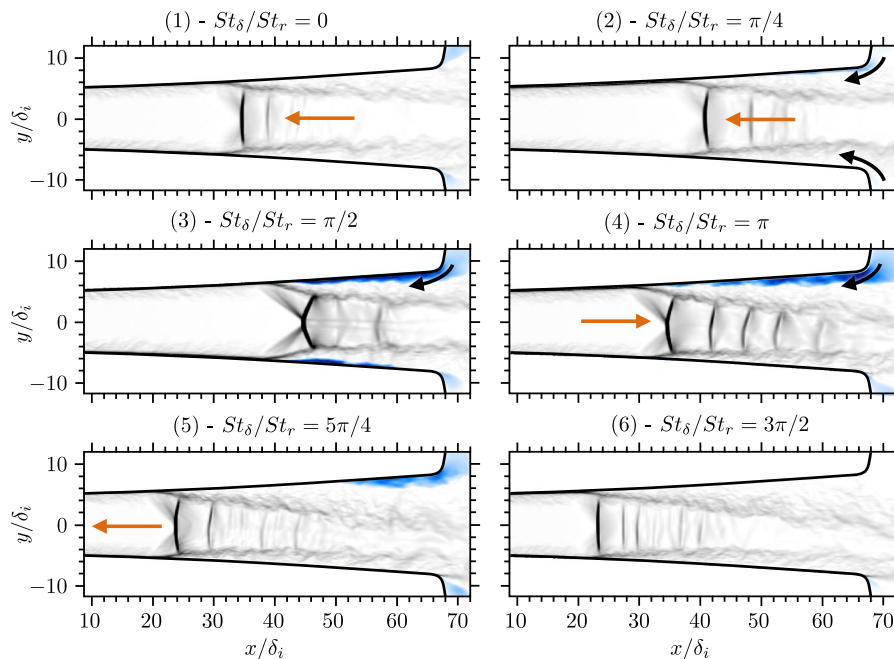


Fig. 7 Shock excursion over one resonant tone period St_r for different time steps. z-averaged schlieren pictures shown in grayscale, blue regions highlight negative x velocity, orange arrows indicate the direction of the shock movement, and black arrows indicate the backflow.

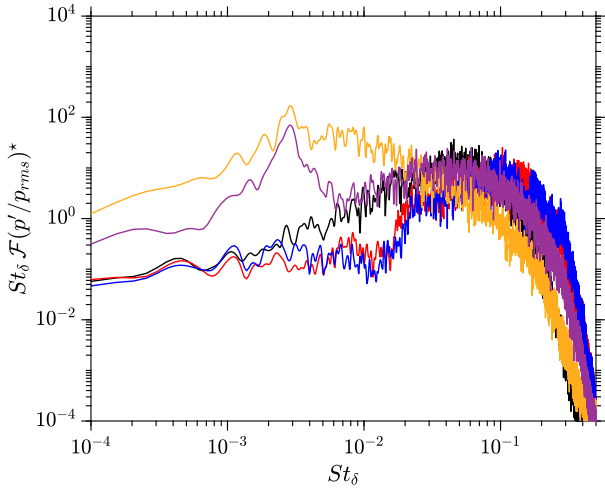


Fig. 8 Premultiplied spectrum of the normalized wall-pressure fluctuations for different streamwise locations. —: inlet; —: $x/\delta_i = -12$ upstream of the throat; —: throat region; —: separation region; —: recirculation zone.

layer to move closer to the walls, increasing the effective area. As for (3), the flow is thermodynamically unbalanced, forcing the shock position to move downstream. The acoustic lag due to the time taken for the pressure waves to acoustically propagate from the back pressure to the shock is maximal at this position, increasing thereby the unsteadiness of the shock.

Hence, a restart cycle from (1) maintains the shock in a closed-loop motion.

Figure 8 shows the normalized premultiplied spectra of pressure probe signals in five different locations. The spectra, defined as $St_\delta \mathcal{F}(p'/p_{rms})^* = St_\delta \mathcal{F}(p'/p_{rms}) / \int_{St_\delta} St_\delta \mathcal{F}(p'/p_{rms}) dSt_\delta$, cover the entire range of frequencies, from very low up to the boundary-layer time scales (i.e., $St_\delta > 1$). The spectrum at the throat shows no

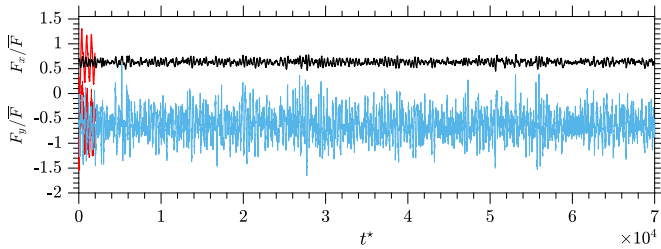


Fig. 9 a) Instantaneous wall-pressure forces integrated along the upper and the lower walls. Data have been filtered with a cutoff Strouhal number of 0.2. —: streamwise forces; —: side loads; —: WR-LES from Piquet [26].

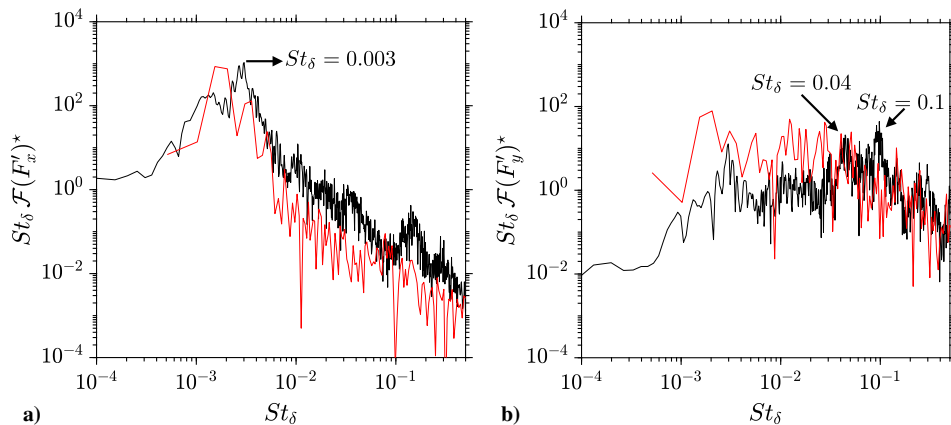


Fig. 10 Normalized premultiplied spectra of dimensionless fluctuations: a) streamwise forces; b) side loads. —: WR-LES from Piquet [26]; —: present WM-LES.

low-frequency activities. The same remark holds for the probe at the inlet and at $x/\delta_i = -12$ upstream of the throat. However, the main tone is captured both at the separation location and at the nozzle exit. In the recirculation zone, most of the spectral energy is contained in a region where $St_\delta \sim 0.04$ as observed by [30]. They showed that the recirculating area exhibits large oscillations in the low-frequency range. Most of the energy captured in the recirculating area is due to the breathing phenomenon caused by an imbalance state between the flow from the shear layer and the backflow near the nozzle lip. The corresponding main tone is captured at the nozzle exit, where both recirculation bubble and lip vortex phenomenon interact. The later, having a small size compared with the main recirculation zone, is created by the confluence of the recirculation zone and the backflow.

Figure 9 shows the time-history of the WM-LES-integrated wall-pressure force compared with the WR-LES results of Piquet [26]. It is worth mentioning that the WM-LES integration time represents 18 times the one found in Piquet [26], Olson and Lele [8], and the experiments in [7]. Thus, the present integrated time is large enough to resolve several shock excursions, therefore having better statistics convergence.

The wall-pressure vector force is integrated along both upper and lower walls as $\mathbf{F} = \int_s (p_w - p_a) \mathbf{n} ds$, where p_w is the wall pressure, p_a the ambient pressure, ds the local surface element where the force is applied, \mathbf{n} the normal vector to the surface, and S the total surface of the nozzle including the upper and lower wall. The forces are decomposed into streamwise and lateral forces (side loads).

Figure 10 shows the normalized premultiplied spectra of the normalized streamwise/side-loads force fluctuations $St_\delta \mathcal{F}(F'_i/F)^* = St_\delta \mathcal{F}(F'_i/F) / \int_{St_\delta} St_\delta \mathcal{F}(F'_i/F) dSt_\delta$, compared with the results of [26]. One can clearly notice that the two spectra are quietly converged for the high frequencies, while the main tone is different. This difference is due to the shock position in both simulations as a direct result of using the NSBC conditions at the outlet in the present simulation, which prevents the reflected acoustic wave from affecting the shock system and causing large-shock oscillations. Figure 10 shows that the streamwise forces fluctuate at a low frequency, whereas the side loads contain a broad range of frequency unsteadiness. In the streamwise force spectrum, three peaks can be observed at $St_\delta \sim 0.003$, $St_\delta \sim 0.04$, and $St_\delta \sim 0.1$, corresponding to the resonant tone, the recirculation bubble, and the mixing layer phenomenon, respectively. High-frequency peaks can be observed in the side-loads spectrum at $St_\delta \sim 0.04$ and $St_\delta \sim 0.15$. It seems that the side loads are highly sensitive to the high-frequency oscillations, whereas the streamwise force is more sensitive to the main tone of the separation line.

Each phenomenon occurring in the nozzle can be characterized by a frequency range. To identify these frequencies (Fig. 10) and to link them to the corresponding physical phenomena, a dynamic mode decomposition (DMD) analysis is performed. Given the wide scale of frequencies involved in this flow and in order to extract the

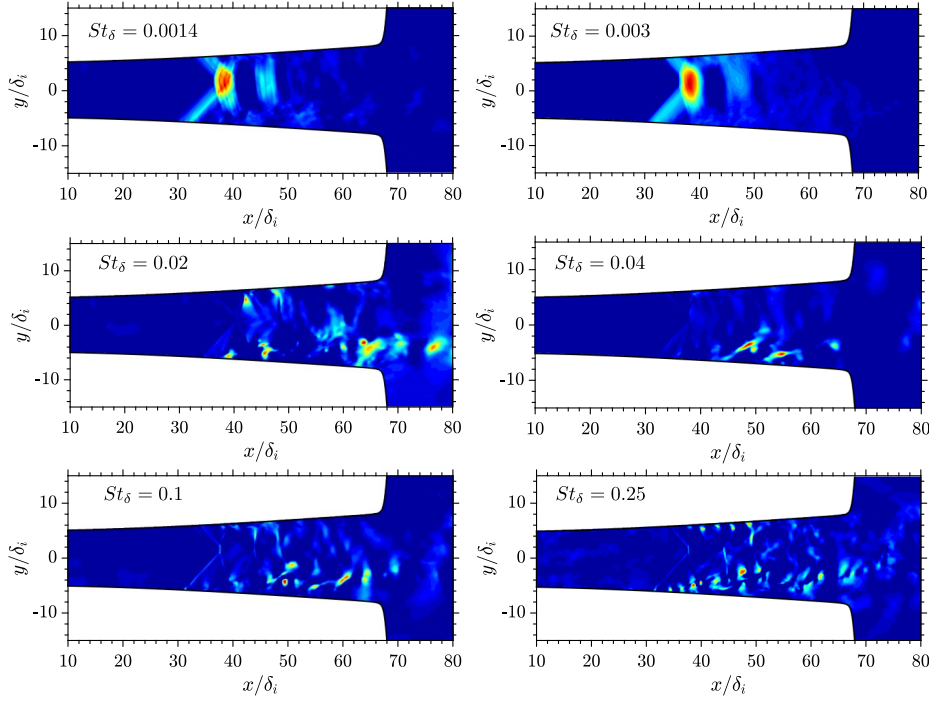


Fig. 11 Reconstructed field of the real part of the pressure fluctuations, p' , for different DMD modes at selected values of St_δ . Red is the highest representative phenomenon of the mode.

corresponding low frequencies, we have used a multiresolution DMD (MrDMD) developed by Kutz et al. [31]. The MrDMD is able to separate robustly the complex systems into a hierarchy of multi-resolution time-scale components. The method is applied to a series of two-dimensional slices of pressure fluctuations p' , where each snapshot represents the full flowfield (the nozzle flow and the ambient region). Equi-time spaced snapshots are used and sampled at $St_\delta = 1$, which gives a Nyquist frequency of $St_\delta = 0.5$. Thus, the entire frequency range can be captured. The results shown in Fig. 11 are summarized as follows:

- 1) $St_\delta \in [\dots, 0.009]$; a frequency range corresponds to the oscillation of the shock system. Note that the resonant tone predicted by Zaman et al. [15] is captured at the separation and downstream at $St = 0.003$.
- 2) $St_\delta \in [0.01, 0.09]$; the subsonic flow downstream of the separation is trapped between the mixing layer and the wall, producing small unsteady eddies that oscillate within this range of frequencies (recirculation bubbles). This phenomenon is strongly affecting the side loads.
- 3) $St_\delta \in [0.1, 0.5]$; the mixing layer developing from the boundary-layer separation to the nozzle exit is observed at these frequencies. The large two-dimensional Kelvin–Helmholtz vortices impact the exit conditions, modifying thereby the effective nozzle exit area and the corresponding shock location.
- 4) $St_\delta \sim 1$; upstream of the separation, the pressure fluctuations are dominant in the range of the turbulent boundary-layer frequencies.

V. Conclusions

A wall-modeled LES approach is used to investigate the unsteady behavior of three-dimensional flow separation in a supersonic planar nozzle. The objective of the study is to provide a better understanding of the main mechanisms driving the shock oscillations. The absence of low-frequency phenomena upstream of the boundary-layer separation and their presence near the separation point and in the downstream region confirm the role of the downstream flow conditions in driving or at least in maintaining the shock oscillations at very low frequencies. A scenario describing the way in which the LFO occur is proposed confirming the earlier findings. The study shows that the deflection angle of the separated shear layer, which represents the effective geometry of the nozzle downstream of the shock, is strongly coupled to the shock position. A phase shift between the motion of these two features, that is, upstream or downstream movement, causes the cycle to constantly overcompensate its pressure to match the exit pressure, giving thereby the self-sustained shock motion behavior already observed in many experimental and numerical setups. Regarding the asymmetry behavior of the separation, the current simulations show that the phenomenon is stable for the studied NPR and does not switch from asymmetric to symmetric flow separation over a very long run time, confirming the experimental findings. This confirmation was possible thanks to the use of the current wall model strategy, which allows, by its ability to correctly model the turbulent boundary layer and consequently the reduction of the number of mesh points, to have very long signals required for the study of the LFO.

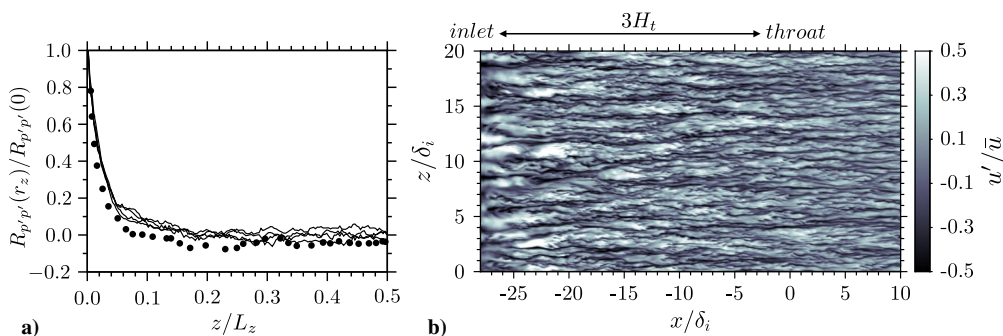


Fig. A1 a) Two-point correlation function of wall pressure fluctuations along the spanwise direction ($L_z = 2H_t$) at $x/\delta_i = 0$ (—: results at different x locations in the preshock boundary-layer zone; •: WR-LES from [8]). b) Instantaneous velocity fluctuations in the x - z plane at $y^+ \sim 20$.

Appendix A: Grid Sensitivity Study

A.1. Periodic Domain Extent and Boundary-Layer Development

To ensure that the domain size in the z direction is large enough to cover most of the length scales present in the flow, a two-point correlation function based on the wall pressure along the spanwise direction, $R_{p'p'}(r_z) = \sum_{n=1}^{N_z} \overline{p'_n p'_{n+n_r}}$, with $n_r = 0, \dots, N_z$; $r_z = n_r \Delta z$, is computed and averaged over time for two x locations. Figure A1a shows $R_{p'p'}(r_z)/R_{p'p'}(0)$ plotted at the throat. The decay of correlation at $z/L_z = 0.1$ demonstrates that the length in the spanwise direction does not affect the dynamics and the development of the coherent structure in the flow.

For the development of the boundary layer, the synthetic turbulence injection starts at $x/\delta_i = -28$, giving 18 boundary-layer thicknesses length for the flow to relax to a converged boundary layer. Xie and Castro [28] have demonstrated that the method of synthetic injection needs at least 10 boundary-layer thicknesses to reach a fully turbulent flow. Figure A1b shows the structure of the turbulence in the boundary layer at the buffer layer through the velocity fluctuations field. The synthetic eddy structures seem to extend to $\Delta x/\delta_i \sim 15$, in agreement with the streaky structures as observed by Xie and Castro [28]. Past this recovery region, the velocity fluctuations exhibit more coherent structures.

A.2. Mesh Grid Convergence

To establish the fidelity of the LES database, we conducted an LES grid convergence study. Three different meshes are used (see Table A1). The normal direction has been excluded from this study because the Kawai and Larsson's [22] recommendations are strictly followed and we believe that it is sufficient for the convergence in the wall-normal direction. Thus, the methodology consists of changing the number of points in both streamwise and spanwise directions. The obtained results are presented in Fig. A2b in terms of normalized mean wall pressure distribution for different grid

Table A1 LES grid parameters

	N_x	N_y	N_z	Number of cells
Mesh A	672	128	160	13.7M
Mesh B	750	128	160	15.4M
Mesh C	672	128	190	18.3M

Table A2 Wall model grid parameters

	Exchanging cell	N_{wm}
Case 1	2	50
Case 2	3	50
Case 3	3	100

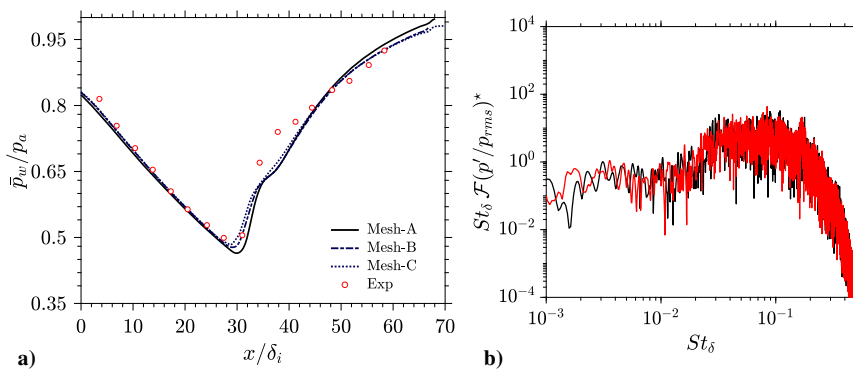


Fig. A2 a) Normalized mean wall-pressure distributions for different meshes. b) Normalized premultiplied spectra of the normalized pressure fluctuations at the throat (—: mesh A; —: mesh B).

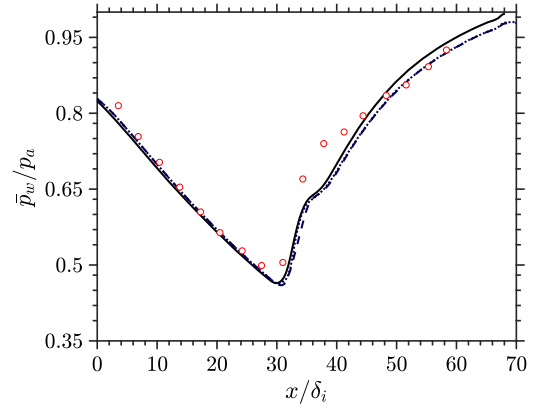


Fig. A3 Normalized mean wall-pressure distribution (—: case 1; ---: case 2; ○: case 3). See Table A2.

resolutions. Although the statistics were not acquired over the same amount of samples, the number of samples used in this study was large enough to consider the results as statistically converged. From Fig. A2b, it is seen that varying the grid resolution does not produce significant differences in the wall pressure before the separation and in the shocked region. Therefore, we consider that the grid resolution, used in this study, is sufficiently fine to only have marginal effects on the statistical results.

Figure 2 shows schematically the concept of WM-LES where the TBLE equations are solved on a separate grid. In the present simulation, the exchange of information between the LES and the wall model occurs at y_{wm} , corresponding to the second LES cell away from the wall. Kawai and Larsson [22] recommended to avoid the log-layer mismatch of the WM-LES when the exchange occurs in the first or in the second cell due to numerical errors in the LES solution at those two first cells. Hence, we have considered adding three cells below. The results are shown in Fig. A3. It is clear that adding one more cell leads to a small underprediction of the wall pressure. Note that all recommendations made by Kawai and Larsson [22] are respected, expect using four or five cells below the exchanging height.

Appendix B: Wall-Model Sensitivity Study

Several authors have shown that the error incurred by neglecting both pressure gradient and convective terms in the TBLE equations can be larger than the error incurred by an equilibrium formulation, that is, not accounting for those two terms in the wall model. For this purpose, a new simulation has been performed using the present wall model without the pressure gradient term (PGT). The wall pressure from the new simulation, together with the previous data and the experiment results from [7], is presented in Fig. B1. Indeed, a quite small improvement is noticed in the recovery region downstream of the separated zone when the pressure gradient term is included, whereas the separation location remains the same in both formulations.

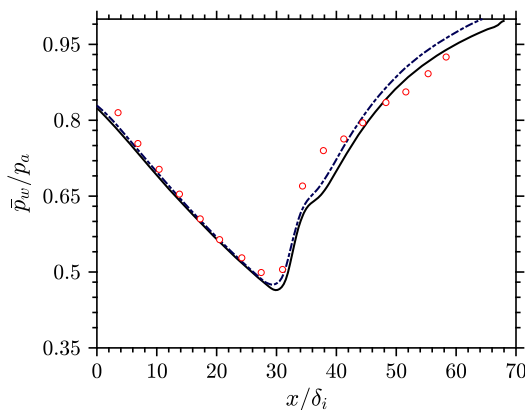


Fig. B1 Normalized mean wall-pressure distribution. —: WM-LES with PGT; - - -: WM-LES without PGT; ○: experimental results from [7].

Acknowledgments

B.Z. gratefully acknowledges support from the Algerian Government through a Ph.D. fellowship. The authors thank Emile Touber from Imperial College London for his valuable discussion on the preliminary version of this work. The use of high performance computing resources from Centre Régional Informatique et d'Applications Numériques de Normandie (CRIANN), Rouen, France, under the allocation 1998022, is acknowledged.

References

- [1] Hadjadj, A., and Onofri, M., "Nozzle Flow Separation," *Shock Waves*, Vol. 19, No. 3, 2009, pp. 163–169.
<https://doi.org/10.1007/s00193-009-0209-7>
- [2] Papamoschou, D., and Johnson, A., "Unsteady Phenomena in Supersonic Nozzle Flow Separation," AIAA Paper 2006-3360, 2006.
- [3] Xiao, Q., Tsai, H. M., and Papamoschou, D., "Numerical Investigation of Supersonic Nozzle Flow Separation," *AIAA Journal*, Vol. 45, No. 3, 2007, pp. 532–541.
<https://doi.org/10.2514/1.20073>
- [4] Hunter, C. A., "Experimental Investigation of Separated Nozzle Flows," *Journal of Propulsion & Power*, Vol. 20, No. 3, 2004, pp. 527–532.
<https://doi.org/10.2514/1.4612>
- [5] Verma, S., and Manisankar, C., "Origin of Flow Asymmetry in Planar Nozzles with Separation," *Shock Waves*, Vol. 24, No. 2, 2014, pp. 191–209.
<https://doi.org/10.1007/s00193-013-0492-1>
- [6] Bourgoing, A., and Reijasse, P., "Experimental Analysis of Unsteady Separated Flows in a Supersonic Planar Nozzle," *Shock Waves*, Vol. 14, No. 4, 2005, pp. 251–258.
<https://doi.org/10.1007/s00193-005-0269-2>
- [7] Johnson, A. D., and Papamoschou, D., "Instability of Shock-Induced Nozzle Flow Separation," *Physics of Fluids*, Vol. 22, No. 1, 2010, Paper 016102.
<https://doi.org/10.1063/1.3278523>
- [8] Olson, B. J., and Lele, S. K., "Large-Eddy Simulation of an Over-Expanded Planar Nozzle," AIAA Paper 2011-3908, 2011.
- [9] Verma, S., Chidambaramathan, M., and Hadjadj, A., "Analysis of Shock Unsteadiness in a Supersonic Over-Expanded Planar Nozzle," *European Journal of Mechanics—B/Fluids*, Vol. 68, March–April 2018, pp. 55–65.
<https://doi.org/10.1016/j.euromechflu.2017.11.005>
- [10] Dussauge, J. P., Dupont, P., and Debiève, J. F., "Unsteadiness in Shock Wave Boundary Layer Interaction with Separation," *Aerospace Science and Technology*, Vol. 10, No. 2, 2006, pp. 85–91.
<https://doi.org/10.1016/j.ast.2005.09.006>
- [11] Dupont, P., Haddad, C., Ardisson, J. P., and Debiève, J. F., "Space and Time Organisation of a Shock Wave/Turbulent Boundary Layer Interaction," *Aerospace Science and Technology*, Vol. 9, No. 7, 2005, pp. 561–572.
<https://doi.org/10.1016/j.ast.2004.12.009>
- [12] Shimshi, E., Ben-Dor, G., Levy, A., and Krothapalli, A., "Asymmetric and Unsteady Flow Separation in High Mach Number Planar Nozzles," *International Journal of Aeronautical Science & Aerospace Research*, Vol. 2, No. 6, 2015, pp. 65–80.
<https://doi.org/10.19070/2470-4415-150008>
- [13] Chaudhuri, A., and Hadjadj, A., "Numerical Investigations of Transient Nozzle Flow Separation," *Aerospace Science and Technology*, Vol. 53, June 2016, pp. 10–21.
<https://doi.org/10.1016/j.ast.2016.03.006>
- [14] Ganapathisubramani, B., Clemens, N. T., and Dolling, D. S., "Effects of Upstream Boundary Layer on the Unsteadiness of Shock-Induced Separation," *Journal of Fluid Mechanics*, Vol. 585, Aug. 2007, pp. 369–394.
<https://doi.org/10.1017/S0022112007006799>
- [15] Zaman, K., Dahl, M. D., Bencic, T. J., and Loh, C. Y., "Investigation of a Transonic Resonance with Convergent–Divergent Nozzles," *Journal of Fluid Mechanics*, Vol. 463, July 2002, pp. 313–343.
<https://doi.org/10.1017/S0022112002008819>
- [16] Touber, E., and Sandham, N. D., "Large-Eddy Simulation of Low-Frequency Unsteadiness in a Turbulent Shock-Induced Separation Bubble," *Theoretical and Computational Fluid Dynamics*, Vol. 23, No. 2, 2009, pp. 79–107.
<https://doi.org/10.1007/s00162-009-0103-z>
- [17] Bruce, P. J. K., and Babinsky, H., "Unsteady Shock Wave Dynamics," *Journal of Fluid Mechanics*, Vol. 603, May 2008, pp. 463–473.
<https://doi.org/10.1017/S0022112008001195>
- [18] Martelli, E., Ciottoli, P. P., Saccoccio, L., Nasuti, F., Valorani, M., and Bernardini, M., "Characterization of Unsteadiness in an Overexpanded Planar Nozzle," *AIAA Journal*, Vol. 57, No. 1, 2019, pp. 239–251.
<https://doi.org/10.2514/1.J057162>
- [19] Lilly, D. K., "A Proposed Modification of the Germano Subgrid-Scale Closure Method," *Physics of Fluids*, Vol. A4, No. 3, 1992, pp. 633–635.
<https://doi.org/10.1063/1.858280>
- [20] Moin, P., Squires, K., Cabot, W., and Lee, S., "A Dynamic Subgrid-Scale Model for Compressible Turbulence and Scalar Transport," *Physics of Fluids*, Vol. 3, No. 11, 1991, pp. 2746–2757.
<https://doi.org/10.1063/1.858164>
- [21] Germano, M., Piomelli, U., Moin, P., and Cabot, W. H., "A Dynamic Subgrid-Scale Eddy Viscosity Model," *Physics of Fluids*, Vol. 3, No. 7, 1991, pp. 1760–1765.
<https://doi.org/10.1063/1.857955>
- [22] Kawai, S., and Larsson, J., "Wall-Modeling in Large Eddy Simulation: Length Scales, Grid Resolution, and Accuracy," *Physics of Fluids*, Vol. 24, No. 1, 2012, Paper 015105.
<https://doi.org/10.1063/1.3678331>
- [23] Duprat, C., Balarac, G., Métais, O., Congedo, P. M., and Brugière, O., "A Wall-Layer Model for Large-Eddy Simulations of Turbulent Flows with/out Pressure Gradient," *Physics of Fluids*, Vol. 23, No. 1, 2011, Paper 015101.
<https://doi.org/10.1063/1.3529358>
- [24] Manhart, M., Peller, N., and Brun, C., "Near-Wall Scaling for Turbulent Boundary Layers with Adverse Pressure Gradient," *Theoretical and Computational Fluid Dynamics*, Vol. 22, Nos. 3–4, 2008, pp. 243–260.
<https://doi.org/10.1007/s00162-007-0055-0>
- [25] Pirozzoli, S., Grasso, F., and Gatski, T. B., "Direct Numerical Simulation and Analysis of a Spatially Evolving Supersonic Turbulent Boundary Layer at $M = 2.25$," *Physics of Fluids*, Vol. 16, No. 3, 2004, pp. 530–545.
<https://doi.org/10.1063/1.1637604>
- [26] Piquet, A., "Physical Analysis and Numerical Simulation of the Separation Phenomenon in Over-Expanded Nozzle Flow," Ph.D. Thesis, Normandie Université, Rouen, France, 2017.
- [27] Deng, X., and Zhang, H., "Developing High-Order Weighted Compact Nonlinear Schemes," *Journal of Computational Physics*, Vol. 165, No. 1, 2006, pp. 22–44.
<https://doi.org/10.1006/jcph.2000.6594>
- [28] Xie, Z. T., and Castro, I. P., "Efficient Generation of Inflow Conditions for Large Eddy Simulation of Street-Scale Flows," *Turbulence & Combustion*, Vol. 81, No. 3, 2008, pp. 449–470.
<https://doi.org/10.1007/s10494-008-9151-5>
- [29] Poinot, T. J., and Lele, S., "Boundary Conditions for Direct Simulations of Compressible Viscous Flows," *Journal of Computational Physics*, Vol. 101, No. 1, 1992, pp. 104–129.
[https://doi.org/10.1016/0021-9991\(92\)90046-2](https://doi.org/10.1016/0021-9991(92)90046-2)
- [30] Simon, F., Deck, S., Guillen, P., Sagaut, P., and Merlen, A., "Numerical Simulation of the Compressible Mixing Layer Past an Axisymmetric Trailing Edge," *Journal of Fluid Mechanics*, Vol. 591, Nov. 2007, pp. 215–253.
<https://doi.org/10.1017/S0022112007008129>
- [31] Kutz, J. N., Xing, F., and Brunton, S. L., "Multiresolution Dynamic Mode Decomposition," *SIAM Journal on Applied Dynamical Systems*, Vol. 15, No. 2, 2016, pp. 713–735.
<https://doi.org/10.1137/15M1023543>

D. Papamoschou
Associate Editor

Low-frequency phenomena in supersonic planar nozzle

Physics of Fluids (under consideration for publication).

Highlights

- More pronounced low-frequency shock oscillations, observed in the case of large-asymmetric λ -shock, are related to the successive contractions and dilatations of the large-opened separated bubble.
- For a wide range of nozzle pressure ratios, it was shown that the timescales of the low-frequency oscillations are strongly correlated to the amount of the reversal flow inside the separation bubble.
- A new formula is proposed to predict the main tones with a reasonable accuracy.

NPR	\bar{x}_s/δ_i	$Max(\frac{\Delta(\bar{x}_s)}{\delta_i})$	\bar{u}_s	Measured main tone	Calculated main tone
1.4	25.95	4.00	55.35	0.00152	0.00167
1.5	26.38	7.56	56.39	0.00196	0.00186
1.6	30.09	8.53	64.61	0.00235	0.00224
1.7	33.44	8.40	72.05	0.00275	0.00259
1.8	37.19	6.83	80.41	0.00308	0.00297
2.5	53.60	3.00	103.15	0.00438	0.00433

Summary of different test cases with a comparison between the measured main-tone Strouhal number and those calculated using the presented formula.

Abstract

Very-long LES runs were conducted to demonstrate the existence of energetic broadband low-frequency shock oscillation (LFO). The absence of any particular upstream low-frequency forcing was evidenced and it was explicitly shown that the observed low-frequency shock oscillations were not related to the incoming boundary layer. This led to conclude that the low frequencies found are likely to be due to the downstream condition. The timescales involved in such a mechanism were shown to be about two orders of magnitude larger than the timescales involved in the boundary-layer turbulence. Furthermore, for large interval of nozzle pressure ratio (NPR), those timescales were shown to be strongly correlated with the amount of reversed flow inside the separation bubble. A parametric study was conducted in order to study the effect of increasing the NPR on the LFO. In the light of this study, six different NPRs were used leading to distinguish three different kinds of separation according to the form of the recirculation bubble and with three different mechanisms. From a qualitative stand point, a description of the shock motion is given and an empirical formula based on the one of Zaman (1991) is given. The formula predicts quite well the main tones with a small rate of error.

5.1 Introduction

When starting a rocket engine on the ground, the chamber pressure is not high enough for the flow to be supersonic in all the nozzle: the latter is recompressed through a shock wave so to adapt to external pressure. This recompression is accompanied by a separation and a loss of symmetry which generates lateral forces. This phenomenon, already observed on several real engines, can have serious consequences linked to its random nature. The shock-induced boundary-layer separation, frequently found in over-expanded nozzle flows, causes significant drawback on the aerodynamic performance. This unsteady phenomenon is associated with more undesirable effects such as; shock oscillations, wall-pressure fluctuations, boundary-layer separation and vortex shedding, mainly leading to vibration, noise and side-loads generations. The side-loads can cause deformations of the nozzle and movements relative to its attachment system. The constraints generated by these efforts, unsteady in module and direction, are likely to be amplified by the dynamic effects. They, therefore, constitute a constraining factor in the design of the structure of the nozzle since they require having thicker nozzles, therefore heavier or shorter, which entails a reduction in the payload transported. Comprehensive reviews of the topic can be found in [Hadjadj & Onofri \(2009\)](#). Several models have been proposed in the literature to define the source of the LFO. First, the researchers looked to the upstream boundary

layer as an obvious source of the LFO, however, it was very difficult for them to reconcile the low frequency of the shock with the high frequency of the incoming boundary layer. To overcome these difficulties, the researchers assumed that the time scale of the incoming velocity fluctuations is much smaller than the shock motion (since the shock speed is generally of the order of 3%). Thus, the link is established and the LFO could be a result of the high-frequency incoming boundary layer [Beresh et al. \(2002\)](#). This was the case of [Plotkin \(1975\)](#)'s model which assumes that the shock is convected by the velocity fluctuations of the incoming boundary layer while the stability of the mean flow ensures the shock's mean location. [Poggie & Smits \(2001\)](#) confirmed the previous findings except for the regions facing low-frequency pressure fluctuations where the turbulent eddy time scale is less likely to be smaller than the shock motion. Further results from [Erengil & Dolling \(1993\)](#) highlighted two possible reasons for the shock-foot motion. First, the upstream boundary layer which causes a high-frequency smaller-scale motion and second, the large-scale pulsations of the separation bubble which induces large-scale motions of the separation shock foot. Another factor that may be considered is the thickening/thinning motion of the incoming boundary layer as found by [Beresh et al. \(2002\)](#), [McClure \(1992\)](#) and [Gramann & Dolling \(1992\)](#). The last possible reason to be reported was proposed by [Ganapathisubramani et al. \(2007\)](#). The authors affirmed that the separation line oscillates in a response to the upstream superstructures found in the incoming boundary layer. That was said for the upstream models. Recently, many studies ([Piponniau et al. 2009](#), [Pirozzoli 2010](#), [Dupont et al. 2005](#), [Clemens & Narayanaswamy 2014](#), [Martelli et al. 2019](#), [Olson & Lele 2011](#), [Zebiri et al. 2020](#)) believe that the plausible model is that the interaction responds as a dynamical system forced by the downstream disturbance including recirculation bubbles, shear layer, acoustic feedback or effective geometry. [Pirozzoli \(2010\)](#) conducted a DNS of a $Ma = 2.25$ impinging shock interaction in which he evoked the existence of an acoustic feedback mechanism playing an important role in driving these low-frequency motions. [Touber & Sandham \(2011\)](#) conducted LES of impinging SBLI reporting the absence of the superstructure found by [Ganapathisubramani et al. \(2007\)](#) while the low-frequency motion still exists. Their observations led to establish the minor role of these superstructures in deriving low-frequency motion. Hence, they referred to the instability of the separation bubble to explain that kind of motion precisising the nature of the mode leading to low-frequency motion as global and stationary. Confirming the previous results, [Dupont et al. \(2005\)](#) found that the separation bubble and the separation shock oscillate as a quasi-linear system. A different model has been suggested by [Piponniau et al. \(2009\)](#) in which they consider the observed LFO as the main result of the mass entrainment across the mixing layer zone. They also suggested that there is a direct link between the Kelvin-Helmholtz convective structures

and the low-frequency motion. Prièbe & Martin (2012) found that the low-frequency dynamics of the flow could be driven by the low-frequency variations of the shear layer. Recent studies of Agostini et al. (2012) and Chen et al. (1994) confirmed the implication of the recirculation bubble in the low-frequency motion generation in one hand. In the other hand, they exclude the white noise to be a possible source of these low-frequency motions. Hence, a multitude of additional insights into the possible mechanisms generating the low-frequency motions, may be gained from the literature. Nevertheless, the unsteady flow behavior conveyed by the SBLI is still not fully understood, remaining a challenging research problem. Additional difficulties can be faced when studying this kind of problem. For instance, when the incoming boundary layer is turbulent the flow usually exhibits higher low-frequency shock motions which are less coupled from the timescales of the incoming turbulence. This situation is more challenging from a computational point of view due to the need to obtain longer time series to resolve the low-frequency motions Toubert (2010). Based on the above state-of-art survey, further studies are believed to be appropriate, in particular, to enlarge the limited information about the mechanism in which occur these LFO and to understand the influence of downstream parameters. Hence, we believe that very long WM-LES based analysis can help achieving improved physical understanding of such phenomenon. Hence, through the WM-LES we will try to answer the numerous questions concerning, in particular, the different mechanisms leading to LFOs. Thus, we mainly focus on the effect of the recirculation bubble, its size, its position and its placement in the generation of LFOs. In addition, we study the shock movement, trying to elucidate the way it moves. Finally, we try to formulate its movement empirically in order to calculate a simple element that is the main tone. The latter represents one of the element that we aim at their formulation with the future goal of realizing a simple model for LFOs. The present chapter is organized as follows. The next section introduces the computational strategy and domain followed by the results and the discussion. Finally, a conclusion is drawn at the end of this chapter.

5.1.1 Computational strategy and domain

The curvilinear solver used for the present analysis is the same as that used in both Piquet et al. (2019), Zebiri et al. (2020). For instance, three-dimensional Navier-Stokes equations are solved with a molecular viscosity μ assumed to follow Sutherland's law. The thermal conductivity k is related to μ through $k = C_p \mu / Pr$ with $Pr=0.72$. The convective fluxes are discretized using sixth-order central scheme for smoothed parts and fifth-order Weighted-Compact-Non-Oscillatory (WCNS) for shocked regions, with a shock sensor controlling the switch between the two. Time advancement is ensured using forth-order Runge-Kutta algorithm (RK4). Then the wall is modeled using the wall model of Piquet

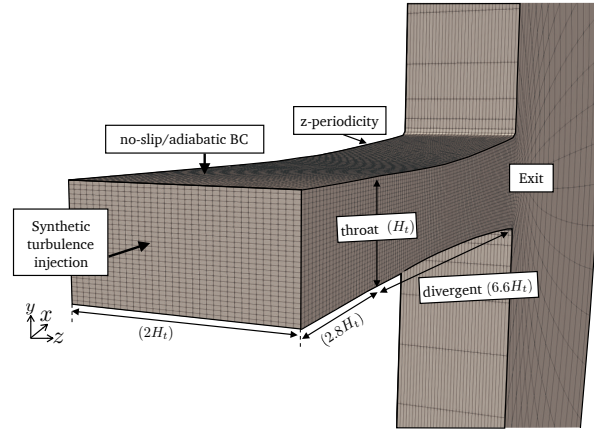


Figure 5.1: Grid representation of the wall-modeled nozzle test-case showing every 5th grid-line. For this WM-LES, the grid is regularly spaced following, $f_{str,y} = (2\eta/N_y - 1)$ with η is the generalized curvilinear coordinate in wall-normal direction. The nozzle throat is located at $x = 0$.

Piquet (2017). The computation mesh, shown in figure 5.1, is generated by mapping a single structured curvilinear mesh. For this purpose, $(C - 2)$ class functions were used to ensure the continuity and the differentiability of these functions in order to avoid the singular points resulting when resolving Navier-Stokes equations. Outside the nozzle, the mesh diverges and grows to form a background mesh that models the conditions of a far-field of the experience and to create a spongy zone to prevent/reduce the intensity of the reflected waves. The grid is exponentially stretched in the vicinity of the divergent to capture the physical phenomena. Further details about the computational domain, the initial and limit boundary conditions can be found in Zebiri et al. (2020).

5.2 Results and discussion

The present LES attempts to reproduce the experimental results of Papamoschou et al. (2009) and the numerical results of Olson (2012) and of Piquet (2017). Olson (2012) performed WR-LES in which he showed the effects of the grid convergence while Piquet (2017) followed the guidelines of Olson study. To reduce the computational cost, Piquet (2017) performed a WM-LES simulation based on the results of his previous WR-LES, where no grid convergence was found. Estimated as necessary and in order to establish the fidelity of the LES database, a grid convergence study is conducted here in order to highlight the effect of the mesh refinement in streamwise and spanwise directions. Table 5.1 shows the overall grid size of the three meshes.

It is important to accurately capture the boundary layer as its interaction with the shock is driving the large-scale instability. Nevertheless in the present case, we can't

Table 5.1: grid parameters

	N_x	N_y	N_z	Nb cells
Mesh-A	672	128	160	13.7M
Mesh-B	750	128	160	15.4M
Mesh-C	750	128	190	18.3M

compare the Van Driest transformed mean velocity profiles and the fluctuating velocities, near the wall, with what was done by [Piquet \(2017\)](#) and [Olson \(2012\)](#) because we do not resolve the BL but we use a wall model instead. Therefore, we compare the mean profiles of pressure, the shock-position probability-density function (PDF) and the spectral content of the shock-position.

5.2.1 Validation

Normalized mean wall pressure is shown in figure [5.2a](#). It is speculated that the wall-pressure evolution would be closer to the experimental findings of [Papamoschou et al. \(2009\)](#) as shown on the figure. It can be seen that the WM-LES predicts quite well the static pressure in both attached and separated zones. Although a pressure plateau can be observed in the WM-LES data towards the recovery zone, as a consequence of the compression waves observed in the wall-modeled case, which does not coalesce within the viscous sublayer because of the low resolution close to the wall $\Delta y^+ \sim 45$. As explained by [Chapman et al. \(1958\)](#) in the free-interaction theory, the separation length L_s reduces linearly with the displacement thickness, which is the case in the present WM-LES due to the unresolved part of the boundary layer. In fact, separation occurs when the viscous sublayer cannot sustain the strong adverse pressure gradient imposed by the inviscid flow. Removing the viscous sublayer of the incoming boundary layer results in stronger compression waves that collapse rapidly into a strong separation shock which forms a lambda shock pattern. From figure [5.2a](#), it is seen that varying the grid resolution does not produce significant differences in the wall pressure before the separation and in the shocked region. Therefore, we consider that the grid resolution of mesh-A is sufficiently fine to only have marginal effects on the statistical results.

The shock-position probability-density functions are computed and shown in figure [5.2b](#). The PDF of both the experimental ([Papamoschou et al. 2009](#)) and the present numerical shock-positions are found to agree unmistakably well. Interestingly, they both seem to match a Gaussian-like distribution which proves the accurate amplitude of the shock excursion captured by the present WM-LES compared to the WR-LES of [Olson & Lele \(2013\)](#). A comparison based on the spectral content of the shock-position is given

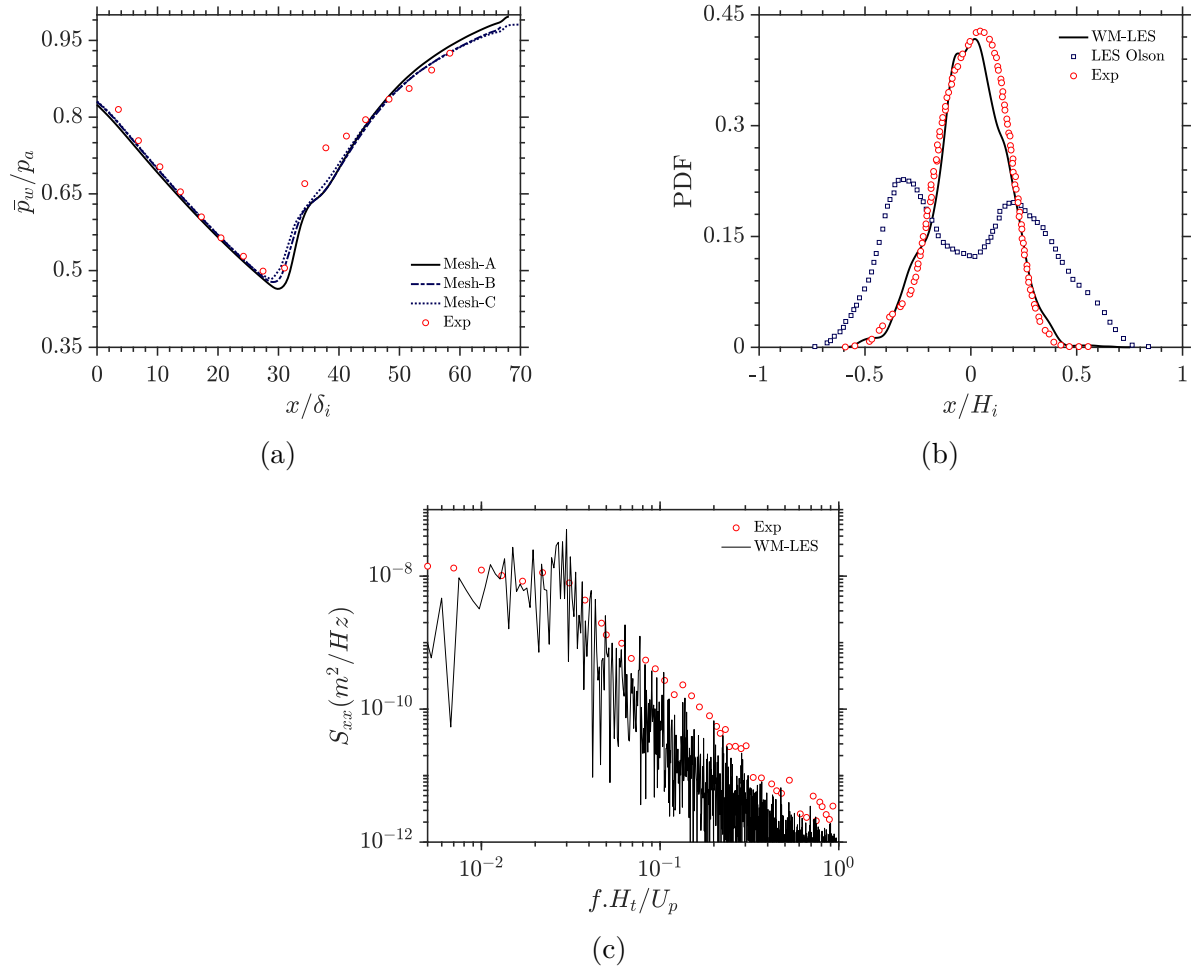


Figure 5.2: (a) Normalized mean wall pressure; (\circ): experimental results Papamoschou et al. (2009), (b) Probability density function (PDF) of the shock position; (—) : present LES, (\circ): experimental results Papamoschou et al. (2009), (\square): previous LES Olson & Lele (2013). (c) Cross power spectral density of the normalized shock position; (\circ): experimental results Johnson & Papamoschou (2010)

in figure 5.2c. The numerical results of the present WM-LES share similar low-frequency dynamics with the experimental results. With the success in reproducing the nozzle flow, LES are found capable of accurately reproducing the low-frequency shock motions.

5.2.2 The inlet influence

A preliminary check is necessary to verify the emptiness of the incoming boundary layer from the low frequencies. To be more convinced of the absence of upstream low frequencies, one can develop the time history of the velocity fluctuations seen along a line-probe just before the throat position, as shown in figure 5.3a, where time is converted into space assuming the fluctuations are convected at the local mean velocity, as in figure 4 in Ganapathisubramani et al. (2007) (Taylor's hypothesis) and in figure 6.9 in Toubert

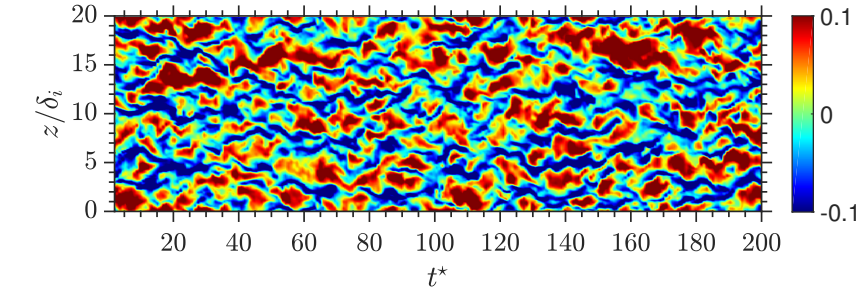
& Sandham (2011). Once inside the computational domain, one can see that structures up to $40\delta_i$ long may develop. Using the scaling argument of Ganapathisubramani et al. (2007), one would thus need to have $120\delta_i$ -long superstructures in the LES to explain the observed energetic low-frequency oscillations. This is nearly three times the size of the longest structures present in this LES, making the incoming superstructures an improbable origin for the observed low-frequency. This does not mean that long coherent upstream disturbances are not important when present in practical applications but they are not found to be necessary to observe the low-frequency shock motions as explained by Toubert (2010). Having established the absence of low frequencies in the incoming boundary layer, we proceed to study the different aspect of this flow.

The autocorrelation functions $R_{\varphi'\varphi'} = \frac{R_{\varphi'(t_0),\varphi'(t_0+\Delta t)}}{R_{\varphi'(t_0),\varphi'(t_0)}}$, is computed and averaged over time for 2 x -locations, obtained from the previous signal (u') recorded at the wall ($z/\delta_i = 10$), were computed and are provided in figure 5.3b. High levels of correlations are noticed over a time lag of $t^* = 10$. The correlation function is seen to drop to zero in about 10 boundary-layer thickness ($10\delta_i$). Furthermore, the correlation function remains at zero for large time intervals leading to conclude that no cyclic patterns have been enforced at the inlet as explained Toubert (2010). The shape of the autocorrelation function is of particular interest. No wavy structures with clear local maxima and minima are found, this indicates that the shock motions are broadband and not made of harmonic motions, also it shows that the LES is well converged at low frequencies.

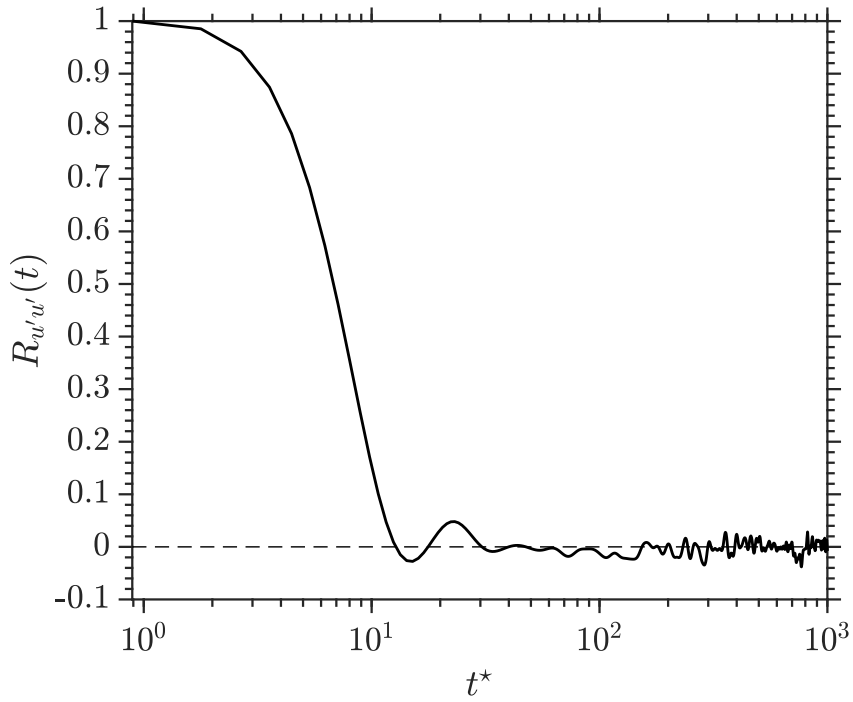
5.2.3 Wall pressure fluctuations

As known, the low-frequency pressure fluctuations near the shock foot are broadband in nature. This implies that in order to guarantee the convergence of the spectral-analysis results, one must capture several times the most significant period. Although the term several times is relatively vague, we suggest that covering about 50 cycles can give a good estimate Toubert & Sandham (2011).

The wall-pressure signals were recorded at the lower wall. At each probe, the normalized autocorrelation was computed to obtain the autocorrelation maps shown in figure 5.4. A clear band with large-scale black and white structures, corresponding to high levels of correlation over large time lags, are noticed for the three NPRs. These large-scale structures start from the mean separation location for each NPR, and to extend until the exit in the case of $NPR = 1.7$. A different configuration is noticed for the two other NPRs, where the large-scale structures collapse just after the separation location. The streaky structures seen afterward correspond to a richer/higher-frequency phenomena resulting from the reattached boundary layer in the case of $NPR = 1.4$ and from the mixing layer



(a)



(b)

Figure 5.3: (a) Reconstructed u'/u_∞ field from a prob located at $x/\delta_i = -4$ and $y/\delta_i = 0.78$. (b) Normalized streamwise-velocity fluctuation (u') autocorrelation at $y/\delta_i = -0.78$ and $z/\delta_i = 10$

in the case of $NPR = 2.5$. This implies that the low-frequency motions are less present upstream of the separation location and more energetic in the separated region. Furthermore, the fact that the large black and white bands, existing only downstream the mean separation location, suggests that the source of the low-frequency is far to be upstream of the separation. This is consistent with many previous findings like [Touber & Sandham \(2011\)](#), [Dussauge & Piponnier \(2008\)](#), [Dupont et al. \(2005\)](#), where low-frequency wall-pressure fluctuations were shown to originate downstream the separation.

The large bands are composed of two parts with small strangulation, clearly seen in the figure, that separates the two regions. Where, the first region corresponds to the movement of the shock often begins before the upstream-mean limit of the recirculation bubble, while the second part corresponds to the recirculation bubbles. The low frequencies spacial extension differs from one NPR to another because of the remarkable difference in the size of the recirculation bubbles, as shown in [Figure 5.5](#). It can also be noticed that the nozzle exit is entirely dominated by high frequencies phenomena, except for $NPR = 1.7$, where a large recirculation bubble opened to the ambient dominates the entire distance between the separation position and the exit of the nozzle. For the upper wall of the same NPR, the bubble closes before the exit which frees the way in front of the high frequency phenomena to manifest towards the exit of the nozzle. Nevertheless, the frequencies of these phenomena are still low compared to the frequency of the turbulent boundary layer which is the case for all the phenomena behind the closed recirculation bubble. (see figures [5.4a, 5.4f](#)).

[Figure 5.6](#) was obtained from the high-spatial/high-temporal resolution pressure field at the wall. A reference point is chosen inside the incoming boundary layer and centered at the separation region. The two-point correlations function in space and time is computed by,

$$R_{\varphi'\varphi'} = \frac{\overline{R_{\varphi'(x_0, t_0), \varphi'(x_0 + \Delta x, t_0 + \Delta t)}}}{\overline{R_{\varphi'(x_0, t_0), \varphi'(x_0, t_0)}}} \quad (5.1)$$

where $\varphi = p'/p_{rms}$ and x_0 is the centered location according to each figure.

In the separation region, when looking more closely at the positive wave region of both figures ([5.6a](#) and [5.6b](#)), a mild ridge corresponding to positive waves propagating at the velocity of c_w seems to emerge. This ridge is related to the acoustic wave traveling outside of the boundary layer. For the three cases, the wall shows the existence of a ridge observed along the convection speed of the mixing layer $u_2 \sim 0.45u_\infty$ corresponding to the development of coherent structures in the shear-layer at the bubble interface. The subsonic acoustic waves $u_\infty - c_w$ seem to be strongly correlated in time for $NPR = 1.7$. This behavior validates the assumption made by many ([Bogar et al. 1983](#), [Johnson & Papamoschou 2010](#), [Olson & Lele 2013](#)) on the two-way coupling between the shock and

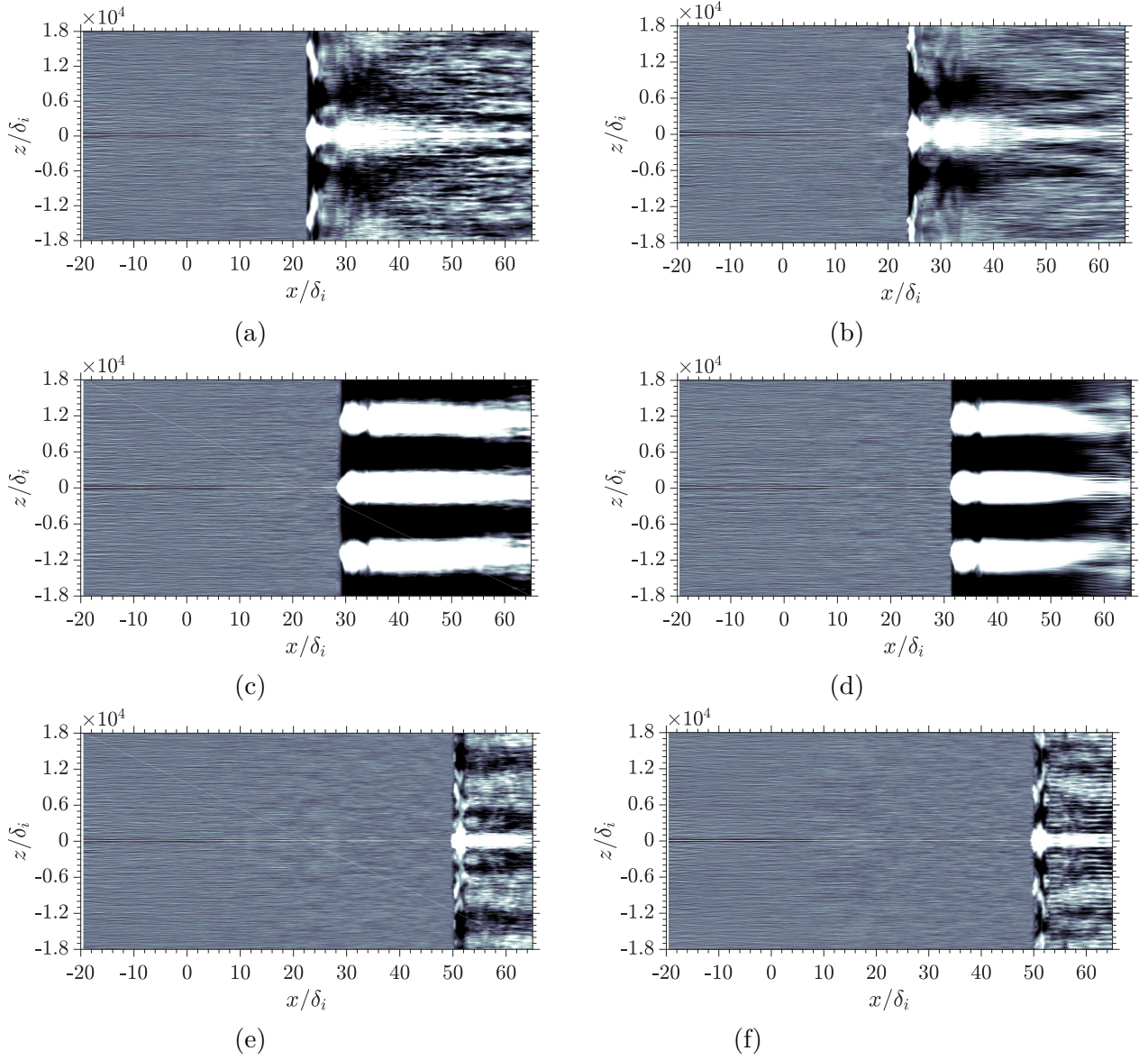


Figure 5.4: Wall-pressure autocorrelation functions, as a function of streamwise location for different NPRs; (a, b): NPR=1.4 lower and upper wall respectively, (c, d): NPR=1.7 lower and upper wall respectively, (e, f): NPR=2.5 lower and upper wall respectively.

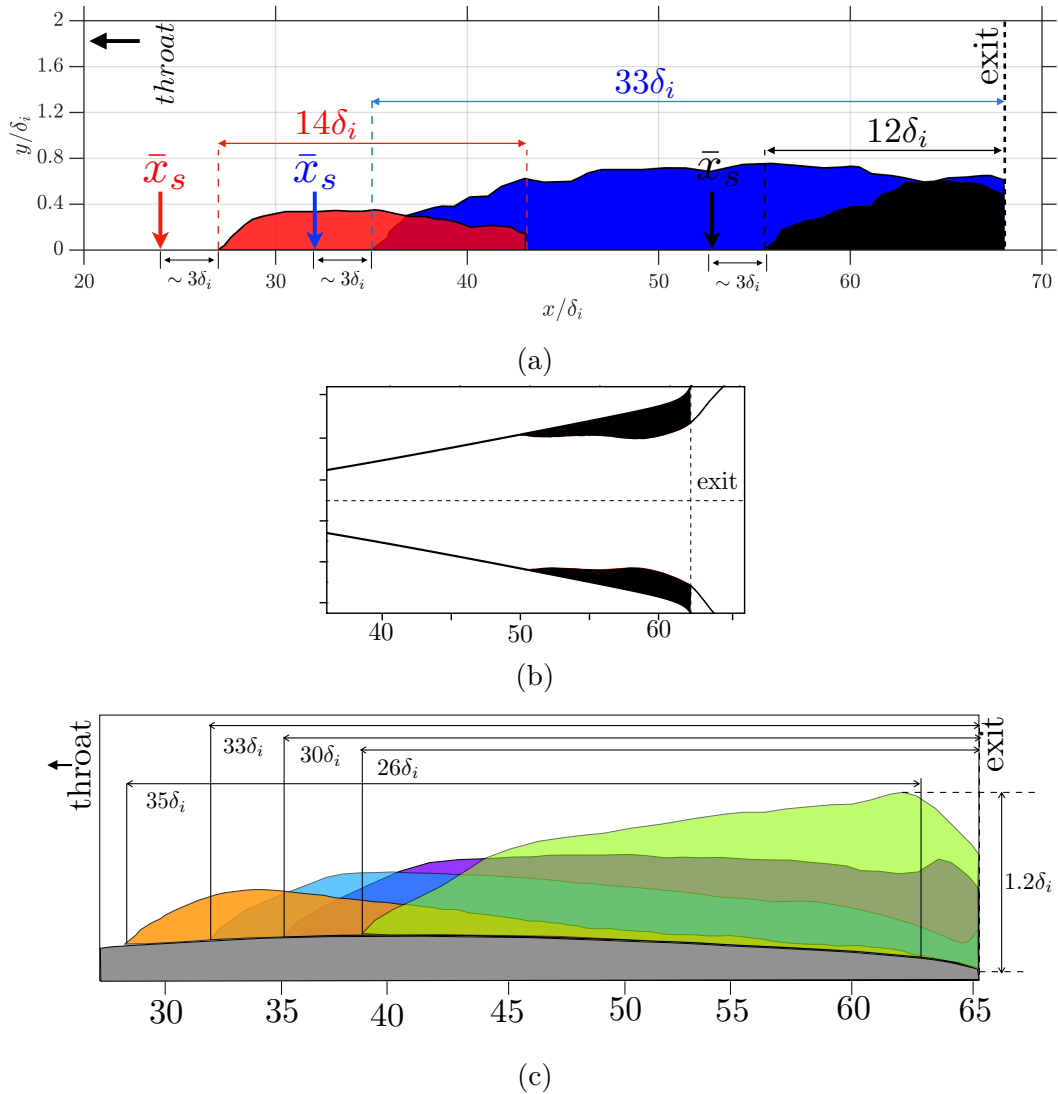


Figure 5.5: (a) Recirculation bubbles at the lower wall for different NPRs; *red*: NPR=1.4, *blue*: NPR=1.7, *black*: NPR=2.5, (b) Recirculation bubbles for NPR=2.5 and (c) Recirculation bubbles at the lower wall for different NPRs; *orange*: NPR=1.5, *sky-blue*: NPR=1.6, *purple*: NPR=1.7 and *green*: NPR=1.8

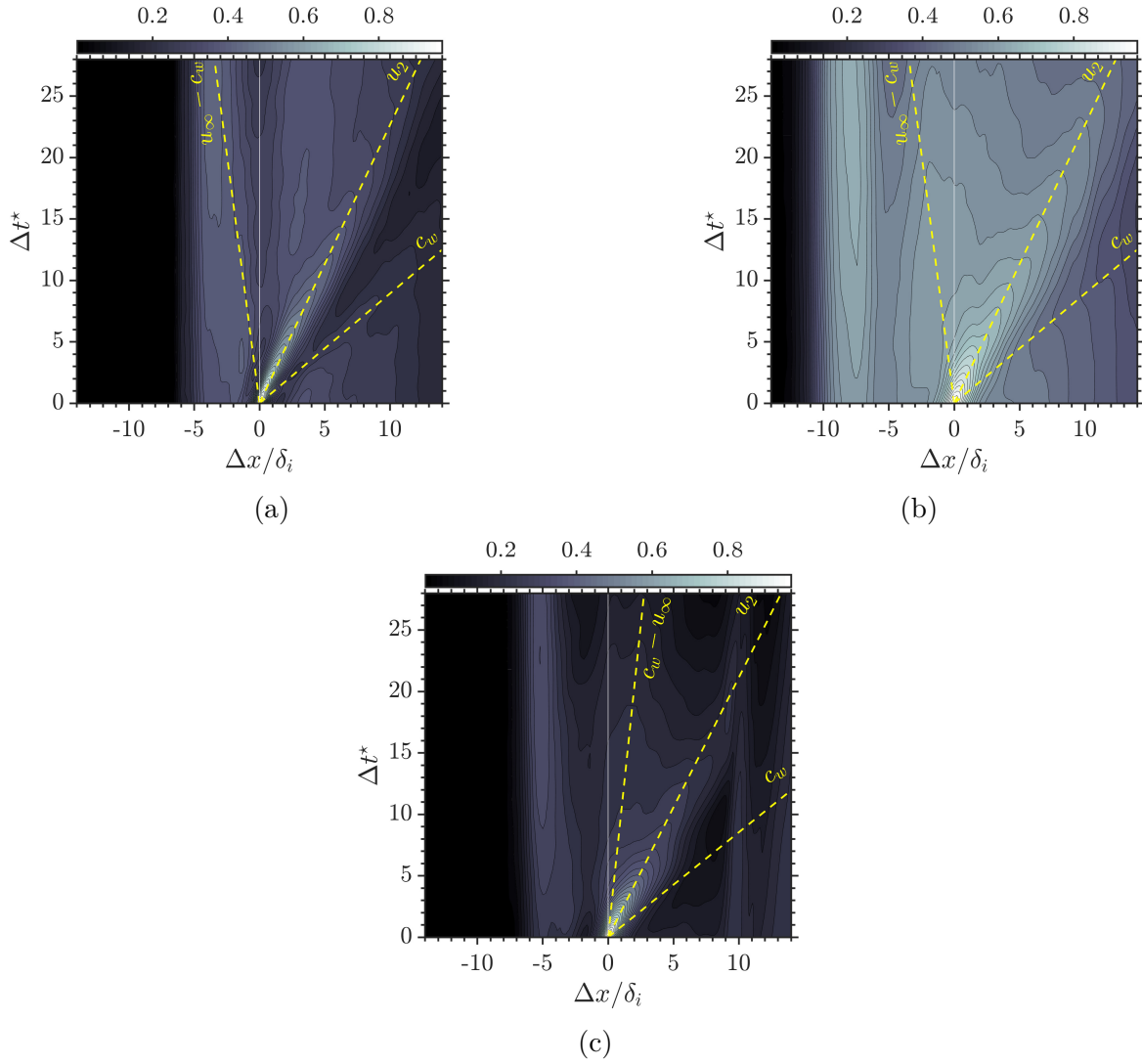


Figure 5.6: Space-time correlation of the normalized pressure field in the separated zone at the separation location for different NPRs; (a): NPR=1.4, (b): NPR=1.7 and (c): NPR=2.5.

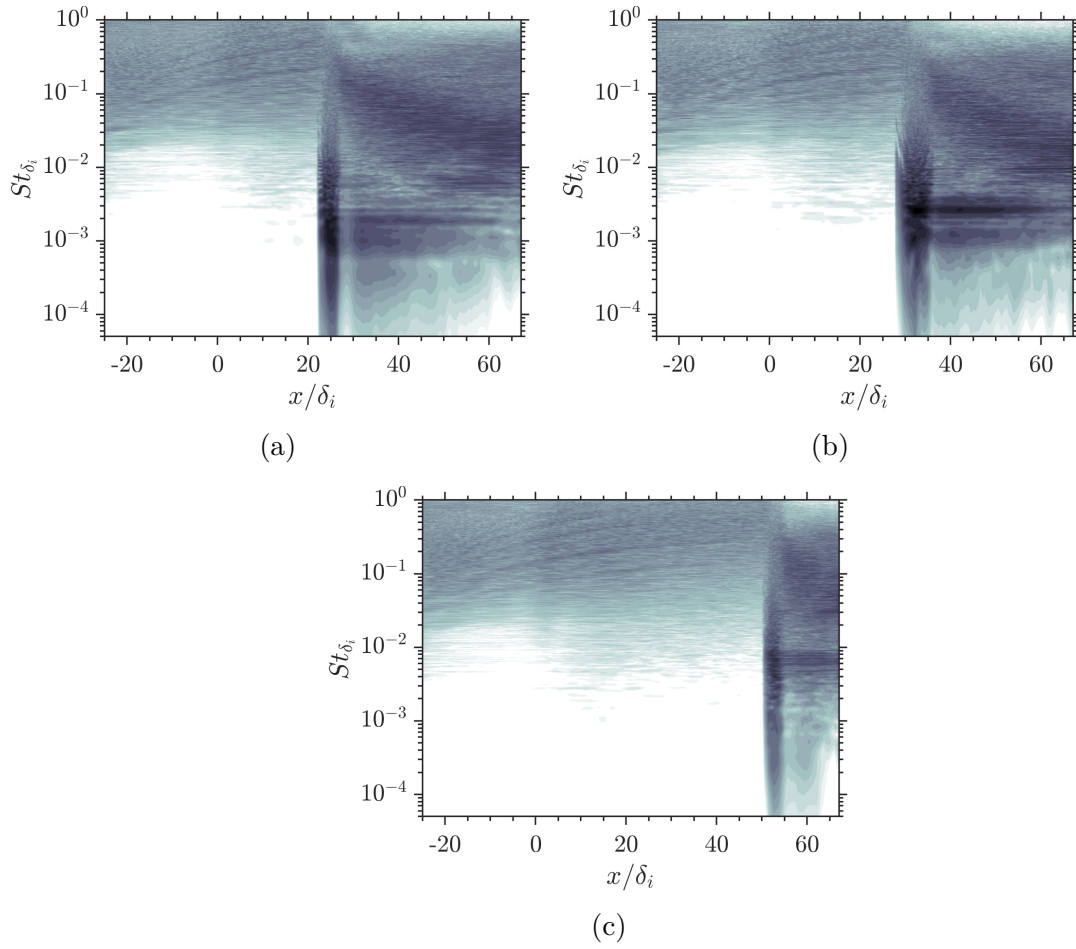


Figure 5.7: Normalized pre-multiplied spectra map of wall-pressure fluctuations $St\mathcal{F}(p/p_{rms})$ at the lower wall, for different NPRs; (a): NPR=1.4, (b): NPR=1.7 and (c): NPR=2.5.

the nozzle exit that leads to the unsteady oscillation of the shock.

Figure 5.7 shows Normalized pre-multiplied spectra map of wall-pressure fluctuations along the streamwise direction. One can notice that the separation region clearly stands out. More precisely, the energetic broadband low-frequency region is very localized near the separation point for the three NPRs. In the remaining part of the separation bubble, the energy is distributed over almost four decades of Strouhal number. Upstream of the separation position, energetic low frequencies are absent whereas high-frequency phenomena can be found leaving a footprint in the spectrum corresponding to the boundary-layer turbulence.

5.2.4 Low-Frequency Oscillations (LFO)

Figure 5.5-a shows three different kind of recirculation bubbles which correspond to three different low-frequency motion behaviors. For low NPRs *i.e.* ($NPR < 1.5$), the recirculation bubble is located upstream far from the outlet of the nozzle, and it is closed, so it communicates very little with the environment. In this situation, the LFO are therefore not mainly governed by the change in the effective geometry of the nozzle resulting from the change in the back flow entering the nozzle. The shock oscillations, in this case, are very limited, they are done at a constant velocity as will be shown later in section 5.2.5. The span of the distance travelled by the shock, during a cycle, is also limited and small (see table 5.2). For $NPR \in [1.5 : 2.3]$, the recirculation bubble takes place in the middle of the divergent and it extends to the exit of the nozzle. In addition, it opens and often communicates with the ambient. The LFO in this case are clear, large and have very low frequency movement. For this case, the LFO are believed to be governed by the changes in the back-flow rate. The amplitude of the oscillations, for this NPR range, is greater being worth of $\sim 8\delta_i$ which is in good agreement with the experiment (Papamoschou et al. 2009) (see table 5.2). A precise explanation seems to be very complicated to give but we can say that having a large recirculation bubble sitting on one side. By sucking and discharging the air, the operation generates a significant change in the size of the bubble and consequently the effective geometry of the nozzle. Last for $NPR \in [2.4 : 2.5]$, the recirculation bubbles are very close to the outlet, open to the ambient all the time. This case is like the first case; fewer oscillations are observed (see table 5.2). This can be explained by the presence of two large bubbles almost identical in the upper and lower walls (see figure 5.5-b). This situation creates a certain balance between the two back flows and causes less change in the symmetry of the nozzle effective geometry. As a result, fewer LFO are noticed. Remains to remember that the jet was quasi-symmetrical in the first and the third case and asymmetrical in the second case.

In what follows, we deeply analyse the second case. To do this, three NPRs in addition

Table 5.2: Summary table of different cases treated.

NPR	\bar{x}_s/δ_i	$Max(\frac{\Delta(\bar{x}_s)}{\delta_i})$	\bar{u}_s	Measured main tone	Calculated main tone
1.4	25.95	4.00	55.35	0.00152	0.00167
1.5	26.38	7.56	56.39	0.00196	0.00186
1.6	30.09	8.53	64.61	0.00235	0.00224
1.7	33.44	8.40	72.05	0.00275	0.00259
1.8	37.19	6.83	80.41	0.00308	0.00297
2.5	53.60	3.00	103.15	0.00438	0.00433

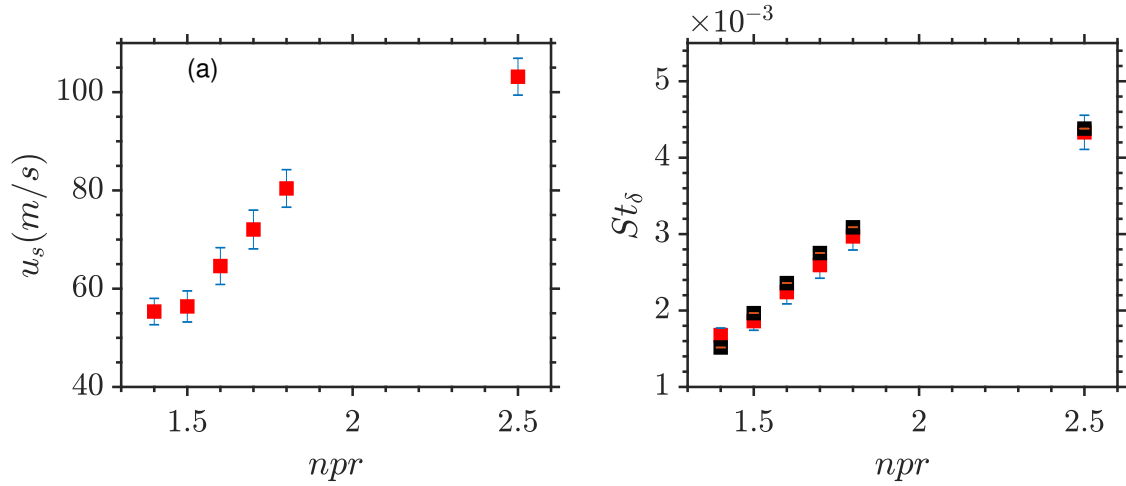


Figure 5.8: (a) Mean shock velocity and (b) Main tone, as a function of the nozzle pressure ratio; (■) theoretical values from Zaman et al. (2002), (■) empirical values.

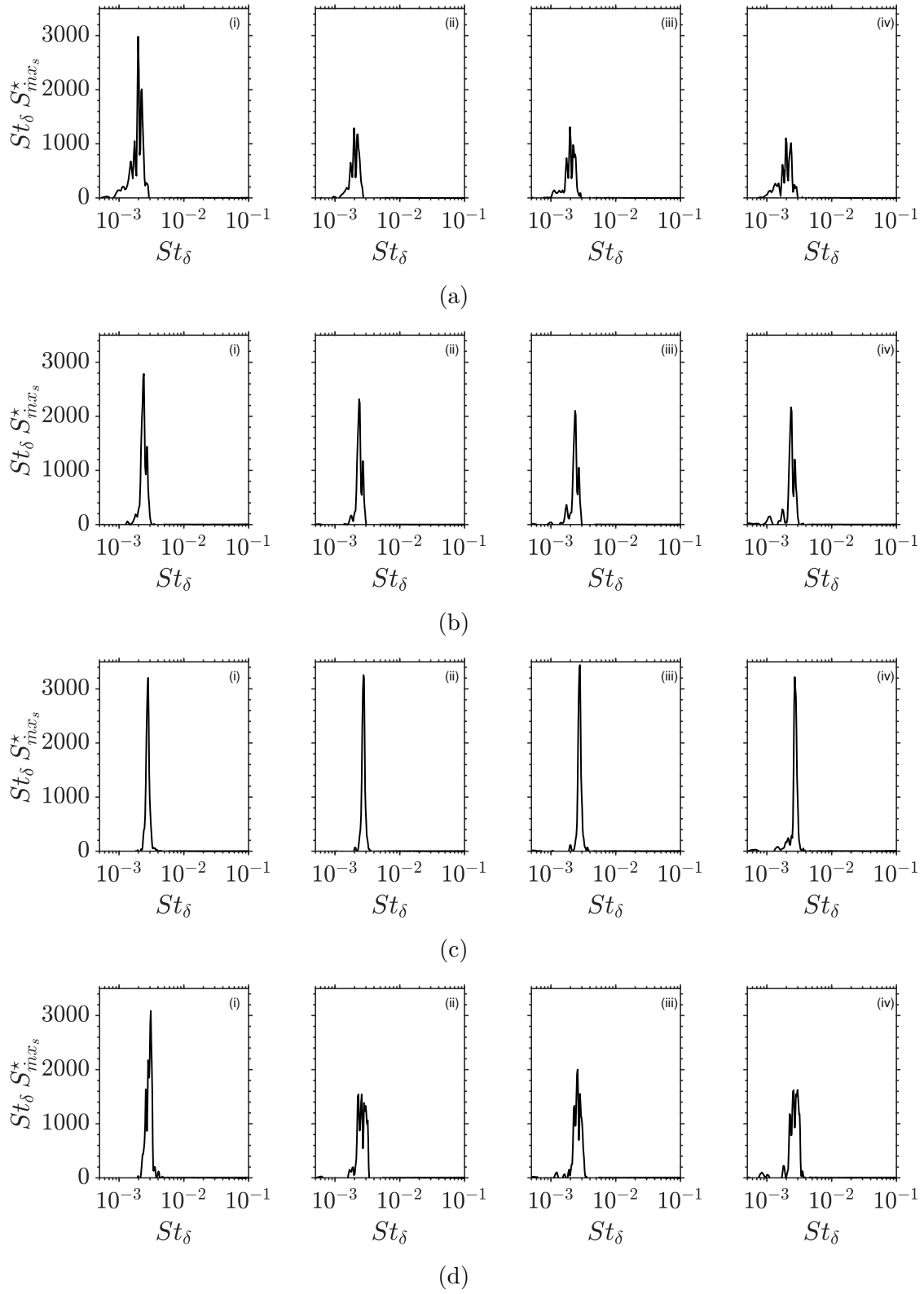


Figure 5.9: Normalized cross power spectral density of the shock position and the entering mass flow rate; (a) NPR=1.5 (b) NPR=1.6 (c) NPR=1.7 (d) NPR=1.8.

to our main case ($\text{NPR} = 1.7$) are developed: 1.5, 1.6 and 1.8. The figure 5.5-c) represents the mean recirculation bubbles. The four bubbles are relatively large, the largest among them is obtained for $\text{NPR} = 1.5$. The latter closes before the nozzle exit while the other bubbles are open to the ambient. The largest of the bubbles opened to the ambient is obtained for $\text{NPR} = 1.6$. At this NPR, the largest amplitude of oscillation is recorded. Afterward, the bubble width necessarily decreases because of the average position of the shock pushed forward by the increase in NPR. On the other hand, the thickness of the bubble increases with the increase in NPR. Concerning the oscillations span shown in the table 5.2, the maximum, as mentioned before, is obtained for $\text{NPR} = 1.6$, the oscillations span tends to decrease and consequently less shock activity is recorded when increasing the NPR. Regarding low frequencies, an increasing trend is noticed for the main tones defined by Zaman et al. (2002) (see table 5.2). This was obvious because the main tone is directly linked to the separation position. In their study, Zaman et al. (2002) proposed a model consisting of a feedback loop within the diverging section of the nozzle. First, they assumed a feedback loop consisting of a disturbance generated near the throat, the disturbance growing (accompanied by the formation of discrete vortices) while propagating downstream the diverging section. Then, an acoustic feedback occurring when the vortex exits the nozzle to generate new disturbance at the throat. After that, they assumed that the disturbance propagates downstream with a convective speed U_c , and the feedback occurs at acoustic speed (through the boundary layer). Thus, they found that the time needed for upstream information transmission through the subsonic zones is given by the relation: $T = L[\frac{1}{U_c} - \frac{1}{c_0}]$ with L is the length of the divergent and c_0 is the celerity of the sound. In this study, we proposed a similar model in which we believe that disturbance is generated near the separation point and the convection speed can be replaced by $(u_\infty - c_{0,w})_s$ with u_∞ defined as the freestream speed and $c_{0,w}$ defined as the celerity of sound at the wall in the separation level. The values of $(u_\infty - c_{0,w})_s$ are given in the table 5.2 for each NPR. These values are used to calculate the main tones, where very good agreement between the theoretical and numerical results is found (see figure 5.8). Still with the aim of revealing the LFO mechanism, we are trying here to find correlations between the shock movements and the various parameters likely to be behind these LFOs. The figure 5.9 shows the normalized cross power spectral density (cpsd) of the position of the shock and the back flow, the whole is plotted for 4 different positions. We note that the oscillations of the shock are very well correlated with the back flow. The degree of correlation varies according to the position and the NPR. The two parameters show some similarities for the low-frequency phenomena more precisely for the main tones obtained for each NPR. This guides us to consider the back flow as a factor very involved in this mechanism. However, a good correlation between the two

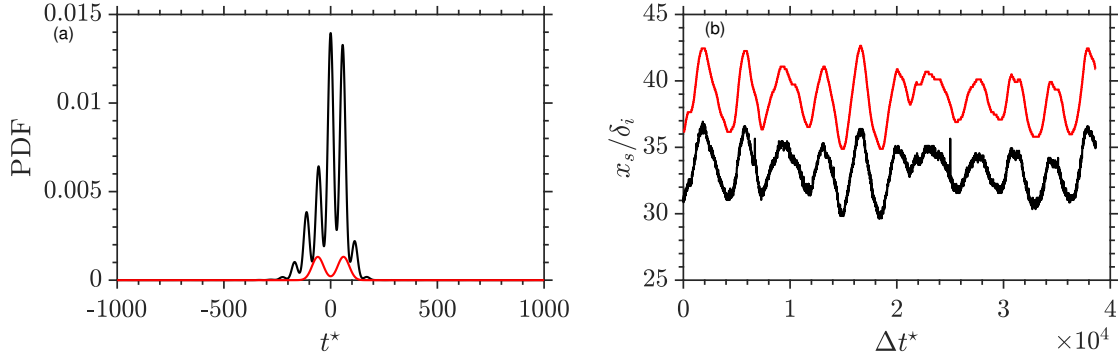


Figure 5.10: (a) Probability density function for the shock velocity; (b) Shock position vs. time; (—) Mach stem, (—) shock foot

parameters does not mean causation that is very difficult to find and there are fewer mathematical tools to verify it.

5.2.5 Shock motion

For the shock movement, a small difference in the way they behave the two parts of the shock, *i.e.* the Mach stem and the shock foot, is noticed. Figure 5.10-a represents the PDF of the shock oscillation. One can noticed that the foot shock is governed by several velocities among them, of course, the speed of the main shock to which is added other velocities related to the location of the shock foot, obviously, they are related to the incoming boundary layer as found by Erengil & Dolling (1993) and also to the mixing layer. It is clear that both of them moves as a response to a low-frequency forcing but it can be noticed that the shock foot movement is accompanied with more high-frequency fluctuations. The figures 5.10-a and 5.11-a clearly show that the Mach stem moves at almost a constant speed in both directions confirming the observation of Gonzalez & Dolling (1993). Further details can be noticed by observing the displacement of the shock. For instance, for the same distance, the Mach stem moves downstream more quickly. This fact can be explained by the way in which this movement is done. Indeed, the shock does not move forward or backward continuously but it pauses and it is this number of pauses, shown in figure 5.11-c as a rate of the time taken by the shock to move upstream/downstream one time. The rate of pauses can vary between the two directions of movement, giving different average velocities (see figure 5.11-b) and thus making one movement faster than the other. Figure 5.11-c shows that the rate of pauses was greater in the upstream movement for ten of eleven oscillations making the shock looking faster when moving downstream.

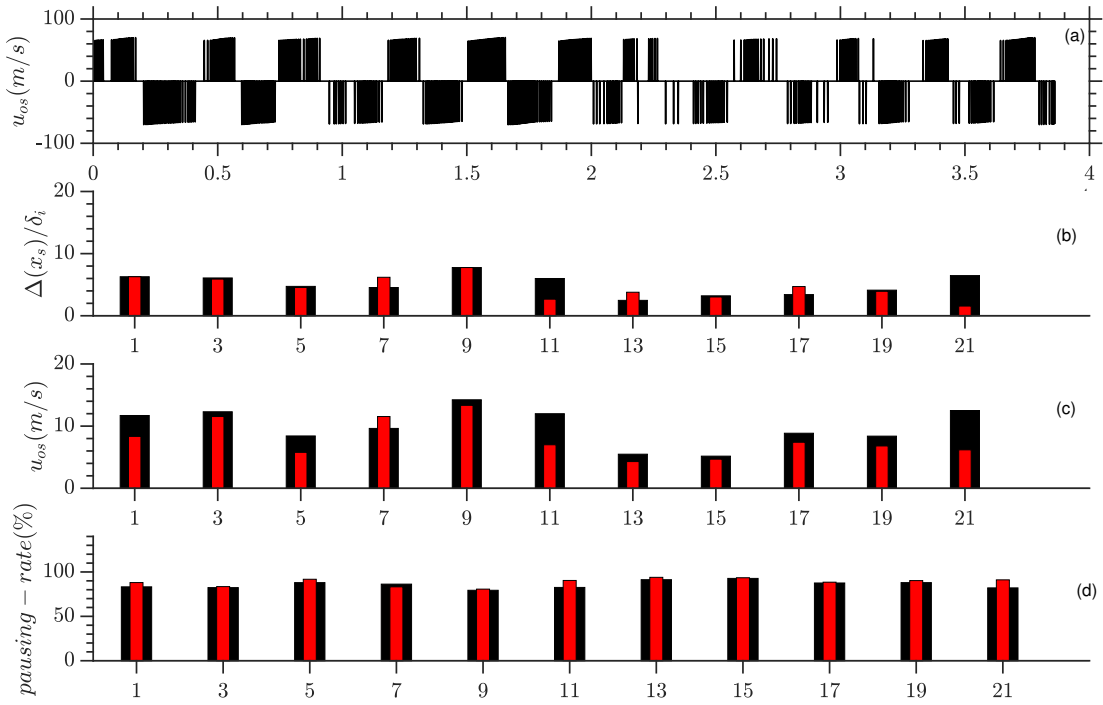


Figure 5.11: (a) Mach stem oscillation velocity vs. time, (b) Averaged Mach stem span by direction by cycle, (c) Mach stem oscillation velocity by direction by cycle and (d) Pausing rate per direction. (■) Upstream-movement, (■) Downstream-movement

5.3 Concluding remarks

The behaviour and the characteristics of the shock induced separation flow in over expanded planar nozzle with a mild divergent angle, has been analyzed by means of very long three-dimensional WM-LES. Detailed flow statistics have been presented, including steady and unsteady parameters. Particular effort has been made to understand the low frequency phenomena occurring inside the nozzle. Consistently with the experiment and the previous numerical simulations, the shock is found to oscillate at a very low frequency. Confirming the previous findings, no low frequencies were captured in the upstream of the separation zone. The present findings lead to consider that the origin of the LFO is the interaction of the downstream conditions. A parametric study was conducted to study the effect of increasing the NPR on the LFO. In the light of this study, the implication of the recirculation bubble in the low-frequency motion generation is proved. Thus, through this study, we have been able to show that the quasi-symmetrical configuration is stable while the asymmetrical configurations are unstable favoring LFOs. Additionally, the reversal flow is found to be well correlated with the LFO leading to consider it as the main factor causing the LFO for this regime. Finally, more light was shed on the shock motion resulting in detailed description of the way in which it moves and an empirical

formula similar to the one proposed by [Zaman et al. \(2002\)](#) was proposed to calculate the main tone.

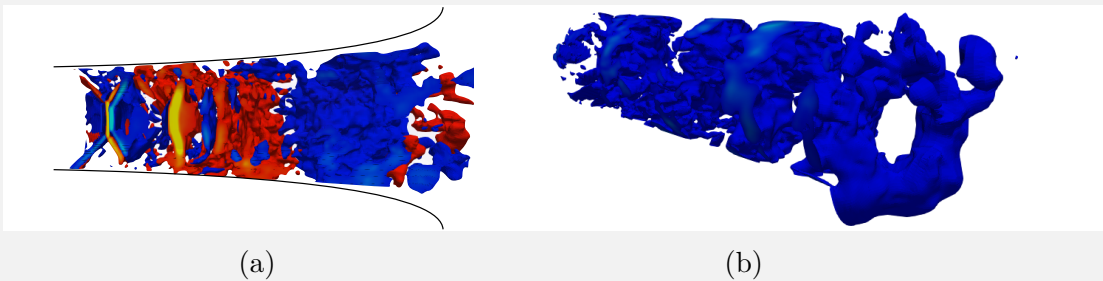
6

Dynamic mode decomposition analysis of shock-wave unsteadiness in conical supersonic nozzles

Aerospace Science and Technology (accepted).

Highlights

- Large-eddy simulations are employed to investigate the 3D unsteady shock-wave boundary-layer interaction.
- Common and distinctive flow features of both conical and planar nozzle flows are highlighted.
- The amplitude of the shock excursion is less pronounced in the conical nozzle compared to the planar case.
- Two main unsteady modes are revealed in conical nozzles; non-helical (low-frequency) and helical (high-frequency) modes.



DMD mode reconstruction; (a) non-helical (b) helical mode in form of the isovolume of the real part with negative and positive pressure fluctuations, p' , for two different frequencies. Red to yellow color indicates positive pressure fluctuations, yellow being the highest. Dark blue to light blue indicates negative pressure fluctuations, light blue being the highest.



Analysis of shock-wave unsteadiness in conical supersonic nozzles

B. Zebiri*, A. Piquet, A. Hadjadj

CORIA-UMR 6614, Normandie University & INSA, Avenue de l'Université, 76000 Rouen, France

ARTICLE INFO

Article history:

Received 5 November 2019
Received in revised form 16 June 2020
Accepted 3 July 2020
Available online 13 July 2020
Communicated by Craig Johansen

Keywords:

Supersonic conical diffuser
Shock unsteadiness
Low-frequency oscillations
Side-loads
Dynamic mode decomposition

ABSTRACT

Large Eddy Simulations (LES) of an over-expanded conical nozzle are performed to study the complex interaction between the turbulent boundary layer, the internal shock wave and the separated mixing layer. Both wall-modeled (WM) and wall-resolved (WR) LES strategies are employed to investigate the three-dimensional unsteady aspect of shock-wave boundary-layer interaction (SWBLI). First, a comparison of flow behavior in a conical nozzle against an equivalent planar nozzle is made. It was found that whilst both configurations may share common flow features such as large-scale turbulent structures and shock-wave patterns, they show contrasts on the symmetry of the flow and the shock dynamics. In particular, the latter was found to have a shorter excursion length in conical nozzle compared to the planar one. The strong adverse pressure gradient tends to reduce the amplitude of the shock movements in conical flows. Additionally, the dynamic mode decomposition (DMD) analysis showed the existence of two unsteady modes; the non-helical modes which are low-frequency based, appearing mainly in the streamwise forces and the helical modes which are high frequency dominated modes and are largely responsible for the side side-loads generation.

© 2020 Elsevier Masson SAS. All rights reserved.

1. Introduction

With the renewed interest in supersonic flights, studying supersonic nozzle flows is becoming of such importance especially for reusable rocket launchers. As a matter of fact, during the take-off and the first phase of flights, the ratio between the atmospheric pressure and the nozzle exit pressure is significantly higher than the nominal ratio. The nozzle then operates in an over-expanded regime. The boundary layer at the wall no longer withstand the adverse pressure gradient and separates from the wall, creating thereby an oblique shock. The distribution of this separation is often random, making the flow asymmetrical and promoting the appearance of lateral (or side) charges. Besides, the fluctuations in the values and directions induced by this separation can affect the characteristics of the resulting thrust vector and adversely affect the overall performance of the vehicle. These unsteady phenomena occur at low frequencies which may involve scales that are likely to constitute a source of aerodynamic excitation of certain eigenmodes of the structure and be detrimental to its integrity. Lateral forces are therefore a limiting factor in the design of nozzle geometries, since they generally result in a choice of thicker (and therefore heavier) nozzles. In such nozzle flows, additional instabilities may also occur resulting from different sources including the

boundary layer, the mixing layer and the recirculation zones, which makes this flow quite complicated and challenging to study. To this end, many studies have been conducted to shed more light on these complex phenomena. In terms of flow separation, two types of configurations can be found; Free Shock Separation (FSS) and Restricted Shock Separation (RSS). The transition between them leads to a sudden change in the wall-pressure distribution resulting in strong side-loads generations [1–3]. A literature review of shock-wave boundary layer interaction (SWBLI) brings clear evidence of the existence of broadband and energetically-significant low-frequency oscillation (LFO) in the vicinity of the separated shock. This phenomenon which is associated with complex flow structures, including vortex shedding, jet oscillations and multiple shock reflections, was investigated by many researchers [4–13]. Two main categories of LFO mechanisms can be broadly found: The first points out the influence of the upstream boundary conditions through the incoming boundary layer [14], while the second concerns the downstream influence via the interaction between the separated boundary layer, the recirculation region, and the shock system. In their experimental studies of SWBLI over a compression ramp, Ganapathisubramani et al. [14] reported the existence of very long coherent structures of fifty boundary-layer thicknesses long in the upstream boundary layer. They found a correlation between the low-frequency response of the separation point and these large-scale regions of the incoming turbulent boundary layer. Furthermore, the structures are found to scale with $\bar{u}/2\lambda$, where \bar{u} is the upstream free-stream velocity and λ is the size of the struc-

* Corresponding author.

E-mail address: boubakr.zebiri@insa-rouen.fr (B. Zebiri).

ture. This scale was confirmed when comparing with the work of [13]. In addition, Ünalmsı et al. [15] considered the LFO as a result of thickening and thinning of the upstream boundary layer. This hypothesis as refused later by Beresh et al. [16]. The later found a correlation between the LFO of the shock and the upstream velocity fluctuations for the same configuration of a compression corner. However, many studies can be found in the second category. They may defer in the mechanism in which the low-frequency phenomena occur but they are all produced by the downstream conditions. Pionnniau et al. [17] propose a model which explains breathing of the separation bubble and low-frequency shock motion in terms of fluid entrainment in the mixing layer, whereby fluid from the separation bubble is continuously entrained in the mixing layer, shed downstream, and must be replenished at a time scale corresponding to the low-frequency shock oscillations. Daussage et al. [12] considers the eddies in the separated region as the main excitation source of the LFO. Pirrozoli et al. [18] proposed that the LFO may be produced by acoustic disturbance resulting from the interaction of the coherent structures, shed by the mixing layer next the separation point, and the incident shock. Zaman et al. [4] investigated experimentally and theoretically the shock-wave oscillation in transonic diffusers. They concluded that the mechanism creating those low-frequency oscillations is stimulated by acoustic resonance, where the low-frequency mode corresponds to the case when the one-quarter wavelength is fitted within the approximate distance from the foot of the shock to the nozzle exit. The same conclusions were made by Johnson et al. [9] when investigating, experimentally, the flow in a supersonic planar nozzle. Olson et al. [10] investigated the same nozzle as [9] numerically and confirmed the previous findings. Martelli et al. [19] found, for the same nozzle, that the self-sustained oscillation is driven by a pressure imbalance between the pressure level downstream the shock and the ambient. Based on the above, it is clear that supersonic nozzle flows, and in particular the associated low-frequency unsteadiness, are still an active research field where no consensus on their origin is found. Intending to shed more light on this complex flow, three-dimensional large-eddy simulations are used in this study. Both wall-resolved WR-LES and wall-modeled WM-LES are used to simulate an over-expanded conical nozzle. A comparison is made with an equivalent planar nozzle. The objective is to gain insightful understanding of the SWBLI phenomena and the LFO in nozzles by means of high-fidelity large eddy simulations. A dynamic mode decomposition is also performed for further analysis of the unsteady aspects of the SWBLI phenomenon.

The present paper is organized as follows. The governing equations and the numerical method are presented in the next section 2. Then, the simulation setup will be presented. Right after, the results and the discussion will be introduced. The last section will be devoted to the DMD analyses, performed based on the spectral analysis results. Concluding remarks are given at the end of the paper.

2. Governing equations and numerical method

In this section, an LES methodology in curvilinear coordinates is developed in which a curvilinear coordinate system and domain decomposition are used to treat accurately complex geometries. The starting point is the filtered Navier-Stokes equations written in arbitrary curvilinear coordinate systems, which implies a transformation from the computational to the physical space. However, the computational space needs an additional transformation to reconstruct the physical space employing the following mapping transformation $\xi^i = (\xi, \eta, \zeta)$. By mapping the chain rule and using metrics, we have:

$$\left(\frac{\partial}{\partial x} \quad \frac{\partial}{\partial y} \quad \frac{\partial}{\partial z} \right)^T = J \left(\frac{\partial}{\partial \xi} \quad \frac{\partial}{\partial \eta} \quad \frac{\partial}{\partial \zeta} \right)^T \quad (1)$$

where $J = \partial(\xi, \eta, \zeta)/\partial(x, y, z)$ is the Jacobian matrix of the transformation. The governing equations are then written in the conservative form as follows:

$$\frac{\partial \bar{\rho}}{\partial t} + \frac{\partial \bar{\rho} \tilde{U}_j}{\partial \xi^j} = 0 \quad (\text{Continuity})$$

$$J \frac{\partial \bar{\rho} \tilde{u}_i}{\partial t} + \frac{\partial \bar{\rho} \tilde{u}_i \tilde{U}_j}{\partial \xi^j} = - \frac{\partial \bar{J} \xi_i^j \bar{p}}{\partial \xi^j} + \frac{\partial \bar{J} \xi_j^k \tau_{ij}}{\partial \xi^k} - \frac{\partial \bar{J} \xi_j^k \tau'_{ij}}{\partial \xi^k} \quad (\text{Momentum})$$

$$J \frac{\partial \bar{\rho} \tilde{e}}{\partial t} + \frac{\partial (\bar{\rho} \tilde{e} + \bar{p}) \tilde{U}_j}{\partial \xi^j} = \frac{\partial \bar{J} \xi_i^k \tau_{ij} \tilde{u}_j}{\partial \xi^k} - \frac{\partial \bar{J} \xi_j^k \dot{q}_j}{\partial \xi^k} - \frac{\partial \bar{J} \xi_i^k \tau'_{ij} \tilde{u}_j}{\partial \xi^k} \quad (\text{Energy})$$

with:

$$\tau_{ij} = \mu(\bar{T}) \left[\left(\xi_i^l \frac{\partial \tilde{u}_j}{\partial \xi^l} + \xi_j^l \frac{\partial \tilde{u}_i}{\partial \xi^l} \right) - \frac{2}{3} \delta_{ij} \xi_m^l \frac{\partial \tilde{U}_m}{\partial \xi^l} \right] \quad (3)$$

$$\bar{q}_j = -\lambda(\bar{T}) \xi_j^l \frac{\partial \bar{T}}{\partial \xi^l}, \quad (4)$$

where $\bar{\rho}$, \tilde{u}_i , \tilde{U}_j , \bar{p} , \bar{T} and \tilde{e} are the filtered density, velocity components, j th contravariant velocity component, pressure, temperature and total energy, respectively.

The subgrid shear-stress tensor, $\bar{\tau}'_{ij}$, and the subgrid heat-diffusion flux, \bar{q}_j , are modeled according to the eddy-viscosity hypothesis [20,21]. $\mu(\bar{T})$ and $\lambda(\bar{T})$ are the viscosity and the thermal conductivity corresponding to the filtered temperature \bar{T} and δ_{ij} is the Kronecker's symbol. Note that the generalized form of the equations contains three times more terms than the Cartesian ones, implying an extra computational time. Although the conical nozzle is best described in cylindrical coordinates, this choice comes with the centerline-singularity issue and the associated time-step restriction. A possible compromised solution is to use a domain decomposition (DD) method. The basic idea of the DD method used in this work is detailed in [22]. As for the wall modeling strategy, we use a wall model which combines two well-known wall models of Kawai et al. [23] and Duprat et al. [24]. The first model is suitable for equilibrium boundary layers at high Reynolds number and non-equilibrium shock/boundary-layer interaction problem, while the second one allows to better account for the presence of streamwise pressure gradient. Following the present methodology, improvements of the mean pressure profile have been obtained, mainly in the recovery regime downstream of the separation zone [25].

3. Simulation setup

The code used in this work is a curvilinear explicit finite-difference Navier Stokes solver with WCNS (Weighted Compact Nonlinear Scheme) /Central hybrid scheme for space discretization and RK4 (4th-order Runge Kutta) for time integration. The code uses the HDF5 library for IO and the MPI library for parallelization, it also uses the wall-model developed in [26]. Fig. 1 shows the wall-resolved grid representation with the two overlapping grids. The internal grid, Ω_1 , uses constant spacing in both y and z directions, while the external grid Ω_2 is stretched in the radial direction to ensure WR-LES grid resolution close to the wall. The overlapping limit between the two grid is set to $R_{\Omega_1} = 0.6 R(x)$, where $R(x)$ is the outer radius of the cross section at the streamwise position x . The buffer zone between the inlet and the throat is approximately

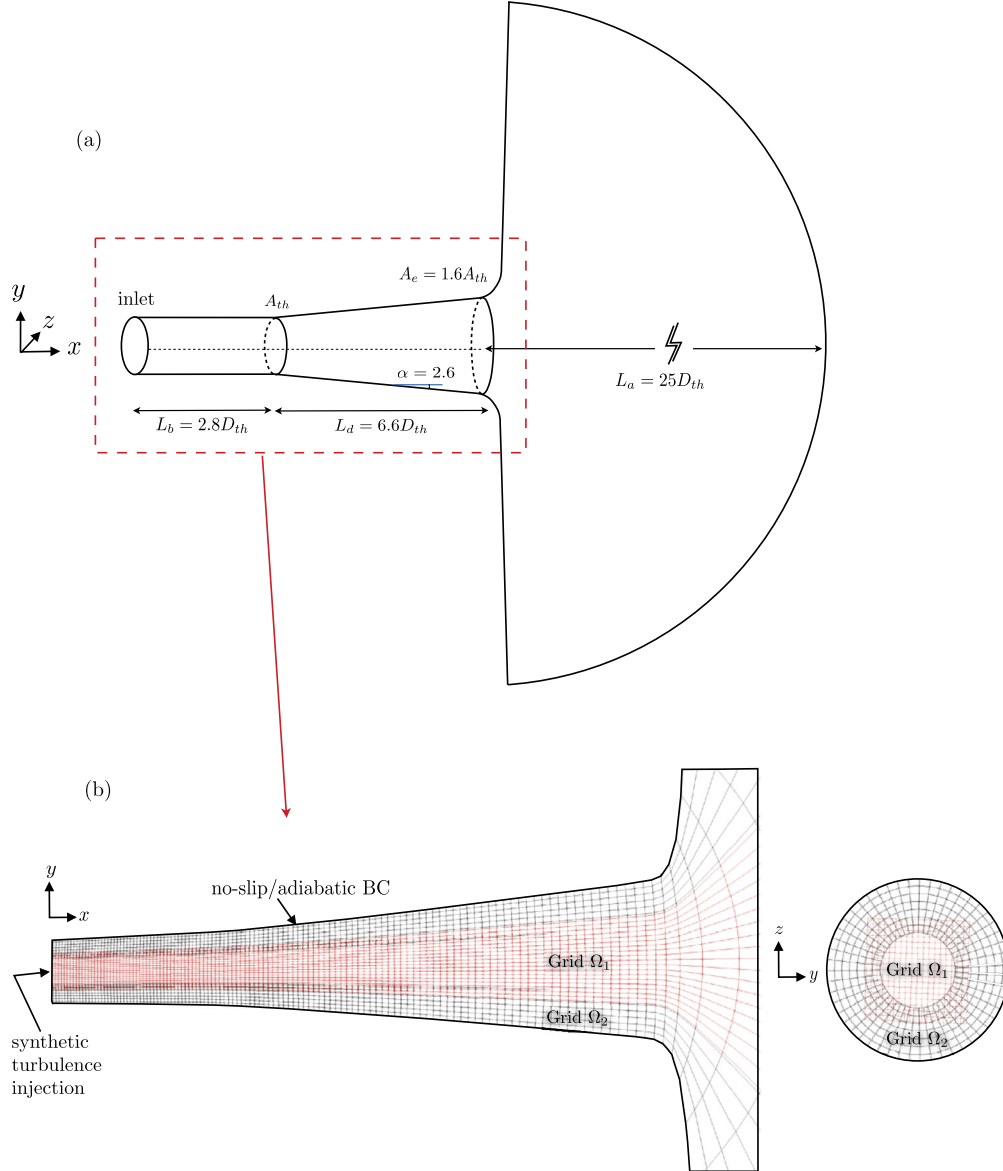


Fig. 1. (a) Schematic of the nozzle geometry, (b) Grid representation from the Wall-Modeled case showing every 5th grid-line, with Ω_1 is the internal mesh (Cartesian coordinates) and Ω_2 is the external mesh (cylindrical coordinates).

28 inlet BL thickness δ_i , allowing sufficient extent for the boundary layer to develop. The outside domain is similar to the planar nozzle flow of [26] with $25H_t$ length where H_t is the nozzle-throat height. For convenience, all figures presented in this paper will use the classical wall-normal notation y equivalent to the radius coordinates $y = (r - R_{\Omega_1}) \cos\theta$. The angular/spanwise direction θ will be represented by the z -direction with $z = (r - R_{\Omega_1}) \sin\theta$, unless otherwise specified.

The incoming boundary layer characteristics are similar to the planar case [26]. The Reynolds number $Re = \frac{u_{i,\infty} R_t}{\nu_{i,\infty}} \simeq 90000$, where $u_{i,\infty}$, $\nu_{i,\infty}$ and R_t are the inlet freestream velocity, the kinematic viscosity and the nozzle throat radius, respectively. The boundary layer conditions at the inlet, use in this work, are the same as [26], using the inflow technique of Xie and Castro [27] extended to compressible flows by [7]. The method has been adapted for the cylindrical coordinates r - θ . For the outlet boundary condition, we use a buffer area combined with pressure far-field boundary conditions to damp the acoustic waves. Both wall-resolved and

wall-modeled simulations are conducted using the same boundary layer parameters compared to the planar flow [26].

The product $\delta R'$ (R' being the curvature of the wall and δ the boundary layer thickness at the point of maximum curvature) is close to zero due to the high radius of curvature of the divergent section. Thus, the present wall-model from [25,26] can be used for the present configuration as long as the transverse curvature compared to the boundary layer thickness is low enough, i.e. $\delta R' < 0.25$. In the present study, the characteristic surface-curvature parameter is about $\delta_{th} R' = 0.05$.

To make the comparison more meaningful, we kept the same incoming boundary layer as in the planar case of [26]. Also, the shock position must be similar for both nozzles. In order to fit the shock position of the planar case, two solutions are proposed: (i) the nozzle geometry is kept but the pressure gradient across the boundary layer will be changed. (ii) The pressure gradient follows the planar case while the geometry (area ratio ε) is decreased. Since reducing the divergent angle to the adequate value (second solution) leads to a pipe flow ($\varepsilon = 1.2$), the first solution is decided. Furthermore, the NPR is adjusted according to the isentropic

Table 1
Grid parameters of the cylindrical nozzle flows.

	N_ξ	$N_{\eta_1}^{\Omega_1}$	$N_{\zeta_1}^{\Omega_1}$	$N_{\eta_2}^{\Omega_2}$	$N_{\zeta_2}^{\Omega_2}$	L_b/H_t	Δx_i^+	Δy_i^+	$R\Delta\theta_i^+$	Nb cells
WR-LES	896	99	99	72	512	2.8	36	[1 : 30]	20	41 M
WM-LES	672	81	81	26	256	2.8	60	45	40	8.8 M

relation and set to 2.0, so that the isentropic profiles between the planar and the cylindrical nozzles are the same.

The grid configurations for both WR- and WM-LES are shown in Table 1. The wall-unit grid spacing is similar to the planar case of [26]. The angular spacing in wall units $R\Delta\theta^+ = 20$ is set up to match the value of the planar nozzle flow. From the literature [28–31], the angular spacing in LES of pipe flow should be in the range of 15–40. The number of points of the internal grid Ω_1 is set as an odd integer, so that we get the centerline aligned with the grid. The wall-normal r -direction is stretched in the wall-resolved case to match the resolution near the wall, i.e. $\Delta y^+ < 1$.

As for the planar case of [26], the WR- and WM-LES are initialized using the Klein method [32]. The results are averaged using slices extracted from the simulation during a dimensionless time ($t^* = t.u_{i,\infty}/\delta_i$) $t^* \sim 4000$ for the wall-resolved simulation and $t^* \sim 18000$ for the wall-modeled simulation.

4. Results and discussion

4.1. Incoming boundary layer

In the present LES, the incoming boundary layer is not fully-developed across the section. The boundary layer thickness is about 5% of the radius at the throat. Fig. 2-a shows the Van Driest velocity profiles downstream of the inlet at $x/\delta_i = -10$ for the wall-resolved simulation. The velocity in the overlap region and the outer layer is shifted upward compared to the planar flow but the slope of the log-law follows the planar case. It confirms the conclusions on the pipe flow of [22] where the Von Karman constant κ of the log-law is constant and the coefficient C is affected by the transverse curvature effects.

Conversely, Fig. 2-b shows the second-order statistics along the wall-normal direction where all the solutions show a good agreement between the cylindrical and the planar flow from [26]. For fully-developed pipe flow, the effect of transverse curvature can be important on the wall-normal Reynolds stress and the wall-normal r.m.s fluctuations [33]. In the present wall-resolved simulation, the wall-normal Reynolds stress is similar to the planar nozzle flow. Second-order statistics do not seem to be influenced by the wall curvature.

Fig. 3 shows the wall turbulent structures at $y^+ \sim 20$. The streaks observed in [26] are again captured by the wall-resolved LES. The effect of the synthetic boundary condition is captured in the region extending from the inlet to $x/\delta_i \sim -15$ corresponding to the length of the coherent structure observed by [27] of about 10–15 δ . Downstream of the throat, the turbulent structures seem to be affected by the favorable pressure gradient present in the divergent section of the nozzle.

Fig. 4-b shows the Clauser's parameter $\beta = \frac{\delta^*}{\tau_w} \frac{dp}{dx}$ along the x -direction. The pressure gradient is increased by 25–40% compared to the planar case. The buffer section, upstream of the throat, is subjected to a stronger pressure gradient due to the reduced cross-section of the nozzle compared to the planar case which does not use side walls. Clauser's parameter is about 0.35 at $x/\delta_i = -10$, while the planar case was about 0.2. The profiles in Fig. 4-b are subjected to more pronounced pressure gradient compared to the planar solution which could explain the gap observed in the log-law Fig. 2-a.

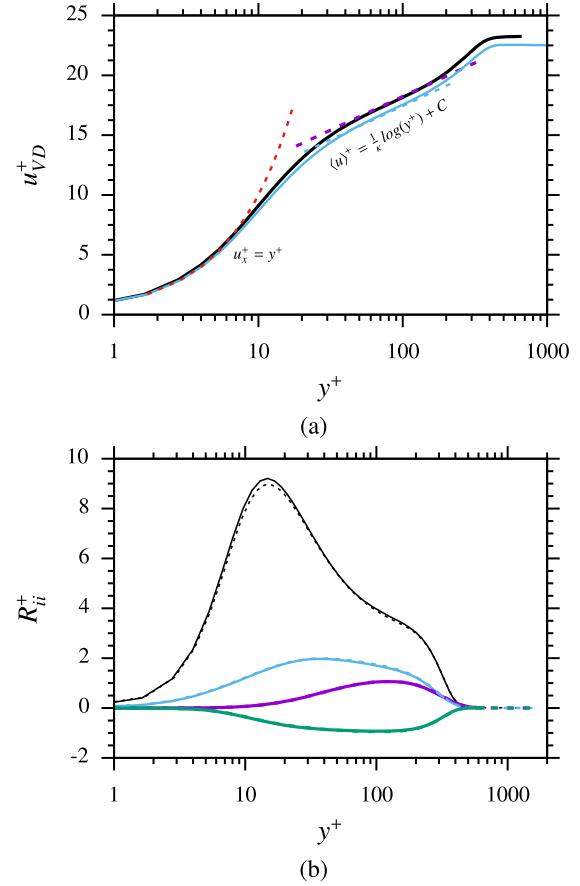


Fig. 2. (a) Van Driest velocity profiles along the wall-normal direction at $x/\delta_i = -10$; —: cylindrical WR-LES, —: planar WR-LES, - - - : $u^+ = y^+$ and - - - : the log-law ($u^+ = \frac{1}{\kappa} \ln(y^+) + C$) with $\kappa = 0.41$ and $C = 6.2$. (b) WR-LES: Normalized velocity RMS along the wall-normal direction at $x/\delta_i = -10$; —: u^+_rms , —: v^+_rms , —: w^+_rms , —: turbulent shear stress, - - - : planar WR-LES [26]. (For interpretation of the colors in the figure(s), the reader is referred to the web version of this article.)

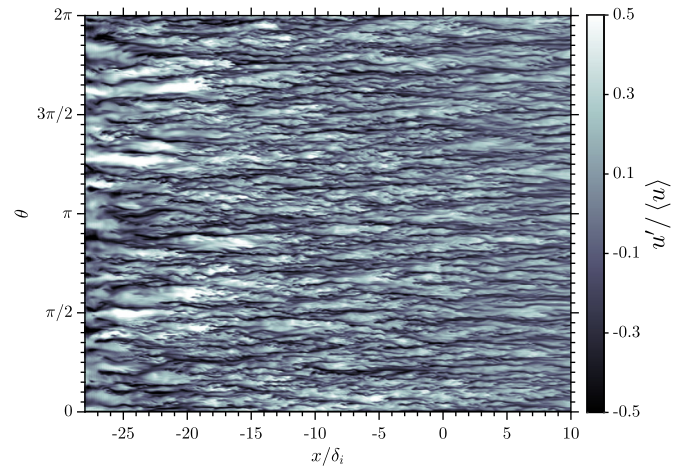


Fig. 3. WR-LES: Instantaneous velocity fluctuations in x - θ plane at $y^+ \sim 20$.

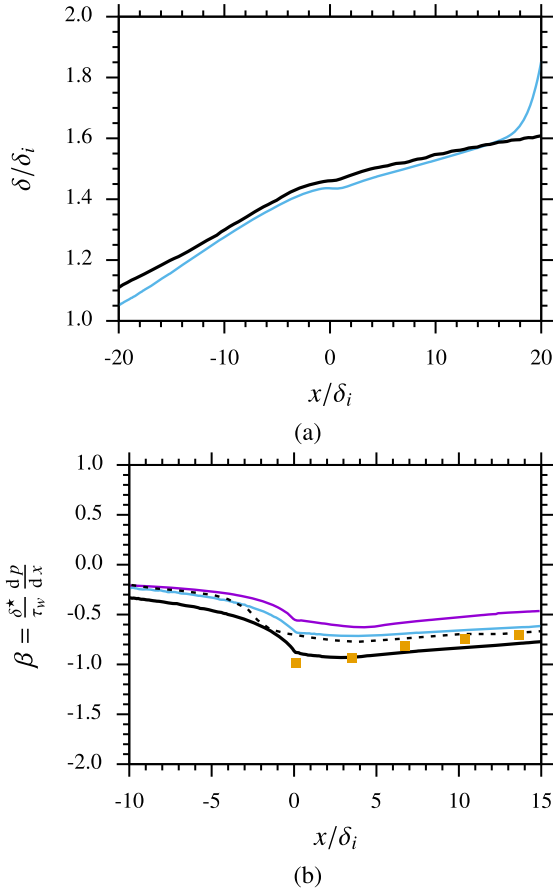


Fig. 4. (a) WR-LES: Boundary layer thickness along the x -direction; —: planar WR-LES, —: cylindrical WR-LES. (b) WR-LES: Normalized pressure gradient along the x -direction; —: planar WR-LES, —: cylindrical WR-LES, - - : planar WR-LES from [10], —: cylindrical WR-LES, —: cylindrical WM-LES, ■: planar experimental results from [9].

Fig. 5-a shows the grid resolution near the wall in wall-unit. The first grid spacing along the nozzle wall of the wall-resolved case satisfies the condition of $\Delta y_{min}^+ \leq 1$. Fig. 5-b shows the wall pressure distribution for the wall-resolved and the wall-modeled simulation. The concordance between the two solutions shows that the wall-modeled simulation is able to properly capture the pressure gradient effect. One can also notice a small difference in the separated region where the wall-resolved distribution is smoother than the wall-modeled one. This behavior is due to stronger compression waves in the wall-modeled simulation in the interaction zone upstream of the separation point. As explained in [26], the coarse grid of the wall-modeled case reduces the length of interaction and increases the strength of the compression waves.

Fig. 6 shows the root mean square (r.m.s) of wall pressure p' for the WM-LES. The p' is slightly reducing along the boundary layer upstream of the separation. At the separation, i.e. $x/\delta_i = 37.1$, the p' is intermittent in the interaction zone, as explained by [34]. In fact, the wall pressure jumps back and forth between a lower mean value p_1 in the region ahead of the separation and a higher value p_2 in the separated region as observed by [34]. The instantaneous fluctuations about p_1 and p_2 are denoted p'_1 and p'_2 , respectively. The mean pressure at the point of interest follows:

$$p = \epsilon p_2 + (1 - \epsilon) p_1 \quad (5)$$

where $\epsilon = (\bar{p}/p_1 - 1)/(p_2/p_1 - 1)$ is the intermittent factor with \bar{p} is the mean pressure at the point of interest. The mean-square fluctuation p'^2 around the wall mean pressure can be predicted using Kistler's equation from [34]:

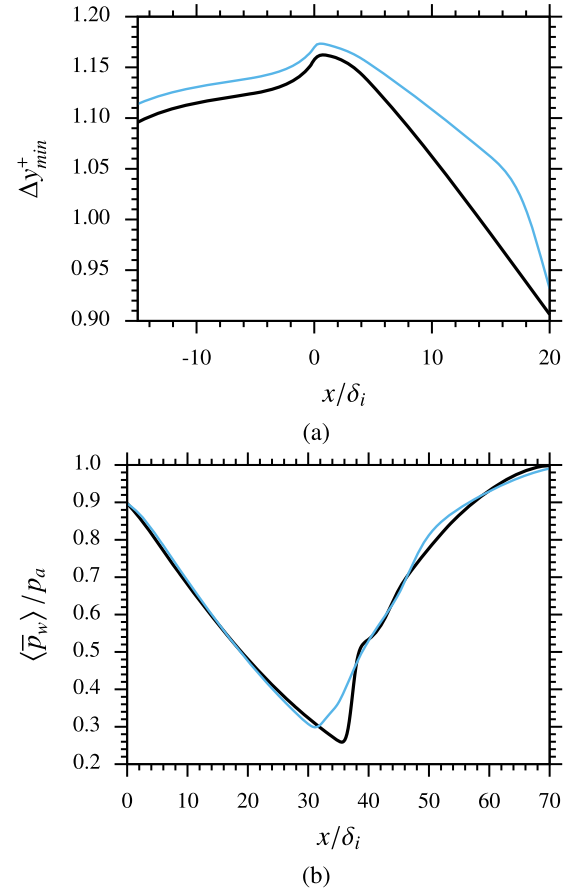


Fig. 5. (a) WR-LES: Wall-unit length Δy^+ at the first near-wall cell along the x -direction; —: planar WR-LES, —: cylindrical WR-LES. (b) WR-LES: Normalized wall pressure along the x -direction; —: cylindrical WR-LES, —: cylindrical WM-LES.

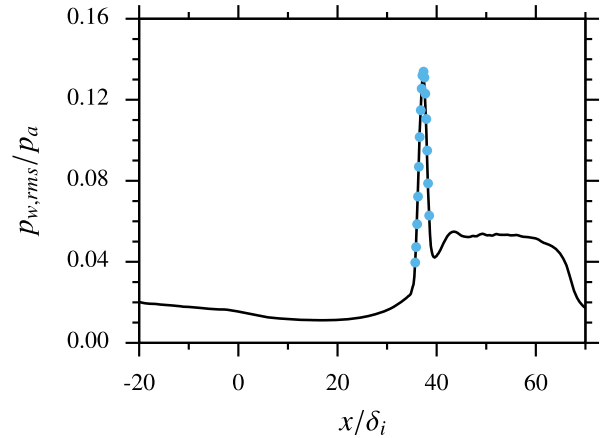


Fig. 6. WM-LES: Normalized pressure r.m.s at the wall along the x -direction; —: present WM-LES, •: Normalized pressure r.m.s located in the separation area given by Kistler's function (Eq. (6)).

$$p'^2 = \underbrace{\epsilon(1 - \epsilon)(p_2 - p_1)^2}_{\text{low-frequency part}} + \underbrace{\overbrace{\epsilon p_2'^2}^{\text{shear layer}} + \overbrace{(1 - \epsilon) p_1'^2}^{\text{boundary layer}}}_{\text{high-frequency part}} \quad (6)$$

Kistler's function is plotted along with the present WM-LES computation (Fig. 6), the result indicates that the theoretical function is accurately capturing the fluctuations of the pressure field within the interaction length.

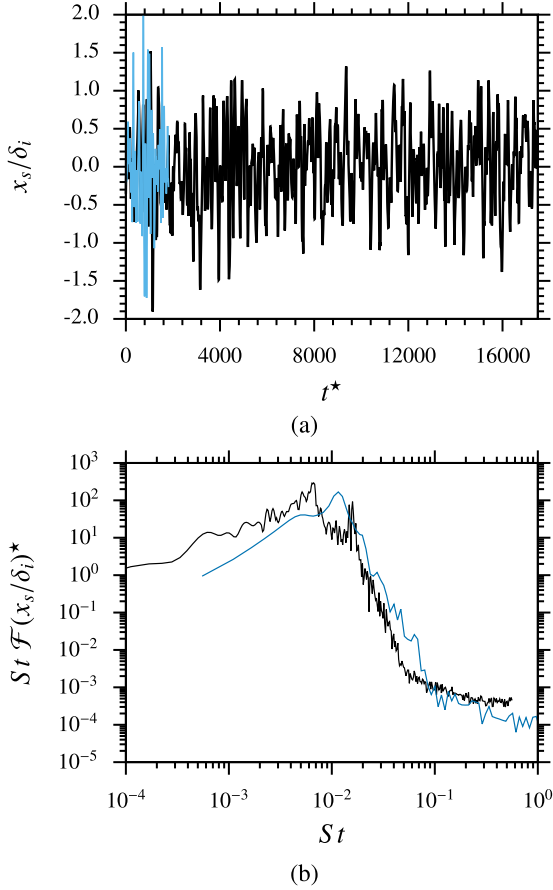


Fig. 7. (a) Separation location over time; —: WM-LES, —: WR-LES. (b) Normalized pre-multiplied spectrum of the separation location from; —: time-resolved WM-LES, —: WR-LES.

Fig. 7-a shows the separation location for both wall-resolved and wall-modeled simulations. The separation location x_s is given by the location where the near-wall velocity becomes negative; $\bar{u}_w(x_s(t), t) < 0$ with \bar{u}_w is the θ -averaged streamwise velocity at the first point near the wall [26]. The amplitude of the separation line is moderate compared to the planar nozzle. In the cylindrical nozzle flow, the amplitude of the separation line is of the order of two boundary-layer thickness magnitude compared to eight in the planar case. The difference of the separation magnitude is due to the strong adverse pressure gradient developing upstream of the separation that acts on the boundary layer in the planar case. Fig. 7-b shows the normalized spectrum of the separation location. Three peaks of energy can be extracted from this spectrum. The tone at a Strouhal number ($St = f \cdot \delta_i / u_{i,\infty}$) of $St = 0.0067$ is the most energetic one and can be assimilated to the resonant tone illustrated in [26]. Zaman proposed the following correlation to compute the resonant tone:

$$f_r = \frac{c_0^2 - u_e^2}{4 c_0 L_{s,e}}, \quad (7)$$

with U_e and c_0 are the averaged velocity at the nozzle exit and the speed of sound, respectively. $L_{s,e}$ is the length between the mean separation location and the nozzle exit. This equation can be used for the present cylindrical nozzle as it fits the requirements proposed by Zaman (mild opening angle of divergent, low-Reynolds number, subsonic Mach jet). The predicted Strouhal number of resonance can be computed by:

Table 2

Averaged/r.m.s forces of the cylindrical WM-LES compared to WR-LES scaled by the isentropic normal force $\bar{F}_{isn} = \int_S (p_{isn} - p_a) \cdot \vec{n} \, ds$.

Case	$\langle F_x \rangle / F_{isn}$	$\langle F_{\vec{n}} \rangle / F_{isn}$	$F_{x,rms} / F_{isn}$	$F_{y,rms}$	$F_{z,rms} / F_{isn}$
WR-LES	0.440	0.780	0.008	0.590	0.590
WM-LES	0.500	0.840	0.014	0.670	0.670

$$St = \frac{1 - M_e^2}{M_e} \frac{\delta_i}{4L_{s,e}}, \quad (8)$$

where M_e is the averaged Mach number at the nozzle exit.

The computed Strouhal number of resonance is about 0.007 which is close to the peak of energy observed in Fig. 7-b. The two-way coupling between the separation and the nozzle exit seems to fit one-quarter wavelength as observed in the planar nozzle flow [26].

A second peak can be observed around Strouhal number 0.015 is due to the recirculation bubbles developing in the separated zone upstream of the nozzle exit. Above $St = 0.015$, the spectrum collapses and no energy can be extracted from the high-frequency range.

4.2. Side-loads analysis

The streamwise force (F_x) and side-loads (wall-normal force F_y , span-wise forces F_z) are computed using the following relation [26]:

$$\vec{F} = \int_S (p_w - p_a) \cdot \vec{n} \, ds, \quad (9)$$

where p_w is the wall pressure, p_a the ambient pressure, ds the local surface element where the force applies, \vec{n} the normal vector to the surface and S the total surface of the nozzle. The forces are integrated along the azimuthal direction θ from the inlet to the exit of the nozzle. Table 2 shows averaged and r.m.s forces in each direction. The averaged y- and z-direction forces are close to zero, which means that the exhaust plume is, on average, mostly symmetric. The side-loads, i.e. y-direction and z-direction forces, can be combined to form a resultant vector ($F_{\vec{n}}$).

$$F_{\vec{n}} = \sqrt{F_y^2 + F_z^2}. \quad (10)$$

The angle (Θ_F) between F_y and F_z using:

$$\Theta_F = \tan^{-1} \left(\frac{F_z}{F_y} \right). \quad (11)$$

Fig. 8-a shows the streamwise force and the side-loads as function of time. One can notice that the fluctuations of the streamwise force are weak compared to the side-loads. The mild opening angle of the divergent and the small fluctuations of the separation line result in a weak r.m.s of the streamwise force. Fig. 8-b shows a typical polar plot of the side-loads. One can notice the isotropic and random behavior of the fluctuating side-loads. Both y-direction and z-direction forces are uncorrelated. They follow a two-dimensional Gaussian distribution with equal variance, and zero mean which fits the Rayleigh distribution:

$$f(x; \sigma) = \frac{x}{\sigma^2} \exp \left(-x^2 / (2\sigma^2) \right), \quad (12)$$

with x is a random value of the side-loads amplitude and σ is the r.m.s level of the amplitude.

The computed side-loads probability density function, depicted in Fig. 9, is compared with experimental results and URANS data from [35]. The present LES seems to indicate that the distribution of

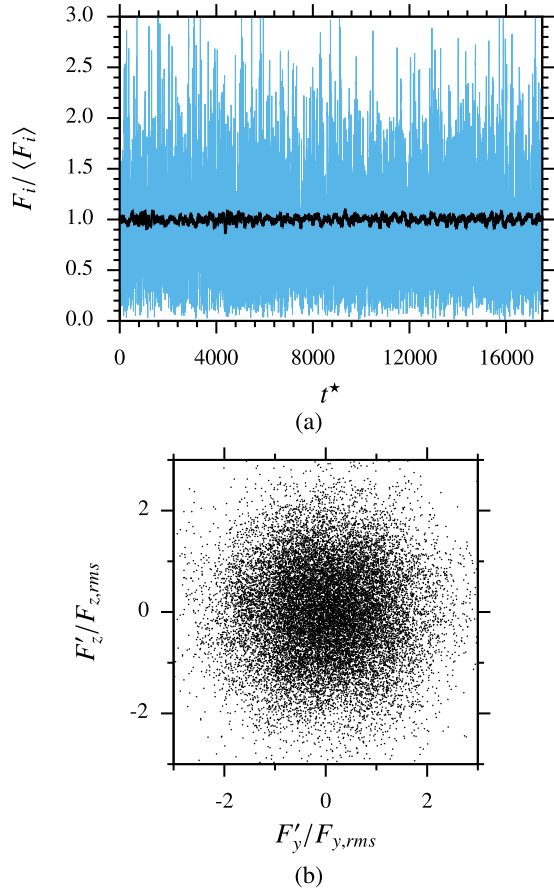


Fig. 8. (a) WM-LES: Forces over time; —: streamwise direction F_x , —: wall-normal direction F_n . (b) WM-LES: Polar plot of the side-loads over time.

the side-loads amplitude follows a Rayleigh distribution as proposed by many authors [35–38]. The scale parameter $\sigma \sim 0.8862$ fits reasonably the prediction of the Rayleigh distribution function ($< 0.1\%$) where the URANS computations of [35] was about 2%. These correlations show that the two components of side-loads are not correlated. Thus, the side-loads do not have any twirling movement and the angle of the force is acting randomly on the structure of the nozzle.

Fig. 10 and 11 show the normalized spectrum of the streamwise force and the side-loads, respectively. The normalized spectrum $St \mathcal{F}(\phi)^*$ of a function ϕ is computed using the following equation:

$$St \mathcal{F}(\phi)^* = \frac{St \mathcal{F}(\phi)}{\int_{St} St \mathcal{F}(\phi) dSt}. \quad (13)$$

As observed in the planar case [26], the streamwise force is sensitive to the low-frequency oscillations of the separation line while the side-loads seems to be receptive to the higher frequency ranges. The same peaks observed in Fig. 7b are captured in the streamwise force spectrum. The main tone computed by the spectrum is about $St = 0.0067$, similarly to the previous analysis of the separation location. The second peak at $St = 0.016$ is also captured within the streamwise force. Another peak of energy is observed in the high-frequency range at $St = 0.1$. As observed in the planar nozzle [26] and according to literature [7,39], the fluctuations of about a tenth of the Strouhal number originate from the mixing layer downstream of the separation.

A mild peak is also noticeable in the low-frequency range at $St \simeq 2 \times 10^{-3}$. This tone originates from the outlet boundary condition reflecting some of the acoustic waves created by the sep-

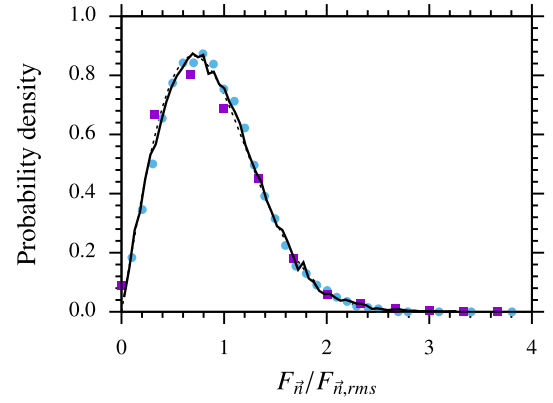


Fig. 9. Probability Density Function of the side-loads F_n ; —: current WM-LES, - - : Rayleigh distribution, •: experiment from [35], ■: URANS from [35].

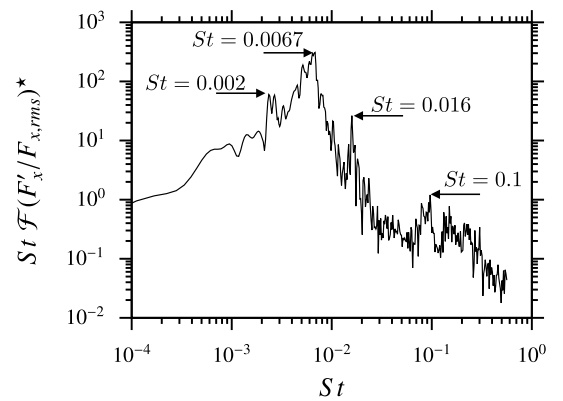


Fig. 10. WM-LES: Normalized pre-multiplied spectrum of the fluctuating streamwise force $F'_x / F_{x,rms}$.

aration unsteadiness. The length between the exit of the nozzle and the outlet boundary condition is about $200 \delta_i$. Using the averaged speed of sound in the ambient region, one can compute the time/frequency of a wave to propagate and reflect from the outlet which ends up to a tone at $St \simeq 2 \times 10^{-3}$. Despite the use of a far-field boundary condition and a sponge layer close to the outlet boundary condition, a part of the acoustic waves created by the separation is reflected by the outlet condition creating this mild peak in the spectrum. This issue has been corrected by implementing non-reflecting boundary conditions.

The side-load spectrum is plotted in Fig. 11. Similarly to the planar nozzle flow [26], the side-loads are affected by the high-frequency range oscillations arising from the separated flow downstream of the shock. The two side-loads components have similar spectrum abroad the frequency range of study. The main peaks around $St = 4 \times 10^{-2}$. When using the Strouhal number based on the nozzle exit conditions defined as $St_D = \varepsilon D_e / (\delta_i M_e) St$, with ε , D_e , δ_i and M_e are the area ratio, the exit diameter, the boundary layer thickness at the inlet and the Mach number at the exit, respectively, the main peak is found at $St_D \simeq 1$. According to the previous studies [40–42], the nozzle lip is known to generate trailing-edge noises at $St_D = 1$. This noise affects the exit pressure field which generates acoustic waves upstream through the subsonic recirculation area (Fig. 15). Changing the lip curvature or reducing the flange width could lead to a shifted range of frequencies as observed by [43].

Based on the side-load spectra, one can characterize and identify the origin of the peaks. As for the planar flow [26], time-resolved probs along the circular wall are used. The probs capture a large range of frequencies from Strouhal number 10^{-4} to 10. Fig. 12 shows the spectra of the normalized fluctuating pressure

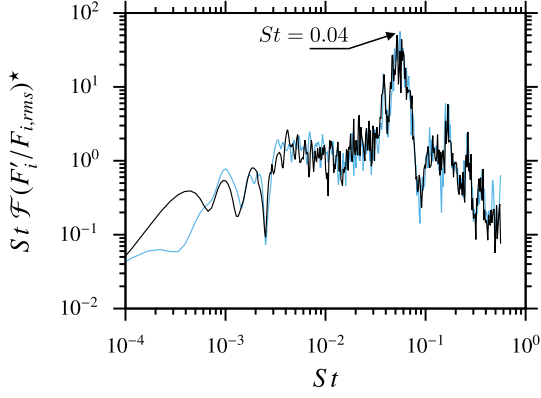


Fig. 11. WM-LES: Normalized pre-multiplied spectra of the fluctuating side-loads; —: $F'_y / F_{y,rms}$, —: $F'_z / F_{z,rms}$.

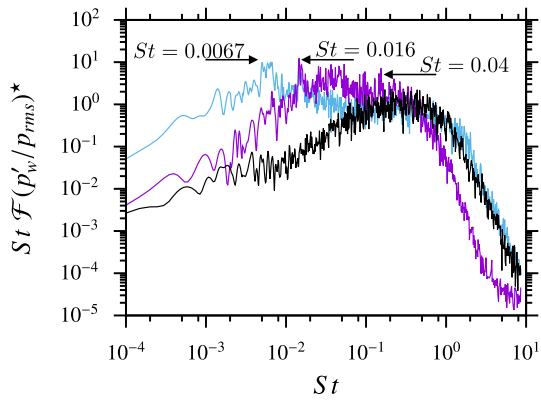


Fig. 12. WM-LES: Normalized pre-multiplied spectra of the fluctuating pressure field at the wall; —: in the incoming boundary layer $x/\delta_i = 0$, —: at the separation $x/\delta_i \sim 37.1$, —: at the exit $x/\delta_i = 66$.

field at the wall for different x -locations. One can notice from the spectrum at the throat that the energy is centered around $St = 1$, following the definition of the Strouhal number based on the boundary-layer characteristics. At the separation location, the peak captured at $St = 6.7 \times 10^{-3}$ similar to the peak observed in the separation spectrum (Fig. 7). The resonant tone is also captured at the nozzle exit along with the recirculation bubble $St = 1.6 \times 10^{-2}$ and with the trailing-edge noises at $St = 4 \times 10^{-2}$.

Fig. 13 shows the frequency analysis using the centerline slice. For each point in the x - y plane, the Strouhal number associated with the maximum energy from the normalized pressure field spectrum is displayed using iso-contours values of the different phenomena captured. A color is associated with each phenomenon,

- $St = 0.0067$, the resonant tone predicted by [4] is captured at the separation, in the λ -shock and in the second shock train at $x/\delta_i \sim 50$. It is interesting to notice that the second shock oscillates at the same resonant tone compared to the first λ -shock (Fig. 14).
- $St = 0.016$, the subsonic flow downstream of the separation, at $x/\delta_i \sim 60$, is trapped between the mixing layer and the wall producing small unsteady eddies oscillating at this specific frequency. This phenomenon is strongly impacting the lateral forces (side-loads).
- $St = 0.04$, the trailing-edge noises from the lip are captured at the nozzle exit and in most of the atmosphere, as explained by [42]. The frequency at which noises are captured is similar to the vortex shedding phenomenon taking place outside of a nozzle jet plume.

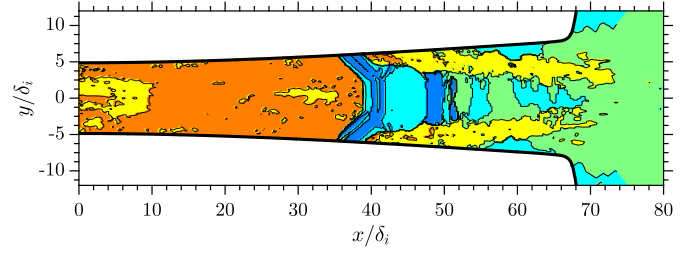


Fig. 13. WM-LES: Frequency analysis in the x - y plane showing the Strouhal number associated with the most dominant frequencies extracted from the normalized pressure field spectra $St F(p'/p_{rms})$; Orange zone ($St \sim 1$): boundary layer turbulence, yellow zone (downstream the shock) ($St \sim 0.1$): mixing layer unsteadiness, (upstream the shock); inlet profile unsteadiness, green zone ($St \sim 0.04$): trailing-edge noises, cyan zone ($St \sim 0.016$): recirculation bubbles and blue zone ($St \sim 0.0067$): resonant tone.

- $St = 0.1$, the mixing layer developing from the separation to the exit is observed at this frequency as explained in section 4.2. The large 2-dimensional Kelvin-Helmholtz vortices impact the exit conditions, modifying the effective exit area and the position of the separation shock.
- $St = 1$, upstream of the separation, the pressure fluctuations are dominant in the range of turbulent boundary layer (Fig. 14) frequencies. The position of the shock is slightly correlated with the upstream condition. However, the asymmetry of the separation is strongly influenced by the incoming boundary layer turbulence, particularly observed in the planar flow.

5. Dynamic mode decomposition

A DMD analysis is conducted in order to identify the selected frequencies in the spectra and to link them with the corresponding physical phenomena.

Given the wide range of frequencies involved in this flow (see Fig. 10 and 11) and in order to focus mainly on the low frequencies, a dedicated Multi-resolution DMD (MrDMD) [49] is used. The algorithm is able to split robustly the complex systems into a hierarchy of multi-resolution time-scale components.

Over 500 equid-time spaced snapshots of pressure fluctuations p' are used and sampled at $St = 1$ which gives a Nyquist frequency of $St = 0.5$. Each snapshot is a full 3D flow field (the entire flow; inside, outside, and downstream of the nozzle). Thus, the entire range of frequency from Fig. 10 and Fig. 11 is covered.

The objective of this analysis is indeed to look for the energetic modes which appear in the different spectra presented, more particularly, we look for the ways in which these modes behave, how and where they act precisely.

First, let us take a quick look at the shape of the modes that we found. In fact, one distinguishes mainly two varieties of mode; non-helical modes and helical modes. Non-helical modes (flopping modes) are low-frequency modes which appear in the spectra of the stream-wise forces Fig. 10. However, helical modes are high-frequencies modes compared to the first type; they appear in the spectra of the side-loads Fig. 11. The degree of torsion of structures, in this type of modes is noticed to be a function of frequency, the higher is the frequency, the greater is the torsion. Fig. 16-c, 20, 21-c. Another important remark to be mentioned concerns the shape of the structures of the modes outside the nozzle. One can notice that for some modes the structures are larger and united whereas for some it is the opposite, in fact, the structures are smaller and divided into several parts, these modes are harmonies of the first type of modes.

Now, we try to track the frequency peaks appearing in both Fig. 10, 11 and highlight the physical meaning of each mode.

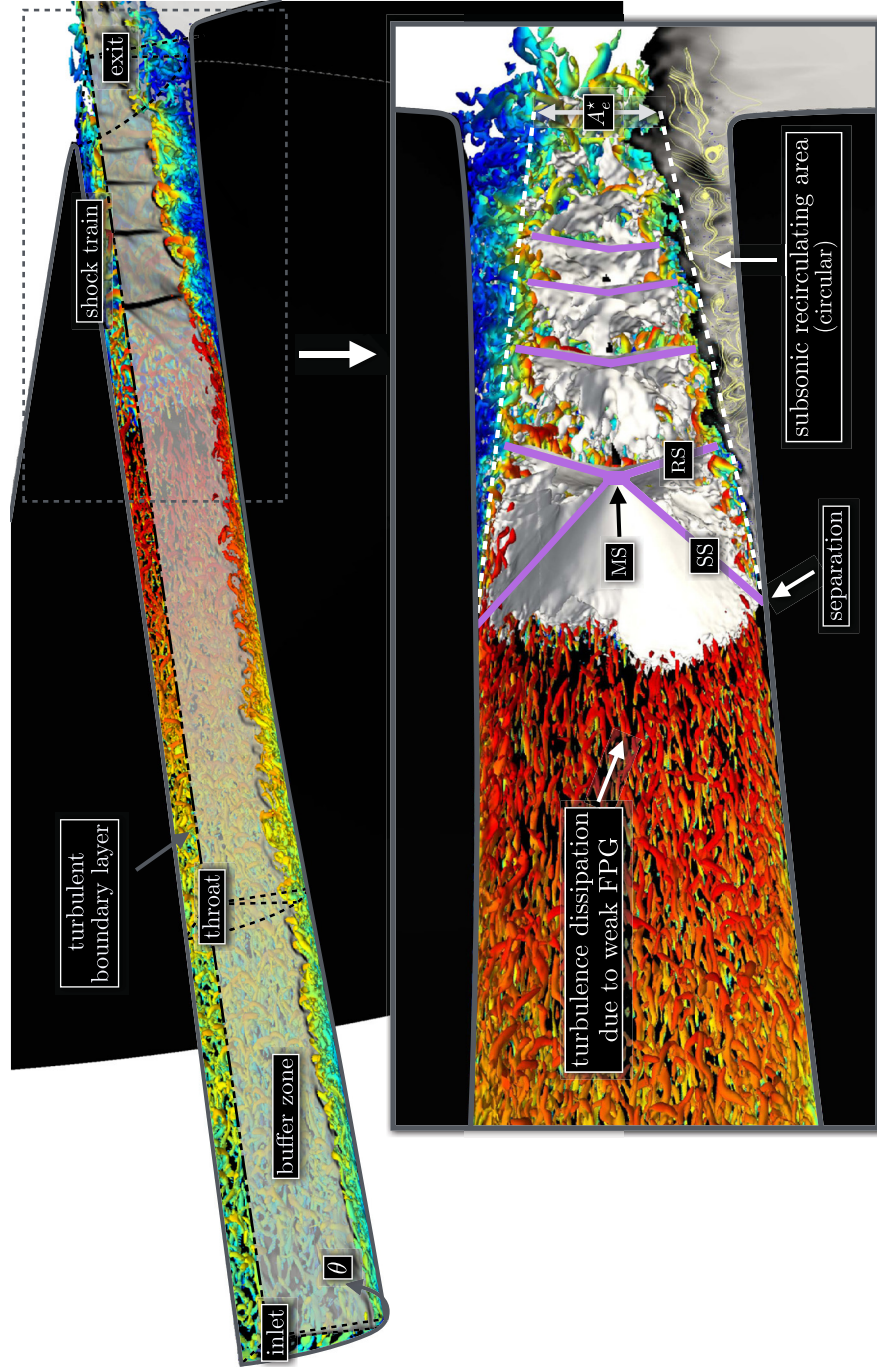


Fig. 14. Cylindrical WR-JES: iso-contour of Q criterion colored by the velocity field (blue: slow, red: fast); MS: Mach stem, SS: separated shock, RS: reflected shock, A_e^* : effective exit area; grayscale surface: Numerical schlieren picture at $\theta = 0$, white volume: iso-volume of the velocity gradient $\nabla||u||$.

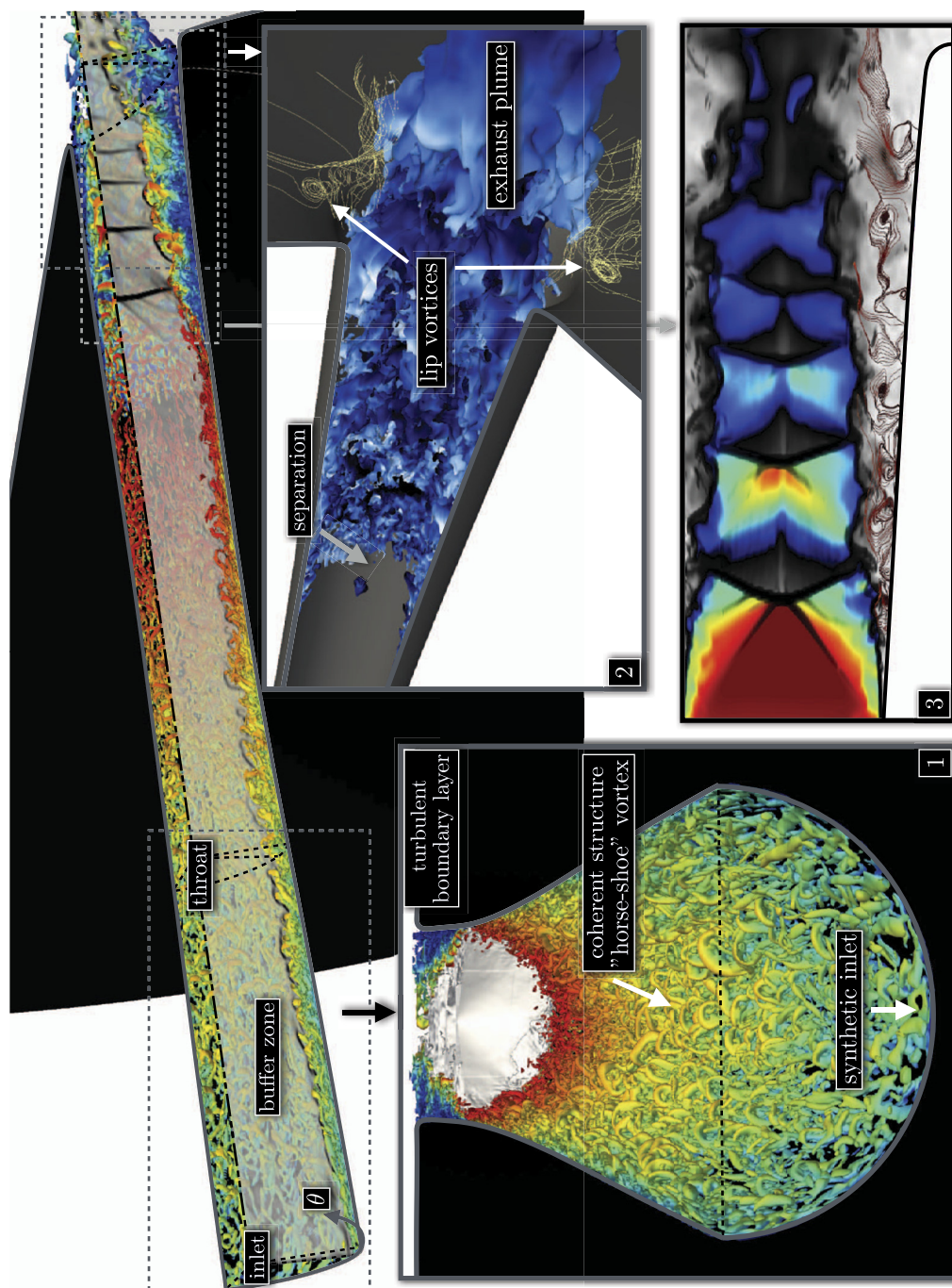


Fig. 15. Cylindrical WR-LES: 3D representation of the different phenomenon observed in cylindrical nozzle flow; legend as in Fig. 14, box 2: iso-contour of temperature $T/T_\infty \sim 0.9$ colored by velocity (blue/black) and streamline near the nozzle lip (yellow), box 3: jet color represents the supersonic field while b/w color represents the subsonic part.

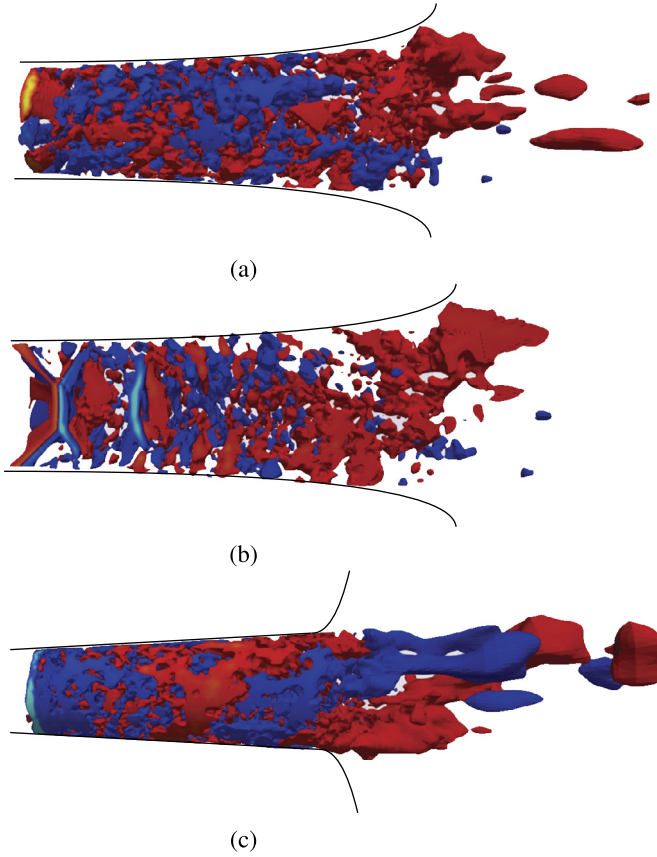


Fig. 16. Isovolume of the real part with negative and positive pressure fluctuations, p' , for DMD mode at $St = 0.0028$. Red to yellow color indicates positive pressure fluctuations, yellow being the highest. Dark blue to light blue indicates negative pressure fluctuations, light blue being the lowest.

The mode corresponding to $St = 0.0028$: This mode observed at a very low frequency is essentially related to the shock structures as shown in Fig. 16. With the presence of a Mach disc rotation and a very slow convection downstream, this mode can be considered as a standing mode as already explained by Larusson [45]. The structures observed in this mode are initially normal, but little by little, they will form under elongated helical structures which stretch between the downstream of the shocked zone and the exit of the nozzle. Fig. 16-c.

The mode corresponding to $St = 0.0068$: This mode, defined as the main tone, is a witness of many physical phenomena such as shock system oscillations and the Mach disc rotation Fig. 17-a,-b. It is also a witness of the presence of some acoustic waves that propagate downstream. The way in which these waves move was already described by [46]. Worthy of being recalled, the hopping movement of the waves starts from this frequency and becomes more and more important as the frequency increases.

The mode corresponding to $St = 0.0168$: the animation of this mode reveals the presence of a very intense convective activity outside the nozzle, with structures that hop, more clearly, when moving downstream towards the atmosphere. This mode can be associated mainly with the shock train and some recirculation bubbles located downstream of the shocked region as shown in Fig. 18. The structures observed, here in this mode, show a tendency to be helical from the beginning, but with a lesser degree of torsion.

The mode corresponding to $St = 0.019$: This mode is very similar to the previous mode but it is more energetic, as a result, it is strongly damped. The only remarkable difference comparing to the previous mode is the presence of more evident helical structures and more explicit hopping movement Fig. 19.

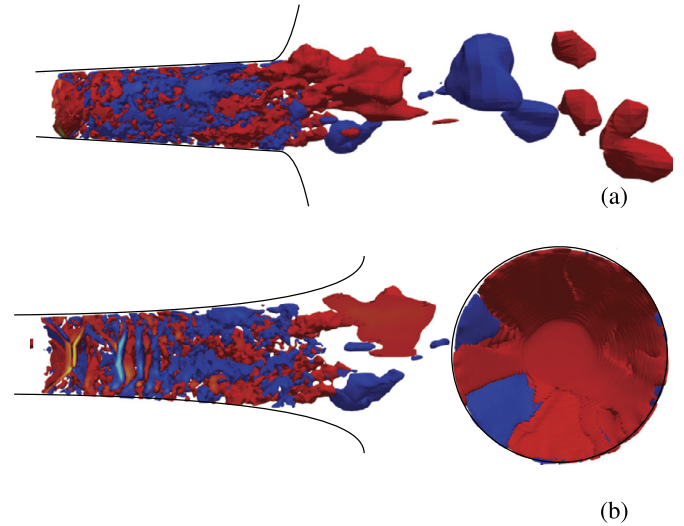


Fig. 17. Isovolume of the real part with negative and positive pressure fluctuations, p' , for DMD mode at $St = 0.0068$. Red to yellow color indicates positive pressure fluctuations, yellow being the highest. Dark blue to light blue indicates negative pressure fluctuations, light blue being the lowest.

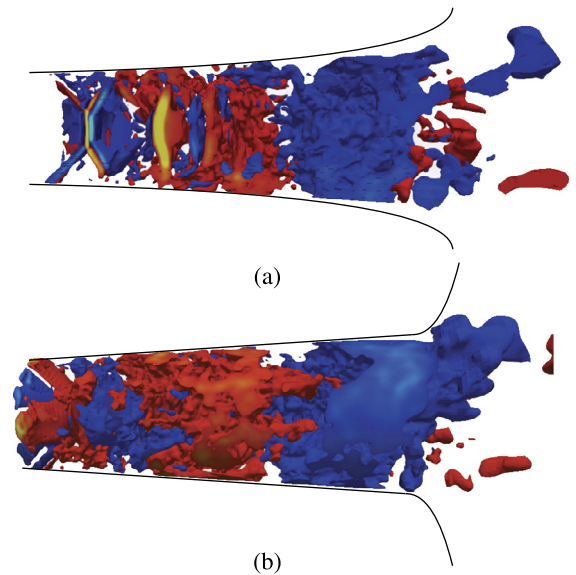


Fig. 18. Isovolume of the real part with negative and positive pressure fluctuations, p' , for DMD mode at $St = 0.0168$. Red to yellow color indicates positive pressure fluctuations, yellow being the highest. Dark blue to light blue indicates negative pressure fluctuations, light blue being the highest.

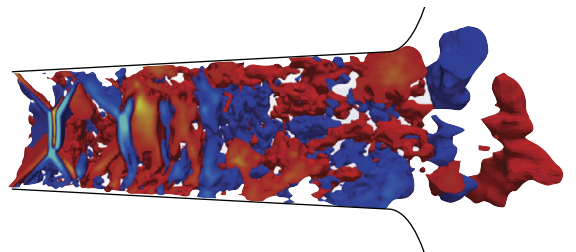


Fig. 19. Isovolume of the real part with negative and positive pressure fluctuations, p' , for DMD mode at $St = 0.0190$. Red to yellow color indicates positive pressure fluctuations, yellow being the highest. Dark blue to light blue indicates negative pressure fluctuations, light blue being the highest.

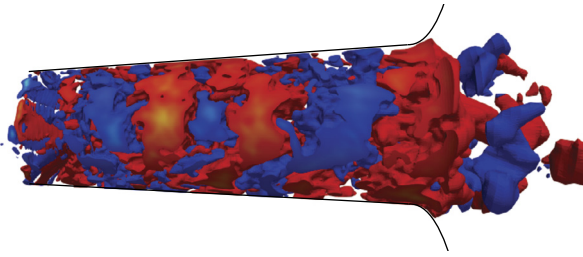
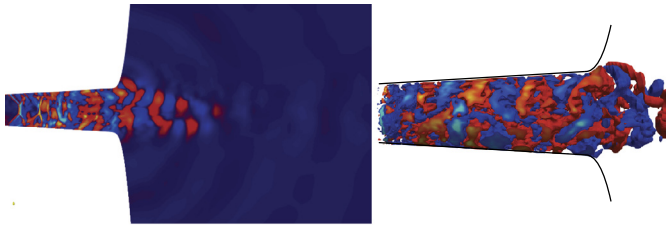
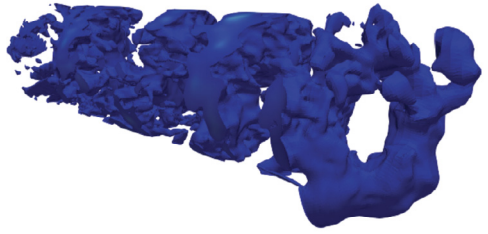


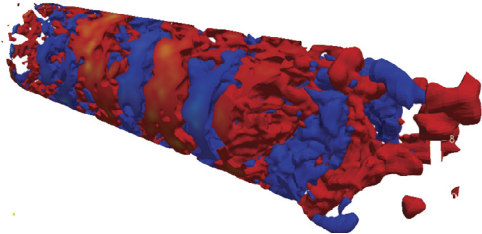
Fig. 20. Isovolume of the real part with negative and positive pressure fluctuations, p' , for DMD mode at $St = 0.0396$. Red to yellow color indicates positive pressure fluctuations, yellow being the highest. Dark blue to light blue indicates negative pressure fluctuations, light blue being the highest.



(a)



(b)



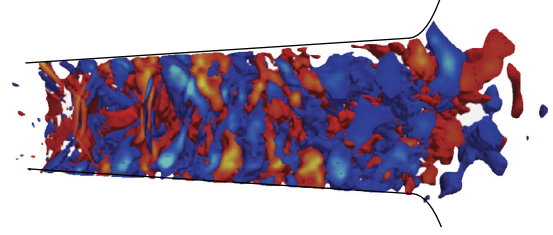
(c)

Fig. 21. Isovolume of the real part with negative and positive pressure fluctuations, p' , for DMD mode at $St = 0.0471$. Red to yellow color indicates positive pressure fluctuations, yellow being the highest. Dark blue to light blue indicates negative pressure fluctuations, light blue being the highest.

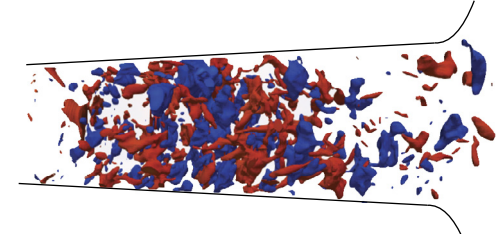
The mode corresponding to $St = 0.0396$: Several physical phenomena can be noticed during the animation of this mode, starting with the back flow noticed in the atmospheric part and which goes up until the interior of the nozzle. This back flow is essentially due to the imperfect none-reflective-boundary-condition used at the outlet of the nozzle. The reason behind the use of this type of condition was explained by [26]. In addition to that, there is a remarkable acoustic activity at the exit of the nozzle. The structures belonging to this mode are clearly helical. Fig. 20.

The mode corresponding to $St = 0.0471$ and $St = 0.0596$: Almost the same physical phenomena observed in the previous mode can be found in these modes. But, they are clearer and stronger Fig. 21. The back flow is now easy to be distinguished especially, inside the nozzle. Also, the hopping movement of the waves is also obvious.

The mode corresponding to $St = 0.1002$: A very energetic mode but strongly damped Fig. 22-b, the same remarks made for the

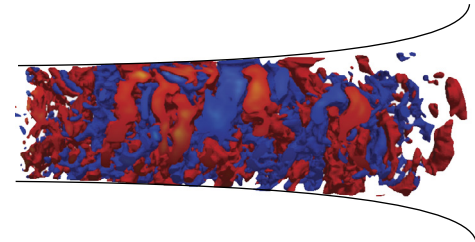


(a)

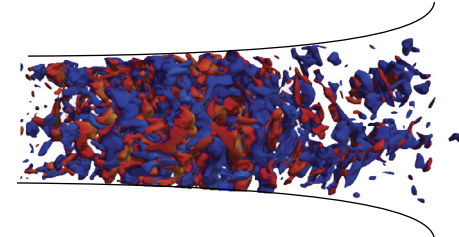


(b)

Fig. 22. Isovolume of the real part with negative and positive pressure fluctuations, p' , for DMD mode at $St = 0.1002$. Red to yellow color indicates positive pressure fluctuations, yellow being the highest. Dark blue to light blue indicates negative pressure fluctuations, light blue being the highest.



(a)



(b)

Fig. 23. Isovolume of the real part with negative and positive pressure fluctuations, p' , for DMD mode at $St = 0.1662$. Red to yellow color indicates positive pressure fluctuations, yellow being the highest. Dark blue to light blue indicates negative pressure fluctuations, light blue being the highest.

two previous modes can be made here except the helical structures which are transformed into small structures organized in the form of a spring.

The mode corresponding to $St = 0.1662$: This mode is linked to the activities of the mixing layer, the animation of which shows that within the nozzle the helical structures are gradually destroyed and replaced by some vortex shedding, Fig. 23-b.

The mode corresponding to $St = 0.2753$: this mode is also associated with the activities of the mixing layer, it is a convective mode with vortex shedding becoming more and more finer. A stronger acoustic activity towards the exit of the nozzle is clearly noticed, Fig. 24.

The mode corresponding to $St = 0.3753$: This mode is convective. It mainly represents mixing layer instabilities. When we look

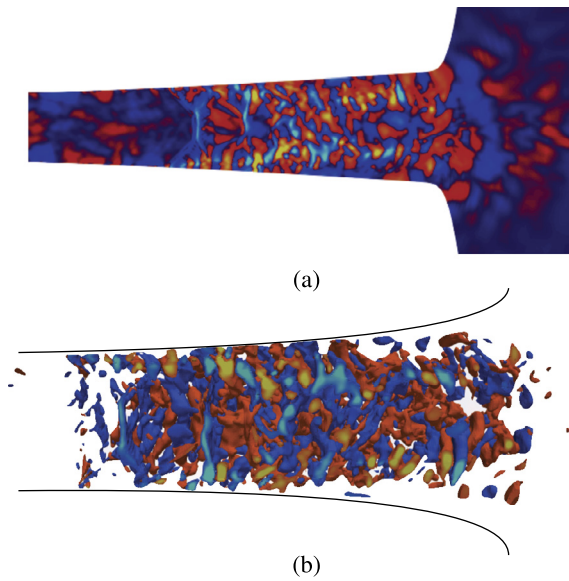


Fig. 24. Isovolume of the real part with negative and positive pressure fluctuations, p' , for DMD mode at $St = 0.2753$. Red to yellow color indicates positive pressure fluctuations, yellow being the highest. Dark blue to light blue indicates negative pressure fluctuations, light blue being the highest.

to the form of the structures just downstream of the exit of the nozzle, we can easily note that this mode is a harmonic mode.

After describing each mode, one can link them to their corresponding phenomena. To do that, we will compare the results of the DMD with the different spectra. As a result, Modes can be classified into three categories:

- $St \in [0, 0.0168]$: the modes in this interval are flopping modes, they are at the origin of the streamwise forces amplification through the oscillatory movement of different structures of the shock.
- $St \in]0.0168, 0.10]$: The modes are found to be helical for this frequency range. They represent vortical structures of different sizes that become finer when increasing the frequency. These structures appear very close to the wall of the nozzle downstream of the shocked area which leads to consider these modes as the major responsible for side-loads amplification.
- $St \in [0.10, 0.40]$: These modes represent high energy vortical structures, of which the origin is the mixing layer. These modes manifest close to the axis of the nozzle and they participate less in the spectrum of the side-loads.

6. Conclusion

In this paper, we have presented results from large-eddy simulations of supersonic conical nozzle flow. A good agreement of the second-order statistics, in the normal direction, between both the cylindrical and the planar nozzle from [26] can be remarked. Thus, second-order statistics seems not to be influenced by the curvature. The turbulent structures seem to be influenced by the favorable pressure gradient present in the divergent section of the nozzle. Furthermore, the amplitude of the separation line is less important in the cylindrical case because of the increased pressure gradient, upstream the throat, resulting from the reduced cross-section in this case compared to the planar one which does not use side walls. The frequency analysis of the flow shows the existence of low-frequency phenomena resulting mainly from the oscillation of the shock system. The same analysis shows that the side-loads are affected by the high-frequency range oscillations arising from the separated flow downstream of the shock. The DMD analysis

was able to capture the same frequencies as the spectral analysis. Also, it shows the existence of two varieties of modes; the non-helical modes (flopping modes) which are low-frequency modes that appear mainly in the spectra of the stream-wise forces and the helical modes which are high frequencies modes compared to the first type, and they appear especially in the spectra of the side-loads.

Declaration of competing interest

The authors declare that they have no known competing financial interests or personal relationships that could have appeared to influence the work reported in this paper.

Acknowledgements

BZ gratefully acknowledges support from the Algerian Government through a Ph.D Fellowship. This work was performed using high-performance computing (HPC) resources from GENCI [CURIE] and from CRIANN (*Centre Régional Informatique et d'Applications Numériques de Normandie*), Rouen, France.

Appendix A

Multiple studies on Dynamic Mode Decomposition applied to nozzles have been performed by several researchers [44–46]. The studies were mainly focused on the acoustic of the issuing jet from the nozzle.

For instance, Larusson et al. [44,45] investigated a supersonic jet using a DMD method. In their case, the algorithm was applied on a set of data resulting from a series of LES simulations of a conical nozzle as well as 2D RANS simulations.

The authors reported that the LES DMD results are comparable to those of RANS DMD. In addition, the modes resulting from the LES DMD are found to be more damped compared to those resulting from the RANS DMD and the Arnoldi method. The authors also noted that the damping of low frequencies decreases by increasing the cycle of perturbations added to the sampling average. The modes extracted in this study mainly correspond to the shock-cell movement and acoustic radiations. Further flow features have been studied through DMD analysis, such as the shear layer which has been studied using the spatio-temporal DMD method developed by Lu et al. [48]. The proposed method can capture the dominant unsteady vortices in the flow field and obtain the quantitative information of the streamwise development. The DMD was, also, applied to the mixing layer [47]. It was found that there is a certain dominant frequency in the flow structure, which can provide a reference for the active mixing enhancement method.

Another interesting study was conducted by Jovanovic et al. [46] in which the screech mode was identified, and described as a flopping mode. Jovanovic et al. linked the upstream propagation of acoustic waves to the time-periodic-compression caused by the oscillations of the shock. They also noticed that acoustic waves propagate upstream by jumping between negative spots. In fact, the mixing layer rotates the shock cells. In this case, the outer end of the cell will pass from upstream to downstream, generating an impulse for the exterior acoustic perturbation which will push it upstream to the next cell.

As explained in the section 5, the DMD method used in this work is the Multi-resolution DMD (MrDMD) [49]. The reason we make this choice is the wide range of frequencies involved in this flow and in order to focus mainly on the low frequencies. The algorithm is able to split robustly the complex systems into a hierarchy of multi-resolution time-scale components. It consists of applying a simple DMD by Schmidt [50] to the given set of snapshots, initially

organized in a matrix, where n is the number of spatial measurement par time snapshot and m is the number of snapshots.

$$Q_0^{m-1} = \{q_0, q_1, q_2, \dots, q_{m-1}\} \quad (14)$$

The eigen-decomposition approximation of the best fit linear operator A , that relates two successive states, is given by $q_{j-1} \simeq Aq_j$. Considering the previous, one can write that $Q_1^{m-1} = \{q_1, Aq_1, A^2q_2, \dots, A^{m-2}q_1\}$. By choosing A that minimizes the Frobenius norm of $[Q_2^m - AQ_1^{m-1}]_F$, one can write according to Kutz [49] $Q_2^m \simeq AQ_1^{m-1}$. Using reduced SVD factorization, Q_0^{m-1} is written as following $Q_0^{m-1} = U\Sigma W^*$ where U contains the left singular vectors (POD modes), W contains the right singular vectors and the singular values are in Σ . The A matrix and its projection onto POD modes (\tilde{A}) are given by:

$$A = Q_2^m V \Sigma^{-1} U^* \quad (15)$$

$$\tilde{A} = U^* A U = U^* Q_2^m V \Sigma^{-1} \quad (16)$$

The eigenvectors (W) and the corresponding eigenvalues (λ_k) are then computed by eigendecomposing \tilde{A} , ($\tilde{A}W = W\Lambda$), where Λ is a diagonal matrix containing λ_k . The damping factor ξ and the frequency f are given by $\arg(\mu) = 2\pi f \Delta t + 2\pi b$ and $\xi = \frac{\ln \|\mu\|}{\Delta t}$, where b is an integer that can be safely assumed to be zero [44]. The solution at a given instant t , $q_{DMD}(t)$, is given by

$$q_{DMD}(t) = \sum_{k=1}^m b_k(0) \psi_k(\xi) e^{(wt)} \quad (17)$$

$$= \Psi \text{diag}(e^{(wt)}) b \quad (18)$$

where ξ is the spatial coordinates, $b_k(0)$ is the initial amplitude of each mode, Ψ is a matrix containing the eigenvectors ψ_k , $\text{diag}(e^{(wt)})$ is a diagonal matrix containing the eigenvalues $e^{(w_k t)}$ and b is the vector of the coefficients b_k .

From the initial pass through the data, the slowest modes ($m1$) are removed, and the set of data is divided into two sets. The size of each set is $m/2$. A DMD is once again performed on each set and again the lowest modes ($m2$) for each set are removed. The algorithm is repeated next until the desired termination. Mathematically, one can write:

$$q_{DMD}(t) = \sum_{k=1}^m b_k(0) \psi_k^{(1)}(\xi) e^{(w_k t)} \quad (19)$$

$$= \underbrace{\sum_{k=1}^{m1} b_k(0) \psi_k^{(1)}(\xi) e^{(w_k t)}}_{\text{Slow modes.}} + \underbrace{\sum_{k=m1+1}^m b_k(0) \psi_k^{(1)}(\xi) e^{(w_k t)}}_{\text{Fast modes.}} \quad (20)$$

The first sum represents the slow mode dynamic, whereas the second one is everything else. The second part $Q_{m/2}$ is divided into two parts:

$$X_{m/2} = X_{m/2}^{(1)} + X_{m/2}^{(2)} \quad (21)$$

For each level, slow modes are computed, the process continues by splitting in half each time, $X_{m/2}$, $X_{m/4}$, $X_{m/8}$, ..., and performing DMD on each part until the desired decomposition is achieved.

References

- [1] A. Hadjadj, Y. Perrot, S. Verma, Numerical study of shock/boundary layer interaction in supersonic overexpanded nozzles, *Aerosp. Sci. Technol.* 18 (2002) 577–584.
- [2] A. Hadjadj, M. Onofri, Nozzle flow separation, *Shock Waves* 19 (2009) 163–169.
- [3] V. Zmijanovic, L. Leger, M. Sellam, A. Chpoun, Assessment of transition regimes in a dual-bell nozzle and possibility of active fluidic control, *Aerosp. Sci. Technol.* 82–83 (2018) 1–8.
- [4] K. Zaman, M.D. Dahl, T.J. Bencic, C.Y. Loh, Investigation of a transonic resonance with convergent-divergent nozzles, *J. Fluid Mech.* 463 (2002) 313–343.
- [5] Y. Han, Y. He, Y. Tian, F. Zhong, J. Le, Assessment of a hybrid RANS/LES simulation method and URANS method in depicting the unsteady motions of flow structures in a scramjet combustor, *Aerosp. Sci. Technol.* 72 (2018) 114–122.
- [6] A. Bourgoing, P. Reijasse, Experimental analysis of unsteady separated flows in a supersonic planar nozzle, *Shock Waves* 14 (2005) 251–258.
- [7] E. Toubert, N.D. Sandham, Large-eddy simulation of low-frequency unsteadiness in a turbulent shock-induced separation bubble, *Theor. Comput. Fluid Dyn.* 23 (2009) 79–107.
- [8] L. Weipeng, L. Hong, Large-eddy simulation of shock-wave/boundary-layer interaction control using a backward facing step, *Aerosp. Sci. Technol.* 84 (2019) 1011–1019.
- [9] A.D. Johnson, D. Papamoschou, Instability of shock-induced nozzle flow separation, *Phys. Fluids* 22 (1) (2010) 16102.
- [10] B.J. Olson, S.K. Lele, Large-Eddy Simulation of an over-expanded planar nozzle, *AIAA Pap.* 3908 (2011) 2011.
- [11] S. Verma, M. Chidambaramathan, A. Hadjadj, Analysis of shock unsteadiness in a supersonic over-expanded planar nozzle, *Eur. J. Mech. B, Fluids* 68 (2018) 55–65.
- [12] J.P. Dussauge, P. Dupont, J.F. Debiève, Unsteadiness in shock wave boundary layer interaction with separation, *Aerosp. Sci. Technol.* 10 (2006) 85–91.
- [13] P. Dupont, C. Haddad, J.P. Ardissonne, J.F. Debiève, Space and time organisation of a shock wave/turbulent boundary layer interaction, *Aerosp. Sci. Technol.* 9 (7) (2005) 561–572.
- [14] B. Ganapathisubramani, N.T. Clemens, D.S. Dolling, Effects of upstream boundary layer on the unsteadiness of shock-induced separation, *J. Fluid Mech.* 585 (2007) 369–394.
- [15] O.H. Ünalms, D.S. Dolling, Decay of wall pressure field and structure of a Mach 5 adiabatic turbulent boundary layer, *AIAA Pap.* 94 (1994) 2363.
- [16] S.J. Beresh, N.T. Clemens, D.S. Dolling, Relationship between upstream turbulent boundary-layer velocity fluctuations and separation shock unsteadiness, *AIAA J.* 40 (12) (2002).
- [17] S. Piponniau, J.-P. Dussauge, J.-F. Debiève, P. Dupont, A simple model for low-frequency unsteadiness in shock-induced separation, *J. Fluid Mech.* 629 (2009) 87–108.
- [18] S. Pirozzoli, F. Grasso, Direct numerical simulation of impinging shock wave/turbulent boundary layer interaction at $M = 2.25$, *Phys. Fluids* 18 (6) (2006).
- [19] E. Martelli, P.P. Ciottoli, L. Saccoccio, F. Nasuti, M. Valorani, M. Bernardini, Characterization of unsteadiness in an overexpanded planar nozzle, *AIAA J.* 57 (2019) 239–251.
- [20] M. Germano, U. Piomelli, P. Moin, W.H. Cabot, A dynamic subgrid-scale eddy viscosity model, *Phys. Fluids* 3 (7) (1991) 1760–1765.
- [21] D.K. Lilly, A proposed modification of the Germano subgrid-scale closure method, *Phys. Fluids* 4 (3) (1992) 633–635.
- [22] A. Piquet, B. Zebiri, A. Hadjadj, M.S. Shadloo, A parallel high-order compressible flows solver with domain decomposition method in the generalized curvilinear coordinates system, *Int. J. Numer. Methods Heat Fluid Flow* 30 (1) (2019) 2–38.
- [23] Soshi Kawai, Johan Larsson, Dynamic non-equilibrium wall-modeling for large eddy simulation at high Reynolds numbers, *Phys. Fluids* 25 (1) (2013) 015105.
- [24] Cédric Duprat, Guillaume Balarac, Olivier Métais, Pietro Marco Congedo, Olivier Brugière, A wall-layer model for large-eddy simulations of turbulent flows with/out pressure gradient, *Phys. Fluids* 13 (1) (2011) 015101.
- [25] B. Zebiri, A. Piquet, A. Hadjadj, S.B. Verma, Shock-induced flow separation in an overexpanded supersonic planar nozzle, *AIAA J.* 58 (5) (2020) 2122–2131.
- [26] A. Piquet, Physical analysis and numerical simulation of the separation phenomenon in over-expanded nozzle flow, Phd. thesis, Normandie Université, 2017, (NNT: 2017NORMIR09). (tel-01689970).
- [27] Z.-T. Xie, I.P. Castro, Efficient generation of inflow conditions for large eddy simulation of street-scale flows, *Flow Turbul. Combust.* 81 (3) (2008) 449–470.
- [28] F. Unger, R. Friedrich, Numerical simulation of fully developed turbulent pipe flow, *Notes Numer. Fluid Mech.* 38 (1993) 201–216.
- [29] J. Eggels, J. Westerweel, F. Nieuwstadt, R. Adrian, Direct numerical simulation of turbulent pipe flow, *Appl. Sci. Res.* 51 (1–2) (1993) 319–324.
- [30] M. Rudman, H.M. Blackburn, Large eddy simulation of turbulent pipe flow, in: *Second International Conference on CFD in the Minerals and Process Industries*, Melbourne, Australia, Dec, 1999, pp. 6–8.
- [31] X. Xu, Large eddy simulation of compressible turbulent pipe flow with heat transfer, Master thesis, Iowa State Univ., 2003.
- [32] M. Klein, A. Sadiki, J. Janicka, A digital filter based generation of inflow data for spatially developing direct numerical or large eddy simulations, *J. Comp. Physiol.* 186 (2) (2003) 652–665.
- [33] S. Ghosh, H. Foysi, R. Friedrich, Compressible turbulent channel and pipe flow: similarities and differences, *J. Fluid Mech.* 648 (2010) 155–181.
- [34] A. Kistler, Fluctuating wall pressure under a separated supersonic flow, *J. Acoust. Soc. Am.* 36 (3) (1964) 543–550.
- [35] S. Deck, A.T. Nguyen, Unsteady side loads in a thrust-optimized contour nozzle at hysteresis regime, *AIAA J.* 42 (9) (2004) 1878–1888.
- [36] G. Dumnov, Unsteady side-loads acting on the nozzle with developed separation zone, in: *32nd Joint Propulsion Conference and Exhibit*, AIAA Paper, 1996, 96-3220.

- [37] M. Terhardt, G. Hagemann, M. Frey, Flow separation and side-load behavior of truncated ideal rocket nozzles, *AIAA Pap.* 3686 (2001).
- [38] S. Deck, P. Guillen, Numerical simulation of side loads in an ideal truncated nozzle, *J. Propuls. Power* 18 (2) (2002) 261–269.
- [39] P. Dupont, C. Haddad, J. Debiève, Space and time organization in a shock-induced separated boundary layer, *J. Fluid Mech.* 559 (2006) 255–277.
- [40] H. Tanna, An experimental study of jet noise part II: shock associated noise, *J. Sound Vib.* 23 (2009) 79–107.
- [41] D.J. Bodony, S.K. Lele, Current status of jet noise predictions using large-eddy simulation, *AIAA J.* 46 (2) (2008) 364–380.
- [42] S. Bühler, L. Kleiser, C. Bogey, Simulation of subsonic turbulent nozzle jet flow and its near-field sound, *AIAA J.* 52 (8) (2014) 1653–1669.
- [43] M. Ponton, J. Seiner, The effects of nozzle exit lip thickness on plume resonance, *J. Sound Vib.* 154 (3) (1992) 53–549.
- [44] R. Larusson, M.O. Burak, N. Andersson, J. Östlund, Dynamic mode decomposition applied to a detached-eddy simulation of separated nozzle flow, in: 55th AIAA Aerospace Sciences Meeting, 2017, AIAA 2017-0527.
- [45] R. Larusson, N. Andersson, J. Östlund, Dynamic mode decomposition of a separated nozzle flow with transonic resonance, *AIAA J.* 55 (4) (2017) 1295–1306.
- [46] M.R. Jovanović, P.J. Schmid, J.W. Nichols, Sparsity-promoting dynamic mode decomposition, *Phys. Fluids* 26 (2) (2014) 024103.
- [47] L. Yang, M. Dong, F. Benshuai, L. Qiang, Z. Chenxi, Direct numerical simulation of fine flow structures of subsonic-supersonic mixing layer, *Aerosp. Sci. Technol.* 95 (2019) 105431.
- [48] X.W. Lu, G. Huang, J. Wang, S. Hong, Spatio-temporal dynamic mode decomposition in a shear layer flow, *Aerosp. Sci. Technol.* 91 (2019) 263–271.
- [49] J.N. Kutz, F. Xing, S.L. Brunton, Multiresolution dynamic mode decomposition, *SIAM J. Appl. Dyn. Syst.* 15 (2) (2016) 713–735.
- [50] P.J. Schmid, Dynamic mode decomposition of numerical and experimental data, *J. Fluid Mech.* 656 (2010) 5–28.

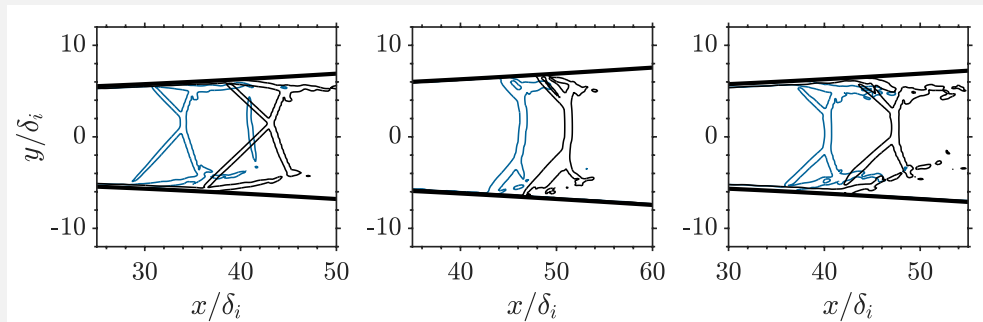
7

Wall temperature effects on shock wave/turbulent boundary layer interactions

Not yet published work.

Highlights

- Consistently with previous numerical simulations, the wall cooling leads to a considerable reduction in the interaction length scales, mainly through the size of the separation bubble, whereas the opposite holds for the wall heating.
- More pronounced λ -shock structure is observed when cooling/heating the walls with a larger Mach stem compared to the adiabatic case.
- An energy decrease at low-frequency shock oscillations is observed when cooling/heating the nozzle walls.



Z-averaged instantaneous numerical "Schlieren" contours showing the extreme positions reached by the shock for $NPR = 1.7$; (left) adiabatic case, (middle) cooled case, (right) heated case.

Abstract

Large-eddy simulation (LES) of supersonic planar-nozzle flow is carried out in this study. Two nozzle-flow configurations, with adiabatic and with isothermal walls, are presented. The effect of the wall-temperature variations on the shock structure as well as on the low-frequency oscillations and on the side loads is demonstrated. The effects of wall-temperature variations on the side loads is also demonstrated.

7.1 Introduction

The problem of shock interactions in the presence of a fixed or mobile wall presents an undeniable interest in aeronautical and space applications. The field of application covers all supersonic aviation and particularly relates to flows in supersonic air intakes, in nozzle flows with separation or in external flows along the fuselage. In fact, when a spacecraft flies at a very high Mach number, shock waves get formed and give rise to very complex flows such as shock wave/turbulent boundary layer interactions (SWBLI). The SWBLI have a large impact on the aerodynamic and thermodynamic design, and being responsible for many problems such as: the increased internal machine losses, the thermal and the structural fatigue due to the increased heat transfer rates, in addition to many flow unsteadiness and the broadband noise emission [Bernardini et al. \(2016\)](#).

Previous studies on SWBLI, whether experimental [Piponnier et al. \(2009\)](#), [Souverain et al. \(2010\)](#) or numerical [Pirozzoli & Grasso \(2006\)](#), [Touber & Sandham \(2009\)](#), [Morgan et al. \(2013\)](#), [Bernardini et al. \(2016\)](#), have focused on the cases with adiabatic walls, with more effort invested in characterizing large scales as well as low-frequency instabilities found in this type of flow. However, less attention has been paid to the wall thermal conditions, even though, the wall thermal conditions are known to have an influence on the characteristics of the flow, moreover its influence on the SWBLI can be considerable. For instance, the strong cooling is capable of (i) shifting the laminar-turbulent boundary layer transition toward higher Reynolds numbers, (ii) producing a fuller incoming boundary layer velocity profile, and (iii) reducing the thickness of the subsonic layer by decreasing the local speed of sound as reported by both [Delery J \(1986\)](#), [Bernardini et al. \(2016\)](#). The same last remark was reported by [Sciacovelli et al. \(2017\)](#) in the case of dense gas, where the high specific heat leads to negligible temperature variations and thus leading to a wall cooling-like situation.

Regrettably, fewer are the studies on this topic and rare are those treating this problem in nozzle flows. For instance, the effect of wall cooling, relative to the adiabatic condition for an oblique shock wave impinging on a turbulent boundary layer at $M_\infty = 3.5$, is to

increase the separation angle and to decrease the separation distance as found by [Back & Cuffel \(1976\)](#). [Delery \(1992\)](#) showed that heating the surface greatly increases the extent of the interaction zone and the separation point move much farther upstream than under adiabatic conditions. [Jaunet et al. \(2014\)](#) reported, for $M_\infty = 2.3$ shock-induced boundary layer separation, that a hot wall increases the interaction length scales and influences the onset of separation. This scale change due to wall thermal conditions also has an effect on the flow unsteadiness, with the lower frequencies becoming more and more important by heating the wall. [Bernardini et al. \(2016\)](#) performed a direct numerical simulation to investigate the effect of the wall temperature on the behavior of oblique shock wave turbulent boundary layer interactions at free-stream Mach number 2.28. They found that cooling the walls decreases the characteristic scales of the interaction in terms of the upstream influence and extends the separation bubble. The opposite behavior is observed in the case of heating, which produces a marked dilatation of the interaction region. Beyond that, all studies addressed the case of adiabatic wall conditions, and to our knowledge, no high-fidelity simulations have been carried out to explore the effect of either wall-nozzle heating or cooling on the shock structure as well as on its low-frequency oscillations and side loads.

In the present study, we look at the effects of wall temperature in nozzle flows by means of both wall-resolved/modeled three dimensional LES simulations. The focus is on the changes in shock structure and the role of these change in controlling the shock movement.

The present chapter is organized as follows. The next section introduces the computational strategy and domain followed by the results and the discussion. Finally, a conclusion is drawn at the end of the chapter.

7.1.1 Computational strategy and computational domain

The curvilinear solver used for the present analysis is the same as the one used in both [Piquet et al. \(2019\)](#) and [Zebiri et al. \(2020\)](#). Three-dimensional Navier-Stokes equations are solved with a molecular viscosity μ assumed to follow Sutherland's law. The thermal conductivity k is related to μ through $k = C_p \mu / Pr$ with $Pr=0.72$. The convective fluxes are discretized using sixth-order central scheme for smoothed parts and five-order Weighted-Compact-Nonlinear Scheme (WCNS) for shocked regions, with a shock sensor controlling the switch between the two. Time advancement is ensured using forth-order Runge-Kutta algorithm (RK4). The wall is modeled using the wall model of [Piquet \(2017\)](#), [Zebiri et al. \(2020\)](#). The computation mesh used for this study is the same as that used in [Zebiri et al. \(2020\)](#). More flow conditions for this case are reported in [Zebiri et al. \(2020\)](#).

Table 7.1: Flow parameters for LES simulations; NPR is the nozzle pressure ration and ε is the nozzle area ratio. The subscript w refers to the wall properties, ∞ to the free stream properties and th to the throat.

Test case	Line style	NPR	ε	$(T_w/T_\infty)_{th}$	Wall conditions
Mesh-A	—	1.7	1.6	1.2	adiabatic
Mesh-B	—	1.7	1.6	1.0	isothermal
Mesh-C	—	1.7	1.6	1.4	isothermal

7.2 The Influence of heating/cooling the walls

7.2.1 Mean flow parameters

For the present study, three wall-resolved LES (WR-LES) and their wall-modeled LES (WM-LES) have been carried out. For, three different wall temperature (T_w) corresponding to adiabatic-, cold-, and hot-wall thermal conditions. The turbulent boundary layer develops under the same nominal adiabatic conditions up to the throat where local cooling or heating started to be effective. The Reynolds number of the incoming boundary layer based on the momentum thickness, evaluated at the inlet, is $Re_{\theta,i} \sim 1100$. The present cases are labeled: case-A, case-B and case-C, for the adiabatic, cooled and heated cases respectively. Some flow parameters for the WR-LES simulations are reported in table 7.1.

The main effect of the heating the wall on the incoming flow can be understood by looking at figure 7.2a, where the temperature-velocity relationship in the boundary layer is reported for the three cases at the throat along the streamwise direction. This representation is very suited for describing the adaptation process of the boundary layer to the new thermal conditions at the wall. The shape of the profiles suggests that the outer region of the boundary layer significantly deviates from the equilibrium Walz solution Bernardini et al. (2016) in both adiabatic and heated cases. A good agreement is observed between the cooled case and Walz solution. This leads to conclude that the boundary layer is strongly perturbed by the heating. The total temperature profiles, for the three cases, are given in figure 7.2b. The profiles were measured at the throat *i.e.* $x/\delta_i = 0$. The internal thermal layer grows relatively rapidly such that it fills up the boundary layer thickness.

The spatial distribution of the mean skin friction coefficient for the three cases is depicted in figure 7.3a. Upstream of the throat, the same behavior is observed for the three cases. When moving downstream, the presence of the shock decreases the skin friction coefficient sharply just before the beginning of the interaction, and for all cases

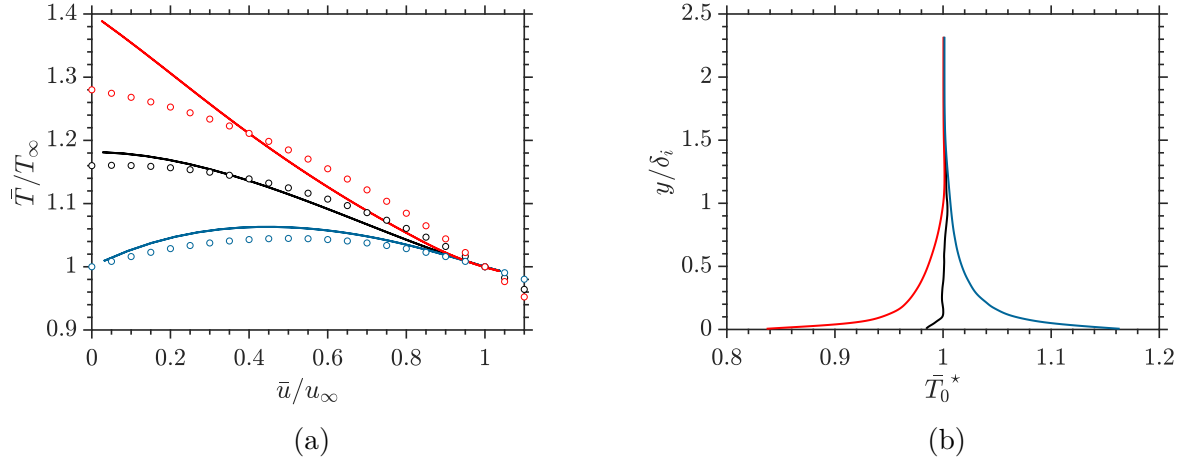


Figure 7.2: (a) Distribution of the temperature-velocity relationship at the throat with the circles indicating the equilibrium solutions, (b) Distribution of total temperature profiles at the throat, with — case-A, — case-B and — case-C.

mean flow separation is well observed. As observed before by [Bernardini et al. \(2016\)](#), the skin friction in the interaction region exhibits, generally, a typical W shape, characterized by two minima, however only one minimum appears for each case. The increase of the wall temperature produces a slight upstream displacement of this minimum, associated with the upstream shift of the separation shock. The influence of cooling/heating the nozzle walls on the mean wall pressure is presented in figure 7.3b. Heating the wall shifts upstream the separation position, leading to a slightly smoother pressure rise. The opposite behavior occurs when cooling the walls (case-B), resulting in a slight downstream shift of the separation position and a steeper variation of p_w within the interaction zone. Similarly, the pressure jump due to the shock that must be sustained in a narrower region, thus, cooling the wall increases the root-mean-square wall pressure p_{rms} , as shown in figure 7.3c.

The WM-LES is introduced through figure 7.4 where the normalized streamwise velocity along the wall-normal direction (at $x/\delta_i = -10$), for the adiabatic case (case-A). The normalized streamwise velocity is compared to previous numerical studies of [Olson & Lele \(2011\)](#) and [Piquet \(2017\)](#). The first near-wall cells are located at $y^+ \sim 20$, *i.e.* $\Delta y^+ \sim 40$. The results are in good agreement with the wall-resolved case, especially in the outer layer of the boundary layer and in the log-law region. The first near-wall point seems to be slightly under-resolved. Having established the properties of the incoming boundary layer, we proceed to describe the main features of the flow. For that purpose, instantaneous three-dimensional flow field is shown in figure 7.5. The flow exhibits for the three cases a similar overall organization, showing interesting shock-wave patterns. The classical shock pattern expected in divergent nozzles exhibits a lambda shock-wave structure. This pattern consists of an incident shock, IS, a reflected shock, RS and a

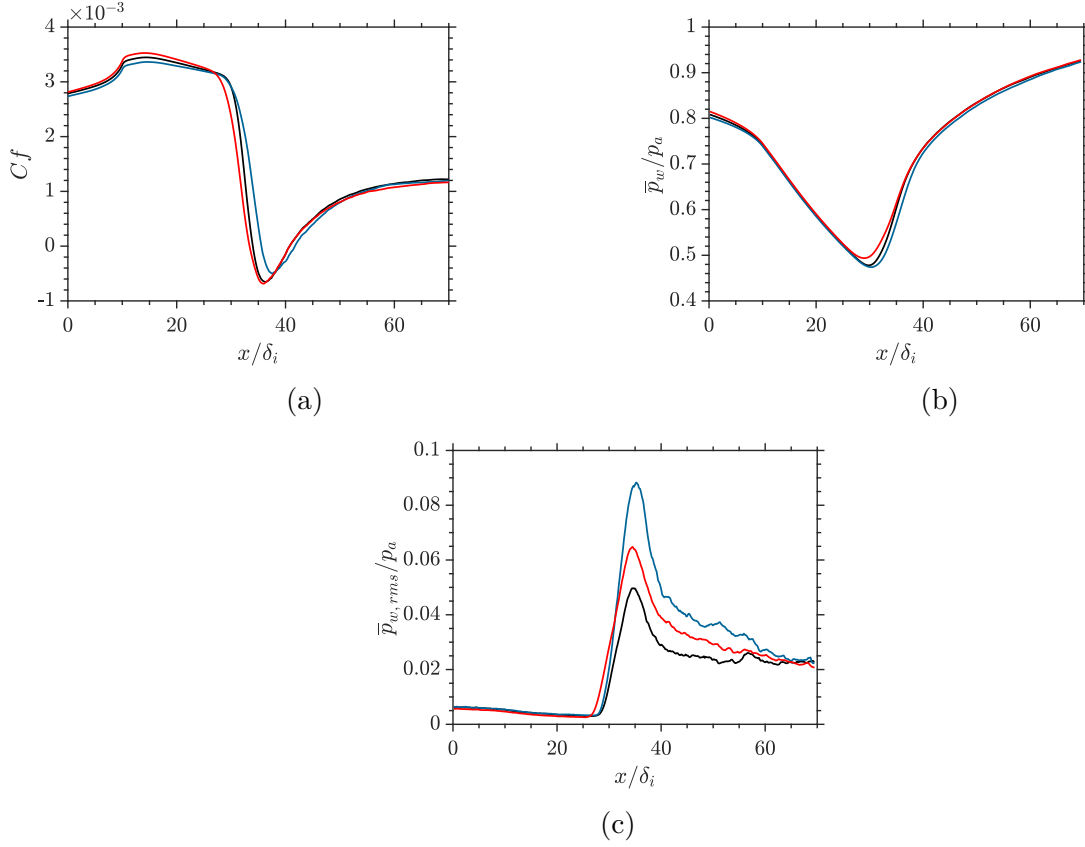


Figure 7.3: (a) skin friction coefficient distribution over the lower wall (C_f), (a) Normalized-mean wall pressure distribution (p_w/p_a) and (c) Normalized root mean square of the wall pressure at the lower wall (p_{rms}/p_a) with — case-A, — case-B and — case-C.

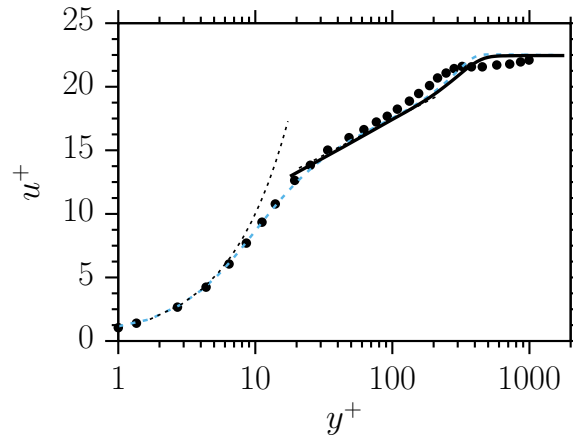


Figure 7.4: Van Driest velocity along the wall-normal direction at $x/\delta_i = -10$; —: WM-LES, -- : WR-LES from Piquet (2017), - - : $u^+ = y^+$ and the log-law with $\kappa = 0.41$ and $C^+ = 6.2$, •: WR-LES from Olson & Lele (2011).

Mach stem, MS (very short in the adiabatic case and larger for the cooled/heated cases) as shown in figure 7.6. In this configuration, the separation of the boundary layer, due to the high adverse pressure gradient, creates an incident shock impinging the Mach stem at the triple point TP. The reflected shock realigns the incident flow to the original direction. The Mach stem is a strong shock which creates a subsonic flow behind it. The slip line that delimits the shear layer is involved in the confinement on the flow, which reaccelerates and produces multiple shocks. The succession of shocks is called a shock train and has been observed in many nozzle flows. The dynamical character of the shock system, which oscillates back and forth may be clearly appreciated in figure 7.6 where we present the two extreme positions of the shock.

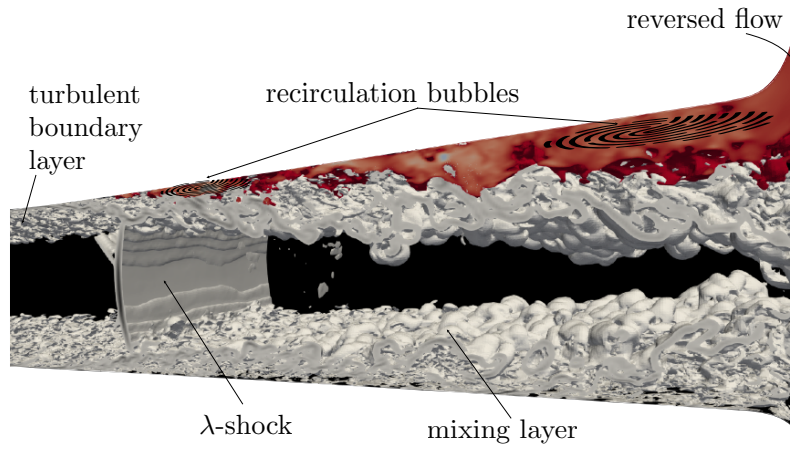


Figure 7.5: 3D representation of the different phenomenon observed in the nozzle flow; the shock system and the turbulent boundary layer represented using the iso-volume of the $\nabla||\rho||$ and the reversed flow using $\nabla||u||$.

To better characterize the unsteady behavior of the flow we show in figure 7.7 contours of the instantaneous skin friction C_f and the instantaneous Stanton number Sr in the lower wall for the three cases. When crossing the interaction zone, where flow patches of the instantaneous reversed flow are found, starting from the beginning of the interaction and extending to the exit of the nozzle. In this region, the local Stanton number exhibits a strong intermittent behavior, characterized by scattered spots with extremely high heat transfer rate. This behavior is more pronounced in the heated case (case-C) and less present or almost absent in the cooled case.

Compared to the adiabatic case (case-A), wall cooling (case-B) pushes the separation location downstream resulting in a significant reduction of the recirculation zone, whereas heating the wall leads to the opposite effect. The location of the separation point is mostly affected by the wall heating. The present observations are in good agreement with those of Bernardini et al. (2016) made for a flat plate.

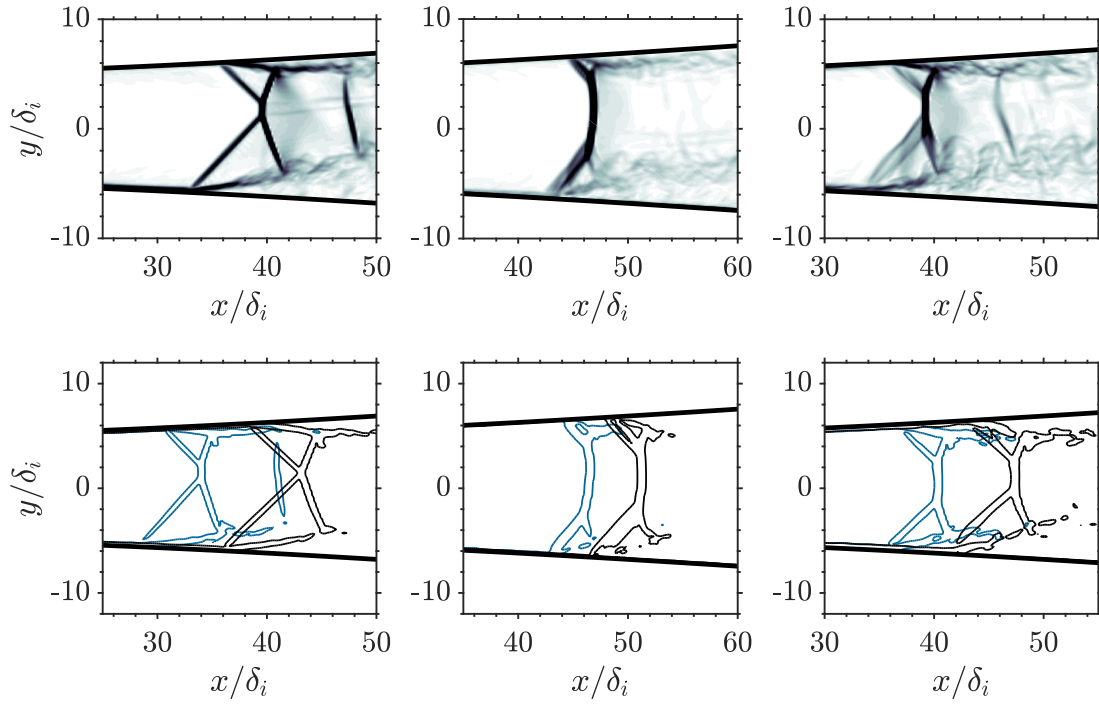


Figure 7.6: Z-averaged instantaneous numerical "Schlieren" contours with the extreme positions reached by the shock are shown below; (*left*) case-A, (*middle*) case-B, (*right*) case-C.

7.2.2 Low-frequency oscillations

To further characterize the flow unsteadiness and to assess the possible influence of heating/cooling the walls on the low-frequency unsteadiness, figure 7.8 shows the pre-multiplied spectra of the pressure fluctuations at the lower wall as a function of Strouhal number and streamwise coordinates. For the three cases, the spectral map is characterized by three different zones. The first one extends from the throat to the separation position. This zone is a typical feature of a turbulent boundary layer. The second zone is associated with the dynamics of the shock system and it is identified by means of substantial energy at low frequency with a broad peak defined as the main tone.

More details can be found in figure 7.9a representing the premultiplied spectra of the shock position. Thus, the figure clearly shows that the cooling/heating of the walls causes a drop in the energy of what is called the main tone. This is essentially due to the change in the structure of the shock caused by the cooling/heating of the walls. In addition to the immediate proximity of the shock from the nozzle exit in the cooled case (case-B) which supposed to reduce the separation length and therefore it decreases the main tone. As for the shock structure, we notice that the cooling/heating actually transforms the λ -shock of the adiabatic case into a more pronounced λ -shock, with a wider Mach stem and with a smaller degree of asymmetry (see figure 7.6). The previous

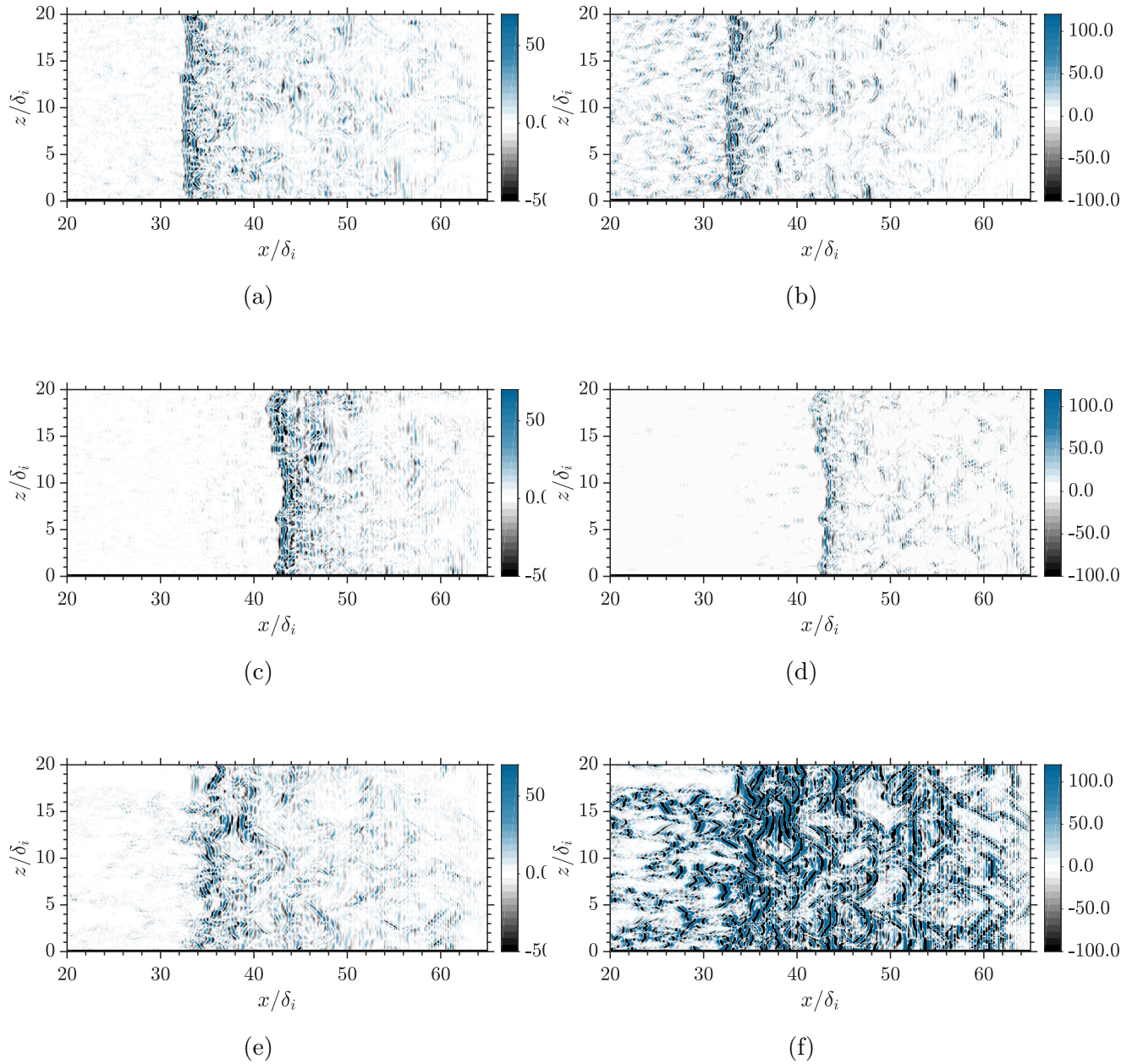


Figure 7.7: Contours of instantaneous skin friction (left) and Stanton number (right); (a,b) case-A, (c,d) case-B, (e,f) case-C.

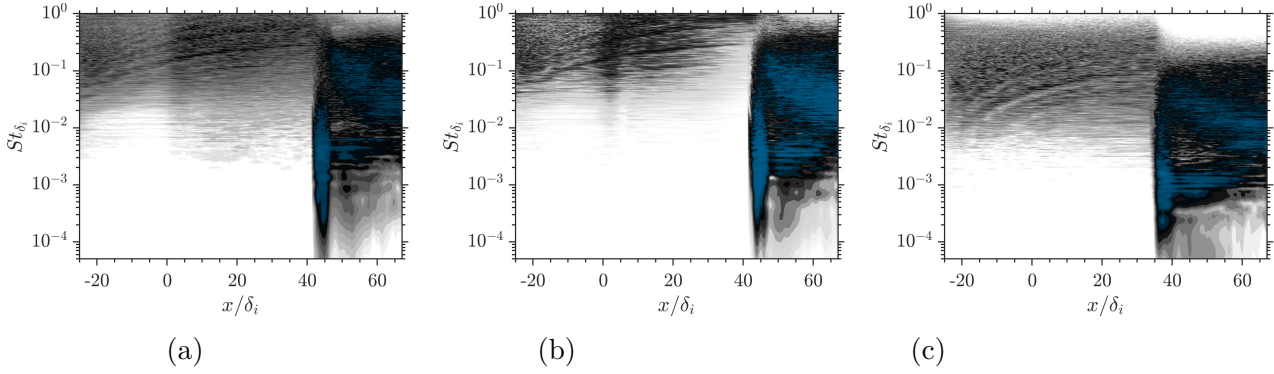


Figure 7.8: Normalized pre-multiplied spectra map of the pressure fluctuations at the lower wall, with blue regions being the most energetic and the white regions the less energetic; (a) case-A, (b) case-B and (c) case-C.

remarks result in more stability for the shock, basically, with less asymmetrical λ -shock, which gives more balance between the reverse flow entering at the bottom and at the top. The shock is, thus, more stable and makes shorter oscillations. Consequently, fewer low frequencies are present in the graph of figure 7.9a. For the graph figure 7.9b representing the premultiplied spectra of side-loads, a drop in the energy of low frequency phenomena falling into the interval $S_t \in [10^{-3} : 10^{-2}]$ is noticed. Behind this drop, we also found the drop in oscillation span resulting from cooling/heating the walls. For the frequencies going on the interval $S_t \in [10^{-2} : 0.5]$, we notice that the graphs are perfectly the same. The phenomena belonging to this interval are mainly due to the activities of the mixing layer, clearly, not affected by cooling/heating the walls.

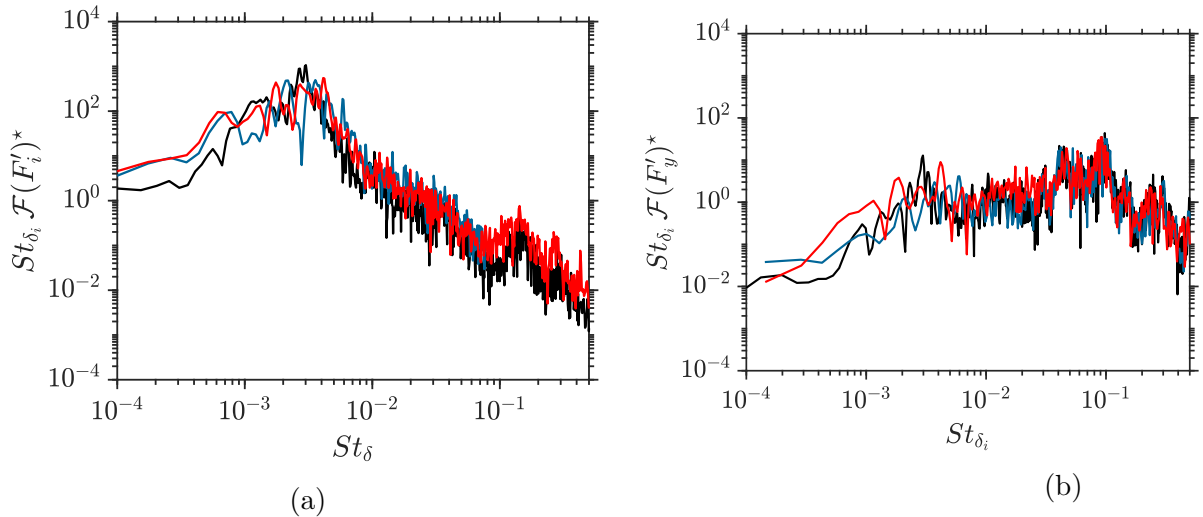


Figure 7.9: Normalized pre-multiplied spectra of: (a) shock position, (b) side loads with — case-A, — case-B and — case-C.

7.3 Concluding remarks

The behavior and the characteristics of the shock induced separation flow under cooling/heating conditions in over expanded planar nozzle with a mild divergent angle, has been analyzed by means of very long three-dimensional WM-LES. Detailed flow statistics have been presented, including steady and unsteady parameters. Particular effort has been made to understand the response of the low frequency phenomena to cooling/heating the walls. Wall cooling leads to a considerable reduction of the interaction scales and of the size of the separation bubble, whereas the opposite holds for wall heating. The multiple premultiplied spectra presented show a small influence of cooling/heating the walls on the low-frequency shock motion, mainly a drop in the energy of very low-frequency phenomena representing the shock motion is observed. The energy drop is more pronounced in the cooled case where the span of the oscillation is less important. However, the decrease in the span oscillation is caused by the modification of the shock structure resulting from the cooling/heating. Interestingly, more pronounced λ -shock is observed when cooling/heating the walls with a larger Mach stem compared to the adiabatic case. This configuration promotes less asymmetry and thus more stability.

Conclusions and perspectives

This thesis is devoted to the analysis of unsteady shock wave/boundary layer interaction (SWBLI) in over-expanded nozzles. The SWBLI phenomenon is usually associated with a low-frequency shock unsteadiness that drives the generation or amplification of the dynamic loads acting on the nozzle wall. These loads, known as side-loads, are prejudicial for the integrity of the mechanical structure of the nozzle and can cause severe damages. This study aims to shed more light into the complex flow physics related to SWBLI in supersonic nozzles, by employing high-fidelity numerical simulations technique, that are capable of reproducing the unsteady aspects of the turbulent flow, the three-dimensional structure of the interaction as well as the shock oscillations, in the low-frequency energy ranges, with large scale excursions.

The manuscript begins with an introduction section that summarizes the most relevant physical aspects of the nozzle flow separation (NFS), before presenting the different scenarios of low-frequency shock oscillations phenomena in SWBLI. The influence of the downstream/upstream disturbances that take place during the SWBLI is also underlined, in addition to the different post-shock instabilities, occurring mainly in the recirculation bubbles and in the mixing layer downstream of the interaction region. Comparison between planar and axisymmetric nozzle flows is provided with emphasis on the symmetry/non-symmetry aspect of the separation.

In terms of numerical simulations, a special effort is made to assess the numerical tool used in the context of the current study. This code, called CHOC-WAVES (Compressible High-Order Code using Weno Adaptive Stencils), solves three-dimensional compressible Navier-Stokes equations with domain decomposition method in the generalized curvilinear coordinates system (for complex geometries). The code is validated through a set of test problems, including (but not limited to) supersonic boundary layer, compressible channel flow, flow over a cylinder, jets and mixing layer. In the context of the LES study, a wall-model, based on a Thin-Layer Boundary-Layer Equations (TLBLE), is used to

account for the near-wall effects, allowing to gain a significant CPU time and to achieve very long integrations. A complete presentation of this model is provided, along with a qualification of the model parameters through *a-priori* as well as *a-posteriori* tests. It is found that, in addition to its relative simplicity of implementation in an existing LES code, the LES wall model is capable of saving a considerable amount of computational time, while providing quite satisfactory results in terms of mean-flow velocity and turbulent Reynolds stresses, boundary-layer separation and shock unsteadiness. Investigating both planar and conical supersonic over-expanded nozzles, the LES results allowed to draw the main concluding remarks:

Shock oscillations in planar nozzles

- The initial objective was to check whether or not a flip-flop jet instability between the top and bottom nozzle walls exists in the range of the selected nozzle pressure ratio (NPR of 1.7). If this phenomenon would happen, it would have a very characteristic low-frequency. For that purpose, very long simulations were carried out over an integration time that is 18 times longer than Piquet (2017), Olson & Lele (2011), and Papamoschou & Johnson (2006). The integration time was large enough to capture several shock excursions, therefore having better statistics convergence. To the best of the author's knowledge, this is the longest time integration in separated nozzle flows never reached so far. During this long simulation, the jet was seen to be stable, sticking on one side of the nozzle wall, without switching to the other side during the entire simulation.
- Various flow configurations with different shock patterns were then investigated. All the simulations clearly established the symmetry/asymmetry behavior of the jet flow as well as the low-frequency shock oscillation (LFO) found in the experiments. The LFO activity is seen to be most prominent in the vicinity of the reflected-shock foot and characterized by a broadband spectrum covering more than three frequencies decades.
- It was established that the peak, corresponding to the low-frequency motions in the weighted spectrum, is located three orders of magnitude below the peak associated with the upstream boundary-layer turbulence. This confirms that the upstream boundary layer is not responsible for the LFO generation.

Furthermore, a parametric study was performed aiming to highlight the effect of the nozzle pressure ratio on the low-frequency shock oscillations. In the light of this study, it was found that:

- The low-frequency motions are related to the successive contractions and dilations of the separated bubble. The wider is the bubble the larger are the span of oscillations.
- Additionally, the reversal flow is found to be strongly correlated to the low-frequency shock motions, confirming previous conclusions of flows with larger λ -shock.
- For the shock movement, a difference in the way the whole shock structure behaves (including the Mach stem and the shock foot) is noticed. It was found that the Mach stem moves as a response to a pure low-frequency forcing. However, the shock foot movement is affected by both the low-frequency and some high-frequency perturbations arising from the fully turbulent regions including the boundary and the mixing layers.
- Careful analysis of the instantaneous flow field indicated that the Mach stem moves at almost a constant speed during its back and forth movements, confirming earlier observations of [Gonsalez & Dolling \(1993\)](#).
- More details are also provided regarding the shock motion. For instance, in its back-and-forth movement, the shock progresses discontinuously with a time break (pause), until it reaches its maximum position. The number of breaks made in one direction (upstream) is greater than that made in the other direction (downstream). Thus, for a given time (t_1), the shock can travel a longer distance going downstream because of fewer breaks. Knowing that the shock has a constant speed in both directions, this makes that the mean speed of the shock downstream appears greater than that upstream.
- Finally, an empirical relationship is proposed to model the main acoustic tone similar to the one proposed by [Zaman et al. \(2002\)](#).

As for the wall-temperature effects on the low-frequency shock oscillations, it was found that:

- The heat transfer by a wall cooling leads to a considerable reduction of the interaction length scales, affecting thereby the size of the separation bubble, whereas the opposite holds for heat transfer with wall heating.
- In terms of shock structure, we notice that the wall cooling actually transforms the λ -shock of the adiabatic case into a quasi-symmetric λ -shock, with a wider Mach stem. This creates a balance between the reversal flow entering from the bottom and the top sides of the nozzle. The shock is, thus, more stable and makes shorter

oscillations. Consequently, less low frequencies energy content is present in the spectra of the cooled wall.

Shock oscillations in conical (axisymmetric) nozzles

A comparison between a conical nozzle flow and an equivalent planar nozzle flow shows that:

- Whilst both configurations may share some common flow features, such as large-scale turbulent structures and shock-wave patterns, they show contrasts on the symmetry of the flow and the shock dynamics.
- The amplitude of the separation location is less important in the cylindrical case because of the increased pressure gradient, upstream of the throat, as a results of the reduced cross-section compared to the planar case.
- The frequency analysis of the flow reveals the existence of low-frequency phenomena arising from the oscillation of the shock system. The DMD analysis highlights the existence of two distinctive modes; i) the non-helical mode (flopping) which is mostly a low-frequency based mode, clearly visible in the spectra of the streamwise forces and ii) the helical mode which is a high-frequency based mode, appearing mainly in the spectra of the side-loads.
- Based on the current analysis, a classification of different modes is proposed, based on the Strouhl number:
 - * $St \in [... , 0.017]$: The mode in this interval is a flopping one, which is at the origin of the streamwise forces amplification through the oscillatory movement of the shock system.
 - * $St \in]0.017, 0.10]$: The mode in this range is found to be helical, which represents vortical structures of different sizes that become finer when increasing the frequency. These structures appear very close to the nozzle wall downstream of the shocked area, leading to consider these modes as the major responsible for side-loads amplification.
 - * $St \in [0.10, 0.40]$: This mode is caused by the high energy vortical structures, due to the mixing layer activities. This mode is less involved in the side-loads spectrum.

Perspectives

In a future work, it would be of particular interest to study the following points:

-
- Taking into account the very huge LES data build during this study, one immediate possible work would consist in further analysis of this database to investigate the implications of the ambient conditions (the far field conditions) on the asymmetry of the jet, more precisely in the choice of the asymmetry side. In fact, we have observed that the jet can change its asymmetry side as a result of shortening the ambient region. Also, it was found that bringing the jet from an asymmetric to symmetric then on asymmetric configurations by increasing then decreasing the NPR would push the jet to change its initial asymmetry side.
 - In the course of this study, we have observed, when visualizing the sonic lines, that a sonic envelope was formed each time the shock moves downstream, preventing the communication between the two boundary layers (*i.e.* upper and lower). But when the shock starts to return back to its upstream position, this envelope opens and a subsonic zone connecting the two boundary layer was formed. Thus, the question of the communication between both the upper and the lower boundary layers, in the presence of spanwise periodic conditions, was raised and it would be of interest to run simulations that account for the flow traceability over time. Also, the presence of the side walls would also be relevant for practical applications.
 - The observed mechanism which drives the shock instability implies that the coupling between the shear layer and the shock wave position is governed by one-dimensional flow quantities. To this end, a simple one-dimensional model could be constructed to capture the unsteadiness of the shock over a range of parameters. This simple model would use the LES data to reproduce the streamwise shock oscillation. In addition, the integration of the viscosity effects as well as the heat transfer, at the wall in the wall-normal direction, would improve this model.
 - Finally, the large database is generated during this thesis, can be used to train a machine learning algorithm that can help modeling subgrid scales which will further reduce the simulation time.

Appendix A

DNS of a turbulent boundary layer with zero-pressure gradient (ZPG)

A DNS of spatially-evolving supersonic boundary layer with ZPG over an adiabatic flat plate at $M_\infty = 2.25$ is performed. The computational domain extends from $x_{in} = 4''$, corresponding to $Re_x = 2.54 \times 10^6$, to $x_{out} = 9''$. The normal direction extends up to $0.5''$ and the grid is stretched with a minimum spacing near the wall of $\Delta y_{min}^+ \sim 1$. The spanwise direction of the domain is $0.175''$, resulting in a number of points of $N_x \times N_y \times N_z = 3584 \times 128 \times 256$. The freestream flow conditions are set at a static temperature of $169K$ with a momentum-thickness Reynolds number post transition equals to $Re_\theta = 4260$ ($Re_x = 4.5 \times 10^6$).

Both temperature and velocity inlet profiles are generated according to procedure given in White's book [White & Corfield \(2006\)](#), while the pressure is kept constant. The imposed perturbation at the wall is similar to the one implemented by Guarini *et al.* [Guarini et al. \(2000\)](#) and is extended from $x = 4.5''$ to $x = 5''$. The random numbers are created by a normal/gaussian distribution using the Mersenne Twister random number generator with a cycle of $2^n - 1$ (with $n = 19937$) to avoid repetitive patterns. The perturbation model follows the specifications of [Pirozzoli et al. \(2004\)](#).

The statistics have been averaged in space and time over 10 characteristic time. Figure [A.1a](#) shows the Van Driest transformed velocity profile, ($Re_x = 4.8 \times 10^6$), compared to the classical log-layer formulation and to DNS data [Pirozzoli et al. \(2004\)](#) and [Gatski & Erlebacher \(2002\)](#). An overall good collapsing between the data is obtained, showing the ability of the wall model to adequately restore the boundary layer velocity profile.

The mean temperature profile is plotted in figure [A.1b](#). The adiabatic wall temperature is also correctly captured by the model. The theoretical temperature is obtained using the Crocco–Busemann relation ([Pirozzoli et al. 2004](#)).

Figure [A.2](#) shows the normal Reynolds stress components and the shear stress tensor.

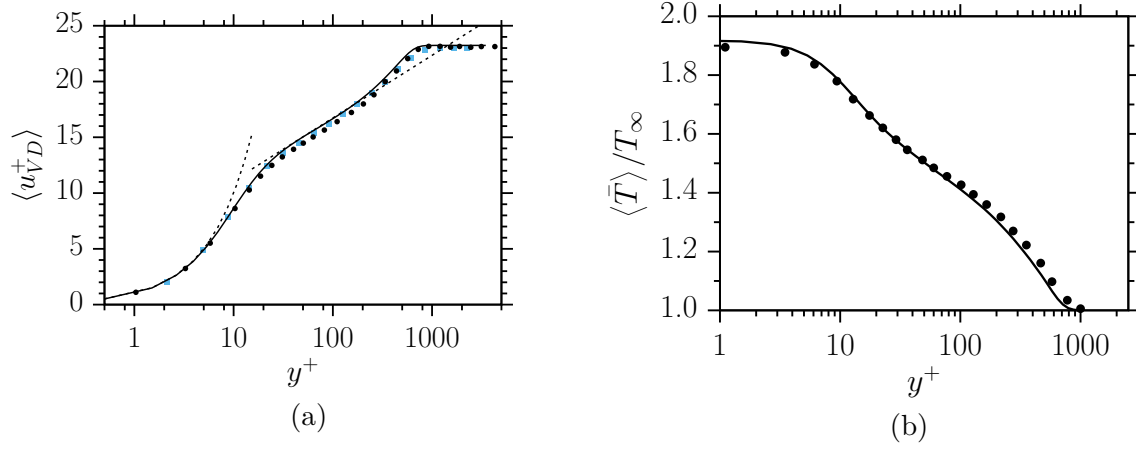


Figure A.1: (a) Van Driest normalized velocity at $Re_x = 5 \times 10^6$; \bullet : Pirozzoli et al. Pirozzoli et al. (2004), \blacksquare : Guarini et al. Gatski & Erlebacher (2002), -- : Log-wall with $C^+ = 5.5$, (b) Averaged temperature profile at $Re_x = 5 \times 10^6$; \bullet : Pirozzoli et al. Pirozzoli et al. (2004).

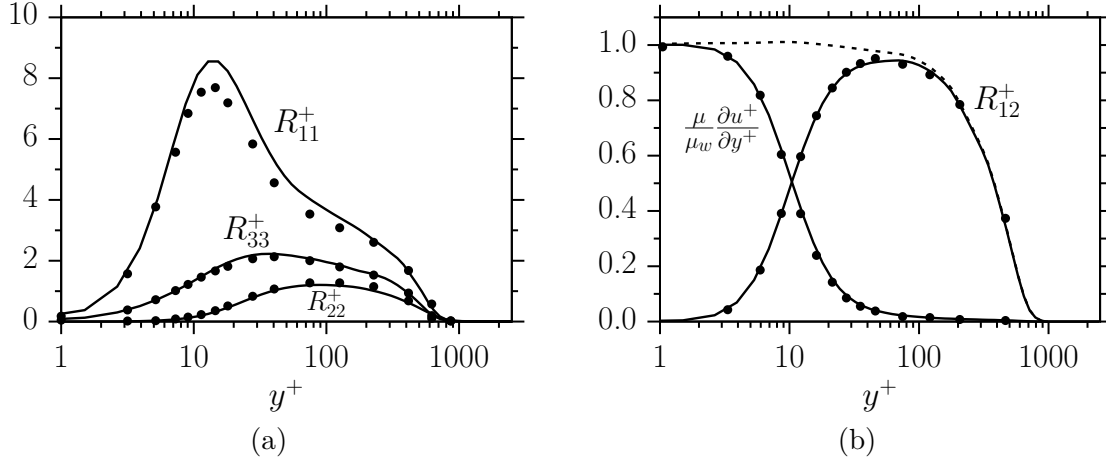


Figure A.2: Streamwise, wall-normal and spanwise Reynolds stress tensor (a) and normalized shear tensor terms (b) at $Re_x = 5 \times 10^6$; \bullet : Pirozzoli et al. Pirozzoli et al. (2004).

A good agreement with the DNS data of Pirozzoli is found. However, the magnitude of the streamwise component is slightly over-predicted in this case (approximately 8%). This difference can be explained by the extra-term $\langle \rho' u_i' u_i' \rangle$, resulting from the difference between the Reynolds fluctuating field, *i.e.* $\langle \rho \rangle \langle u_i' u_i' \rangle$ used by Pirozzoli and the Favre averaging operator, *i.e.* $\langle \rho \rangle \widetilde{u_i'' u_i''}$ used in the current simulation, which is not negligible in the outer part of the boundary layer. The shear stress tensor shows a good agreement with the results of Pirozzoli and confirms their findings on the fact that the density scaled Reynolds stress does not exceed unity as predicted by Maerder et al. (2001). As expected, the total stress is almost constant in the inner layer.

Appendix B

Multi-resolution Dynamic Mode Decomposition.

Multiple studies on Dynamic Mode Decomposition applied to nozzles have been performed by several researchers [Larusson et al. \(2017\)](#), [Jovanovic et al. \(2014\)](#), [Hiroshi et al. \(2017\)](#). The studies were mainly focused on the acoustic of the issuing jet from the nozzle.

For instance, [Larusson et al. \(2017\)](#) investigated a supersonic jet using a DMD method. In their case, the algorithm was applied on a set of data resulting from a series of LES simulations of a conical nozzle as well as 2D RANS simulations.

The authors reported that the LES DMD results are comparable to those of RANS DMD. In addition, the modes resulting from the LES DMD are found to be more damped compared to those resulting from the RANS DMD and the Arnoldi method. The authors also noted that the damping of low frequencies decreases by increasing the cycle of perturbations added to the sampling average. The modes extracted in this study mainly correspond to the shock-cell movement and acoustic radiations. Further flow features have been studied through DMD analysis, such as the shear layer which has been studied using the spatio-temporal DMD method developed by [Weiyu et al. \(2019\)](#). The proposed method can capture the dominant unsteady vortices in the flow field and obtain the quantitative information of the streamwise development. The DMD was, also, applied to the mixing layer [Yang et al. \(2019\)](#). It was found that there is a certain dominant frequency in the flow structure, which can provide a reference for the active mixing enhancement method.

Another interesting study was conducted by [Jovanovic et al. \(2014\)](#) in which the screech mode was identified, and described as a flopping mode. [Jovanovic et al. \(2014\)](#) linked the upstream propagation of acoustic waves to the time-periodic-compression caused by the oscillations of the shock. They also noticed that acoustic waves propa-

gate upstream by jumping between negative spots. In fact, the mixing layer rotates the shock cells. In this case, the outer end of the cell will pass from upstream to downstream, generating an impulse for the exterior acoustic perturbation which will push it upstream to the next cell.

As explained in 6, the DMD method used in this work is the Multi-resolution DMD (MrDMD)(Kutz et al. 2016). The reason we make this choice is the wide range of frequencies involved in this flow and in order to focus mainly on the low frequencies. The algorithm is able to split robustly the complex systems into a hierarchy of multi-resolution time-scale components. It consists of applying a simple DMD by Schmid (2010) to the given set of snapshots, initially organized in a matrix, where n is the number of spatial measurement par time snapshot and m is the number of snapshots.

$$Q_0^{m-1} = \{q_0, q_1, q_2, \dots, q_{m-1}\} \quad (\text{B.1})$$

The eign-decomposition approximation of the best fit linear operator A , that relates two successive states, is given by $q_{j-1} \simeq Aq_j$. Considering the previous, one can write that $Q_1^{m-1} = \{q_1, Aq_1, A^2q_2, \dots, A^{m-2}q_1\}$. By choosing A that minimizes the Frobenius norm of $[Q_2^m - AQ_1^{m-1}]_F$, one can write according to Kutz et al. (2016):

$$Q_2^m \simeq AQ_1^{m-1} \quad (\text{B.2})$$

Using reduced SVD factorization, Q_0^{m-1} is written as following

$$Q_0^{m-1} = U\Sigma W^* \quad (\text{B.3})$$

where U contains the left singular vectors (POD modes), W contains the right singular vectors and the singular values are in Σ . The A matrix and its projection onto POD modes (\tilde{A}) are given by:

$$A = Q_2^m V \Sigma^{-1} U^* \quad (\text{B.4})$$

$$\tilde{A} = U^* A U = U^* Q_2^m V \Sigma^{-1} \quad (\text{B.5})$$

The eigenvectors (W) and the corresponding eigenvalues (λ_k) are then computed by eigendecomposing \tilde{A} , ($\tilde{A}W = W\Lambda$), where Λ is a diagonal matrix containing λ_k . The damping factor ξ and the frequency f are given by

$$\arg(\mu) = 2\pi f \Delta t + 2\pi b \quad (\text{B.6})$$

$$\xi = \frac{\ln \|\mu\|}{\Delta t} \quad (\text{B.7})$$

where b is an integer that can be safely assumed to be zero (Larusson et al. 2017). The solution at a given instant t , $q_{DMD}(t)$, is given by

$$q_{DMD}(t) = \sum_{k=1}^m b_k(0) \psi_k(\xi) e^{(wt)} \quad (\text{B.8})$$

$$= \Psi \text{diag}(e^{(wt)}) b \quad (\text{B.9})$$

where ξ is the spatial coordinates, $b_k(0)$ is the initial amplitude of each mode, Ψ is a matrix containing the eigenvectors ψ_k , $\text{diag}(e^{(wt)})$ is a diagonal matrix containing the eigenvalues $e^{(w_k t)}$ and b is the vector of the coefficients b_k .

From the initial pass through the data, the slowest modes ($m1$) are removed, and the set of data is divided into two sets. The size of each set is $m/2$. A DMD is once again performed on each set and again the lowest modes ($m2$) for each set are removed. The algorithm is repeated next until the desired termination. Mathematically, one can write:

$$q_{DMD}(t) = \sum_{k=1}^m b_k(0) \psi_k^{(1)}(\xi) e^{(w_k t)} \quad (\text{B.10})$$

$$= \underbrace{\sum_{k=1}^{m1} b_k(0) \psi_k^{(1)}(\xi) e^{(w_k t)}}_{\text{Slow modes.}} + \underbrace{\sum_{k=m1+1}^m b_k(0) \psi_k^{(1)}(\xi) e^{(w_k t)}}_{\text{Fast modes.}} \quad (\text{B.11})$$

The first sum represents the slow mode dynamic, whereas the second one is everything else. The second part $Q_{m/2}$ is divided into two parts:

$$X_{m/2} = X_{m/2}^{(1)} + X_{m/2}^{(2)} \quad (\text{B.12})$$

For each level, slow modes are computed, the process continues by splitting in half each time, $X_{m/2}, X_{m/4}, X_{m/8}, \dots$, and performing DMD on each part until the desired decomposition is achieved.

List of Figures

1.1	Simplified diagrams of different generic nozzle configurations and their flow effects from Sutton & Biblarz (2016)	3
1.2	Nozzle flow regime during flight.	4
1.3	(a) Different shock reflections found in a nozzle flow from left to right: normal shock Papamoschou & Johnson (2006) , regular-reflection (RR) and Mach-reflection (MR) Grossman & Bruce (2018) , (b) A schematic showing different shock reflections found in nozzle flows.	5
1.4	Isovolume of $ \nabla u $ showing the topology of a λ -shock Olson & Lele (2011)	5
1.5	Color schlieren images of the exhaust flow from Verma & Manisankar (2014) showing flow topology with (<i>left</i>) Free Shock Separation (FSS) and (<i>right</i>) Restricted Shock Separation (RSS).	6
1.6	A schematic representation of (<i>left</i>) Free Shock Separation (FSS) and (<i>right</i>) Restricted Shock Separation (RSS).	6
1.7	Schematic representation of the SWBLI.	10
1.8	(a) Schematic of Kelvin-Helmholtz vortices originating from a separated mixing layer in a planar nozzle. (b) Different topologies of the Kelvin-Helmholtz instabilities; (a) a shadowgraph visualization of Kelvin-Helmholtz vortices originating from a subsonic plane mixing layer Brown & Roshko (1974) , (b) Kelvin-Helmholtz vortices emanating from the triple point Hadjadj et al. (2004)	18
1.9	Schematic representation showing a recirculation zone in a planar nozzle.	19
1.10	Trapped vortex at the nozzle lip, see Hadjadj et al. (2015)	20
1.11	A sequence of images of an externe flapping jet at $St = 7.0 \cdot 10^{-4}$ obtained by laser induced fluorescence, see Mi et al. (2001)	21
1.12	z-averaged numerical “Schlieren” imaging contour $\nabla \rho $; (a) planar nozzle, (b)conical nozzle for identical flow conditions, from Piquet (2017)	22
1.13	Iso-volume of pressure showing the toroidal shape of the lip vortices from Georges-Picot (2014)	24

2.1	Grid of the vortex test case	39
2.2	Comparison of centered schemes with different order of accuracy; $-$: 2th order, $-$: 4th order, $-$: 6th order, $-$: 8th order, \cdot : Exact solution.	40
2.3	Grid of the cylindrical vortex test case (<i>left</i>) and shifted pressure distribution at different time step (<i>right</i>); $-$: $t^* = 0$, $-$: $t^* = 5.9$, $-$: $t^* = 11.8$	41
2.4	Pressure field contour at different time step.	41
2.5	Grid of the compressible flow over a circular cylinder test case	43
2.6	Mach number contours; <i>Left</i> : current simulation, <i>Right</i> : Burbeau & Sagaut (2002)	43
2.7	Grid representation for Mesh 1 (<i>left</i>) and Mesh 2 (<i>right</i>) showing every 4th grid-line	44
2.8	Streamwise velocity (<i>left</i>) and temperature (<i>right</i>) profiles; $-$: Poiseuille analytical solution, \bullet : Mesh 1, \times : Mesh 2.	45
2.9	Configuration of the channel flow	46
2.10	Averaged velocity profile along the wall-normal direction; \bullet : Foyi et al. (2004)	47
2.11	Averaged temperature ($-$), pressure ($-$) and density ($-$) profile along the wall-normal direction; \bullet : Foyi et al. (2004)	47
2.12	Van Driest velocity profile along the wall-normal direction; the dashed line: viscous sublayer and logarithmic law, \bullet Foyi et al. (2004) . Here, κ and C are the Von Karman and log-law constants, respectively.	48
2.13	Instantaneous contours of the fluctuating streamwise velocity in $x-z$ plane at $t^* \approx 150$ for different y^+	48
2.14	Reynolds stress tensor along y-direction along the wall-normal direction; $-$: $\langle \rho \rangle \widetilde{u''u''}/\tau_w$, $-$: $\langle \rho \rangle \widetilde{v''v''}/\tau_w$, $-$: $\langle \rho \rangle \widetilde{w''w''}/\tau_w$, \bullet : Foyi et al. (2004)	49
2.15	Schematic of the Experimental setup.	50
3.1	(a) Normalized velocities, (b) Normalized velocities RMS along the wall-normal direction in the presence of an adverse pressure gradient; $-$: WM-LES, $-$: DNS.	51
3.2	Schematic representation of the TBLE and the WM-LES mesh.	57
3.3	Color maps of Mach-number flow field in the $x-y$ plane (<i>top</i>) strong pressure gradient, (<i>bottom</i>) moderate pressure gradient. Red color being the highest positive value and dark-blue color the lowest value.	59
3.4	Van Driest velocity along the wall-normal direction; $-$: zero-pressure gradient $\Delta p^+ = 0$, $-$: adverse pressure gradient $\Delta p^+ = 0.0075$, $-$: favorable pressure gradient $\Delta p^+ = -0.0025$	59

- 3.5 Wall-shear stress over time with zero-pressure gradient(a) and adverse pressure gradient (b); —: Wall-resolved data, —: Reconstructed data using the STBLE model. 60
- 3.6 Van Driest velocity along the wall-normal direction with zero-pressure gradient (a) and adverse pressure gradient (b); —: Wall-resolved data (....: Subtracted data), •: Reconstructed data using the STBLE model showing every 4th-grid line. 61
- 3.7 Normalized velocity along the wall-normal direction, zero-pressure gradient (a) and adverse pressure gradient (b); —: WM-LES, —: DNS. 64
- 3.8 Normalized velocities RMS along the wall-normal direction, zero-pressure gradient (a) and adverse pressure gradient (b); —: WM-LES, —: DNS. . . 64
- 3.9 Grid representation of both WR nozzle (in black) and WM nozzle (in cyan) test-cases showing every 10^{th} grid-line. The nozzle throat is located at $x = 0$. 66
- 3.10 (a) Instantaneous z-averaged numerical “Schlieren” imaging contour $|\nabla\rho|$ in the $x - y$ plane for $npr=1.7$, (b) Schematic representation of the density-gradient field showing different phenomena occurring inside the nozzle. . 66
- 3.11 (a) Pressure distribution at the center of the nozzle; --: WR-LES, - : WR-LES from [Olson & Lele \(2011\)](#), —: WM-LES and ■: Experimental results from [Johnson & Papamoschou \(2010\)](#). (b) Van Driest velocity along the wall-normal direction at $x/\delta_i = -10$; --: WR-LES,: $u^+ = y^+$ —: WM-LES, - : WR-LES from [Olson & Lele \(2011\)](#). 67
- 3.12 (a) Mean velocity-defect normalized by the friction velocity along the wall-normal direction at —: $x/\delta_i = -10$;—: $x/\delta_i = -5$, —: $x/\delta_i = 0$ and —: $x/\delta_i = 5$ with dash line representing WR-LES and solid line representing WM-LES. (b) WR-LES Log-law diagnostic function $\Xi = y^+ du^+/dy^+$ at $x/\delta_i = 0$. 68
- 3.13 Numerical Schlieren pictures and mean density flows contours for: (a) and (b) NPR=1.4, (c) and (d) NPR=1.7, (e) and (f)NPR=2.5. Red lines represent the trapped recirculation bubbles 69
- 3.14 (a) Pressure distribution at the lower wall , (b) P_{rms} distribution at the lower wall and (c) Root-mean-square level of wall pressure fluctuations normalized by the wall shear stress (τ_w), with p_i is the inlet static pressure, (—) NPR=1.4, (—) NPR=1.7, (—) NPR=2.5. 70
- 3.15 Normalized pre-multiplied spectra of wall-pressure fluctuations distribution along the streamwise direction for $NPR = 1.7$ 71

3.16	Normalized pre-multiplied spectra of the pressure fluctuations at the lower wall at: (a) throat, (b) nozzle exit, (c) mean separation position, (d) the separation zone, for different NPRs with (—) NPR=1.4, (—) NPR=1.7, (—) NPR=2.5.	72
4.1	Instantaneous wall-pressure forces integrated along the upper and the lower walls, data have been filtered with a cutoff Strouhal number of 0.2; —: streamwise forces, —: side loads. —WR-LES from Piquet (2017).	75
5.1	Grid representation of the wall-modeled nozzle test-case showing every 5 th grid-line. For this WM-LES, the grid is regularly spaced following, $f_{str,y} = (2\eta/N_y - 1)$ with η is the generalized curvilinear coordinate in wall-normal direction. The nozzle throat is located at $x = 0$	91
5.2	(a) Normalized mean wall pressure; (○): experimental results Papamoschou et al. (2009), (b) Probability density function (PDF) of the shock position; (—) : present LES, (○): experimental results Papamoschou et al. (2009), (○): previous LES Olson & Lele (2013). (c) Cross power spectral density of the normalized shock position; (○): experimental results Johnson & Papamoschou (2010)	93
5.3	(a) Reconstructed u'/u_∞ field from a prob located at $x/\delta_i = -4$ and $y/\delta_i = 0.78$. (b) Normalized streamwise-velocity fluctuation (u') autocorrelation at $y/\delta_i = -0.78$ and $z/\delta_i = 10$	95
5.4	Wall-pressure autocorrelation functions, as a function of streamwise location for different NPRs; (a, b): NPR=1.4 lower and upper wall respectively, (c, d): NPR=1.7 lower and upper wall respectively, (e, f): NPR=2.5 lower and upper wall respectively.	97
5.5	(a) Recirculation bubbles at the lower wall for different NPRs; red: NPR=1.4, blue: NPR=1.7, black: NPR=2.5, (b) Recirculation bubbles for NPR=2.5 and (c) Recirculation bubbles at the lower wall for different NPRs; orange: NPR=1.5, sky-blue: NPR=1.6, purple: NPR=1.7 and green: NPR=1.8	98
5.6	Space-time correlation of the normalized pressure field in the separated zone at the separation location for different NPRs; (a): NPR=1.4, (b): NPR=1.7 and (c): NPR=2.5.	99
5.7	Normalized pre-multiplied spectra map of wall-pressure fluctuations $St\mathcal{F}(p'/p_{rms})$ at the lower wall, for different NPRs; (a): NPR=1.4, (b): NPR=1.7 and (c): NPR=2.5.	100

5.8	(a) Mean shock velocity and (b) Main tone, as a function of the nozzle pressure ratio; (■) theoretical values from Zaman et al. (2002), (■) empirical values.	102
5.9	Normalized cross power spectral density of the shock position and the entering mass flow rate; (a) NPR=1.5 (b) NPR=1.6 (c) NPR=1.7 (d) NPR=1.8.	103
5.10	(a) Probability density function for the shock velocity; (b) Shock position vs. time; (—) Mach stem, (—) shock foot	105
5.11	(a) Mach stem oscillation velocity vs. time, (b) Averaged Mach stem span by direction by cycle, (c) Mach stem oscillation velocity by direction by cycle and (d) Pausing rate per direction.(■) Upstream-movement, (■) Downstream-movement	106
6.1	DMD mode reconstruction; (a) non-helical (b) helical mode in form of the isovolume of the real part with negative and positive pressure fluctuations, p' , for two different frequencies. Red to yellow color indicates positive pressure fluctuations, yellow being the highest. Dark blue to light blue indicates negative pressure fluctuations, light blue being the highest.	109
7.1	Z-averaged instantaneous numerical "Schlieren" contours showing the extreme positions reached by the shock for $NPR = 1.7$; (left) adiabatic case, (middle) cooled case, (right) heated case.	125
7.2	(a) Distribution of the temperature-velocity relationship at the throat with the circles indicating the equilibrium solutions , (b) Distribution of total temperature profiles at the throat, with — case-A, — case-B and — case-C.	129
7.3	(a) skin friction coefficient distribution over the lower wall (C_f), (a) Normalized-mean wall pressure distribution (p_w/p_a) and (c) Normalized root mean square of the wall pressure at the lower wall (p_{rms}/p_a) with — case-A, — case-B and — case-C.	130
7.4	Van Driest velocity along the wall-normal direction at $x/\delta_i = -10$; —: WM-LES, -- : WR-LES from Piquet (2017), -- : $u^+ = y^+$ and the log-law with $\kappa = 0.41$ and $C^+ = 6.2$, •: WR-LES from Olson & Lele (2011).	130
7.5	3D representation of the different phenomenon observed in the nozzle flow; the shock system and the turbulent boundary layer represented using the iso-volume of the $\nabla \rho $ and the reversed flow using $\nabla u $	131
7.6	Z-averaged instantaneous numerical "Schlieren" contours with the extreme positions reached by the shock are shown below; (left) case-A, (middle) case-B, (right) case-C.	132

7.7	Contours of instantaneous skin friction (left) and Stanton number (right); (a,b) case-A, (c,d) case-B, (e,f) case-C.	133
7.8	Normalized pre-multiplied spectra map of the pressure fluctuations at the lower wall, with blue regions being the most energetic and the white regions the less energetic; (a) case-A, (b) case-B and (c) case-C.	134
7.9	Normalized pre-multiplied spectra of: (a) shock position, (b) side loads with — case-A, — case-B and — case-C.	134
A.1	(a) Van Driest normalized velocity at $Re_x = 5 \times 10^6$; •: Pirozzoli <i>et al.</i> Pirozzoli et al. (2004) , ■: Guarini <i>et al.</i> Gatski & Erlebacher (2002) , -- : Log-wall with $C^+ = 5.5$, (b) Averaged temperature profile at $Re_x = 5 \times 10^6$; •: Pirozzoli <i>et al.</i> Pirozzoli et al. (2004)	144
A.2	Streamwise, wall-normal and spanwise Reynolds stress tensor (a) and normalized shear tensor terms (b) at $Re_x = 5 \times 10^6$; •: Pirozzoli <i>et al.</i> Pirozzoli et al. (2004)	144

List of Tables

1.1	A summary of the most pertinent sources of the LFO found in the literature.	11
2.1	Channel flow domain	46
2.2	Channel flow properties	46
2.3	The geometrical parameters of Papamoschou <i>et al.</i> 's planar nozzle. . . .	50
3.1	Results of the <i>a priori</i> test using the DNS results.	61
3.2	Grid requirements for the WM-LES	62
3.3	Grid parameters for the WR/WM-LES of the planar nozzle flow.	66
3.4	Main tone comparison	71
5.1	grid parameters	92
5.2	Summary table of different cases treated.	102
7.1	Flow parameters for LES simulations; NPR is the nozzle pressure ration and ε is the nozzle area ratio. The subscript w refers to the wall properties, ∞ to the free stream properties and th to the throat.	128

Bibliography

- Ackeret, J., Feldmann, F. & Rott, N. (1947), ‘investigations of compression shocks and boundary layers in gases moving at high speed’, *NACA TM 1113*. (Cited on page 9).
- Aeschliman, D. P. & Oberkampf, W. L. (1998), ‘Experimental methodology for computational fluid dynamics code validation’, *AIAA J.* **36**(5), 733–741. (Cited on page 10).
- Agostini, L., Larcheveque, L., Dupont, P., Debiève, J. F. & Dussauge, J. P. (2012), ‘Zones of influence and shock motion in a shock/boundary-layer interaction’, *AIAA J* **50**(6), 1377–1387. (Cited on pages 13 & 90).

- Ahlberg, J., Migdal, S. & Nilson, N. (1961), ‘Truncated perfect nozzles in optimum nozzle design’, pp. 614–620. (Cited on page 2).
- Andreopoulos, J. & Muck, K. C. (1987), ‘Some new aspects of the shock-wave/boundary-layer interaction in compression-ramp flows’, *J. Fluid Mech.* **180**, 405–428. (Cited on page 11).
- Back, L. H. & Cuffel, R. F. (1976), ‘Shock wave/turbulent boundary-layer interactions with and without surface cooling’, *AIAA Journal* **14**(4), 526–532. (Cited on page 127).
- Balaras, E., Benocci, C. & Piomelli, U. (1996), ‘Two-layer approximate boundary conditions for large-eddy simulations’, *AIAA journal* **34**(6), 1111–1119. (Cited on page 55).
- Beresh, S. J., Clemens, N. T. & Dolling, D. S. (2002), ‘Relationship between upstream turbulent boundary-layer velocity fluctuations and separation shock unsteadiness’, *AIAA J.* **40**(12), 2412–2422. (Cited on pages 11, 12 & 89).
- Bernardini, M., Asproulis, I., Larsson, J., Pirozzoli, S. & Grasso, F. (2016), ‘Heat transfer and wall temperature effects in shock wave turbulent boundary layer interactions’, *Physical Review Fluids* **1**(8). (Cited on pages 126, 127, 128, 129 & 131).
- Boccaletto, L. (2011), Maitrise du d’écoulement de tuyère. Analyse du comportement d’une tuyère de type TOC et définition d’un nouveau concept : le BOCCAJET, PhD thesis.
URL: <http://www.theses.fr/2011AIX10012/document> (Cited on page 19).
- Bogar, T., Sajben, M. & Kroutil, J. (1983), ‘Characteristic frequencies of transonic diffuser flow oscillations’, *AIAA journal* **21**(9), 1232–1240. (Cited on pages 23 & 96).
- Boin, J.-P. & Robinet, J.-C. (2004), ‘Three-dimensional unsteady laminar shock-wave/boundary layer interaction’, *NATO RTO-AVT-111 10-1/10-10*. (Cited on page 15).
- Borodai, S. G. & Moser, R. D. (2001), ‘The Numerical Decomposition of Turbulent Fluctuations in a Compressible Boundary Layer’, *Theor. and Comp. Fluid Dynamics* **15**(1), 35–63. (Cited on page 15).
- Bourgoing, A. & Reijasse, P. (2005), ‘Experimental analysis of unsteady separated flows in a supersonic planar nozzle’, *Shock Waves* **14**, 251–258. (Cited on page 8).
- Brown, G. L. & Roshko, A. (1974), ‘On density effects and large structure in turbulent mixing layers’, *Journal of Fluid Mechanics* **64**(4), 775–816. (Cited on pages 18 & 149).

- Burbeau, A. & Sagaut, P. (2002), ‘Simulation of a viscous compressible flow past a circular cylinder with high-order discontinuous galerkin methods’, *Computers & Fluids* **31**(8), 867–889. (Cited on pages 42, 43 & 150).
- Cabot, W. & Moin, P. (2000), ‘Approximate wall boundary conditions in the large-eddy simulation of high Reynolds number flow’, *Flow, Turbulence and Combustion* **53**(1-4), 269–29. (Cited on pages 52 & 61).
- Chapman, R., Kuehn, M. & Larson, K. (1958), Investigation of separated flows in supersonic and subsonic streams with emphasis on the effect of transition. (Cited on pages 9 & 92).
- Chaudhuri, A. & Hadjadj, A. (2016), ‘Numerical investigations of transient nozzle flow separation’, *Aerospace Science & Tech.* **53**, 10 – 21. (Cited on pages 8 & 33).
- Chaudhuri, A., Hadjadj, A. & Chinnayya, A. (2011), ‘On the use of immersed boundary methods for shock/obstacle interactions’, *Journal of Computational Physics* **230**(5), 1731–1748. (Cited on page 33).
- Chaudhuri, A., Hadjadj, A., Chinnayya, A. & Palerm, S. (2011), ‘Numerical study of compressible mixing layers using high-order weno schemes’, *Journal of Scientific Computing* **47**(2), 170–197. (Cited on page 33).
- Chaudhuri, A., Hadjadj, A., Sadot, O. & Glazer, E. (2012), ‘Computational study of shock-wave interaction with multiple obstacles using immersed boundary method’, *International Journal for Numerical Methods in Engineering* **89**(8), 975–990. (Cited on page 33).
- Chen, C. L., Chakravarthy, S. R. & Hung, C. M. (1994), ‘Numerical investigation of separated nozzle flows’, *AIAA J.* **32**(9), 1836–1843. (Cited on pages 7 & 90).
- Cinnella, P. & Cedric, C. (2015), *Assessment of time implicit discretizations for the computation of turbulent compressible flows*. (Cited on page 38).
- Clemens, N. T. & Narayanaswamy, V. (2014), ‘Low-frequency unsteadiness of shock wave/turbulent boundary layer interactions’, *Annual Review of Fluid Mechanics* **46**(1), 469–492. (Cited on page 89).
- Coleman, G., Kim, J. & Moser, R. (1995), ‘A numerical study of turbulent supersonic isothermal-wall channel flow’, *Journal of Fluid Mechanics* **305**, 159–183. (Cited on page 48).

- Crighton, D. G. & Gaster, M. (1976), ‘Stability of slowly diverging jet flow’, *Journal of Fluid Mechanics* **77**(2), 397–413. (Cited on page 17).
- Dallmann, U. (1988), ‘Three-dimensional vortex structures and vorticity topology’, *Fluid Dynamics Research* **3**(1), 183 – 189. (Cited on page 15).
- Delery, J. (1992), ‘Experimental investigation of the reflection of a shock wave on a heated surface in presence of a turbulent boundary layer’, *Recherche aerospaciale Technical translation* (1), 1–23. (Cited on page 127).
- Delery J, M. J. (1986), ‘Shock-wave boundary layer interactions’, *AGARDograph 280. Brussels: NATO* . (Cited on page 126).
- Deng, X. & Zhang, H. (2000), ‘Developing high-order weighted compact nonlinear schemes’, *Journal of Computational Physics* **165**(1), 22–44. (Cited on pages 33 & 34).
- Dolling, D. S. (2001), ‘Fifty years of shock-wave/boundary-layer interaction research: What next?’, *AIAA J.* **39**(8), 1517–1531. (Cited on page 14).
- Don, L., Hui-Li, H. & Yong-Lai, Z. (2018), ‘A high-order method for simulating convective planar poiseuille flow over a heated rotating sphere’, *International Journal of Numerical Methods for Heat & Fluid Flow* **28**(8). (Cited on page 42).
- Ducros, F., Ferrand, V., Nicoud, F., Weber, C., Darracq, D., Gacherieu, C. & Poinso, T. (1999), ‘Large-eddy simulation of the shock/turbulence interaction’, *Journal of Computational Physics* **152**(2), 517–549. (Cited on page 36).
- Dupont, P., Haddad, C., Ardisson, J. & Debiève, J. (2005), ‘Space and time organisation of a shock wave/turbulent boundary layer interaction’, *Aerospace Science & Tech.* **9**(7), 561 – 572. (Cited on pages 8, 12, 14, 89 & 96).
- Duprat, C., Balarac, G., Métais, O., Congedo, P. M. & Brugière, O. (2011), ‘A wall-layer model for large-eddy simulations of turbulent flows with/out pressure gradient’, *Physics of Fluids (1994-present)* **23**(1), 015101. (Cited on pages 52, 53, 55, 56, 60, 61, 62, 63 & 73).
- Dussauge, J. P., Dupont, P. & Debiève, J. F. (2006), ‘Unsteadiness in shock wave boundary layer interaction with separation’, *Aerospace Science & Tech.* **10**, 85–91. (Cited on pages 8 & 14).
- Dussauge, J. P. & Piponnier, S. (2008), ‘Shock/boundary-layer interactions: Possible sources of unsteadiness’, *J. Fluids and Struct.* **24**(8), 1166–1175. (Cited on pages 11, 12, 13, 14, 15 & 96).

- Edwards, J. R., Choi, J.-I. & Boles, J. A. (2008), ‘Large eddy/reynolds-averaged navier-stokes simulation of a mach 5 compression-corner interaction’, *AIAA J.* **46**(4), 977–991. (Cited on page 14).
- Erengil, M. E. & Dolling, D. S. (1993), ‘Physical causes of separation shock unsteadiness in shock-wave/turbulent boundary layer interactions’, *AIAA P.* **93**, 31–34. (Cited on pages 11, 89 & 105).
- Fage, A. & Sargent, R. F. (1947), ‘Shock-wave and boundary-layer phenomena near a flat surface’, *Proceedings of the Royal Society of London. Series A. Mathematical and Physical Sciences* **190**(1020), 1–20. (Cited on page 9).
- Ferri, A. (1940), ‘Experimental results with airfoils tested in the high speed tunnel at guidonia’, *NACA TM 946*. (Cited on page 9).
- Fournier, G., Chpoun, A., Fraigneau, Y. & Tenaud, C. (2018), *Direct Numerical Simulations of the Shock-Induced Separation of a Laminar Boundary Layer*, Vol. 24, pp. 327–332. (Cited on pages 9 & 12).
- Fournier, G., Sellam, M., Chpoun, A., Fraigneau, Y. & Tenaud, C. (2015), Dns of the interaction between an oblique shock wave and a boundary layer developing along a flat plate. (Cited on page 12).
- Foysi, H., Sarkar, S. & Friedrich, R. (2004), ‘Compressibility effects and turbulence scalings in supersonic channel flow’, *Journal of Fluid Mechanics* **509**, 207–216. (Cited on pages 45, 46, 47, 48, 49 & 150).
- Frey, M. & Hagemann, G. (2000), ‘Restricted shock separation in rocket nozzles’, *J. Prop & Power* **16**(3), 478–484. (Cited on page 7).
- Frey, M., Makowka, K. & Aichner, T. (2017), ‘The TICTOP nozzle: a new nozzle contouring concept’, **9**(2), 175–181. (Cited on page 2).
- Ganapathisubramani, B., Clemens, N. T. & Dolling, D. S. (2007), ‘Effects of upstream boundary layer on the unsteadiness of shock-induced separation’, *J. Fluid Mech.* **585**, 369–394. (Cited on pages 11, 12, 13, 14, 89, 93 & 94).
- Garnier, E. (2009), ‘Stimulated detached eddy simulation of three-dimensional shock/boundary layer interaction’, *Shock Waves* **19**, 479–486. (Cited on page 15).
- Gatski, T. & Erlebacher, G. (2002), ‘Numerical simulation of a spatially evolving supersonic turbulent boundary layer’. (Cited on pages 143, 144 & 154).

- Georges-Picot, A. (2014), Développement de modèles physiques et numériques pour la simulation aux grandes échelles des écoulements dans les tuyères supersoniques, PhD thesis, Normandie Université. 2014ISAM0024.
URL: <http://www.theses.fr/2014ISAM0024/document> (Cited on pages 24 & 149).
- Germano, M., Piomelli, U., Moin, P. & Cabot, W. H. (1991), ‘A dynamic subgrid-scale eddy viscosity model’, *Physics of Fluids A: Fluid Dynamics* **3**(7), 1760–1765. (Cited on page 55).
- Gonsalez, J. & Dolling, D. (1993), *Correlation of interaction sweepback effects on unsteady shock-induced turbulent separation*. (Cited on pages 105 & 139).
- Gramann, R. & Dolling, D. (1992), *A preliminary study of the turbulent structures associated with unsteady separation shock motion in a Mach 5 compression ramp interaction*. (Cited on page 89).
- Grossman, I. J. & Bruce, P. J. K. (2018), ‘Confinement effects on regular–irregular transition in shock-wave–boundary-layer interactions’, *Journal of Fluid Mechanics* **853**, 171–204. (Cited on pages 5 & 149).
- Grötzbach, G. (1987), ‘Direct numerical and large eddy simulation of turbulent channel flows’, *Encyclopedia of Fluid Mechanics* **13**, 376 – 404. (Cited on page 52).
- Guarini, S., Moser, R., Shariff, K. & Wray, A. (2000), ‘Direct numerical simulation of a supersonic turbulent boundary layer at mach 2.5’, *Journal of Fluid Mechanics* **414**, 1–33. (Cited on pages 57 & 143).
- Hadjadj, A. (2012), ‘Large-eddy simulation of shock/boundary-layer interaction’, *AIAA Journal* **50**(12), 2919–2927. (Cited on page 33).
- Hadjadj, A. & Kudryavtsev, A. (2005), ‘Computation and flow visualization in high-speed aerodynamics’, *Journal of Turbulence* **6**(16), 1–25. (Cited on page 33).
- Hadjadj, A., Kudryavtsev, A. N. & Ivanov, M. S. (2004), ‘Numerical investigation of shock-reflection phenomena in overexpanded supersonic jets’, *AIAA Journal* **42**(3), 570–577. (Cited on pages 18 & 149).
- Hadjadj, A. & Onofri, M. (2009), ‘Nozzle flow separation’, *Shock Waves* **19**, 163–169. (Cited on pages 8 & 88).
- Hadjadj, A., Perrot, Y. & Verma, S. (2015), ‘Numerical study of shock/boundary layer interaction in supersonic overexpanded nozzles’, *Aerospace Science and Technology*

42, 158 – 168.

URL: <http://www.sciencedirect.com/science/article/pii/S1270963815000255> (Cited on pages 20 & 149).

Hiroshi, K., Seiji, T. & Takanori, H. (2017), *Sparsity-Promoting Dynamic Mode Decomposition Analysis on Aeroacoustics of a Clustered Supersonic Jet*. (Cited on page 145).

Ho, C.-M. & Huang, L.-S. (1982), ‘Subharmonics and vortex merging in mixing layers’, *Journal of Fluid Mechanics* **119**, 443–473. (Cited on page 17).

Holder, D. W., Pearcey, H. H. & Gadd, G. E. (1954), ‘The interaction between shock wave and boundary layers’, *British Aeronautical Research Council Current Paper, 180* . (Cited on page 9).

Hunt, D. & Nixon, D. (1991), ‘A very large eddy simulation of an unsteady shock wave/turbulent boundary layer interaction’, *Fluid Dynamics Conference* . (Cited on page 11).

Hunter, C. A. (2004), ‘Experimental investigation of separated nozzle flows’, *J. Propulsion & Power* **527-532**. (Cited on pages 8, 21 & 23).

Irrenfried, C. & Steiner, H. (2017), ‘Dns based analytical p-function model for rans with heat transfer at high prandtl numbers’, *International Journal of Heat and Fluid Flow* **66**, 217 – 225. (Cited on page 52).

Jaunet, V., Debiève, J. F. & Dupont, P. (2014), ‘Length scales and time scales of a heated shock-wave/boundary-layer interaction’, *AIAA Journal* **52**(11), 2524–2532. (Cited on page 127).

Johnson, A. D. & Papamoschou, D. (2010), ‘Instability of shock-induced nozzle flow separation’, *Phys. Fluids* **22**(1), 16102. (Cited on pages 8, 12, 22, 65, 67, 75, 93, 96, 151 & 152).

Jovanovic, M. R., Schmid, P. J. & Nichols, J. W. (2014), ‘Sparsity-promoting dynamic mode decomposition’, *Physics of Fluids* **26**(2), 024103. (Cited on page 145).

Kawai, S. & Larsson, J. (2012), ‘Wall-modeling in large eddy simulation: Length scales, grid resolution, and accuracy’, *Physics of Fluids (1994-present)* **24**(1), 015105. (Cited on pages 53, 61 & 65).

Kawai, S. & Larsson, J. (2013), ‘Dynamic non-equilibrium wall-modeling for large eddy simulation at high Reynolds numbers’, *Physics of Fluids (1994-present)* **25**(1), 015105. (Cited on pages 52, 53, 56, 62, 63 & 73).

- Kawai, S. & Lele, S. K. (2008), ‘Localized artificial diffusivity scheme for discontinuity capturing on curvilinear meshes’, *Journal of Computational Physics* **227**(22), 9498–9526. (Cited on page 39).
- Kiya, M. & Sasaki, K. (1983), ‘Structure of a turbulent separation bubble’, *Journal of Fluid Mechanics* **137**, 83–113. (Cited on page 18).
- Kutz, J. N., Fu, X. & Brunton, S. L. (2016), ‘Multiresolution dynamic mode decomposition’, *SIAM Journal on Applied Dynamical Systems* **15**(2), 713–735. (Cited on page 146).
- Larusson, R., Andersson, N. & Östlund, J. (2017), ‘Dynamic mode decomposition of a separated nozzle flow with transonic resonance’, *AIAA Journal* **55**(4), 1295–1306. (Cited on pages 145 & 147).
- Lee, J.-H. & Sung, H. J. (2009), ‘Structures in turbulent boundary layers subjected to adverse pressure gradients’, *Journal of Fluid Mechanics* **639**, 101–131. (Cited on page 59).
- Lesshafft, L., Semeraro, O., Jaunet, V., Cavalieri, A. V. G. & Jordan, P. (2019), ‘Resolvent-based modeling of coherent wave packets in a turbulent jet’, *Phys. Rev. Fluids* **4**, 063901. (Cited on page 17).
- Liepmann, H. W. (1946), ‘The interaction between boundary layer and shock waves in transonic flow’, *J. of the Aeronautical Scien.* **13**(12), 623–637. (Cited on page 9).
- Lilly, D. K. (1992), ‘A proposed modification of the germano subgrid-scale closure method’, *Physics of Fluids A: Fluid Dynamics* **4**(3), 633–635. (Cited on pages 32 & 55).
- Maerder, T., Adams, N. & Kleiser, L. (2001), ‘Direct simulation of turbulent supersonic boundary layers by an extended temporal approach’, *Journal of Fluid Mechanics* **429**, 187–216. (Cited on page 144).
- Manhart, M., Peller, N. & Brun, C. (2008), ‘Near-wall scaling for turbulent boundary layers with adverse pressure gradient’, *Theoretical and Computational Fluid Dynamics* **22**(3-4), 243–260. (Cited on pages 53 & 56).
- Martelli, E., Ciottoli, P. P., Saccoccio, L., Nasuti, F., Valorani, M. & Bernardini, M. (2019), ‘Characterization of unsteadiness in an overexpanded planar nozzle’, *AIAA J.* **57**(1), 239–251. (Cited on pages 11, 13, 23 & 89).

- Martini, E., Cavalieri, A. V. G. & Jordan, P. (2019), ‘Acoustic modes in jet and wake stability’, *Journal of Fluid Mechanics* **867**, 804–834. (Cited on page 16).
- McClure, W. (1992), An experimental study of the driving mechanism and control of the unsteady shock induced turbulent separation in a Mach 5 compression corner flow, PhD thesis, Univ. Texas, Austin. (Cited on page 89).
- Mi, J., Nathan, G. J. & Luxton, R. E. (2001), ‘Mixing Characteristics of a Flapping Jet from a Self-Exciting Nozzle’, *Flow, Turbulence and Combustion* **67**(1), 1–23. (Cited on pages 20, 21 & 149).
- Moin, P., Squires, K., Cabot, W. & Lee, S. (1991), ‘A dynamic subgrid-scale model for compressible turbulence and scalar transport’, *Physics of Fluids A: Fluid Dynamics* **3**(11), 2746–2757. (Cited on page 55).
- Morgan, B., Duraisamy, K., Nguyen, N., Kawai, S. & Lele, S. K. (2013), ‘Flow physics and rans modelling of oblique shock/turbulent boundary layer interaction’, *J. Fluid Mech* **729**, 231–284. (Cited on pages 13 & 126).
- Morris, G. J., Jurewicz, J. T. & Palmer, G. M. (1992), ‘Gas-Solid Flow in a Fluidically Oscillating Jet’, *Journal of Fluids Engineering* **114**(3), 362–366. (Cited on page 20).
- Mouronval, A.-S. (2004), Etude Numérique Des phénomènes aeroélastiques en aérodynamique supersonique. Application aux tuyères propulsives., PhD thesis, INSA de Rouen. (Cited on page 1).
- Nagano, Y., Tagawa, M. & Tsuji, T. (1993), Effects of adverse pressure gradients on mean flows and turbulence statistics in a boundary layer, in ‘Turbulent Shear Flows 8’, Springer, pp. 7–21. (Cited on page 59).
- Nagib, H. M. & Chauhan, K. A. (2008), ‘Variations of von kármán coefficient in canonical flows’, *Physics of Fluids* **20**(10), 1518. (Cited on page 59).
- Nave, L. & Coffey, G. (1973), ‘Sea level side loads in high-area-ratio rocket engines’, *9th Propulsion Conference* . (Cited on page 7).
- Nichols, J. W. & Lele, S. K. (2011), ‘Global modes and transient response of a cold supersonic jet’, *Journal of Fluid Mechanics* **669**, 225–241. (Cited on page 17).
- Nicoud, F. & Ducros, F. (1999), ‘Subgrid-Scale Stress Modelling Based on the Square of the Velocity Gradient Tensor’, *Flow, Turbulence and Combustion* **62**(3), 183–200. (Cited on page 31).

- Nituch, M., Sjolander, S. & Head, M. (1978), ‘An improved version of the Cebeci-Smith eddy-viscosity model’, *Aeronautical Quarterly* **29**, 207–225. (Cited on pages 55 & 60).
- Nonomura, T. & Fujii, K. (2013), ‘Robust explicit formulation of weighted compact nonlinear scheme’, *Computers & Fluids* **85**, 8–18. (Cited on page 34).
- Nonomura, T., Iizuka, N. & Fujii, K. (2010), ‘Freestream and vortex preservation properties of high-order weno and wcns on curvilinear grids’, *Computers & Fluids* **39**(2), 197–214. (Cited on page 34).
- Nonomura, T., Terakado, D., Abe, Y. & Fujii, K. (2015), ‘A new technique for freestream preservation of finite-difference weno on curvilinear grid’, *Computers & Fluids* **107**, 242–255. (Cited on page 34).
- Olson, B. J. (2012), Large-eddy simulation of multi-material mixing and over-expanded nozzle flow, PhD thesis, Stanford university. (Cited on pages 91 & 92).
- Olson, B. J. & Lele, S. K. (2011), ‘Large-eddy simulation of an over-expanded planar nozzle’, AIAA P. **3908**. (Cited on pages 5, 8, 13, 49, 50, 65, 67, 75, 89, 129, 130, 138, 149, 151 & 153).
- Olson, B. J. & Lele, S. K. (2013), ‘A mechanism for unsteady separation in over-expanded nozzle flow’, *Physics of Fluids (1994-present)* **25**(11), 110809. (Cited on pages 92, 93, 96 & 152).
- Örlü, R., Fransson, J. H. & Alfredsson, P. H. (2010), ‘On near wall measurements of wall bounded flows - the necessity of an accurate determination of the wall position’, *Progress in Aerospace Sciences* **46**(8), 353–387. (Cited on page 59).
- Papamoschou, D. & Johnson, A. (2006), ‘Unsteady phenomena in supersonic nozzle flow separation’, AIAA P. **3360**. (Cited on pages 5, 8, 13, 49, 138 & 149).
- Papamoschou, D., Zill, A. & Johnson, A. (2009), ‘Supersonic flow separation in planar nozzles’, *Shock Waves* **19**(3), 171–183. (Cited on pages 21, 23, 91, 92, 93, 101 & 152).
- Pilinski, C. (2002), Etude numérique du décollement en tuyères supersoniques, PhD thesis, INSA de Rouen. (Cited on pages 7 & 19).
- Piomelli, U. & Balaras, E. (2002), ‘Wall-layer models for large-eddy simulations’, *Annual Review of Fluid Mechanics* **34**(1), 349–374. (Cited on pages 52 & 55).
- Piponniau, S., Dussauge, J. P., Debiève, J. F. & Dupont, P. (2009), ‘A simple model for low-frequency unsteadiness in shock-induced separation’, *J. Fluid Mech.* **629**, 87–108. (Cited on pages 11, 12, 14, 15, 18, 23, 89 & 126).

- Piquet, A. (2017), Physical analysis and numerical simulation of the separation phenomenon in over-expanded nozzle flow, PhD thesis, Normandie Université ; Imperial College London. (Cited on pages 22, 23, 32, 33, 36, 49, 50, 63, 75, 91, 92, 127, 129, 130, 138, 149, 152 & 153).
- Piquet, A., Roussel, O. & Hadjadj, A. (2016), ‘A comparative study of brinkman penalization and direct-forcing immersed boundary methods for compressible viscous flows’, *Computers and Fluids* **136**(1), 272–284. (Cited on page 33).
- Piquet, A., Zebiri, B., Hadjadj, A. & Safdari-Shadloo, M. S. (2019), ‘A parallel high-order compressible flows solver with domain decomposition method in the generalized curvilinear coordinates system’, *International Journal of Numerical Methods for Heat and Fluid Flow* **30**(1), 2–38. (Cited on pages 53, 90 & 127).
- Pirozzoli, S. (2010), ‘Generalized conservative approximations of split convective derivative operators’, *Journal of Computational Physics* **229**(19), 7180 – 7190.
URL: <http://www.sciencedirect.com/science/article/pii/S0021999110003219> (Cited on pages 34 & 89).
- Pirozzoli, S. (2011), ‘Stabilized non-dissipative approximations of Euler equations in generalized curvilinear coordinates’, *Journal of Computational Physics* **230**(8), 2997–3014. (Cited on page 39).
- Pirozzoli, S. & Grasso, F. (2006), ‘Direct numerical simulation of impinging shock wave/turbulent boundary layer interaction at $m=2.25$ ’, *Physics of Fluids* **18**(6), 065113. (Cited on pages 11, 12, 13, 14 & 126).
- Pirozzoli, S., Grasso, F. & Gatski, T. B. (2004), ‘Direct numerical simulation and analysis of a spatially evolving supersonic turbulent boundary layer at $m=2.25$ ’, *Physics of Fluids* **16**(3), 530–545.
URL: <https://doi.org/10.1063/1.1637604> (Cited on pages 57, 143, 144 & 154).
- Platzer, M. F., Simmons, J. M. & Bremhorst, K. (1978), ‘Entrainment characteristics of unsteady subsonic jets’, *AIAA Journal* **16**(3), 282–284. (Cited on page 20).
- Plotkin, K. J. (1975), ‘Shock wave oscillation driven by turbulent boundary-layer fluctuations’, *AIAA Journal* **13**(8), 1036–1040. (Cited on page 89).
- Poggie, J. & Smits, A. (2001), ‘Shock unsteadiness in a reattaching shear layer’, *Journal of Fluid Mechanics* **429**(2), 155–185.
URL: <https://doi.org/10.2514/3.60501> (Cited on page 89).

- Poinsot, T. & Lelef, S. (1992), ‘Boundary conditions for direct simulations of compressible viscous flows’, *Journal of Computational Physics* **101**(1), 104 – 129. (Cited on page 50).
- Powell, A. (1953), ‘The noise of choked jets’, *The Journal of the Acoustical Society of America* **25**(3), 385–389. (Cited on page 17).
- Prièbe, S. & Martin, M. P. (2012), ‘Low-frequency unsteadiness in shock wave, turbulent boundary layer interaction’, *J. of Fluid Mech.* **699**, 1–49. (Cited on pages 13 & 90).
- Raman, G. & Rice, E. J. (1994), ‘Development of phased twin flip-flop jets’, *Journal of Vibration and Acoustics* **116**, 263–268. (Cited on page 20).
- Rao, G. V. R. (1958), ‘Exhaust nozzle contour for optimum thrust’, *Journal of Jet Propulsion* **28**(6), 377–382. (Cited on page 2).
- Rao, G. V. R. (1960), ‘Approximation of optimum thrust nozzle contours’, *ARS Journal* p. 561. (Cited on page 2).
- Rizzetta, D. P., Visbal, M. R. & Gaitonde, D. V. (2001), ‘Large-eddy simulation of supersonic compression-ramp flow by high-order method’, *AIAA J.* **39**(12), 2283–2292. (Cited on page 12).
- Robinet, J.-C. (2007), ‘Bifurcations in shock-wave/laminar-boundary-layer interaction: global instability approach’, *Journal of Fluid Mechanics* **579**, 85–112. (Cited on page 13).
- Roe, P. L. (1981), ‘Approximate Riemann solvers, parameter vectors, and difference schemes’, *Journal of Computational Physics* **43**(2), 357–372. (Cited on page 35).
- Schlichting, H. & Gersten, K. (2003), *Boundary-layer theory*, Springer Science and Business Media. (Cited on page 42).
- Schmid, P. J. (2010), ‘Dynamic mode decomposition of numerical and experimental data’, *Journal of Fluid Mechanics* **656**, 5–28. (Cited on page 146).
- Schmidt, O. T., Towne, A., Rigas, G., Colonius, T. & Brès, G. A. (2018), ‘Spectral analysis of jet turbulence’, *Journal of Fluid Mechanics* **855**, 953–982. (Cited on page 17).
- Schumann, U. (1975), ‘Subgrid scale model for finite difference simulations of turbulent flows in plane channels and annuli’, *Journal of Computational Physics* **18**(4), 376 – 404. (Cited on page 52).

- Sciacovelli, L., Cinnella, P. & Gloerfelt, X. (2017), ‘Direct numerical simulations of supersonic turbulent channel flows of dense gases’, *Journal of Fluid Mechanics* **821**, 153–199. (Cited on page 126).
- Sellam, M., Fournier, G., Chpoun, A. & Reijasse, P. (2014), ‘Numerical investigation of overexpanded nozzle flows: Asymmetrical configuration and hysteresis phenomenon’, *Shock Waves* **24**. (Cited on page 7).
- Shadloo, M. & Hadjadj, A. (2017), ‘Laminar-turbulent transition in supersonic boundary layers with surface heat transfer: A numerical study’, *Numerical Heat Transfer, Part A: Applications* **72**(1), 40–53. (Cited on page 33).
- Sharma, S., Shadloo, M. & Hadjadj, A. (2019), ‘Turbulent flow topology in supersonic boundary layer with wall heat transfer’, *International Journal of Heat and Fluid Flow* **78**, 108430. (Cited on page 53).
- Shimshi, E., Ben-Dor, G., Levy, A. & Krothapalli, A. (2015), ‘Asymmetric and unsteady flow separation in high mach number planar nozzles’, *IJASAR* pp. 65–80. (Cited on page 8).
- Simpson, R. L. (1983), ‘A model for the backflow mean velocity profile’, *AIAA journal* **21**(1), 142–143. (Cited on page 56).
- Souverein, L. J., Dupont, P., Debiève, J. F., Dussauge, J. P., Van Oudheusden, B. W. & Scarano, F. (2010), ‘Effect of interaction strength on unsteadiness in turbulent shock-wave-induced separations’, *AIAA Journal* **48**(7), 1480–1493. (Cited on page 126).
- Spalding, D. (1961), ‘A single formula for the law of the wall’, *Journal of Applied Mechanics* **28**(3), 455–458. (Cited on page 52).
- Steiner, H. & Irrenfried, C. (2019), ‘Modelling of thermal wall boundary conditions with temperature-dependent material properties for use in rans’, *International Journal of Heat and Fluid Flow* **80**, 108495. (Cited on page 52).
- Sun, B., Wang, C. & Zhuo, C. (2020), ‘Theoretical model and numerical analysis for asymmetry of shock train in supersonic flows’, *Symmetry* **12**(4), 518. (Cited on page 22).
- Sutton, G. P. & Biblarz, O. (2016), *Rocket Propulsion Elements*, 9 edn, Wiley. (Cited on pages 3 & 149).
- Taieb, D. (2010), Simulation numérique des écoulements turbulents dans les canaux de refroidissement, Master’s thesis, INSA de Rouen. (Cited on page 46).

- Telega, J., Szwaba, R. & Doerffer, P. (2019), ‘Shock waves asymmetry in a symmetric nozzle’, *Symmetry* **11**(12), 1477. (Cited on page 22).
- Touber, E. (2010), Unsteadiness in shock-wave/boundary layer interactions, PhD thesis. **URL:** <http://eprints.soton.ac.uk/161073/> (Cited on pages 13, 14, 15, 90 & 94).
- Touber, E. & Sandham, N. D. (2009), ‘Large-eddy simulation of low-frequency unsteadiness in a turbulent shock-induced separation bubble’, *Theor. and Comp. Fluid Dynamics* **23**, 79–107. (Cited on pages 13 & 126).
- Touber, E. & Sandham, N. D. (2011), ‘Low-order stochastic modelling of low-frequency motions in reflected shock-wave/boundary-layer interactions’, *Journal of Fluid Mechanics* **671**, 417–465. (Cited on pages 89, 93, 94 & 96).
- Ünalımis, O. & Dolling, D. (1994), ‘Decay of wall pressure field and structure of a mach 5 adiabatic turbulent boundary layer’, *Fluid Dynamics Conference* . (Cited on page 11).
- Verma, S. B. & Manisankar, C. (2014), ‘Origin of flow asymmetry in planar nozzles with separation’, *Shock Waves* **24**(2), 191–209. (Cited on pages 6, 8, 9, 21, 23 & 149).
- Verma, S., Chidambaranathan, M. & Hadjadj, A. (2018), ‘Analysis of shock unsteadiness in a supersonic over-expanded planar nozzle’, *Eur. J. Mech./B Fluids* **68**, 55–65. (Cited on page 8).
- Viets, H. (1975), ‘Flip-flop jet nozzle’, *AIAA Journal* **13**(10), 1375–1379. (Cited on page 20).
- Visbal, M. R. & Gaitonde, D. V. (2002), ‘On the use of higher-order finite-difference schemes on curvilinear and deforming meshes’, *Journal of Computational Physics* **181**(1), 155–185. (Cited on page 39).
- Wang, M. & Moin, P. (2002), ‘Dynamic wall modeling for large-eddy simulation of complex turbulent flows’, *Physics of Fluids (1994-present)* **14**(7), 2043–2051. (Cited on pages 53, 55 & 61).
- Weiyu, L., Guoping, H., Jinchun, W. & Shuli, H. (2019), ‘Spatio-temporal dynamic mode decomposition in a shear layer flow’, *Aerospace Science and Technology* **91**, 263 – 271. (Cited on page 145).
- White, F. M. & Corfield, I. (2006), *Viscous fluid flow*, McGraw-Hill New York. (Cited on pages 57 & 143).

- Williamson, J. (1980), ‘Low-storage Runge-Kutta schemes’, *Journal of Computational Physics* **35**(1), 48–56. (Cited on page 37).
- Wu, M. & Martin, M. P. (2008), ‘Analysis of shock motion in shockwave and turbulent boundary layer interaction using direct numerical simulation data’, *J. Fluid Mech* **594**, 71–83. (Cited on page 14).
- Wu, P. & Miles, R. (2000), ‘Mhz rate visualization of separation shock structure’, *38th Aerospace Sciences Meeting and Exhibit* . (Cited on pages 11 & 14).
- Xiao, Q., Tsai, H. M. & Papamoschou, D. (2007), ‘Numerical investigation of supersonic nozzle flow separation’, *AIAA J.* **45**(3), 532–541. (Cited on pages 8 & 22).
- Xie, Z.-T. & Castro, I. P. (2008), ‘Efficient generation of inflow conditions for large eddy simulation of street-scale flows’, *Flow, Turbulence and Combustion* **81**(3), 449–470. (Cited on page 50).
- Yang, L., Dong, Ma and Benshuai, F., Qiang, L. & Chenxi, Z. (2019), ‘Direct numerical simulation of fine flow structures of subsonic-supersonic mixing layer’, *Aerospace Science and Technology* **95**, 105431. (Cited on page 145).
- Zaman, K., Dahl, M., Bencic, T. & Loh, C. (2002), ‘Investigation of a transonic resonance with convergent–divergent nozzles’, *Journal of Fluid Mechanics* **463**, 313–343. (Cited on pages 11, 12, 23, 71, 73, 102, 104, 107, 139 & 153).
- Zebiri, B., Piquet, A., Hadjadj, A. & Verma, S. B. (2020), ‘Shock-Induced Flow Separation in an Overexpanded Supersonic Planar Nozzle’, *AIAA Journal* (58:5), 2122–2131. **URL:** <https://doi.org/10.2514/1.J058705> (Cited on pages 26, 65, 89, 90, 91 & 127).